**Universidad Autónoma de Madrid**
**Facultad de Ciencias Físicas**
**Departamento de Física Teórica**

# An infrared study of galactic OH/IR stars

**Francisco M. Jiménez Esteban**
**Madrid, 2004**

**Universidad Autónoma de Madrid**
Facultad de Ciencias Físicas
Departamento de Física Teórica

# An infrared study of galactic OH/IR stars

Supervised by
**Dr. Pedro García Lario**
and
**Dr. Dieter Engels**

PhD Thesis presented by
**Francisco M. Jiménez Esteban**
to obtain the degree of
**Doctor in Physics**

Madrid, June 2004

*A Marta,*
*la estrella más hermosa.*

# Agradecimientos

Han sido muchos años de duro trabajo y enorme sacrificio los que me han permitido presentar esta tesis doctoral. Largos años en los cuales me he preguntado más de una vez si todo este esfuerzo realmente merecía la pena. Y no me lo he preguntado por mí, ya que, en el fondo, la investigación en astrofísica me apasiona y he podido disfrutar cada gota de sudor vertida en ello. No, me lo he preguntado por las personas más cercanas a mí, las cuales han tenido que compartir en mayor o menor medida todos estos años de sacrificio. Es especialmente por ellos por los que me animo a escribir estas líneas, no para tratar de compensarles, ya que eso sería imposible, pero sí para hacerles llegar mi más profundo agradecimiento y para decirles que sin ellos ésto no hubiera sido posible. También me gustaría aprovechar para agradecer a un sin fin de personas su ayuda desinteresada o simplemente, aunque mucho más importante, su amistad.

Así me gustaría empezar agradeciendo con todas mis fuerzas a la persona que lleva compartiendo su vida conmigo desde hace más de 8 años. Gracias a Marta, gracias por estar a mi lado y por compartir todo este tiempo conmigo. Gracias por todos esos fines de semana dedicados a trabajar, por esos viajes suspendidos y vacaciones anuladas. Gracias por aguantar mis despistes, olvidos y ausencias. Gracias por haber aprendido a vivir con un futuro incierto e inestable. Gracias por ayudarme y apoyarme siempre, incluso cuando no me lo merecía. En definitiva, gracias de todo corazón por ser el amor de mi vida. A ti va dedicado este trabajo porque sin ti no hubiera sido posible.

Quisiera dar las gracias a mis padres, Fausto y Esperanza, por haberme enseñado todas esas cosas que no se aprenden en los libros, por haberme inculcado valores tan necesarios para realizar una tesis como el sacrificio y el trabajo duro, y por darme su cariño y apoyo incondicional. También me gustaría dar las gracias a mis hermanos, Espe, Mamen y Javi, por todos esos buenos ratos, por ser mi familia y por todo su cariño.

Quiero agradecer a mi mejor amigo, Alber, por ser como es, por estar siempre a mi lado, por estar siempre dispuesto a salir a correr o a pasear por la sierra, por todo ese amor y esa alegría que sabe contagiar como nadie.

Quisiera agradecer a mi familia adoptiva, Rosa, Pepi, Mari, Camila y Siska, por haberme abierto su corazón y haberme dejado entrar de lleno en su familia. También quiero agradecer especialmente a Rosa todo la ayuda que nos ha prestado, sobretodo a lo largo de esta última etapa de la tesis.

No puedo dejar de dar las gracias a Pedro por dirigirme esta tesis, por haber confiado en mí desde el primer momento, por tener siempre un hueco para atenderme, aunque lo tuviera que sacar del tiempo de estar con su familia, por su paciencia y dedicación. Gracias por empeñarte en que escribiera la tesis en inglés, a pesar de que ello te ha supuesto mucho más trabajo, y gracias muy especialmente por el enorme esfuerzo que te ha tocado hacer en el sprint final de esta tesis.

También quiero agradecer a Dieter, no sólo por codirigir esta tesis con Pedro, si no también por su hospitalidad, acogiéndome en su casa durante una de mis estancias en el Observatorio de Hamburgo. Gracias por su paciencia, especialmente con mi nefasto inglés, y por su siempre sensata opinión.

Gracias a Benja, porque hace ya un montón de años escuchó a un grupo de estudiantes ilusionados que querían hacer una tesis doctoral en astrofísica, y sin pensárselo dos veces les ofreció la posibilidad de visitar VILSPA. De esta manera pude empezar a trabajar con Pedro.

Gracias a todos los del LAEFF, a los que están y a los que estuvieron. Gracias por haberme acogido entre vosotros durante mis años itinerantes sin un lugar fijo donde trabajar. Gracias por hacer que el LAEFF sea un oasis donde refugiarse, y un lugar donde siempre tener un amigo. Espero que no cambiéis nunca.

Gracias a toda la gente de VILSPA, por convertir este lugar en un sitio privilegiado para trabajar. Gracias especialmente a toda la gente del club de futbolín, por permitirme descargar mi adrenalina con ellos, y hacerme pasar estupendas sobremesas con emocionantes partidas. También quiero dar las gracias a todos los del running club, por tener la paciencia de estar pendientes de uno que les sigue a distancia con la lengua fuera.

A mi compañero de footing, Bruno, por esas carreras que nos ayudaban a despejar la mente, y por esos ánimos que mutuamente nos hemos dado durante este nuestro último año de tesis.

También tengo que agradecer a mi familia de la UEM, Adeli, Águeda, Luis, Susi, Ricardo, Rosa y Bea, por haberme hecho sentir como en casa durante los dos años que estuve con ellos. Y muy especialmente, quiero dar las gracias a Ricardo, por esas jornadas de footing donde no sólo compartíamos esfuerzo, si no que además él compartía conmigo toda su experiencia y sensatez a nivel tanto profesional como personal. Gracias.

No puedo dejar de agradecer a Bea y a Susi, por sus jornadas nocturnas en la UEM, cuando los bedeles nos tenían que recordar que nos esperaban en casa.

Finalmente, gracias a mis amigos de toda la vida, a Emi, Fer, Javi, Juan y Rubén, gracias a todos ellos por haber mantenido su amistad durante más de 20 años, por no haberme dado la espalda cuando por mis acciones lo hubiera merecido, y por seguir siendo mis mejores amigos.

Francisco M. Jiménez Esteban

23 de Junio de 2004

# List of contents

# List of Figures

# List of Tables

## Summary

In this thesis work we present a study of galactic OH/IR stars carried out mainly in the infrared wavelength range, although we have also used optical and radio data for the analysis.

Firstly, we have analysed 371 IRAS sources belonging to the so-called 'Arecibo sample of OH/IR stars'. Accurate astrometry and single-epoch near-infrared photometry have been obtained, and the main photometric properties of the OH/IR stars in the sample have been determined. The relative distribution of sources with and without optical counterpart in the IRAS two-colour diagram and their characteristic near infrared colours have been interpreted as the consequence of the increasing thickness of their circumstellar shells.

Subsequently, we have extend the same kind of analysis to a sample of 94 OH/IR stars belonging to the GLMP catalogue (the 'GLMP sample') presenting much redder colours.

As a byproduct, we have created the largest atlas of OH/IR stars existing up to date. This atlas consists of optical and near-infrared finding charts for a total of 465 OH/IR stars, all of them studied in this thesis.

With the whole sample of OH/IR stars (what we have called the 'extended sample', including both Arecibo and GLMP sources) we have interpreted the colour sequence displayed by the OH/IR stars in the IRAS two colour [12]–[25] vs. [25]–[60] diagram (the 'O-rich AGB sequence') in terms of evolutionary stage and/or progenitor masses. To reach this goal we have previously determined the luminosity distribution of a subsample of GLMP OH/IR stars located in the direction of the Galactic Bulge, assuming that they are all bulge population stars and, thus, a common distance for all them equivalent to the distance to the Galactic Centre. Because of the strongly peaked distribution found (at a luminosity of $3\,500\,\mathrm{L}_\odot$) we have assumed this value for the remaining OH/IR stars as a first guess of their true luminosity. This way we have explored both their distance and galactic height distribution.

Finally, we have studied in detail the variability properties of a "small" sample of 25 galactic sources selected from the IRAS Point Source Catalogue as candidate long-period variable stars in the late-AGB phase. The results presented are the output of a monitoring program carried out over a period of more than 10 years. Our study also includes the detailed analysis of the light curves derived, which show that in many cases they are far from symmetrical and show secular variations which are yet unexplained. The results obtained are discussed in the context of stellar evolution.

## Resumen

En esta tesis presentamos un estudio de estrellas OH/IR galáticas llevado a cabo principalmente en el rango de longitudes de onda del infrarrojo, aunque para el análisis hemos usado también datos del óptico y de radio.

En primer lugar, hemos analizado 371 fuentes IRAS pertenecientes a la llamada ‘muestra de estrellas OH/IR de Arecibo’. Se ha obtenido astrometría de precisión y fotometría en el infrarrojo cercano, y se han determinado las principales propiedades fotométricas de las estrellas OH/IR de la muestra. La distribución relativa en el diagrama de colores IRAS [12]–[25] vs. [25]–[60] de las fuentes con y sin contrapartida óptica, al igual que sus característicos colores en el infrarrojo cercano, se han interpretado como una consecuencia del incremento de espesor de sus envolturas circumestelares.

Posteriormente, este análisis se ha ampliado con una muestra de 94 estrellas OH/IR mucho más enrojecidas pertenecientes al catálogo GLMP.

Como un subproducto, hemos creado el atlas de estrellas OH/IR más extenso existente hasta la fecha. Este atlas consiste en cartas de identificación en el óptico y en el infrarrojo cercano para un total de 465 estrellas OH/IR, todas ellas estudiadas en esta tesis .

Con esta amplia muestra de estrellas OH/IR recopilada (que incluye tanto las fuentes de Arecibo como las del catálogo GLMP) hemos interpretado la secuencia de colores mostrada por dichas estrellas en el diagrama de colores IRAS (la llamada ’O-rich AGB sequence’) en términos del estado evolutivo y/o de la masa de la estrella progenitora. Para ello, previamente hemos determinado la distribución de luminosidad de un grupo de estrellas OH/IR pertenecientes al catálogo GLMP localizadas en la dirección del Bulbo Galáctico, y asumiendo que todas estas estrellas son parte de la población del bulbo hemos podido asignarles una distancia común equivalente a la distancia al Centro Galáctico. Dado que la distribución de luminosidad obtenida para estas estrellas esta fuertemente concentrada entorno a $3\,500\,\mathrm{L}_\odot$, hemos asignado este valor al resto de estrellas OH/IR como una primera aproximacion a su verdadera luminosidad. De este modo, hemos podido explorar tanto su distribución de distancia como de altura galáctica.

Para concluir el trabajo de esta tesis, hemos estudiado en detalle las propiedades de variabilidad de una “pequeña” muestra de 25 fuentes galácticas, seleccionadas todas ellas del Catálogo de Fuentes Puntuales IRAS como posibles candidatas a estrellas variables de largo periodo en una etapa avanzada de la fase AGB. Los resultados presentados son el producto de un programa de seguimiento llevado a cabo durante un periodo superior a 10 años. Nuestro estudio incluye también el análisis detallado de las curvas de luz derivadas, el cual demuestra que, en muchos casos, las curvas de luz están lejos de ser simétricas y muestran variaciones seculares que aún están por explicar. Estos resultados son analizados en el contexto de la evolución estelar.

# Chapter 1

# Introduction

The study of the stellar evolution in the *Asymptotic Giant Branch* (AGB) is interesting from many points of view. It is one of the final stages of stellar evolution for the great majority of stars ($1-8\,\mathrm{M}_{\odot}$), just before becoming Planetary Nebulae (PNe). During this phase the stars experience a large mass-loss which contributes to the enrichment and chemical evolution of the galaxies. In addition, due to their high luminosity, they are not only an important part of the integrated light of the galaxies, but they can also be used as probes of their overall structure and dynamics. On the other hand, this type of stars provides us with fascinating systems where complicated physico-chemical processes are taking place. We should not forget that the Sun, our source of energy and thanks to which the life on the Earth exists, sooner or later may go through this evolutionary stage. These reasons, among others, make the study of the AGB evolutionary phase of great interest for astrophysics.

## 1.1 Stellar Evolution

Stars at the moment of their birth are constituted mainly of hydrogen. A fast process of contraction due to the gravity action of the *Protostellar Cloud*, produces an increase of pressure and temperature in the core, which reaches the necessary conditions to start nuclear reactions. It is at this moment when the most stable and longer phase of the life of stars begins, the phase in which the hydrogen is burnt into helium. This stage is denominated *Main Sequence* and its duration depends fundamentally on the initial mass of stars. For example, stars of $1\,\mathrm{M}_{\odot}$ spend $\approx 10^{10}$ years in this phase, while much longer main sequence lifetimes are expected for stars of smaller mass, and much shorter lifetimes are predicted by the models for stars with larger mass. When stars leave the Main Sequence they begin a long and complex way through the Hertzsprung-Russell (H-R) diagram that will also come determined by their initial mass, being different for stars of low, intermediate or high mass.

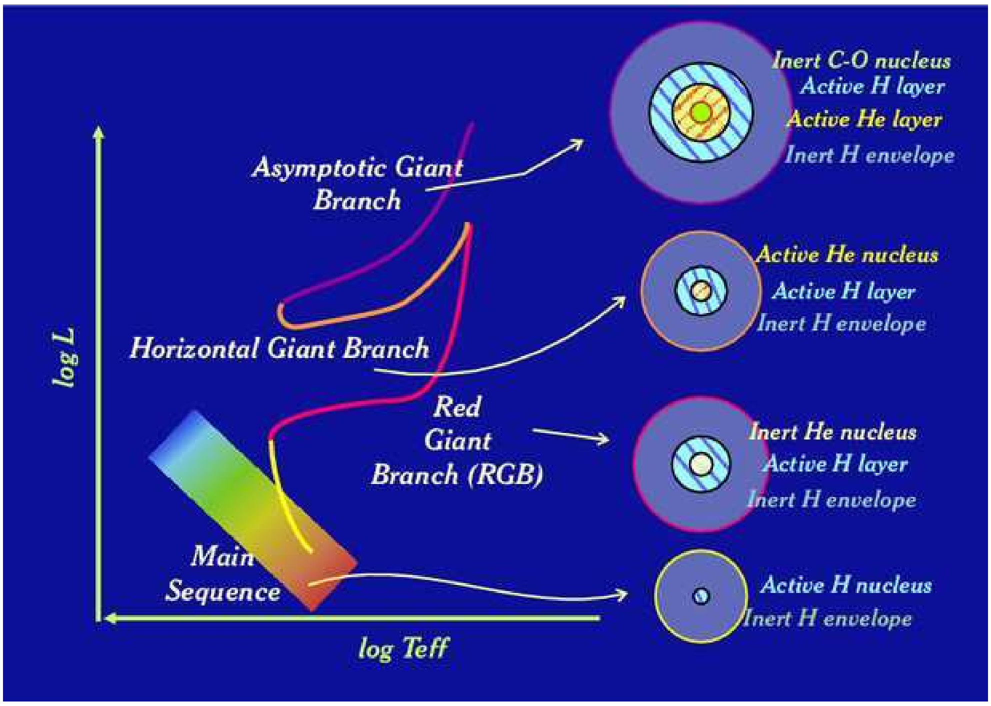

**Figure 1.1**: Hertzsprung-Russell diagram for stars of low and intermediate mass

If stars have low mass, they consume their hydrogen creating an inert core of helium and degenerated electron gas, surrounded as well by an active hydrogen layer that we will call *mantle*[1]. It is in this mantle where stars produce energy through the hydrogen burning. Stars leave the Main Sequence with the contraction of the core, which increases its temperature and warms up the mantle of hydrogen, increasing at the same time the energy generation rate. This causes the expansion of the mantle, reaching a very high luminosity and a low effective temperature. At this moment stars receive the name of *Red Giants*, and during a short period of time in comparison with the one spent in the Main Sequence, stars will follow in the H-R diagram the *Red Giant Branch* (RGB) (see Figure 1.1).

At the end of the RGB phase, a sudden contraction of the core takes place, which reaches the necessary temperature to break the degeneration of the electron gas. Then, the helium burns in an explosive way, in what is denominated the *helium flash*. The increase of temperature due to the helium flash produces an expansion of the core, which is followed by a decrease of the core temperature at the same time that the energy production rate becomes smaller. All of this causes a reduction of the stellar radius, and the subsequent loss of luminosity. During this phase two nuclear active zones exist: the core, where the

---

[1] Although normally this region between core and atmosphere is denominated envelope, we have preferred to reserve this term for the circumstellar matter that is beyond the atmosphere.

helium is transformed into carbon and oxygen, and the inner regious of the mantle, where the hydrogen is transformed into helium. Stars are now in the *Horizontal Giant Branch* (HGB).

After some time, stars will have formed a new core, this time of carbon, oxygen and not degenerated electron gas, the hydrogen mantle will stop its activity and will expand again increasing the stellar luminosity. Stars describe at this stage in the H-R diagram the so-called *Asymptotic Giant Branch* (AGB), an evolutionary track which asymptotically approaches the RGB but with a higher luminosity. During the first stage of this new phase, or *Early Asymptotic Giant Branch* (E-AGB), the core contracts considerably increasing its density, although the temperature will only increase a little since the electron gas will become degenerated again. At this point stars will be formed by a small and compact degenerated core of carbon and oxygen, surrounded by a thin helium burning layer and a hydrogen mantle of enormous dimensions and very low density. This phase is similar to the Red Giant phase, but now the energy is obtained from the burning of helium instead of hydrogen. The combustion of the helium is unstable, and the energy generated produces the expansion of the helium layer, its subsequent cooling and the cessation of the nuclear reaction. Then in the inner regions of the mantle of hydrogen the ignition is restarted. The combustion of the hydrogen feeds the helium layer until the point of restarting its combustion again in a so-called *'thermal pulse'*, with, in this case, the subsequent cessation of the nuclear reactions in the hydrogen mantle. This new phase, where stars alternate the region where they produce their energy (the majority of the time in the hydrogen mantle and occasionally in the helium layer) is denominated *Thermal Pulsing Asymptotic Giant Branch* (TP-AGB) (Schwarzschild & Härm 1965).

The scenario showed above is followed by stars of low mass ($< 1-2\,\mathrm{M}_\odot$). For stars of intermediate mass the evolution is somehow different, since the helium core created during the Main Sequence is sufficiently hot to prevent degeneration of the electron gas, and then the helium combustion forms a core of carbon and oxygen. This will cause that stars will not go along the RGB. In due time helium burning will continue in a shell around a core of carbon and oxygen and at some point the electron gas in this core will degenerate, forcing stars to continue this way their evolution towards the TP-AGB (Habing 1996). During this phase the convective zone of the mantle can reach the inner layer where the nuclear reactions are taking place, producing a dredge-up of processed material from the interior to the stellar atmosphere (*third dredge-up*), changing the chemical abundance of the stellar surface. The changes can be dramatic in terms of dominant chemistry if the number of carbon atoms in the stellar atmosphere becomes larger than the number of oxygen atoms after several 'thermal pulses' (Wallerstein & Knapp 1998). These stars are known as *carbon stars.*

During the brief ($\approx 10^3$ years) 'thermal pulses' in which the energy is obtained from helium, and which periodically occur in timescales of $10^4 - 10^5$ years (longer timescales for lower masses; Wagenhuber & Groenewegen 1998), a strong instability is generated, which causes stellar pulsation with typical periods $> 100^d$ and large amplitude variations in luminosity (the stars become *large amplitude long period variables* (LALPV)). The pulsation of the star causes the transfer of mechanical energy to the most external zones of the atmosphere that are weakly bound by the gravity, therefore the gas can easily reach the escape velocity helped by the radiation pressure on dust grains. This way stars undergo processes of enormous mass-loss which lead to the formation of a *Circumstellar Envelope* (CSE) of gas and dust around the central star. The dust grains of the CSE absorb the optical radiation coming from the central star and reemit it in the infrared, becoming strong infrared sources from 1 to 100 $\mu$m. At the end of the TP-AGB the mass-loss that some stars undergo can be enormous, reaching $10^{-4}\,M_\odot \mathrm{year}^{-1}$ (Bedijn 1987). This causes an increase of the optical thickness of the CSE, with the subsequent obscuration of the light coming from the central star, which in some cases can eventually become invisible in the optical, being only detectable at longer wavelengths. *Mira variables* and *variable OH/IR stars* are clear examples of this evolutionary phase. In the case of Mira variables, their CSE are optically thin allowing the light coming from the central star reaching us at optical wavelengths, while, variable OH/IR stars have thicker envelopes that prevent the detection of the central star in the optical range, being the CSE only detectable in the infrared or at radio wavelengths, mainly in the light of an OH maser at 1612 MHz.

Both low and intermediate mass stars suddenly stop the mass-loss and the variability when they have lost practically all its mantle . This moment will mark the beginning of a new phase of the stellar evolution so-called *Post-AGB*, where nuclear reactions in the star stop for ever. During this phase stars are composed of an inert carbon-oxygen core and an expanding gas-dust envelope (Sivagnanam & Le Squeren 1990). From now on, the temperature on the central star will increase until the envelope becomes ionized and a new *Planetary Nebula* is formed. Finally, the CSE will dissipate into the interstellar medium, while the central star slowly gets colder, becoming a *White Dwarf.*

The previously described evolutionary scenario is not followed by stars with high mass. They have cores so hot that the electron gas never becomes degenerated, and the process of combustion of the helium core is followed by the combustion of the carbon-oxygen core. The process continues with forming new cores of heavier and heavier elements until iron is formed. Massive stars will have at this stage an “onion structure” and can be very red in the optical and be surrounded by thick gas-dust CSE, but they will never pass through the AGB phase. They will finish their life exploding as *type II Supernovae*, enriching interstellar medium with the elements formed in their core.

## 1.2 Precedents in the study of OH/IR stars

In the last years, with the access to the infrared (IR) and radio wavelengths, a considerable advance in the study of the last stages of the stellar evolution, both theoretical and observational, has taken place. Shklovskii suggested in 1956 the possibility that the red giants were the progenitors of planetary nebulae. For this to happen, the star must experience an enormous mass-loss in a very short period of time, which implies the formation of a thick circumstellar shell, and subsequently, total obscuration of the light coming from the central star in the optical range in the most extreme cases. This is the main reason why the search for these objects has to be made at radio and/or IR wavelengths.

Systematic survey programs in the near-infrared of these objects were very useful. In 1969, Neugebauer & Leighton published the IRC catalogue of sources detected at $2.2\,\mu$m. Some of these objects were indeed completely invisible in the optical, which corroborated predictions. By those days, an important discovery was carried out: some of infrared stars recently detected showed maser emission of the hydroxyl molecule (OH) with a typical double peaked shape (Wilson & Barrett 1968). This shape was interpreted as the consequence of the existence of an expansion envelope. One year later the emission of a new maser due to the water molecule ($H_2O$) was discovered in the supergiant VY CMa (Knowles et al. 1969). A third maser, this time due the silicon oxide molecule (SiO) was discovered in 1975 in late type stars (Kaifu et al. 1975). In the following years, using the rising space technology, several systematic survey programs in the IR were carried out, as the atmosphere absorbs great part of the infrared radiation. Thus, studies were carried out from airplanes that flew over the terrestrial atmosphere, stratospheric globes and rockets, which increased a lot the number of known infrared objects. In 1976, Price & Walker published the AFGL catalogue of infrared sources ($4.2\,\mu$m, $11.0\,\mu$m, $19.8\,\mu$m, and $27.4\,\mu$m). On the other hand, radio telescopes were used to search for OH maser sources among objects previously detected in the infrared (IRC, AFGL) (Caswell & Haynes 1975; Johansson et al. 1977a,b; Bowers & Sinha 1978; Baud et al. 1979a,b,1981a,b; Caswell et al. 1981). When optical identification was possible, the OH maser was found to be associated with Mira variables and M-Supergiants (Wilson & Barrett 1972). Furthermore, optically unidentified IRC objects with OH maser emission (OH-IRC) were also classified as Mira variables or M-Supergiants (Hyland et al. 1972) on the basis of the characteristics absorption bands of $H_2O$ ($1.9\,\mu$m) and CO ($2.3\,\mu$m). The OH emitting optically unidentified AFGL objects (OH-AFGL) were also associated to late M-stars similar to OH-IRC sources, but extending to even redder colours (Allen et al. 1977). Schultz et al. (1976), and Evans & Beckwith (1977) confirmed that a great number of these OH emitters were associated to infrared sources. Then, it was agreed to designate these objects as ***"OH/IR stars"***, which were soon identified as the missing link between red giants and planetary nebulae.

A model describing the physical conditions of the envelopes where OH masers are detected was developed by Goldreich & Scoville (1976). Based on this model, Elitzur et al. (1976) proposed that the OH molecule is excited by far IR radiation, mainly at $35\,\mu$m. This pump mechanism would work at distances of about $10^{16}$ cm from the star, where a suitable density of OH molecules and low temperature ($< 200$ K) are expected. This idea was supported by the fact that the OH maser emission and the IR emission vary simultaneously (Harvey et al. 1974), and by the correlation found between OH maser luminosity and IR colours. In the model proposed by Reid et al. (1977), the OH maser comes from the expanding envelope of gas and dust, where the blue peak is emitted by the nearest part to us, and the red peak from the remote part of the envelope. From this theory it should be possible to measure the expansion velocity of the envelope just from the difference of the peak velocities, the radial velocity of the star being the average of the two observed peak velocities.

All these results confirmed the theory that the planetary nebula formation is preceded by an intense mass-loss phase. In this context Renzini (1981) introduced the so-called *'Superwind'* theory, according to which the mass-loss would increase substantially at the end of the AGB phase and this would cause the loss of the outer layers of the central star in a very short time, compared with the whole duration of this evolutionary phase. This theory was later confirmed by OH maser observations of OH/IR stars and extreme Mira variables (Baud & Habing 1983; Herman & Habing 1985b).

Thanks to the *Infrared Astronomical Satellite* (IRAS), launched in 1983 and which was operative during 10 months, a great advance in the study of these objects in the mid-far-infrared was achieved. This satellite made a survey of practically all the sky (96%) in four photometric bands centered at $12\,\mu$m, $25\,\mu$m, $60\,\mu$m and $100\,\mu$m. This survey allowed the generation of the IRAS Point Source Catalogue (IRAS-PSC) (Beichman et al. 1988) which contains more than 250 000 entries. To be included in this catalogue an object must have been detected at least in two different epochs separated by hours, days or months. Comparing the density fluxes measured at $12\,\mu$m and $25\,\mu$m in different orbits, an *IRAS Variability Index* (VAR) was derived, which represented the probability that the source could be variable. The index can have values between 0 (no variability) and 99 (clearly variable). Nevertheless, this VAR parameter should be handled with care as the reliability of its value is strongly dependent on the intrinsic variability of the source and on the number and time distribution of the different observations made by the satellite. An object with a high value of VAR can be considered as variable without any doubt, however an object with low value of VAR may be or not variable, since a variable star could be classified as non-variable just because the different observations were not sufficiently spaced in time to allow the detection of an appreciable difference in brightness, or because it was observed with equal brightness just by chance during the different observations made by IRAS. Another important result of the IRAS mission was the obtaining of Low Resolution Spectra (LRS), from 7.5 to 23 $\mu$m with a resolving power of about 20, for the subsample formed by the brightest point sources (F $\gtrsim$ 5 Jy at 12 $\mu$m and F $\gtrsim$ 10 Jy at 25 $\mu$m). However, not all LRS were included in the resulting catalogue because of the adopted stringent selection criteria (see IRAS Explanatory Supplement for a more extensive explanation; Beichman et al. 1988). They allow us to determine the dominant chemistry of the dust grains in the CSE: carbonaceous compounds in C-rich stars and silicates in O-rich stars. C-rich stars have their LRS characterized by the presence of a strong feature of SiC at 11.3 $\mu$m, while O-rich stars are characterized by the presence of a strong feature of SiO at 9.7 $\mu$m and another one of $SiO_2$ at 18 $\mu$m. LRS also allowed us to distinguish between optically thin or optically thick CSEs at mid-IR wavelengths as a function of whether these spectral features appear in emission or absorption in the spectrum (e.g. Volk and Cohen 1989; Kwok et al. 1997). In some cases, however, the classification is not possible, because the spectrum is featureless. This may be caused by the presence of the the silicate emission feature self-absorbed.

One of the most important tools for studying stars in the AGB is the *IRAS Colour-Colour Diagram* [12]–[25] vs. [25]–[60], where the colours are defined in the standard way:

$$\left.\begin{array}{l} [12]-[25] = -2.5\log\frac{F_\nu(12)}{F_\nu(25)} \\ \\ [25]-[60] = -2.5\log\frac{F_\nu(25)}{F_\nu(60)} \end{array}\right\}$$

Just after the release of the IRAS-PSC, well-known variable OH/IR stars were found to follow a well defined sequence in the IRAS colour-colour diagram with its blue end connected with the colours shown by Mira variables (Olnon et al. 1984). This is consistent with the theory which considers that OH/IR stars are the result of the evolution of Mira variables in their way to become planetary nebula.

In 1987 Bedijn interpreted the IRAS colours for Mira variables and OH/IR stars for the first time, with the help of models which predicted their spectral energy distribution and that assumed that the stars have CSEs of increasing thickness with their inner radius located at a distance from the central star corresponding to the condensation radius of the dust grains. In order to reproduce the observed infrared colours it was necessary to introduce in the model a continuously increasing mass-loss rate along the sequence. However, this can only explain satisfactorily the position of variable OH/IR stars in the IRAS colour-colour diagram. To be able to explain also the colours shown by the non-variable OH/IR stars it was necessary to assume that their central stars had completely stopped their mass-loss. This idea had previously been suggested by Herman & Habing (1985b).

In 1988 van der Veen & Habing defined several regions which separate different kind of objects in the IRAS two colour-colour diagram (See Figure 1.2). This way, they described the position of various types of sources in the diagram including not only the sequence showed by O-rich AGB stars (Miras and OH/IR stars; I − II − IIIa − IIIb − IV) but also the position where C-rich AGB stars are dominant (VII) and also the position where PNe and post-AGB stars are preferentially located (V).

Van der Veen & Habing (1988) also combined the photometric information contained in the IRAS colour-colour diagram with that coming from the IRAS LRS spectroscopy. They showed for O-rich AGB stars how objects placed in the blue part of the diagram (mainly regions I & II) had thin CSE, and those placed in the red part of the diagram (mainly regions IIIb & IV) had thick CSE. Thus, they concluded that the sequence predicted by the model of Bedijn (discontinuous line) is a sequence of CSE thickness, and they interpreted this as an evolutionary sequence essentially as a function of incresing mass-loss rates. Nowadays the IRAS two colour-colour diagram continues being an object of study.

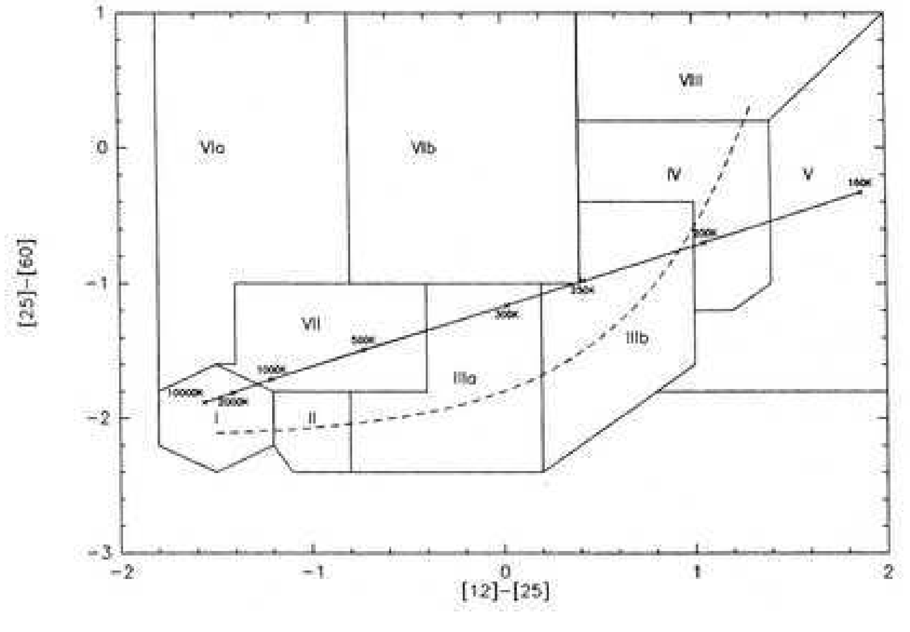

**Figure 1.2**: Regions in the IRAS colour-colour diagram that separate different sort of stars with dust-gas CSE (See van der Veen and Habing 1988). The dashed line represent the 'O-rich AGB main sequence' (see text).

Observationally, García-Lario (1992) found that the location of OH/IR stars in the IRAS colour-colour diagram follow very closely the equation:

$$[25]-[60] = -2{,}42 + 0{,}72\, \mathrm{e}^{1.096([12]-[25])}$$

This sequence agrees very well with the model predictions by Bedijn. In the following, we will refer to this sequence as the **"O-rich AGB Sequence"**.

The IRAS-PSC served as starting point for systematic searches for OH masers based on the characteristic infrared IRAS colours that these stars showed. As a consequence of this, hundreds of new OH maser sources were discovered, many of them with no optical counterpart (Eder et al. 1988; Sivagnanam et al. 1990; te Lintel Hekkert et al. 1991; Benson et al. 1990; Lewis et al. 1990b; te Lintel Hekkert 1991; Chengalur et al. 1993). Other more recent searches for OH/IR stars based on the detection of the OH maser have been made by Sevenster et al. (1997a,b,2001). All of these surveys raise up the number of known OH/IR stars up to $\approx 2\,000$.

As the variability properties of OH/IR stars are expected to be directly related to the properties of their central stars, a great effort has been made during the last years in this area. Thus, some monitoring programs were started. In most cases, the selected samples were volume limited or concentrated on specific parts of the Galaxy. Monitoring programs of OH/IR stars have been carried out in the solar neighbourhood (Jura 1994; Olivier et al. 2001); in the south galactic cap (Whitelock et al. 1994); in the Galactic Center (Jones et al. 1994; Wood et al. 1998; Glass et al. 2001); in the Galactic Bulge (van der Veen & Habing 1990; Whitelock et al. 1991; Glass et al. 1995); and in the Galactic Disk (Herman et al. 1984; van Langevelde et al. 1990; Jura & Kleinmann 1992; Nakashima et al. 2000). In addition, a few monitoring programs have also been carried out in the Large Magellanic Clouds (Glass & Reid 1985; Wood et al. 1985,1992; Reid et al. 1988,1995; Feast et al. 1989; Wood 1998).

## 1.3 OH/IR properties

### 1.3.1 Mass

AGB stars are one of the latest stages of the evolution of stars with low and intermediate mass ($\approx 1-8\,\mathrm{M}_{\odot}$). They present a mean galactic scale height (H) of $\approx 300$ pc (Ortiz and Maciel 1996). However, studies of the galactic distribution of AGB stars suggest 3 different categories of them as function of their masses:

1- The less massive stars are the Mira variables (also named 'optically bright variable OH/IR stars'), with $\mathrm{H} \approx 315$ pc (Wood and Cahn 1977).

2- The intermediate mass group is formed by the subsample of C-rich AGB stars, with $\mathrm{H} \approx 200$ pc (Claussen et al. 1987; Groenewegen et al. 1992).

3- The most massive group is formed by the "genuine" variable OH/IR stars (also named 'infrared Mira variables'), without optical counterpart and with $\mathrm{H} \approx 95$ pc (Likkel 1989).

This division as a function of the mass is consistent with that recently postulated by García-Lario & Perea-Calderón (2003) on the basis of the the analysis of ISO data of galactic AGB and post-AGB stars. They propose the existence of three different chemical branches of AGB stars, depending on their progenitor mass: (i) low-mass oxygen-rich stars; (ii) intermediate mass carbon-rich stars; and (iii) high-mass oxygen-rich stars.

### 1.3.2 Variability

One of the main characteristics of OH/IR stars is their large amplitude and long period variability (LALPV). Mira variables have periods that usually go from $100^d$ to $300^d$ and rarely surpass $500^d$, with the maximum of the distribution around $275^d$, and amplitudes in the K-band which are typically between $0.5^m$ and $1^m$ (Whitelock et al. 1994). Variable OH/IR stars have periods from $500^d$ up to $3\,000^d$, with amplitudes up to $4^m$ at K (Engels et al. 1983; Wood et al. 1998). Although most of the OH/IR stars are variables, there also exists a small fraction of them that do not show any variability or this is very small and irregular. These objects have been designated as *non-variable OH/IR stars* and they have been proposed to be stars which have already left the AGB (Bedijn 1987).

The studies of the galactic distribution of Mira variable stars suggest that sources with periods smaller than $300^d$ belong to the thick galactic disk ($\mathrm{H} \approx 600\,\mathrm{pc}$) (Jura 1994). While those with $300^d < \mathrm{P} < 400^d$ are part of the population of the thin galactic disk ($\mathrm{H} \approx 240\,\mathrm{pc}$) (Jura & Kleinmann 1992). These studies suggest that the period increases with the mass. This hypothesis is supported by the fact that obscured variable OH/IR stars with $\mathrm{P} < 800^d$ have masses between 2 and $3\,\mathrm{M}_\odot$ (Blommaert et al. 1994; Wood et al. 1998). If this hypothesis is correct, one should expect that variable OH/IR stars with periods longer than $750^d$, should have masses larger than $4\,\mathrm{M}_\odot$, since this is the theoretical mass limit for carbon stars whose periods are always lower than $750^d$ (Le Bertre 1992).

There are a large number of parameters that have been suggested to be correlated with the period. Engels et al. (1983) found that the K–L colour increases with period, although with substantial scatter. A similar correlation was found between the period and the OH-expansion velocity in Miras (Dickinson et al. 1975). The data obtained by Le Bertre (1993) for objects with period shorter than $800^d$ are consistent with the correlation found by Dickinson et al. However, it is clear that the OH/IR sources with very long periods do not follow the same relationship. For example, for the period of $1600^d$ determined for OH/IR 26.5+0.6 on the basis of its IR variability, one would expect an OH-expansion velocity of $100\,\mathrm{km\,s^{-1}}$, instead of the $29\,\mathrm{km\,s^{-1}}$ measured. Olnon (1981) showed that the dependence on the expansion velocity with period can not be expected to be linear, when the expansion is driven by radiation pressure on dust grains.

Periods are also related with the amplitude of the variability. Jones et al. (1990) found that the mean amplitude increases with the period at least for Mira variables.

However, this tendency is not so clear if we consider variable OH/IR stars (Jones et al. 1994). The amplitude is also found to increase for sources with redder colours (Wood et al. 1998) in variable OH/IR stars.

Multi-wavelength studies have shown on the other side that periods are independent of the wavelength where they were determined (Jones et al. 1994; Alcolea et al. 1999). However, the amplitude gets smaller at longer wavelengths (Smith 2003).

### 1.3.3 Luminosity

In general, OH/IR stars are found to have luminosities ranging from a few $10^3\,\mathrm{L}_\odot$ to a few $10^4\,\mathrm{L}_\odot$ although the latter are not frequent (Herman & Habing 1985a; Habing 1996). Van Langevelde et al. (1990) found that OH/IR stars with very long periods ($1\,000^d < \mathrm{P} < 2\,800^d$) are the most luminous objects in our Galaxy, with a $\mathrm{M}_{bol}$ of up to $-7.5^m$ ($\approx 80\,000\,\mathrm{L}_\odot$).

A relation between pulsation periods and luminosity exists for stars with periods shorter than $500^d$ (Feast et al. 1989; Groenewegen & Whitelock 1996). Thus, Mira variables with $\mathrm{P} \approx 200^d$ correspond to $\mathrm{L} \approx 3\,100\,\mathrm{L}_\odot$; Mira variables with $\mathrm{P} \approx 350^d$ correspond to $\mathrm{L} \approx 5\,800\,\mathrm{L}_\odot$; Mira variables with $\mathrm{P} \approx 450^d$ correspond to $\mathrm{L} \approx 8\,000\,\mathrm{L}_\odot$; and variable OH/IR stars with $\mathrm{P} \approx 1\,000^d$ would correspond to $\mathrm{L} \approx 20\,000\,\mathrm{L}_\odot$ (Habing 1996). However, the period-luminosity relationship is observationally found to disappear in the OH/IR stars with the longest periods (Wood et al. 1998).

Furthermore, one has to keep in mind that the individual luminosities are phase pulsation dependent. Engels et al. (1983) found $\mathrm{M}_{bol} = -5.0^m$ during the minimum and $\mathrm{M}_{bol} = -7.1^m$ during the maximum of OH 32.8–0.3, a bolometric luminosity variation of more than $2^m$ ($\Delta\mathrm{L} \approx 37\,000\,\mathrm{L}_\odot$; more than a factor of 6 in luminosity change between minimum and maximum).

Stellar atmosphere models provide relationships between L, $\mathrm{T}_{eff}$ and near-infrared colours (Bessell et al. 1998), although serious discrepancies between the models and the observations still exist.

As we have explained in Section 1.1, OH/IR stars are strong infrared emitters since they are surrounded by a dust-gas (some times very thick) CSE which reemit the radiation coming from the central star at the infrared wavelengths. Usually, the *Spectral Energy Distribution* peaks around $12-25\,\mu$m (See Figure 1.3). Thus, only objects with thin CSE (Mira variables) are expected to be visible in the optical range, while those with thick CSE ("genuine" variable OH/IR stars) are expected to be only visible at longer wavelengths.

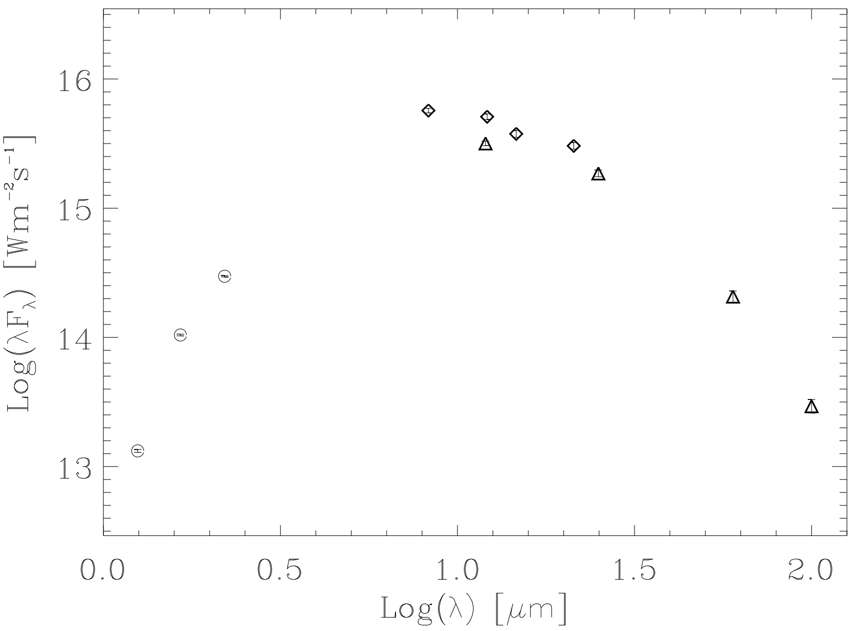

**Figure 1.3**: Spectral Energy Distribution of a typical OH/IR star (IRAS 19192+0922) from the Arecibo sample. Near infrared data have been plotted with circles, IRAS data with triangles and MSX data with diamonds. All photometric data have been plotted with error bars.

### 1.3.4 Mass-Loss

The evolution of stars throughout the AGB phase is accompanied by an increasing mass-loss rate ($\dot{\mathrm{M}}$), that goes from $10^{-7}$ to $10^{-5}$ $\mathrm{M}_\odot\mathrm{year}^{-1}$ (Whitelock et al. 1994). In the most extreme cases it can reach values of $\approx 10^{-4}\mathrm{M}_\odot\mathrm{year}^{-1}$(Bedijn 1987). On the other hand, all stars between $1-8\,\mathrm{M}_\odot$ end up as white dwarfs which are known to have masses strongly concentrated around $0.5-0.6\,\mathrm{M}_\odot$ (Weidemann 1990), and always below the limit of Chandrasekhar ($1.4\,\mathrm{M}_\odot$). This means that huge mass-loss must be experienced by these stars in a very short lapse of time at the end of the AGB phase.

Engels et al. (1983) postulated that the reddening of the IR colours from Mira variables to OH/IR stars is mainly due to an increasing of their mass-loss rate. Thus, this mass-loss rate should be correlated with the pulsation properties of the stars. Then, in the same way that there seems to be a correlation between period and luminosity, there must also be a correlation between $\dot{\mathrm{M}}$ and luminosity, the mass-loss rate being larger for the most luminous stars. Finally, we also have to consider the role that the metallicity can play, since larger values of the metalicity are expected to produce a larger expansion velocity of the gas, and therefore a larger mass-loss rate (Wood 1998). This strong $\dot{\mathrm{M}}$

declines by several ordes of magnitude just at the moment when the star leaves the AGB.

### 1.3.5 Chemistry

The relative abundance of C vs. O in AGB stars determines the stellar spectrum, wich will be dominated by either C-rich or O-rich molecules (this chemistry will later be reflected also in the dust grains of the CSE). Since all OH/IR stars are expected to be oxygen rich, the formation of oxygen-rich molecules (and later oxygen-rich dust grains) will predominantly occur if the most external part of the mantle of hydrogen gets sufficiently cold ($< 3\,500\,\mathrm{K}$).

The complexity of the chemical composition of these CSE is evidenced by the more than 60 different molecular species (Olofsson 1999) detected so far. These molecules form and survive only in layers of the CSE with different radii and widths as a function of their resistance to ultraviolet radiation. This radiation, mainly coming from the interstellar medium (but also from the central star during the post-AGB phase), is mainly responsible for their dissociation. Oxygen-rich (O-rich) stars usually present several molecular masers at radio or submillimeter frequencies, like the hydroxyl (OH) maser, or the water ($H_2O$) maser and the silicon oxide (SiO) maser. Now it is known that these masers form at different zones of the CSE, being the OH maser the most external one and the SiO maser the innermost one. On the other hand, C-rich stars are usually characterized by thermal emission from the CO molecule and/or the HCN molecule, among others.

The different composition of the dust grains will also affect the infrared spectrum of the stars. As we have explained in Section 1.1, carbonaceous compounds are predominant in C-rich stars and silicates in O-rich stars. Both type of features are easily detectable with low relosution mid-infrared spectroscopy, as ISO has recently confirmed.

## 1.4 Open questions

Despite of the huge efforts made in the last years on the study of the AGB phase, the number of questions that are still awaiting for an answer is very large, since in many occasions the theoretical models do not agree with the observations and the results derived from the observations are still controversial. At the present time a model does not exist, able to predict satisfactorily the temporal evolution of the mass-loss processes in the AGB, nor its dependency with other parameters such as the initial mass of the star or the stellar metallicity.

It is also not yet settled, if low-mass oxygen-rich AGB stars evolve into the large mass loss regime observed in high-mass oxygen-rich AGB stars, and if so, how long they stay in this regime. Low-mass progenitors are expected to experience only moderate mass loss rates during their AGB lifetime and, thus, they will be detected preferentially in the optical and near-infrared. However, the identification of the optical and near-infrared counterparts of OH/IR stars is also a difficult task, as we will see in this thesis. It is therefore not clear, what fraction of low-mass stars is present in OH/IR star samples. Actually, the relation between AGB star samples selected in different wavelength ranges remains to be explored. Available samples of AGB stars are in many cases biased. Depending on whether the selection is made at optical/near-infrared wavelengths or in the far-infrared the sample under analysis contains a larger number of low-mass or high-mass AGB stars, respectively. A well defined AGB star sample, observed over an adequate long period of time, would be required to test current evolutionary models of this short-lived phase of stellar evolution.

Although the rough description of the evolution of OH/IR stars made in Section 1.1 is widely accepted and as a first approach it is probably correct, there are still many points which need some additional clarification. The trends observed in infrared colours and the variability properties support a scenario in which the pulsation amplitudes, mass-loss rates, and opacities of OH/IR stars increase as they evolve on the AGB, while their infrared colours become progressively redder. In this picture, they first evolved from Mira variables to variable OH/IR stars (van der Veen 1988). The true evolutionary picture, however, may not be that simple.

There is not a clear distinction between Mira variables and variable OH/IR stars, in the sense that a considerable number of infrared sources may have an optical counterpart provided enough sensitive is available. These objects essentially differ only in the envelope optical thickness, and, thus the line that separates both kind of objects is not well-defined. Moreover, it is not clear whether the difference between Mira variables and variable OH/IR stars is only based on their different evolutionary stage or in their different progenitor mass. Some authors (e.g. van der Veen 1988) postulate that AGB stars evolve from Mira variable to variable OH/IR star becoming redder as they undergo an increasing mass-loss rate. In this scenario the different location in the IRAS two colour-colour diagram would be just a consequence of their different evolutionary stage. Other authors (e.g. Ortiz & Maciel 1994; Lepine et al. 1995) postulate that the main difference is with respect to their progenitor masses. In this case their different location in the IRAS two colour-colour diagram would be just a consequence of their different initial mass which would determinate the mass-loss rate (assumed to be constant) experienced in the AGB. However, other authors (Likkel 1989; García-Lario 1992) suggest that the O-rich AGB sequence is a combination of both effects, evolutionary stage and progenitor mass. AGB stars would start their evolution as Mira variables although only the more massive ones would be able to become variable OH/IR stars and reach the upper end of the sequence.

AGB stars undergo convective processes that transport part of the carbon created as a consequence of nuclear burning in the inner region of the star to the outer layers of the stellar atmosphere (Chan & Kwok 1988). As a consequence of this dredge-up of processed material, some AGB stars may become C-rich. However, not all the AGB stars are transformed into C-rich. The range of masses for which the ratio carbon-oxygen becomes larger than the unity and for which this radical change of chemistry occur is still not well known. The theoretical models predict a lower mass limit for the generation of carbon stars of $1.5\,M_{\odot}$ for a solar metallicity (Straniero et al. 1997). However, for the most massive AGB stars ($\gtrsim 4\,M_{\odot}$) the models predict that the convective zone of the mantle will get hot enough ($T \gtrsim 2{\cdot}10^{7}$ K) to efficiently transform $^{12}C$ into $^{13}C$ and finally into $^{14}N$ through the CN cycle. This process, that has been denominated *´Hot Bottom Burning´* (HHB) (Boothroyd and Sackmann 1992), predicts also the formation of $^{7}Li$, $^{26}Al$ and s-process elements where $^{13}C$ seems to be the necessary neutron source. HBB would prevent the formation of massive C-rich AGB stars. Based on this chemical segregation as a function of the progenitor stars, García-Lario & Perea-Calderón (2003) have recently postulated the existence of three different chemical branches of AGB, depending on their progenitor mass, from the analysis of ISO data of galactic AGB and post-AGB stars: (i) low-mass oxygen-rich stars; (ii) intermediate mass carbon-rich stars; and (iii) high-mass O-rich stars. Still the border between one class and another is not yet well defined and is expected to be strongly dependent on the stellar metallicity.

There has been quite a lot of discussion in the literature about carbon stars with oxygen-rich circumstellar shells (de Jong 1989; Little-Marenin 1986; Willems & de Jong 1986). These stars may have recently become carbon stars but still preserve their outer relic oxygen-rich shell. However, Smith (2003) and Skinner et al. (1990) found a few oxygen-rich AGB stars surrounded by a carbon-rich shell. As the carbon stage is supposed to follow the oxygen-rich stage, it is difficult to explain how a carbon-rich shell can form around an oxygen-rich star.

One of the questions not yet solved is if all the stars of low and intermediate mass will become planetary nebulae. The upper limit of mass that stellar evolution theory predicts for a star to evolve as an AGB star and become a planetary nebulae is also a matter of controversy. Baud et al. (1981b) found that the difference in galactic density distribution between OH/IR sources, with a maximun of density at $R \approx 5$ kpc, and planetary nebulae indicates that the OH/IR stars are not the precursors of the majority of the planetary nebulae. The Planetary Nebula phase not necessarily would be reached by all stars. Possibly very low mass AGB stars will not reach the temperature necessary to ionize the CSE in time when they evolve as post-AGB stars. They may evolve so slowly that the CSE would have already dissipated in the interstellar medium, when the central star becomes hot enough to ionize the gas in the envelope, and therefore they would never become observable planetary nebulae. It is not clear either whether objects of larger mass are observable as planetary nebulae in the optical, since in this case, they may evolve so fast that they would reach the temperature of ionization so soon that the CSE would still be optically thick, evolving as an infrared source all the way down to the white dwarf stage.

Another important aspect that it is still not well known is the pulsation mode of OH/IR stars (whether they pulsate in the fundamental mode or in the first overtone). The form of the light curves is also not yet well established, and in most cases these are far from a sinusoidal. Some authors (e.g. van Langevelde et al. 1990) have suggested asymmetric light curves. In many cases the variability observed can only be explained as multiperiodic curves (e.g. Wood et al. 1998; Whitelock et al. 1995). Deviation of individual measurements from a sinusoidal are generally observed not only in amplitude and periodicity but also as bumps and asymmetries in the light curves which are certainly present in the light curves of most OH/IR stars (e.g. Engels et al. 1983; Jones et al. 1990; Whitelock 1997). Linear and non-linear models used until now are not enough to explain the observed behaviour (Barthès & Luri 2001).

As we have explained before (Section 1.3) there seems to be a correlation between period and expansion velocity, and between period and luminosity in Mira variables. However, this correlation do not seem to operate for objects with P $\gtrsim 800^d$ which are considered to be ‘extreme’ OH/IR stars. A clear correlation between period and near-infrared colours also exist. However, a correlation between period and [12]–[25] colours was not found yet (Nakashima et al. 2000).

OH/IR stars are found to be preferentially distributed at small galactic latitudes (disk population) and towards the galactic center (bulge population). In particular, it seems that there is a correlation between the pulsation periods and the galactic latitude, the longer periods corresponding to the lower galactic latitudes. This could be interpreted as the period depending on the initial mass of the progenitor star. There are authors who have also suggested that the periods also increase with the evolutionary stage, so that AGB stars will always start their evolution as short-period AGB stars. As they evolve they would increase their periods up to $2\,500^d$, but only in the more massive casses. In order to be able to make a better study of objects with longer periods than $500^d$ it is necessary to increase the number of sources known with such long periods.

So far only a few OH/IR stars are known to show such long periods. This is mainly due to the poor knowledge of periods in ‘extreme’ OH/IR stars, since very long term monitoring programs are needed to determine them. In addition, they have to be carried out in the infrared or radio wavelengths because they are heavily obscured sources without optical counterparts. Thus, only a few ‘extreme’ sources have well determined periods (Engels et al. 1983; Jones et al. 1990,1994; van Langevelde et al. 1990,1993; Le Bertre 1993; Nakashima et al. 2000; Wood et al. 1998; Wood 1998; Olivier et al. 2001), and any progress in this field would represent an important contribution to the study of these objects.

## 1.5 Thesis outline

This thesis contains the detailed analysis of the infrared properties of 3 different samples of galactic variable OH/IR stars.

*Chapter 2:* In this chapter we present optical and near infrared finding charts, accurate astrometry ($\approx 1''$) and single-epoch near infrared photometry for 371 IRAS sources, 96% of those included in the so-called 'Arecibo sample of OH/IR stars' The main photometric properties of the stars in the sample are presented and discussed as well as the problems found during the process of identification of the optical/near-infrared counterparts.

*Chapter 3:* In this chapter we extend the photometric study made on the Arecibo sample to another sample of 94 OH/IR stars with very red infrared colours taken from the GLMP catalogue. We also present optical and near infrared finding charts, and accurate astrometry ($\approx 0.2''$) for these objects.

*Chapter 4:* In this chapter, using all OH/IR stars compiled in the previous two chapters (457) we study the sequence of infrared colours showed in the IRAS two colour-colour diagram by these stars. We calculate the galactic scale height of different subgroups of stars located in different regions of this diagram in order to describe the sequence of colours observed in terms of main progenitor mass.

*Chapter 5:* Here we present the results of a monitoring program carried out during more than 10 years over a small sample of 25 OH/IR stars. We analyse their variability using three different types of light curves.

*Chapter 6:* In the last chapter we present the conclusions of this thesis.

The Atlas of optical/near-infrared finding charts associated to the sources studied in Chapters 2 and 3 are provided as an appendix to this thesis in the attached CD-Rom. They can also be accessed electronically.

# Chapter 2

# The ‘Arecibo sample’ of OH/IR stars

### Abstract

In this chapter we present optical and near-infrared finding charts, accurate astrometry ($\approx 1''$) and single-epoch near-infrared photometry for 371 IRAS sources, 96% of those included in the so-called ‘Arecibo sample of OH/IR stars’ (Eder et al. 1988; Lewis et al. 1990a; Chengalur et al. 1993). The main photometric properties of the stars in the sample are presented and discussed as well as the problems found during the process of identification of the optical/near-infrared counterparts. In addition, we also identify suitable reference stars in each field to be used for differential photometry purposes in the future.

We find that 39% of the sources (144 in number) have no optical counterpart, 8 of them being invisible even at near infrared wavelengths. The relative distribution of sources with and without optical counterpart in the IRAS two-colour diagram and their characteristic near infrared colours are interpreted as the consequence of the increasing thickness of their circumstellar shells. Among the objects not detected at near infrared wavelengths four non-variable sources are proposed to be heavily obscured post-AGB stars which have just very recently left the AGB. Eight additional sources objects with unusually bright and/or blue near-infrared colours are identified as candidate post-AGB stars and/or proto-planetary nebulae.

## 2.1 Introduction

Stars with masses between 0.8 and 8 $M_\odot$ pass through the Asymptotic Giant Branch (AGB) towards the end of their evolution. Approaching the tip of the AGB they start to pulsate and appear as large-amplitude ($> 0.5^m$ at K-band) long-period ($> 1$ year) variables. The pulsation is accompanied by heavy mass loss which forms a circumstellar envelope of gas and dust. If the mass loss rate surpasses $\dot{\mathrm{M}} \geq 10^{-6}\,\mathrm{M}_\odot\mathrm{year}^{-1}$ the dust shell eventually becomes opaque to visible light (Habing 1996).

Stellar evolution models predict that stars close to the tip of the AGB (the so-called 'TP-AGB') experience thermal pulses leading to variations in luminosity and mass loss rates on timescales of several ten-thousand years. In addition, they may change their photospheric chemistry from oxygen- to carbon-rich. The determination of the current evolutionary state of a particular AGB star is difficult due to the strong variability and the increasing obscuration which limits our observational capabilities. Moreover, their pulsation on timescales of $1-5$ years usually requires long observational monitoring programs to determine representative parameters. Hence, well defined AGB star samples, observed over an adequate long period of time, are required to test current evolutionary models of this short-lived phase of stellar evolution.

Available samples of AGB stars are in many cases biased. Depending on whether the selection is made at optical/near-infrared wavelengths or in the far-infrared the samples under analysis contain a larger number of low-mass or high-mass AGB stars, respectively. Low-mass progenitors are expected to experience only moderate mass loss rates during their AGB lifetime and, thus, they will be detected preferentially in the optical and near-infrared. An example is the 'dust-enshrouded AGB sample' of Jura & Kleinmann (1989), which contains stars with typical main-sequence masses $\mathrm{M}_{\mathrm{MS}} \approx 1.3\,\mathrm{M}_\odot$ (Olivier et al. 2001). In contrast, AGB stars descending from progenitors with larger main-sequence masses ($\mathrm{M}_{\mathrm{MS}} \gtrsim 2\,\mathrm{M}_\odot$) probably spend a larger fraction of their TP-AGB life in an obscured state. This is a consequence of the higher mass loss rates, which favours their detection in the far-infrared. Less biased AGB samples covering the complete TP-AGB and all kind of chemistries should therefore include these far-infrared sources, something which is possible only since the infrared survey by the IRAS satellite was completed (Beichman et al. 1988).

Samples of oxygen-rich AGB stars ('OH/IR stars') can be constructed using surveys of OH maser emission. In such surveys AGB stars are easily picked up due to their conspicuous double-peaked maser profile. However, these samples are also incomplete, as only part of the oxygen-rich AGB stars exhibit OH maser emission (Lewis & Engels 1995). Monitoring of early samples (e.g. Baud et al. 1981b) revealed either very long periods or rather weak variations (Engels et al. 1983; Herman & Habing 1985b). These OH/IR stars were considered as massive AGB stars ($\mathrm{M}_{\mathrm{MS}} = 3-8\,\mathrm{M}_\odot$ on the main sequence), with the long-period variables shortly before and the non-variables probably shortly after the

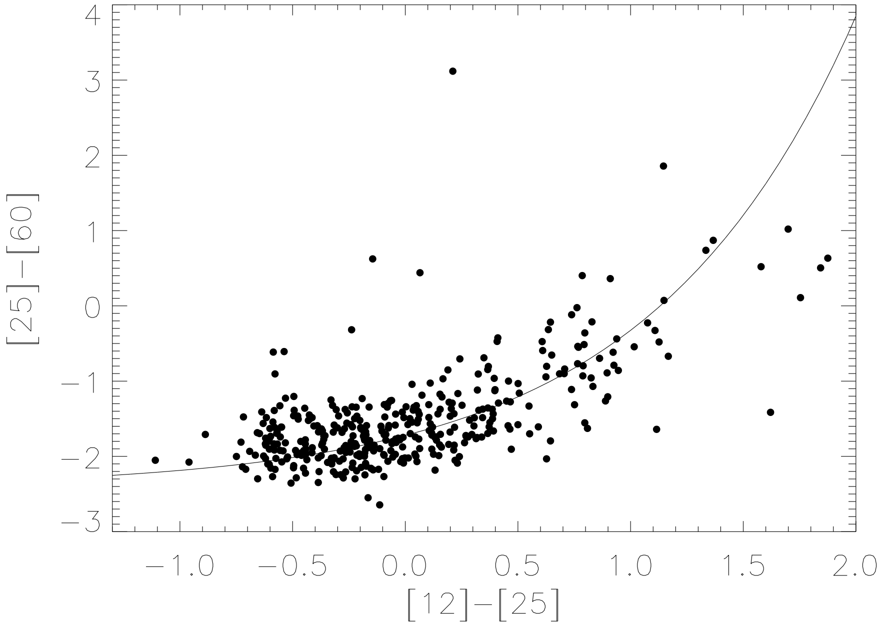

**Figure 2.1**: The position in the IRAS two-colour diagram of the stars in the 'Arecibo sample', where the IRAS colours are defined as: $[12]-[25]=-2.5\log\frac{F_\nu(12)}{F_\nu(25)}$ and $[25]-[60]=-2.5\log\frac{F_\nu(25)}{F_\nu(60)}$. The continuous line is what we call the 'O-rich AGB sequence' (see text).

departure from the AGB. From the analysis of ISO data of galactic AGB and post-AGB stars, García-Lario & Perea-Calderón (2003) have recently postulated the existence of three different chemical branches of AGB stars, depending on their progenitor mass: (i) low-mass oxygen-rich stars; (ii) intermediate mass carbon-rich stars; and (iii) high-mass O-rich stars, where 'hot bottom burning' is active at the base of the convective envelope preventing the formation of carbon (instead, the production of nitrogen is favoured). It is however not yet settled, if low-mass oxygen-rich AGB stars evolve into the large mass loss regime observed in high-mass oxygen-rich AGB stars, and if so, how long they stay in this regime. It is therefore not clear, what fraction of low-mass stars is present in OH/IR star samples. Actually, the relation between AGB star samples selected in different wavelength ranges remain to be explored.

A well-defined sample of far-infrared selected oxygen-rich AGB stars is provided by the Arecibo survey of OH/IR stars (Eder et al. 1988; Lewis et al. 1990a; Chengalur et al. 1993). It consists of $\approx 390$ IRAS sources, which were detected in the 1612 MHz OH maser line with the Arecibo radio telescope. The sample was obtained from a complete survey of IRAS sources with flux densities $\geq 2$ Jy at 25 $\mu$m, with declination $0° < \delta < 37°$

and appropriate colours of AGB stars (Olnon et al. 1984). The OH maser detection qualifies the IRAS source as an oxygen-rich AGB star. The position of the sources in the IRAS two-colour diagram is shown in Figure 2.1, together with a solid line which corresponds to the sequence of colours predicted for oxygen-rich AGB stars with increasing mass-loss (Bedijn 1987), that we have named the ‘O-rich AGB sequence’. The broad range of colours suggests that this sample bridges the gap between the optically/near-infrared selected AGB samples and the OH/IR stars discovered by OH maser surveys.

In order to study the variability properties of the ‘Arecibo sample’ (periods, amplitude, and colour variations) we started in 1999 a near-infrared monitoring program that we are still carrying on. At the end of 2003, we have already completed 11 observing runs with more than 110 nights of observation. A subsample is also being monitored optically. The first results of this multi-wavelength long-term monitoring program are reported in this thesis. Our ultimate goal is to study in particular the oxygen-rich AGB stars with $\mathrm{M_{MS}} \gtrsim 2\,\mathrm{M_\odot}$ which are probably rare among AGB stars discovered optically and in the near-infrared, but are common in samples discovered by blind OH maser surveys.

In this chapter we will focus on the determination of the optical/near-infrared counterparts of all the OH/IR stars in the ‘Arecibo sample’ and on the identification of suitable reference stars in each field to be used for differential photometry purposes in the future. The result is an atlas of finding charts combining optical images from the *Digitized Sky Survey* (Djorgovski et al. 2001) and our own near-infrared images, obtained in the J, H, and K bands.

Section 2.2 describes the observations performed and the acquisition and data analysis techniques applied. In Section 2.3 we explain how we identified the optical/near-infrared counterparts and how we determined new accurate coordinates. This is followed by a brief description of the atlas. In Section 2.4 we present the near-infrared photometry, while the results obtained are discussed in Section 2.5. Finally, the main conclusions are presented in Section 2.6.

## 2.2 Observations and data reduction

Our ‘Arecibo sample’ of OH/IR stars contains 385 objects, and comprises most of the original sources listed in Eder et al. (1988), Lewis et al. (1990a), and Chengalur et al. (1993). The only objects not considered here were sidelobe responses or serendipitous OH maser discoveries, as described in Engels & Lewis (1996), plus another three objects (IRAS 18534+0215, IRAS 19175+1344, and IRAS 19226+1401) that were left out, because they were re-classified by Lewis (1997) as molecular cloud sources. Finally IRAS 19200+2101 was also removed, as it turned out to be an erroneous entry in the IRAS PSC (see Lewis et al. 2004).

### 2.2.1 Observations

The infrared observations under discussion here were performed during 20 nights in July 1999 and July 2000 at Calar Alto Observatory (Almería, Spain) using the 1.23 m telescope equipped with the infrared camera MAGIC (Herbst et al. 1993). All sources in the sample, except 13 objects not accessible at this time of the year (with $4^h < \alpha < 12^h$) and the very bright, detector saturating, Mira variable R Aql (IRAS 19039+0809), were observed in the J (1.25 $\mu$m), H (1.65 $\mu$m) and K (2.20 $\mu$m) near infrared bands. The sources observed (N = 371) are listed in Table B.1. All except one (IRAS 18549+0208) were observed at least once under photometric weather conditions. The MAGIC camera uses a 256 × 256 pixels NICMOS3 array which provides an approximate field of 5' × 5'. Typical on-source integration times were 1 minute for the J and H bands, and 30 seconds for the K band, resulting in typical upper detection limits of around $15^m$, $14^m$ and $13^m$, respectively. To avoid saturation when observing the brightest sources a small aperture configuration was used. Standard stars from Elias et al. (1982) were observed during each night for photometric calibration. They were followed over a range of airmasses to determine the atmospheric extinction corrections.

The main difficulty to observe in the infrared is the high sky background level and its fast temporal and spatial variation. For the accurate determination of the background we took for each object and every filter 5 images with the object centered at different positions in the image (dithering or 'moving sky' technique). Thus, each measurement consisted of a set of 5 individual images. Taking the median average of the 5 images we obtained a temporally and spatially well determined sky image which was subtracted from the object image. Flat-field images were also taken every night for each individual filter in each of both aperture configurations to correct for pixel-to-pixel sensitivity variations during the data reduction process.

### 2.2.2 Data reduction

During each of the two observing epochs we obtained of the order of ten thousand images covering the full sample twice. Within the long-term monitoring project we expect to take ≈150 000 images, which makes a high level of automation in data reduction desirable. Thus, a semi-automated reduction procedure was developed combining a self-written IDL (Interactive Data Language; Research Systems Inc.) routine with preexisting routines within the IRAF[1] software package. The IDL routine first reads in all images taken in a particular observing night from the observing logfile provided by the MAGIC camera software. Then it writes an IRAF macro, which combines several IRAF

---

[1] IRAF is distributed by the National Optical Astronomy Observatories, which are operated by the Association of Universities for Research in Astronomy, Inc., under cooperative agreement with the National Science Foundation.

routines to perform the data reduction which consisted of the following steps. First, a detector mask was used in order to remove the bad pixels from the images. Then these images were divided by the appropriate flat-field images and subsequently the median-averaged sky images were subtracted. The sky-subtracted images were then inspected for cosmic ray hits and cleaned by interpolating over the neighbouring pixels. Finally, each set of 5 images obtained per source and filter were aligned and combined to yield the final near-infrared atlas image.

## 2.3 Identification of the optical/near-IR counterparts

In order to determine the optical/near-infrared counterparts of the sources in our sample we first considered the best coordinates available from the literature or from existing catalogues and then searched for plausible counterparts at these locations both on the optical images from the *Digitized Sky Survey* and on our near-infrared images.

Improved coordinates with respect to those originally provided by the IRAS Point Source Catalogue (accuracy typically between $10'' - 15''$) were obtained in many cases by cross-correlating our sample with the MSX6C Point Source Catalogue (Egan et al. 2003), which provides coordinates with an accuracy of $\approx 2''$. Although the MSX survey was limited to low galactic latitudes ($\leq 6^\circ$ in absolute value), its accuracy is in many cases essential to identify the near-infrared counterpart, in particular in crowded regions along the galactic plane and for extremely red objects only marginally detectable in the K band, as we will see later.

Out from the 269 objects (73% of the observed sample) located within the region of the sky surveyed by MSX, (essentially $|b| < 6^\circ$), we found that 249 objects (93% of them) had a mid-infrared counterpart in the MSX6C Point Source Catalogue (see Table 2.1 and Table A.1). The missing objects are all located at the edges of the MSX survey area, at galactic latitudes in the range $4.9^\circ < |b| < 6^\circ$. Two sources (IRAS 19161+2343 and IRAS 19206+2517), although not included in the Point Source Catalogue, were identified directly on the MSX images, from which we also derived the improved coordinates that were later used in the identification process.

Additional improved coordinates were taken from Lewis et al. (1990b), who determined positions of the OH masers by radio interferometry at the VLA for 46 sources in our list. These coordinates have errors $< 1''$. Note that part of these objects are also MSX detections.

Once the best coordinates available were determined for each source in the sample we searched for their near-infrared counterparts in our images obtained at Calar Alto. For this, we inspected a $30'' \times 30''$ box (or smaller, depending on the accuracy of the available - IRAS, MSX or VLA - coordinates) centered at the nominal Arecibo source position and searched for a plausible (i.e. redder than average) counterpart within the box. Usually only one 'red' source was found close to the expected position, being in many cases the brightest source in the near-infrared field and/or showing extremely red colours.

In parallel, we searched also the corresponding position in the Second Digitized Sky Survey (DSS2) using the red filter image, which covers the spectral range 6 000 – 7 000 Å with a maximum efficiency around 6 700 Å. In many cases it was easy to confirm the previous identification made in the near-infrared since no optical counterpart (or a very faint one) was seen at the corresponding position.

However, in several cases additional information was needed to verify the optical and near-infrared identification. For a few Arecibo sources more than one candidate was found with appropriate colours. The right counterpart was then uniquely identified by searching for variability between two observing epochs. The same verification was applied for near-infrared counterparts which were detected only in the K band, and for which therefore colour information was lacking.

In most cases (61%), a single, point source counterpart was found both in the optical and in the near-infrared. For less than one third of the sample (28%), a bright near-infrared counterpart was found but so heavily obscured in the optical that nothing was seen on the DSS2 image above the detection limit of $\approx 20.8^m$. 11% of the sources are so strongly obscured that neither in the near-infrared the counterpart was identified above the detection limit (2%), or only in the K-band (9%), being completely invisible at shorter wavelengths.

The identification strategy provided in all but 8 cases a plausible counterpart to the Arecibo source, either in the optical and in the near-infrared or only in the near-infrared. The 8 sources without counterpart are listed in Table 2.1. All have MSX and/or VLA coordinates, and their counterparts must have been fainter than our detection limits at the two epochs of observation considered. Two of these objects, IRAS 18498−0017 (OH 32.8−0.3, a well known long-period variable OH/IR star, Engels et al. 1983) and IRAS 19440+2251 (Lawrence et al. 1990) were reported as detected sources in the past but only at wavelengths beyond 3 $\mu$m. They do not appear to have a counterpart in the 2MASS Point Source Catalogue (Cutri et al. 2003) either. IRAS 18596+0315 (OH 37.1−0.8, GLMP 862) is a non-variable OH/IR star which has already left the AGB (Engels 2002). Two of the sources in Table 2.1, IRAS 18517+0037 and IRAS 19374+1626, were classified as variable OH/IR stars in the GLMP catalogue (García-Lario 1992), based on the large value of their IRAS variability index (quoted in column 9). The same classification applies also to IRAS 18475+0353 and the above mentioned IRAS 18498−0017. In contrast, other sources in Table 2.1 show a remarkably low value of this index, like IRAS 18501+0013, IRAS 18596+0315 (above mentioned as a candidate post-AGB star), IRAS 19006+0624 and IRAS 19440+2251, and might have already left the AGB.

**Table 2.1**: Arecibo OH/IR stars without optical/near-infrared counterpart. Coordinates are from radio interferometry or from MSX.

| IRAS | Coordinates (J2000) | | MSX−IRAS $\Delta\alpha$ [″] | MSX−IRAS $\Delta\delta$ [″] | VLA−IRAS $\Delta\alpha$ [″] | VLA−IRAS $\Delta\delta$ [″] | MSX6C_G | VAR |
|---|---|---|---|---|---|---|---|---|
| 18475+0353 | 18 50 00.5 | +03 56 33 | 6 | 1 | | | 036.2795+02.1143 | 99 |
| 18498−0017 | 18 52 22.2 | −00 14 11 | −2 | −2 | | | 032.8276−00.3152 | 96 |
| 18501+0013 | 18 52 40.02 | +00 16 46.9 | 4 | 0 | 5 | 0 | 033.3208−00.1459 | 15 |
| 18517+0037 | 18 54 20.8 | +00 41 05 | −2 | 3 | | | 033.8728−00.3350 | 85 |
| 18596+0315 | 19 02 06.3 | +03 20 16 | −2 | 1 | | | 037.1185−00.8473 | 17 |
| 19006+0624 | 19 03 03.4 | +06 28 54 | 1 | 2 | | | 040.0220+00.3818 | 16 |
| 19374+1626 | 19 39 39.2 | +16 33 41 | −17 | −3 | | | 053.1355−02.7609 | 60 |
| 19440+2251 | 19 46 09.27 | +22 59 24.0 | 6 | 0 | 7 | 0 | 059.4784−00.8969 | 16 |

Taking into account that IRAS 18498−0017 (OH 32.8−0.3) has a period $P > 1\,500^d$ (Engels et al. 1983) and that the other stars in Table 2.1 are among the most obscured objects in the sample, we conclude that the variable sources are probably OH/IR stars with very long periods ($> 1\,000^d$) at the very end of the AGB, while the non-variable ones must be heavily obscured post-AGB stars, already in the transition to the planetary nebula stage.

### 2.3.1 The atlas of optical and near-infrared counterparts

The selected counterparts are displayed as an atlas of finding charts. An example of the atlas images is given in Figure 2.2. For each Arecibo source in our sample a chart was put together as a mosaic of 4 frames containing the optical image taken from the DSS2 in the upper left panel, and the J, H and K images from our observations in the upper right, lower left and lower right panels, respectively. The size of the field showed in each filter is $4.6' \times 4.6'$. For each source we marked the position of the optical/near-infrared counterpart with a circle in each of the available frames, as well as the position of the reference stars used for the astrometric measurements (with small circles surrounded by squares). These are the same stars which are used for differential photometry purposes in our on-going long-term monitoring program. In those cases where an optical/near-infrared counterpart was not found the circle was drawn at the position where the source should be located according to the best coordinates available (MSX or VLA). The complete atlas can be accessed electronically at:

http://www.hs.uni-hamburg.de/DE/Ins/Per/Engels/engels/ir_catalogue/index.html

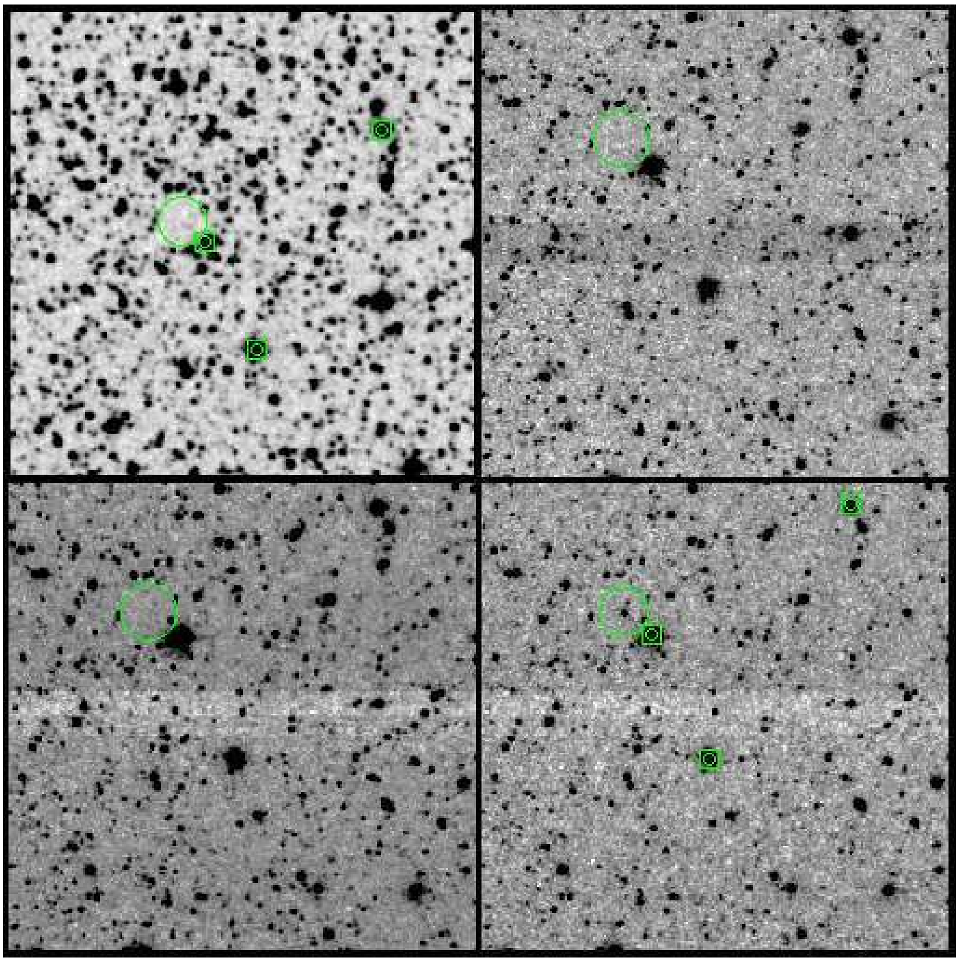

**Figure 2.2**: Atlas images for IRAS 19323+1952. The upper row gives the optical DSS2 R band and the Calar Alto J band images, and the lower row the H- and K-band images. The adopted counterpart is marked by a big circle, the reference stars by small circles surrounded by squares.

### 2.3.2 Derivation of improved coordinates

Once the counterparts were identified, we used the set of reference field stars (usually three) visible in both optical and near-infrared images to derive new accurate coordinates of the target stars. Using the relative distances between the Arecibo source and the reference stars in the near-infrared, we can determine the position of the counterpart with an accuracy equivalent to less than one pixel on the optical image. If a source was found at that precise position, it was considered to be the optical counterpart of the Arecibo source.

In a few cases (4%) the near-infrared counterpart was so bright that the short integration time used to avoid saturation was insufficient to detect any reference star in the field. In these cases, a unique very bright object was also visible at the nominal position on the DSS2 image and this was taken as the optical counterpart. The plausibility of this identification is supported by the blue IRAS colours associated with these extremely bright near-infrared sources, which imply that they are not expected to be heavily obscured in the optical. Because of the very bright near-infrared counterpart of these stars the variability monitoring is being performed in the optical to avoid saturation problems during their maximum of luminosity.

Taking advantage of the astrometric accuracy ($1''$/pixel) of the DSS2 images we systematically improved the accuracy of the astronomical coordinates of all sources in the sample for which either an optical or a near-infrared counterpart was found. If the Arecibo source had both an optical and a near-infrared counterpart, the coordinates were taken directly from the DSS2 image by determining the centroid of the point-like emission associated to the optical counterpart. If only a near-infrared counterpart was found, the position of the Arecibo source was determined from its relative position to the reference stars in the near-infrared field, which were always chosen to have point-like optical counterparts. In both cases, the typical astrometric errors are estimated, from the pixel scale of the DSS2 images, to be of $\approx 1''$ both in RA and DEC. The complete list (363 objects) of new coordinates is displayed in Table A.1, where we also list the relative distance from the optical/near-infrared counterpart found to the original IRAS coordinates. When available, the distance of the associated MSX and VLA counterparts to the IRAS position is also provided for comparison.

If the Arecibo source had neither an optical nor a near-infrared counterpart, then the coordinates assigned are the best ones available for the source in the mid-infrared (MSX) or at radio wavelengths (for the two with VLA measurements). These are listed in Table 2.1

## 2.4 Near infrared photometry

Near infrared photometry was performed on each of the sources in the sample for which a near infrared counterpart was found considering the whole set of images available. The SEXtractor software package (Bertin & Arnouts, 1996) was used in combination with IDL routines to determine for each source the residual background noise $\sigma$ in each of the five frames available per filter and to generate a catalogue with the accurate position and the aperture photometry (in integrated counts) of all the point sources detected in the field with at least a $3\,\sigma$ signal above the background. The count measurements corresponding to the source identified as the Arecibo counterpart were then extracted from these files and averaged, and a standard error $\sigma'$ was calculated. Individual measurements exceeding the average value by more than $3\,\sigma'$ were not considered for the subsequent flux determination and error calculation. The count numbers were then transformed into absolute fluxes taking into account the calibration observations made on standard stars which were used to derive the zero-point of our photometric system and the atmospheric extinction. The associated errors were calculated by the application of standard error propagation analysis, yielding typical values of $\approx 0.03^m$ for 'well-detected' sources in the three filters considered.

In Table B.1 we present the near infrared magnitudes (or lower magnitude limits) derived for the Arecibo OH/IR stars observed. Only for IRAS 18549+0208 no photometric data are available, because it could not be observed under photometric conditions in any of the observing epochs, nor for IRAS 19029+0933 and IRAS 20149+3440, because these sources were found to be strongly blended with a field star. Ten objects were barely detected in the K band, and were therefore too faint to perform a reliable photometry. For them, lower magnitude limits in the three filters are given. Because of various technical problems we were not able to derive the K band magnitude of IRAS 19422+0933, and the H band magnitude of IRAS 20440+0412. We noticed during the data reduction process that several bright OH/IR stars observed with the large aperture were measured in the non-linear regime of the detector resulting in an underestimation of their brightness. For these objects upper magnitude limits for their magnitudes are given.

## 2.5 Discussion

A number of consistency checks involving positional correlations and the analysis of colours can be made, to validate the near-infrared counterparts selected and to single out exceptional objects.

### 2.5.1 Positions of the near-infrared counterparts

We have compared our new positions: i) with those originally listed in the IRAS Point Source Catalogue for all the sources in the sample; ii) with those for a subsample of 243 objects with MSX counterpart; and iii) with the accurate VLA radio coordinates of 44 OH/IR stars. In Table 2.2 we list the median and the mean separation in right ascension ($\alpha$) and declination ($\delta$) between our Calar Alto coordinates and the IRAS, MSX and VLA ones, together with the associated standard deviations.

Our new coordinates are in excellent agreement with those obtained at the VLA, with an average offset in both RA and Dec. of $\approx 1''$. The only exception is IRAS 18554+0231 with an offset of $7''$ (cf. Table A.1). Lewis at al. (1990b) lists for this source a larger astrometric uncertainty than for the rest, implying that the difference is probably due to an error in the radio position.

In addition, there are 243 sources with available MSX coordinates in our 'Arecibo sample'. The angular separation between the MSX coordinates and our new coordinates

**Table 2.2**: Median and mean separation (and standard deviation) between Calar Alto (CA) coordinates and IRAS, MSX and VLA ones.

| | N | $\Delta\alpha$ median | $\Delta\alpha$ ($\sigma_{\Delta\alpha}$) mean | $\Delta\delta$ median | $\Delta\delta$ ($\sigma_{\Delta\delta}$) mean |
|---|---|---|---|---|---|
| CA–IRAS | 363 | 3.1″ | 5.6″ (7.1″) | 2.0″ | 2.3″ (2.2″) |
| CA–MSX | 243 | 1.4″ | 1.5″ (1.4″) | 1.0″ | 1.3″ (1.4″) |
| CA–VLA | 44 | 1.0″ | 1.0″ (0.8″) | 0.6″ | 1.1″ (1.4″) |

is shown in Figure 2.3. The median angular separation found is $\approx 1.7''$. The very good positional agreement with the MSX data reinforces the reliability of our identifications.

As expected, much larger deviations are found when we compare our new coordinates with the original IRAS coordinates. Misidentifications are in this case more difficult to determine, especially if neither MSX nor VLA coordinates are available to support our choice of a given counterpart. Figure 2.4 shows the histograms of these deviations. While in declination they are within $6''$ with just a few exceptions, in right ascension we find a considerable number of objects ($\approx 20\%$) showing deviations of the order of $10''$ and even larger. The larger errors in RA is a well known feature of the IRAS Point Source Catalogue (Herman et al., 1986; Bowers & Knapp, 1989; Lewis et al., 1990b). The problem is related with the differential accuracy of the IRAS survey in the cross-scan and in-scan directions (Beichman et al. 1988).

As part of our quality checks we verified that the differences found between Calar Alto and IRAS coordinates were similar to those found between MSX/VLA and IRAS coordinates (for the objects with MSX/VLA data available). Large but consistent deviations can be attributed to the large errors associated to the IRAS coordinates. For the remaining Arecibo sources (those with no MSX or VLA counterparts) it is more difficult to verify that the coordinate deviations are not due to a misidentification. In Table A.1 there are 14 sources with extremely large differences in RA ($\geq 20''$). 9 of them have MSX coordinates showing very similar deviations with respect to the original IRAS coordinates. The remaining five sources (IRAS 18033+2229, IRAS 19346+0913, IRAS 20127+2430, IRAS 20194+1707 and IRAS 21305+2118) are bright IRAS as well as near-infrared sources. They also have blue IRAS colours and are located at galactic latitudes $|b| > 5^\circ$, where confusion is unlikely. We conclude therefore that the identification of these counterparts is correct and that deviations with respect to the IRAS coordinates up to $\approx 60''$ are possible, although not frequent, and are due to the large errors in the IRAS astrometry.

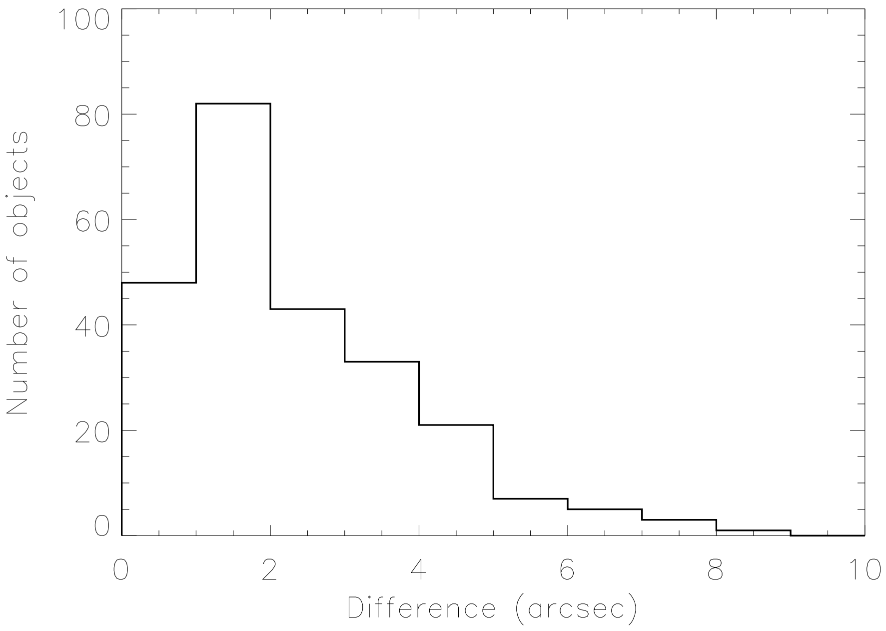

**Figure 2.3**: Angular separation between Calar Alto and MSX coordinates for the 243 OH/IR stars in common for which an optical/near-infrared counterpart was found.

### 2.5.2 Near-infrared magnitude distribution of the 'Arecibo sample'

Figure 2.5 shows the J, H, and K magnitude distribution of the 351 Arecibo sources with a near-infrared counterpart for which a photometric measurement was performed at least in the K band. Most of the sources observed have bright near-infrared counterparts with the magnitude distribution peaking around $6.0^m$ in K, $6.5^m$ in H, and $7.5^m$ in J. The distributions are however not strongly peaked and have a long tail extending to the sensitivity limit of our observations. We estimate that the distributions in Figure 2.5 become incomplete in all filters at $\approx 12^m$. 18% of the observed sources were not detected in the J-band, and 10% were not detected in the H band. As already mentioned in Section 2.3.1, for 18 sources (5% of the sample) the counterpart was too weak to derive a reliable photometric measurement in the K band.

The observed distribution can in principle be attributed: i) to the different intrinsic brightness of the sources in the sample; ii) to the different apparent luminosity expected from sources located at a wide range of distances; and iii) to the different optical thickness of their CSE. Based on the photometric data alone it is unfortunately not possible to disentangle the relative contribution of these three effects for individual sources. However, considered as a whole, we can derive some statistical conclusions from Figure

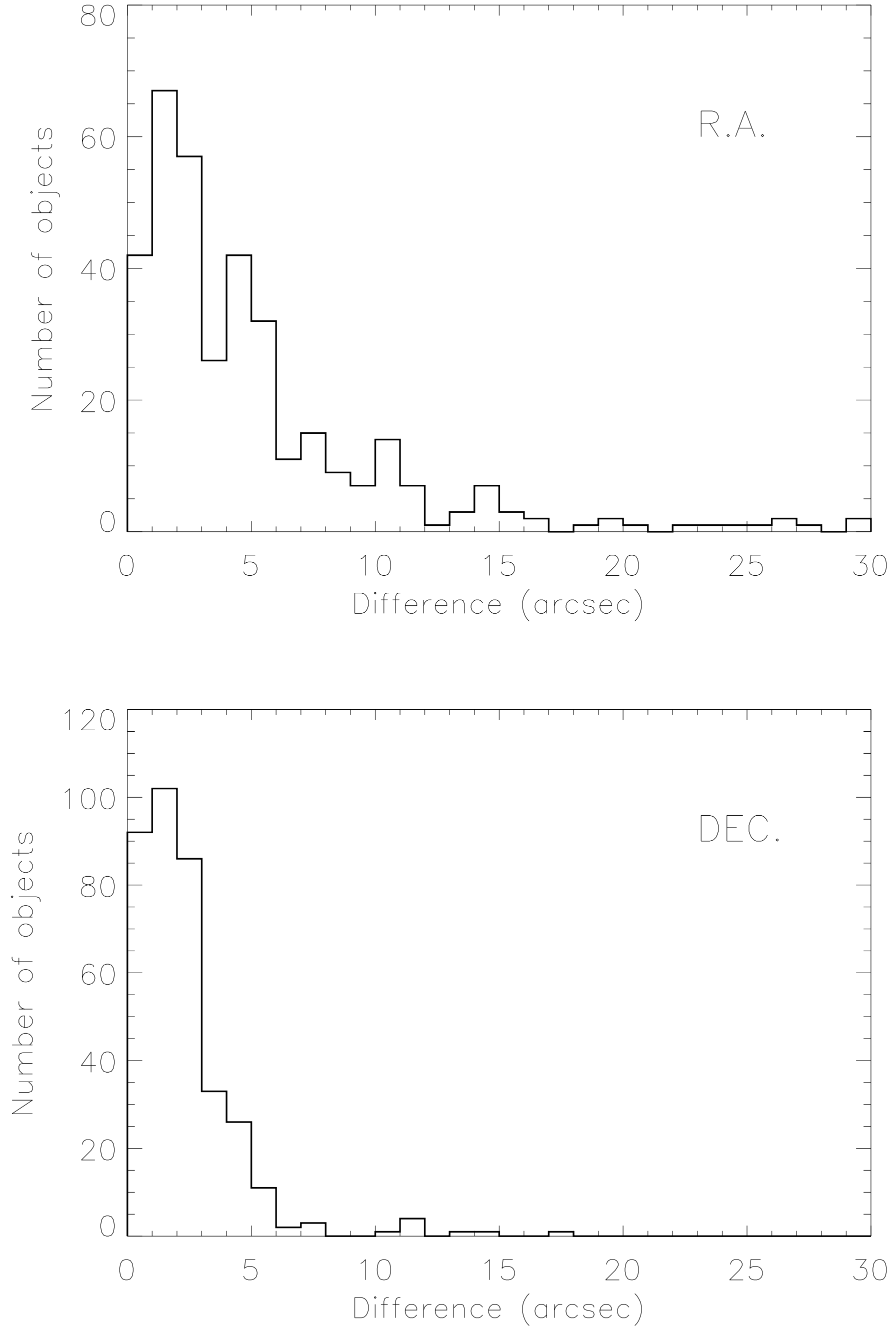

**Figure 2.4**: Absolute coordinate differences in right ascension (upper panel) and declination (lower panel) between Calar Alto and IRAS coordinates for the 363 OH/IR stars for which an optical/near-infrared counterpart was found. Not included are six sources with $30'' < |\Delta\alpha| < 61''$.

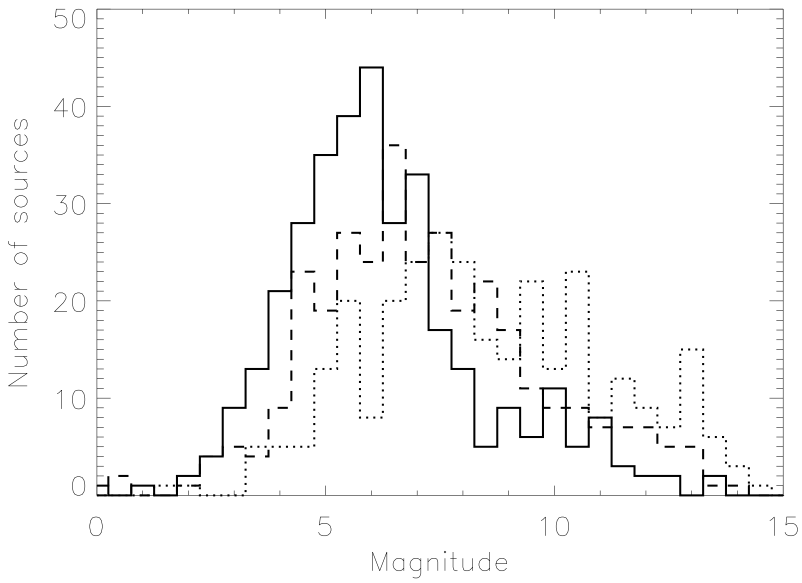

**Figure 2.5**: J band (*dotted line*), H band (*dashed line*), and K band (*solid line*) magnitude distribution of the sources included in the 'Arecibo sample'.

2.5. According to previous studies reported in the literature (cf. Habing 1996), and the results obtained by us in Section 4.6 the distribution of intrinsic luminosities expected in our sample of OH/IR stars covers the range between $\approx 2\,500\,\mathrm{L}_\odot$ and $\approx 26\,000\,\mathrm{L}_\odot$. This would translate into a dispersion in observed brightness of the order of $\approx 2.5^m$. Moreover, in Section 4.6 we will see that the distribution of luminosities is actually strongly peaked around $3\,500-4\,000\,\mathrm{L}_\odot$ (see Figure 4.7). This implies that the dispersion in the observed brightness due to the scatter of intrinsic luminosities must be even smaller when statistically considered. On the other hand, in Section 4.7 we will show that most of our sources are estimated to be randomly distributed at distances spanning from 1 to 5 kpc (see Figure 4.8). This would mean that their apparent luminosities would cover a brightness range equivalent to $\approx 3.5^m$. The combination of these two effects is not enough to explain the wide range of brightness shown in Figure 2.5 (more than $8^m$ in all filters). Thus, the different optical thickness of the CSE of individual OH/IR stars must contribute significantly to the observed scatter.

### 2.5.3 The J–H vs. H–K colour-colour diagram

In Figure 2.6 we have plotted the near-infrared colour-colour diagram J−H vs. H−K of all sources with a detection at least in the H and K bands. For objects not detected in J, lower limits for the J−H colours were calculated and these are indicated

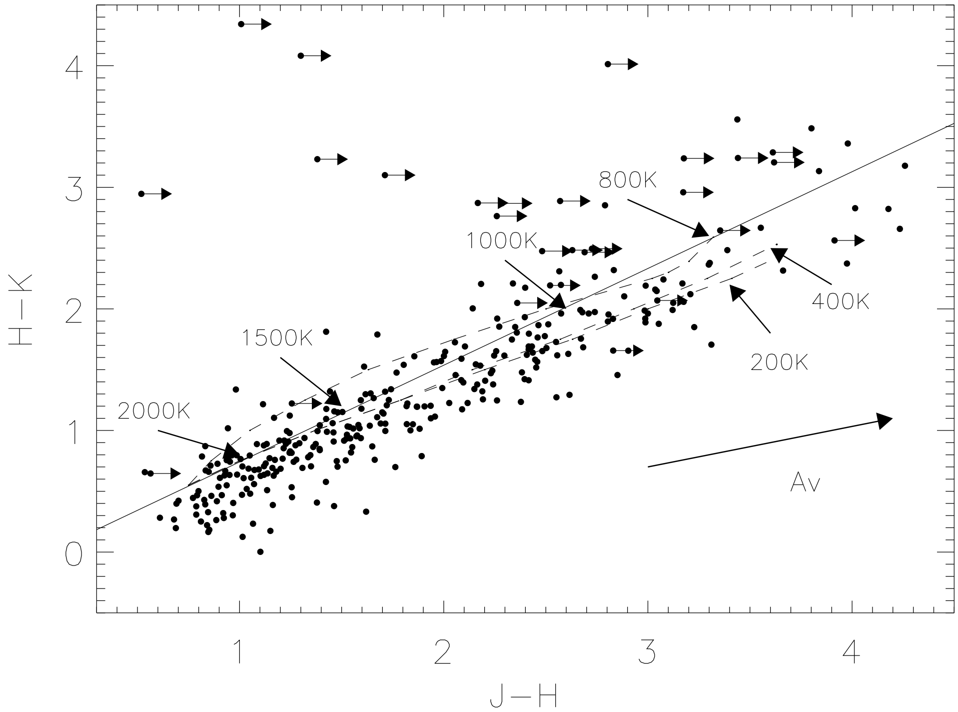

**Figure 2.6**: Near-infrared J–H vs. H–K colour-colour diagram of all Arecibo sources with photometry at least in the H and K bands. J–H lower limits are indicated by arrows. The solid line shows the location of black-bodies of different temperatures and the dashed lines show the location of the combination of a 2 500 K black-body with dust shells of temperatures 200, 400 and 800 K following Whitelock (1985). In addition we also indicate the reddening vector corresponding to $A_V = 10^m$.

with an arrow in this diagram.

The J−H and H−K colours show an almost linear correlation extending from (J−H = 0.5; H−K = 0.3) up to (J−H = 4.2; H−K = 3.2). The scatter in the range 0.5 < J−H < 3.0 is $0.26^m$, which is a factor 5 − 10 larger than expected from the errors of our photometry. Beyond J−H = 3.0 the scatter increases to $\approx 0.40^m$.

The colour-colour distribution is similar to that obtained by Lewis et al. (2004) from 2MASS data for one third of the 'Arecibo sample'. At its blue end it encompasses also the region where Mira variables are found (Whitelock et al. 1994). Unfortunately, the limited sensitivity of our observations especially in the J band prevents the full exploration of the red end of the distribution. Extrapolating the correlation found, the reddest objects in our sample with H–K > $4^m$ would have associated colours J–H ≈ 6, well beyond the limit of J−H = 4.2 shown in Figure 2.6.

In general, the position of the sources in Figure 2.6 can be explained as the result of the combined emission of a cool star ($T \approx 2\,500$ K) and a much cooler dust shell ($T < 800$ K). The main effect of the shell in the near-infrared colours would be to increase the circumstellar reddening which, together with differential interstellar extinction effects from source to source, could explain the width of the distribution observed.

But the correlation shown in the near-infrared colour-colour diagram J−H vs. H−K essentially represents a sequence of increasing optical thickness of the circumstellar shells, where Mira variables with still optically thin circumstellar envelopes are placed in the bluer part, and OH/IR stars with thicker circumstellar shells are located in the redder part of the diagram. We expect therefore that the rate of objects with optical counterparts will decrease with increasing near-infrared colours.

In Figure 2.7 we have plotted the fraction of optically identified counterparts on the DSS2 images versus the near-infrared colour H−K. As expected, the percentage of detections decreases with H–K colour. For H–K $\lesssim 1$ almost all Arecibo sources have optical counterparts, while at H–K $\gtrsim 1.5$ the fraction decreases rapidly to $< 50\%$. The two very blue (H–K $< 0.7$) Arecibo sources without optical counterpart are IRAS 18409+0431 ($J = 6.8^m$) and IRAS 19178+1206 ($H = 14.2^m$) (cf. Table A.1). The non-detection of IRAS 18409+0431 might be caused by variability or extraordinary high extinction, while IRAS 19178+1206 will be later identified in this chapter as a non-variable OH/IR star already in an early post-AGB stage. Beyond H–K $= 2$ the fraction of optical detections decreases further but does not go down completely to zero. The very red stars (H–K $> 2.5$) with optical counterparts are probably highly variable OH/IR stars optically detected during a maximum of luminosity. Another possibility is that the proposed optical counterparts are misidentified and they are actually faint field stars unrelated with the IRAS sources.

Figure 2.8 shows the position of the Arecibo sources in the IRAS colour-colour diagram as a function of their near-infrared colours. Blue near-infrared sources with H−K $\leq 1.0$ are located preferentially in the bluer part of the diagram ($[12]-[25] < -0.1$), while those with a red near-infrared colour (H−K $> 2.0$), most of them heavily obscured sources without an optical counterpart as we have just shown, occupy the red part of the diagram ($[12]-[25] > 0.1$). Those with intermediate near-infrared colours occupy an intermediate range of $[12]-[25]$ colours, as expected. There are however large overlaps between these groups.

The smooth correlation found between near- and mid-infrared colours corroborates the generally accepted interpretation that both the H−K and the $[12]-[25]$ colour sequences are good indicators of the optical thickness of the CSE. The wide range of colours observed cover the whole optical thickness range, from the optically thin shells of Mira variables to the thick shells of OH/IR stars. As the transparency of the shells decreases, stars are expected to get obscured first in the optical range and later continuously also in the near-infrared range. The very red objects which could not be detected in the H band

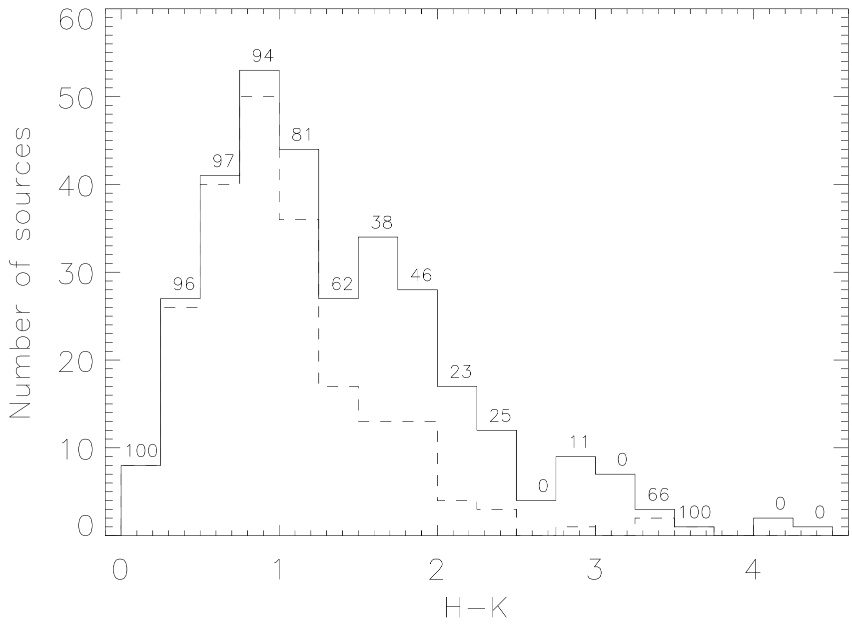

**Figure 2.7**: The total number of sources in the sample (*solid line*) is compared with the number of sources with optical counterpart on the DSS2 images (*broken line*) as a function of the H–K colour. The numbers on top of each bin indicate the percentage of optical counterpart detections.

represent the most extreme AGB population of obscured stars. Most of them are actually located among the reddest sources also in the IRAS two colour-colour diagram, as we can see in Figure 2.8.

The detection of a few blue near-infrared (H–K $< 1.0$) counterparts with very red [12]$-$[25] ($> 0.55$) colours could be an indicator of the end of the high mass loss regime in these stars, which should then be classified as post-AGB stars. Stars in the post-AGB phase are expected to reappear again as bright sources first in the near-infrared and later in the optical range, while the remnant circumstellar shell dissipates away. Alternatively, they could also be field stars, and the true counterparts being heavily obscured beyond our detection limits. We will analyse this small group of stars later more in detail.

### 2.5.4 The K$-$[12] vs. [12]$-$[25] colour-colour diagram

Another way to analyse the near- and mid-infrared properties of the sources in our sample is to study their distribution in the K$-$[12] vs. [12]$-$[25] colour-colour diagram (Figure 2.9). In stars with optically thin shells in the near-infrared the K$-$[12] colour provides information on the relative contribution of the near-infrared emission, dominated

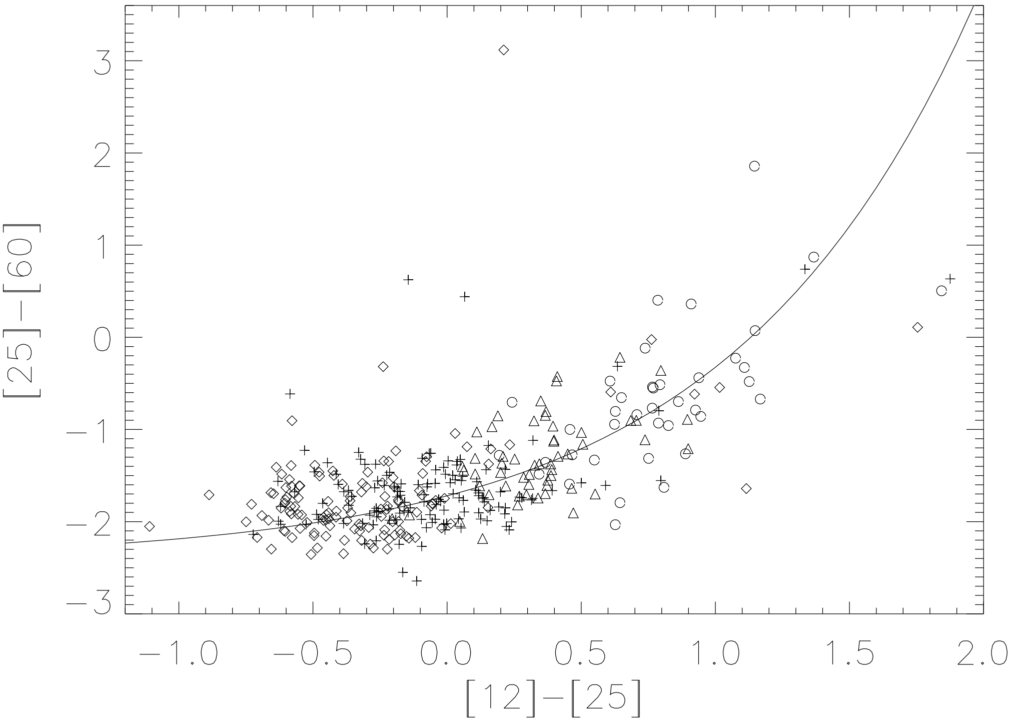

**Figure 2.8**: IRAS two-colour diagram with the Arecibo sources distinguished according to the H−K colours of their near-infrared counterparts. Diamonds (◇) are sources with H−K ≤ 1.0, crosses (+) are those with 1.0 < H−K ≤ 2.0, and triangles (△) those with 2.0 < H−K. Circles (○) correspond to sources with H brightness below the detection limit. The solid line is the 'O-rich AGB sequence'.

by the central star and by the hot dust surrounding it, and of the mid-infrared emission, mainly coming from the cool dust in the circumstellar shell, to the overall spectral energy distribution. The correlation of the K−[12] with the IRAS [12]−[25] colour can then be interpreted as an additional indicator of the optical thickness of the CSE of a given source. To calculate the K−[12] colour we adopted a zero-magnitude flux in the K band of 665 Jy (Koornneef 1983b).

Although a clear correlation exists between the K−[12] and the [12]−[25] colours as it is shown in Figure 2.9, there is a very large scatter in both axes. Only a small part of this scattering can be attributed to the intrinsic errors associated to the photometric measurements, mainly in the IRAS data, as the errors associated to our K band photometry are in most cases negligible. Typical errors are in the 10 − 15% range at 12 and 25 $\mu$m for the sources in our sample which translate into a dispersion of just $0.1-0.2^m$ in the [12]−[25] colour. However, in the case of the K−[12] colour the largest contribution to the

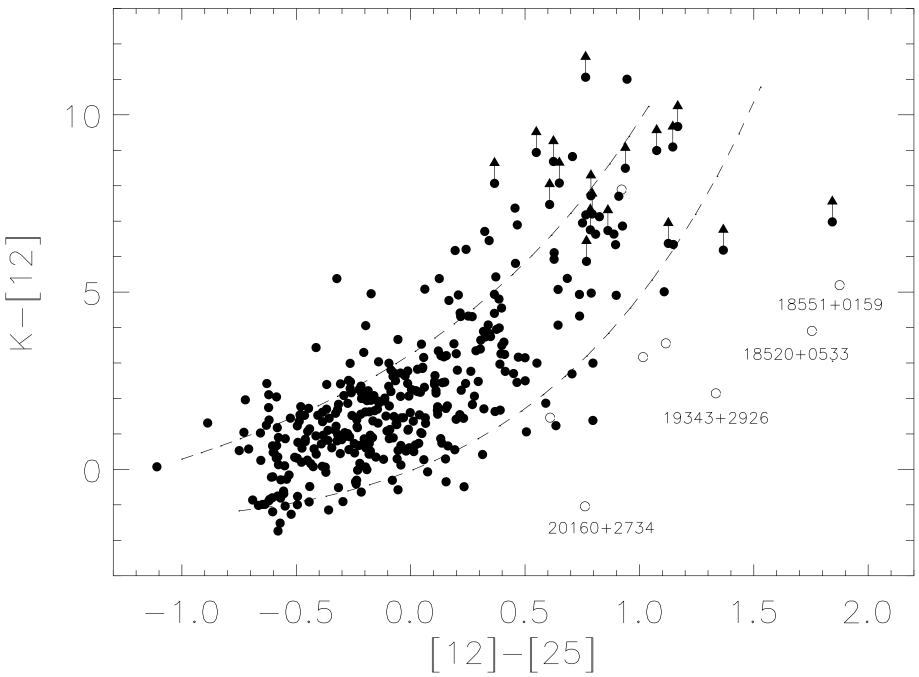

**Figure 2.9**: K−[12] vs. [12]−[25] colour-colour diagram of all Arecibo OH/IR stars with K band photometry. Lower magnitude limits in K were converted to lower limits in the K−[12] colour (*arrows*). The dashed lines correspond to the dispersion expected from the variability of the sources in the K band and at 12 $\mu$m and from the intrinsic errors associated to the photometric measurements. Candidate post-AGB stars are labelled with their IRAS names and/or with open symbols (see text).

dispersion observed is expected to come from the strong variability of the sources in our sample and not from the photometric errors, which are only a second-order effect. The near- and mid-infrared observations under analysis were made non-contemporaneously and this adds a substantial scatter. From data in the literature we know that optically bright Miras show typical K band amplitudes of $0.5-1.0^m$ while the most extreme OH/IR stars can reach amplitudes in the K band of up to $4^m$ (Engels et al. 1983; Le Bertre 1993; Olivier et al. 2001). In addition, the bluest Miras with OH maser emission show a variability at 12 $\mu$m of $\approx 0.6^m$ (Smith 2003) while this variability can reach up to $1.8^m$ in the most extreme OH/IR stars. This latter value has been estimated by comparing the measured flux in 12 $\mu$m both by IRAS and MSX satellites for those Arecibo sources for which these photometric data exist. If we reflect all these uncertainties in the K−[12] vs. [12]−[25] colour-colour diagram we obtain a wide area delimited by the dashed lines plotted in Figure 2.9, where the majority of the stars are located. This would imply that in most cases, the intrinsic variability of the sources could explain the scatter observed.

### 2.5.5 Early post-AGB candidates

Figure 2.9 shows, however, at least four clear outliers displaying a near-infrared counterpart much brighter than expected from their red [12]−[25] colours. They are labelled with their IRAS name in the K−[12] vs. [12]−[25] diagram. Namely, they are IRAS 18520+0533, IRAS 18551+0159, IRAS 19343+2926 and IRAS 20160+2734. The more natural interpretation for their peculiar position in this diagram would be that they are already in the post-AGB stage. As we have already mentioned, once the large mass-loss rates at the end of AGB evolution ceases, the optical depth of the circumstellar envelope decreases and the central star is expected to reappear again at shorter wavelengths while the mid-infrared colours redden further for some time (Bedijn 1987; Vassiliadis & Wood 1993). The cessation of the high mass-loss is connected to the end of the large amplitude pulsation of regular OH/IR stars. Thus, non-variability is expected to be an additional post-AGB stage indicator.

In addition, we have also indicated with open symbols in Figure 2.9 the position of those sources with very red [12]−[25] colours and unusually blue near-infrared counterparts that were also tentatively classified as candidate post-AGB stars or proto-planetary nebulae in Section 2.5.3. As we can see, two of these sources, IRAS 18520+0533 and IRAS 20160+2734, are in common with the outliers that we have just identified as candidate post-AGB stars, which supports our classification.

Both samples of candidate post-AGB stars are listed together in Table 2.3, where we give their photometric colours H−K, K−[12] and [12]−[25], the IRAS variability index and the proposed identification.

As we can see, several of these stars are already identified as post-AGB stars, proto-planetary nebulae or even as planetary nebulae in the literature.

This is the case of IRAS 18095+2704 a well known high-galactic latitude post-AGB star, with an F3Ib spectral type (Hrivnak et al. 1988), for which a detailed spectroscopic analysis including determination of chemical abundances can be found in Klochkova (1995).

The NIR photometry of IRAS 18520+0533 shows no variability between our two observing epochs and it has a low IRAS variability index. Eder et al. (1988) found that this source shows a peculiar 1612 MHz spectrum. The morphology of its two strongest peaks show the standard profile observed in OH/IR stars, but, exterior to these there are a pair of small flat peaks which may be due to a second shell of circumstellar material expanding at a larger velocity. This points to a peculiar nature of this OH/IR star, but we note that the location in the K−[12] vs. [12]−[25] diagram depends strongly on the IRAS 12 $\mu$m flux, which is declared as upper limit in the IRAS PSC for this source.

**Table 2.3**: Very red sources with unusually bright and/or blue near-infrared counterparts identified as candidate post-AGB stars or proto-planetary nebulae.

| IRAS | H−K | K–[12] | [12]–[25] | VAR | Comments |
|---|---|---|---|---|---|
| 18095+2704 | 0.26 | 3.55 | 1.11 | 15 | Post-AGB star |
| 18520+0533 | 0.93 | 3.90 | 1.76 | 3 | Peculiar OH/IR star |
| 18551+0159 | 1.66 | 5.20 | 1.87 | 25 | Infrared Planetary nebula |
| 19065+0832 | 0.70 | 3.17 | 1.02 | 98 | Non-variable OH/IR star? |
| 19178+1206 | 0.65 | 7.89 | 0.92 | 1 | Non-variable OH/IR star |
| 19200+1035 | 0.82 | 1.46 | 0.61 | 0 | Planetary nebula |
| 19343+2926 | 1.79 | 2.15 | 1.33 | 0 | Bipolar proto-planetary nebula |
| 20160+2734 | 0.29 | −1.04 | 0.76 | 0 | Semi-regular variable |

IRAS 18551+0159 was first identified as an infrared planetary nebula by Kistiakowsky & Helfand (1995) on the basis of its strong radio continuum emission at 20 cm and the large F([S III] $\lambda$ 9 532Å) / F(Paschen 9 $\lambda$ 9 225Å) ratio, which discards its classification as an ultracompact H II region. The source is extremely red and has no optical counterpart on the DSS2 image, which is probably a signature of its recent departure from the AGB.

IRAS 19065+0832 (OH 42.6+0.0, GLMP 876) is the only source in Table 2.3 showing a large IRAS variability index. It was classified in the GLMP catalogue as a variable OH/IR star (García-Lario 1992) on the basis of its large IRAS variability index, together with the detection of a strong silicate absorption feature in its IRAS Low Resolution Spectrum (it is a ‘class 39’ source). However, this is not consistent with the blue colours observed in the near-infrared nor with the non-variability which is suggested by the very similar photometry in our two epochs (only $0.07^m$ difference in the K-band). Our suggestion is that, if the near-infrared source was correctly identified, the star must be already in the post-AGB stage, but we cannot discard the possibility of a misidentification. This is why our classification in Table 2.3 is only tentative for the moment.

We identify IRAS 19178+1206 (GLMP 899) as a non-variable OH/IR star in a very early post-AGB stage. The source is completely invisible in the optical while it shows a relatively blue near-infrared counterpart. The non-variability and the blue near-infrared colours are confirmed with our two different epochs. However, it could be possible that the near-infrared counterpart of this source is in fact a field star, and that the true IRAS source is invisible even in the K band.

IRAS 19200+1035 (K 3−33) is included as a compact planetary nebula in the

Strasbourg-ESO Catalogue of Galactic Planetary Nebulae (Acker et al. 1992) although with a wrong finding chart. It is clearly identified as a bright source in our near-infrared images while it is very faint in the optical. Again the non-variability and the blue near-infrared colours are confirmed with our two different observing epochs.

IRAS 19343+2926 (M 1−92), also known as the Minkowski's Footprint, is a very well known young, bipolar proto-planetary nebula (Bujarrabal et al. 1998). The photometry for this source shows a very low variation between our two observing epochs ($< 0.04^m$ in K).

IRAS 20160+2734 (AU Vul) is classified as a semi-regular pulsating star in the SIMBAD database. It was first considered as a post-AGB star by Jiménez-Esteban et al. (2001) during a first analysis of our present sample. Lewis et al. (2004) supported this classification on the basis of the erratic detection of its different masers, being detected in the 1612 MHz OH maser at the sensitivity limit of the telescope by Eder et al. (1988), non-detected later in a water maser survey by Engels & Lewis (1996) or as a mainline OH maser by Lewis (1997), and recently again detected at 1667 MHz but not in 1665 MHz by Lewis et al. (2004).

## 2.6 Conclusions

We have presented an atlas of optical/near-infrared finding charts and near-infrared photometric observations for 371 objects taken from the 'Arecibo sample of OH/IR stars'. Except for 8 sources, we successfully identified their near-infrared counterparts and determined new positions for each source in the sample with an accuracy of $\approx 1''$. The correctness of the identifications was carefully assessed using improved positional information (MSX, VLA), analysing the near- and mid-infrared colour measurements, and in some cases searching for variability. The few sources for which no near-infrared counterpart was found were identified either as heavily obscured variable OH/IR stars at the very end of the AGB or as non-variable OH/IR stars in a very early post-AGB stage.

The wide dispersion observed in the JHK magnitudes measured is mainly attributed to their different optical thickness of the CSE, rather than to the different apparent luminosity expected from sources located at a wide range of distances, or to the different intrinsic luminosities of the sources in the sample.

The distribution of the Arecibo sources in the near-infrared J−H vs. H−K colour-colour diagram is interpreted as a sequence of increasing optical thickness of their circumstellar envelopes, where Mira-like variables with still optically thin shells are placed in the blue part of this diagram while the more extreme OH/IR stars with thicker shells are located in the redder part of the diagram. Their near-infrared colours can be reproduced with the combination of the emission coming from a cool central star (T $\approx$ 2 500 K) and from a much cooler dust shell ($T < 800\,K$). The dispersion of colours observed along the sequence can be explained as differential circumstellar and/or interstellar reddening.

This interpretation was confirmed by determining the detection rate of optical counterparts as a function of the H−K colour. We found that most of the Arecibo sources with $H-K < 1.0$ are detected in the optical range while those with $H-K > 2.0$ are heavily obscured sources with no optical counterpart on the DSS2 images. These sources are also located in different regions of the IRAS [12]−[25] vs. [25]−[60] colour-colour diagram, suggesting that both near- and mid-infrared colours are good indicators of the optical thickness of the shell.

The connection between the near- and the mid-infrared data was analyzed with the help of the K−[12] vs. [12]−[25] colour-colour diagram. We found that there is also a clear correlation between these two colours which can also be interpreted as an indication of the increasing contribution of the mid-infrared component (emission from the cool dust in the circumstellar shell) with respect to the near-infrared component (emission from the central star plus the hot dust surrounding it) to the overall spectral energy distribution as these stars evolve along the ‘O-rich AGB sequence’. However, the scatter of this correlation is found to be very large, partly because of the strong variability of these sources in the near- and mid-infrared and the non-contemporaneous of the observations under comparison. The expected variability goes from 0.5 to more than $4^m$ in the K band and from 0.5 to $1.8^m$ at $12\,\mu$m, both increasing toward redder [12]−[25] colours. Once these uncertainties are considered, the distribution observed in the K−[12] vs. [12]−[25] diagram can be explained as a consequence of the different optical thickness of the CSE, with the exception of a few outliers which were found to be much brighter than expected in the near-infrared according to their [12]−[25] colour.

The few sources showing very red [12]−[25] colours in combination with unusually blue near-infrared counterparts as well as the outliers in the K−[12] vs. [12]−[25] diagram have been identified as candidate post-AGB stars (some of them are well known proto-planetary nebulae or planetary nebulae).

The results here presented are the first byproduct of a long-term infrared and optical monitoring program started in 1999, which is aimed at determining the variability properties of all the sources in the ‘Arecibo sample of OH/IR stars’ and combine the information collected in the near-infrared with data available at other wavelengths in order to study more in detail the photometric behaviour of these stars in the context of stellar evolution.

**Acknowledgements:**

Based on observations collected at the German-Spanish Astronomical Centre, Calar Alto, operated jointly by Max-Planck-Institut für Astronomie and Instituto de Astrofísica de Andalucía (CSIC). This work has been supported by the Deutsche Forschungsgemeinschaft through travel grants (En 176/24-1 and 25-1) and by the Spanish Ministerio de Ciencia y Tecnología through grant AYA2003−09499. Part of the data reduction was supported by a grant of the Deutscher Akademischer Auslandsdienst (DAAD) to FJE. This research has made use of the SIMBAD database, operated at CDS, Strasbourg, France. We acknowledge also the use of the Digitized Sky Survey, based on photographic data obtained using the UK Schmidt Telescope. The UK Schmidt Telescope was operated by the Royal Observatory Edinburgh, with funding from the UK Science and Engineering Research Council, until 1988 June, and thereafter by the Anglo-Australian Observatory. Original plate material is copyright (c) of the Royal Observatory Edinburgh and the Anglo-Australian Observatory. The plates were processed into the present compressed digital form with their permission. The Digitized Sky Survey was produced at the Space Telescope Science Institute under US Government grant NAG W-2166.

# Chapter 3

# The ‘GLMP sample’ of OH/IR stars

**Abstract**

In this chapter we present optical and near-infrared finding charts, and accurate astrometry ($\approx 0.2''$) of 94 IRAS sources selected from the GLMP catalogue (García-Lario 1992). The main photometric properties of the stars in this sample are presented, discussed and compared to the results previously obtained in Chapter 2 for the ‘Arecibo sample’ of OH/IR stars, as well as the problems found during the process of identification of the optical/near-infrared counterparts.

We find that in this case up to 93% of the sources (87 in number) have no optical counterpart, 43% of them (40 in number) being invisible even at near infrared wavelengths. This confirm our preliminary expectation that the ‘GLMP sample’ of variable OH/IR stars presented in this chapter constitutes an extension of the properties observed in the ‘Arecibo sample’ toward redder colours and thicker envelopes.

## 3.1 Introduction

In Chapter 2 we have showed the main optical/near-infrared properties of a well-defined sample of far-infrared selected AGB stars showing OH maser emission. This sample, the so-called 'Arecibo sample', consists of 385 IRAS sources, which were detected in the 1612 MHz OH maser line with the Arecibo radio telescope (Eder et al. 1988; Lewis et al. 1990b; Chengalur et al. 1993). The sample, as already mentioned, was obtained from a complete survey of IRAS sources with flux densities $\geq 2$ Jy at 25 $\mu$m, with declination $0 < \delta < 37°$ and appropriate colours of AGB stars (Olnon et al. 1984), the OH maser detection qualifies the IRAS source as an O-rich AGB star. We have just seen also in Chapter 2 that this sample is mainly constituted by optically visible sources ($\approx 2/3$ of the sample), with thin CSE, with a minor contribution of optically invisible ones ($\approx 1/3$ of the sample), with thick CSE. These OH/IR stars are located in a wide area of the near-infrared J-H vs. H-K colour-colour diagram, which was shown to be an extension toward redder colours of the area where optically visible Mira variables are normally found (Whitelock et al. 1994).

However, the 'Arecibo sample' predominantly represents the bluer (and probably less massive) population of galactic OH/IR stars. The purpose of the following analysis is to determine the optical/near-infrared properties of a sample of redder OH/IR stars and probably higher mass, taken this time from the GLMP catalogue (García-Lario 1992), and establish connections with the properties showed by the 'Arecibo sample'. As a byproduct we have also created an atlas of finding charts combining optical images from the DSS2 (Djorgovski et al. 2001) and near-infrared images from the 2MASS (Cutri et al. 2003), in the same way as we did for the Arecibo sources.

Section 3.2 contains a description of the selected sample. In Section 3.3 the process of identification of the optical/near-infrared counterparts is explained. This is followed by a brief description of the atlas contents. The results obtained are discussed in Section 3.4. Finally, the main conclusions are presented in Section 3.5.

## 3.2 Sample selection

The GLMP catalogue (García-Lario 1992) is formed by 1084 IRAS sources with [12]–[25] vs. [25]–[60] colours similar to those shown by planetary nebulae (PNe). The selection criteria employed by García-Lario to include an object in this catalogue were such that the source must be well detected (IRAS-FQual = 3) in at least the three IRAS photometric bands centred at 12, 25 and 60 $\mu$m with the following additional constraints:

i) $F_\nu(12\mu m)/F_\nu(25\mu m) \leq 0.50$

ii) $F_\nu(25\mu m)/F_\nu(60\mu m) \geq 0.35$

**Table 3.1**: Objects in common to the GLMP catalogue and to the ‘Arecibo sample’

| IRAS | | | |
|---|---|---|---|
| 18517+0037 | 18549+0208 | 19065+0832 | 19067+0811 |
| 19081+0322 | 19183+1148 | 19188+1057 | 19283+1944 |
| 19352+2030 | 19374+1626 | 19565+3140 | 19576+2814 |
| 20023+2855 | 20043+2653 | 20137+2838 | 20272+3535 |

iii) $F_\nu(60\mu m)/F_\nu(100\mu m) \geq 0.60$ when a good measurement (IRAS-FQual$\,=\,$3) was available in the 100$\,\mu$m band.

Thus, the GLMP catalogue is formed by a heterogeneous collection of far-infrared selected sources distributed over the full sky with very red IRAS colours ([12]–[25]$\,\geq\,$0.75), containing PNe, as it was the initial purpose of the catalogue but also a considerable number of AGB and pot-AGB stars (appart from a small percentage of ’contaminant’ sources like T-Tauris stars, Herbig Ae-Be stars, ultracompact H II regions and even a few Seyfert galaxies). Among the AGB stars, it is possible to pick up those showing OH maser emission and/or are located in a characteristic region of the IRAS two colour diagram with a high ($>$50) IRAS variability index, and these ones, classified in the GLMP catalogue as ’variable OH/IR stars’ were the ones selected for our study (the ‘GLMP sample’ in the following). Two sources, namely IRAS 11438–6330 and IRAS 12358–6323 were also taken for the analysis and included in the sample because, although their VAR were low, near infrared photometric observations taken from the literature confirmed that both objects were still strongly variable in the near-infrared (Gaylard et al. 1989; Lepine et al. 1995; Hu et al. 1993; García-Lario et al. 1997) and, thus, they can also be identified as AGB stars.

On the other hand, although most of the sources in the ‘GLMP sample’ are detected in OH at 1612 MHz, which confirms that these sources are actually O-rich AGB stars, there is also a small number of them which either were never observed in OH or they were tried and not detected. These sources without confirmation of the presence of the OH maser, were still classified by García-Lario as variable OH/IR stars based on the large VAR index and on their characteristic position in the IRAS colour-colour diagram, very close to the ‘O-rich AGB sequence’ and, as such, we include them also in the sample.

The variability cut, while efficient in excluding non-AGB objects, may introduce a bias. Indeed, only $\approx$70% of the sky was surveyed three times during the IRAS mission, while 20% was observed only twice, and thus the variable sources in some parts of the sky were more likely to be detected than others. Furthermore, the variability detection could significantly depend on the colour. Due to the short lifetime of the IRAS satellite

(≈10 months), it was more probable to observe variability in OH/IR stars with the shorter periods (bluer IRAS colours) than in those with the longer periods (redder IRAS colours) (Beichman et al. 1988).

Thus, the selected sources form a group of 110 OH/IR stars taken all them from the GLMP catalogue and distributed over the full sky for which indications of a strong variability in the mid- to far-infrared exist. 16 of them were also part of the ‘Arecibo sample’ of OH/IR stars (see Table 3.1). Since the optical/near-infrared characteristics of the sources in the ‘Arecibo sample’ were already presented and discussed in Chapter 2, we have not analysed again the few objects in common. Then, after these are excluded, the resulting ‘GLMP sample’ is formed by a total of 94 OH/IR stars with very red IRAS colours.

The position of the sources belonging to the ‘GLMP sample’ in the IRAS two-colour diagram is shown in Figure 3.1, together with the ‘O-rich AGB sequence’ as defined in Section 1.2, and the position of the well known ‘Arecibo sample’ of OH/IR stars analysed in the previous Chapter 2. The sources in common are shown with a different symbol. It is clearly visible from this figure that the ‘GLMP sample’ occupies a significantly redder position in this diagram, increasing enormously the number of objects classified as OH/IR stars in this region.

## 3.3 Identification of the optical/near-IR counterparts

In order to determine the optical/near infrared counterparts of the 94 OH/IR stars in our sample we first considered the best coordinates available from existing catalogues and then searched for plausible counterparts at these locations both on the optical images taken from the DSS2 and on near-infrared images taken from the 2MASS (http://irsa.ipac.caltech.edu/applications/2MASS/QL).

### 3.3.1 Cross-correlation with the MSX

Improved coordinates with respect to those originally provided by the IRAS Point Source Catalogue (accuracy typically between $10'' - 15''$) can be obtained by cross-correlating our sample with the MSX Point Source Catalogue (MSX6C) (Egan et al. 2003), which provides coordinates of the mid-infrared counterparts with an accuracy of $\approx 2''$. However, the MSX survey is limited to low galactic latitudes ($\leq 6^\circ$ in absolute value) and, thus, not all GLMP sources has an associated MSX entry. In any case, the accuracy of MSX is in many cases essential to identify the near-infrared counterpart, in particular in crowded regions along the galactic plane and/or close to the Galactic Centre, and for extremely red objects only marginally detectable in the K band, as we will see later.

We searched for the MSX counterpart of all sources in the ‘GLMP sample’ located

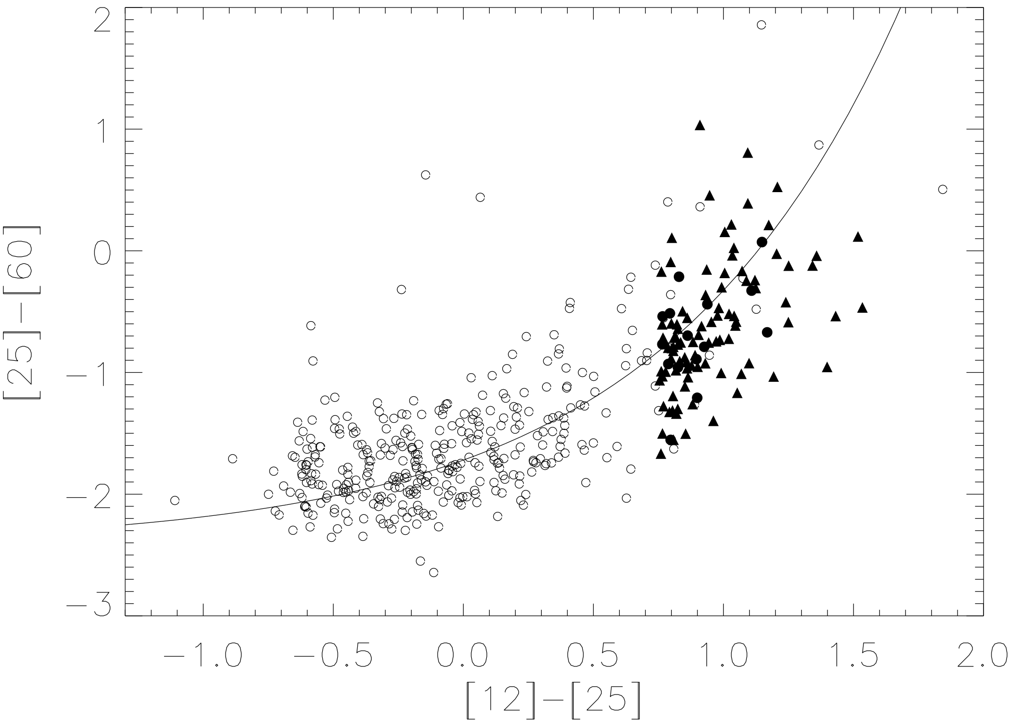

**Figure 3.1**: The position in the IRAS two-colour diagram of OH/IR stars in the 'GLMP sample' (filled triangles) is compared with the position of the OH/IR stars in the 'Arecibo sample' (open circles). Filled circles are used for the few objects in common. The solid line is the 'O-rich AGB sequence', and the IRAS colours are defined as: $[12]-[25] = -2.5\log\frac{F_\nu(12)}{F_\nu(25)}$ and $[25]-[60] = -2.5\log\frac{F_\nu(25)}{F_\nu(60)}$.

at low galactic latitudes ($|b| < 6°$) in an area of $60''$ radius around the original IRAS coordinates. When more than one MSX source was found within this small area, we selected the reddest MSX counterpart, which was not always the nearest. Usually only the reddest sources showed MSX photometric data consistent with the IRAS photometry.

Out of a total of 85 objects located within the MSX survey sky area (essentially $|b| < 6°$), we found that 82 objects (96% of them) had a clear mid-infrared counterpart in the MSX6C (see Tables 3.2 and 3.3). This high rate is similar to that found for the 'Arecibo sample' (Chapter 2). The 3 sources without MSX counterpart were actually missed probably because they are located at the edges of the MSX survey area, at galactic latitudes $|b| > 5.3°$. For these 3 sources, plus the 9 additional ones not covered by MSX, we could not improved the original IRAS astrometry.

### 3.3.2 Near-infrared counterparts

An additional improvement to the accuracy of the available coordinates can be achieved by searching for their near-infrared counterparts in the 2MASS Point Source Catalogue (2MASS-PSC), which has an astrometric accuracy of $\approx 0.2''$. For this, we inspected a $30'' \times 30''$ or a $6'' \times 6''$ box, depending on whether the available coordinates were from IRAS or from MSX respectively, centered at the nominal source position and searched for a plausible (i.e. redder than average) counterpart within the box.

Approximately in one third of the cases only one source was found within the searched area showing extremely red colours. However, in another third of cases there were more than one object within the searched area. Then we always selected the redder object, that turned out to be also the nearest in all cases with just two exceptions: IRAS 17367–2722 and IRAS 17392–3020. In 16 cases (20% of the sources with associated MSX counterparts) no object was found within the MSX searching box. Out of the 12 objects without MSX coordinates, which had to be search for using the IRAS astrometry, we were able to find suitable near-infrared counterparts in 10 cases. Only two objects (IRAS 18479–2514 and IRAS 18195-2804) did not show any plausible counterpart in 2MASS.

Despite the use of a searching box relatively small ($< 6''$ of radius) for the majority of the sources, the probability of misidentification is still high. On one side, stellar fields were in many cases very crowded since some of them correspond to regions of very low galactic latitude and/or located in the direction of the Galactic Center, and more than one 2MASS point source was usually ($\approx 30\%$) found within the searching box. On the other hand, the kind of objects under analysis in this work are expected to develop very thick CSE which may not allow us to see the central source even in the near-infrared. Thus, in some cases the source found within the searched area, can be in fact a field star, being the true counterpart of the IRAS source, hidden by its thick CSE, completely invisible at near-IR wavelengths. In Chapter 2 we showed that all Arecibo source with red IRAS colours ([12]–[25] $> 0.5$) and blue near-infrared colours (H–K $< 1$) were not expected to be variable OH/IR stars and they were identified as candidate post-AGB stars. The ‘GLMP sample’ of OH/IR stars, however, was selected imposing that all sources must have a high IRAS variability index (VAR $> 50$), which excludes the possibility of finding stars which are not any more in the AGB phase. Thus, to avoid potential misidentifications, we imposed an additional near-infrared colour constraint, H–K $> 1$, to qualify a source as the near infrared counterpart of any star in the ‘GLMP sample’. In the case of sources only detected in the K-band, but with only an upper limit measurement in the H-band, we still considered the possibility of them being the most probable counterparts but many of them should be considered only as tentative detections. The same decision was taken for IRAS 14562–5637 and IRAS 17276–2846, that were just barely detected both in the K and H filters. Only in one case, IRAS 18000–2835, the near-infrared counterpart selected had H–K$\,<\,$1. The 2MASS counterpart of this IRAS source was found only $\approx 1.8''$ off the MSX position, and showed the brightest (K$\,=\,5.05^{m}$) near-infrared brightness of the sample. Variable OH/IR stars are among the most luminous near-infrared objects in our Galaxy. Thus, the probability of this very bright near-infrared source being a field star is very low. However, the only way to be completely sure that the selected 2MASS counterparts are the right ones is by searching for variability among different observing epochs. Further photometric observations of this source and of the other two targets above mentioned would be desirable to confirm their variable OH/IR star nature.

The identification procedure was not simple in many cases, due to various other reasons. Some counterparts were not correctly identified by the 2MASS software due to blending with other nearby sources and to insufficient S/N. Sometimes the presence of a nearby bright source is hiding faint sources which are not included in the Point Source Catalogue. This was actually the case of IRAS 17151–3642. Around the MSX position of IRAS 17151–3642 only a very bright source (2MASS 259.622353–36.768497) appeared in the catalogue, but in the near-infrared images an invisible object in the band J appeared clearly visible in the H and K band images very close to the bright source, which was the only one included in the 2MASS-PSC. This very red object was selected as the most reliable counterpart for the IRAS source in our sample. IRAS 17495–2534 was also identified as a source only visible in the K-band located very close to a brighter object (2MASS 268.164447–25.577236) for which 2MASS had not assigned any entry in the PSC. IRAS 18182–1504 appeared clearly in the H- and K-band images but there was no entry in the 2MASS-PSC for this star. The near-infrared counterparts of IRAS 18091–2437 and IRAS 17428–2438 were very faint stars only visible in the K-band, and probably with a flux under the detectability threshold. Thus, these two objects neither had any associated entry in the 2MASS-PSC. For all these sources we derived their astrometric coordinates directly from the 2MASS images by determining the centroid of the point-like emission associated to the near-infrared counterpart.

**Table 3.2**: 2MASS coordinates of the subgroup of OH/IR stars in the 'GLMP sample' for which a plausible near-infrared counterpart was found, compared to IRAS and MSX coordinates.

| IRAS | 2MASS Coordinates (J2000) | | IRAS–2MASS | | IRAS–MSX | | MSX6C_G |
|---|---|---|---|---|---|---|---|
| | | | $\Delta\alpha$ [″] | $\Delta\delta$ [″] | $\Delta\alpha$ [″] | $\Delta\delta$ [″] | |
| 08425−5116 | 08 44 04.36 | −51 27 41.9 | 3 | 0 | 2 | −1 | 269.4419−05.4504 |
| 11438−6330 | 11 46 14.00 | −63 47 14.2 | −2 | 2 | −2 | 3 | 295.8065−01.8214 |

*Continue in the next page.*

*Table 3.2: 2MASS astrometry for the ‘GLMP sample’ (continued)*

| | 2MASS | | IRAS–2MASS | | IRAS–MSX | | |
|---|---|---|---|---|---|---|---|
| IRAS | Coordinates | | $\Delta\alpha$ | $\Delta\delta$ | $\Delta\alpha$ | $\Delta\delta$ | MSX6C_G |
| | (J2000) | | [″] | [″] | [″] | [″] | |
| 12158−6443 | 12 18 35.48 | −65 00 14.2 | 2 | −3 | 3 | −3 | 299.4688−02.3533 |
| 12358−6323 | 12 38 48.35 | −63 39 39.4 | −1 | 1 | 0 | 0 | 301.5309−00.8231 |
| 14247−6148 | 14 28 30.73 | −62 01 35.7 | 0 | 0 | 3 | 0 | 314.0494−01.2684 |
| 14562−5637 * | 15 00 02.39 | −56 49 44.2 | 6 | −3 | 7 | −2 | 319.8669+01.7534 |
| 15471−4634 | 15 50 40.33 | −46 43 16.9 | 2 | −1 | −2 | −3 | 331.9853+05.7905 |
| 15514−5323 | 15 55 21.13 | −53 32 44.6 | −26 | 8 | −22 | 10 | 328.2246+00.0418 |
| 16040−4708 | 16 07 39.47 | −47 16 26.3 | 3 | −2 | 3 | −2 | 333.8253+03.4834 |
| 16219−4823 | 16 25 41.89 | −48 30 33.9 | −1 | 0 | 0 | −1 | 335.1416+00.4939 |
| 16582−3059 | 17 01 29.83 | −31 04 19.0 | −6 | 0 | | | |
| 17004−4119 * | 17 03 55.97 | −41 24 00.8 | 1 | 2 | −2 | 0 | 344.9293+00.0136 |
| 17030−3053 | 17 06 14.07 | −30 57 38.3 | −2 | 0 | −3 | 2 | 353.5472+05.9448 |
| 17107−3330 | 17 14 05.06 | −33 33 58.0 | −2 | −1 | −4 | −2 | 352.4216+03.0672 |
| 17151−3642 * | 17 18 29.74 | −36 46 07.2 | −5 | 5 | −4 | 0 | 350.3340+00.4777 |
| 17171−2955 * | 17 20 20.25 | −29 58 22.8 | −3 | 1 | −3 | −1 | 356.1310+04.0515 |
| 17242−3859 * | 17 27 38.65 | −39 02 10.1 | 12 | −2 | 12 | −1 | 349.4829−02.2940 |
| 17276−2846 * | 17 30 48.35 | −28 49 01.7 | 3 | 1 | 5 | −2 | 358.3668+02.8054 |
| 17316−3523 | 17 34 57.50 | −35 25 52.6 | 6 | 0 | 6 | 1 | 353.2979−01.5367 |
| 17317−3331 | 17 35 02.72 | −33 33 29.4 | −7 | −1 | −5 | 0 | 354.8833−00.5384 |
| 17341−3529 | 17 37 30.29 | −35 31 04.7 | −17 | 3 | −17 | 4 | 353.5039−02.0204 |
| 17350−2413 | 17 38 08.85 | −24 14 49.3 | −2 | 0 | −3 | 0 | 003.1080+03.8899 |
| 17351−3429 | 17 38 26.29 | −34 30 41.0 | −2 | −1 | −4 | −2 | 354.4579−01.6437 |
| 17367−3633 * | 17 40 07.63 | −36 34 41.4 | −4 | −3 | −2 | −2 | 352.8880−03.0333 |
| 17392−3020 * | 17 42 30.81 | −30 22 07.3 | −22 | −2 | −17 | 0 | 358.4249−00.1744 |
| 17417−1630 | 17 44 39.87 | −16 31 42.1 | −4 | −2 | | | |
| 17428−2438 * | 17 45 56.97 | −24 39 57.8 | −2 | −2 | −3 | −2 | 003.6854+02.1592 |
| 17467−4256 | 17 50 20.50 | −42 57 18.5 | −3 | −1 | | | |
| 17495−2534 * | 17 52 39.59 | −25 34 39.5 | 0 | 0 | 0 | −2 | 003.6848+00.3883 |
| 17504−3312 | 17 53 50.24 | −33 13 26.3 | −41 | 2 | −41 | 0 | 357.2197−03.7085 |
| 17545−3317 | 17 57 49.20 | −33 17 47.6 | 1 | −1 | 0 | −2 | 357.5737−04.4663 |
| 17577−1519 | 18 00 36.12 | −15 19 44.6 | −13 | −2 | −15 | −2 | 013.4930+03.9153 |
| 17583−3346 | 18 01 39.27 | −33 46 00.5 | −5 | −1 | | | |
| 18000−2835 | 18 03 12.89 | −28 35 41.9 | −28 | 1 | −29 | 2 | 002.2442−03.1547 |
| 18006−1734 | 18 03 36.86 | −17 34 00.4 | −4 | −1 | −4 | −1 | 011.8974+02.1862 |
| 18015−1608 | 18 04 28.28 | −16 07 52.3 | −8 | 0 | −10 | 0 | 013.2508+02.7102 |
| 18081−0338 | 18 10 49.48 | −03 38 14.2 | −6 | 0 | | | |
| 18091−2437 * | 18 12 16.13 | −24 36 42.9 | −6 | −2 | −5 | −1 | 006.7152−02.9972 |
| 18107−0710 | 18 13 30.01 | −07 09 48.2 | −3 | −1 | −4 | −2 | 022.1975+05.0855 |
| 18152−0919 | 18 17 58.57 | −09 18 31.5 | −20 | −1 | −21 | −1 | 020.8254+03.0967 |

*Continue in the next page.*

*Table 3.2: 2MASS astrometry for the 'GLMP sample' (continued)*

| | 2MASS | | IRAS–2MASS | | IRAS–MSX | | |
|---|---|---|---|---|---|---|---|
| IRAS | Coordinates | | $\Delta\alpha$ | $\Delta\delta$ | $\Delta\alpha$ | $\Delta\delta$ | MSX6C_G |
| | (J2000) | | [″] | [″] | [″] | [″] | |
| 18182−1504 * | 18 21 06.83 | −15 03 20.0 | −12 | −4 | −13 | −2 | 016.1169−00.2903 |
| 18187−0208 | 18 21 18.76 | −02 07 01.1 | −4 | −2 | −3 | −4 | 027.5923+05.7240 |
| 18201−2549 | 18 23 12.28 | −25 47 58.7 | −1 | 2 | | | |
| 18211−1712 | 18 24 05.54 | −17 11 11.9 | −6 | −1 | −7 | −1 | 014.5704−01.9215 |
| 18257−1052 | 18 28 30.97 | −10 50 48.5 | 3 | −6 | 4 | −2 | 021.4566+00.4911 |
| 18262−0735 | 18 28 59.86 | −07 33 23.0 | −5 | −2 | −6 | −3 | 023.6510+01.5062 |
| 18266−1239 | 18 29 28.74 | −12 37 53.1 | 8 | 1 | 9 | 3 | 019.2086−00.9527 |
| 18277−1059 | 18 30 30.92 | −10 57 33.4 | 28 | 1 | 29 | 1 | 020.8085−00.4024 |
| 18298−2111 | 18 32 48.56 | −21 09 37.6 | 28 | 1 | | | |
| 18299−1705 | 18 32 50.75 | −17 02 48.5 | −4 | 0 | −4 | −1 | 015.6638−03.7108 |
| 18310−2834 | 18 34 13.78 | −28 32 21.6 | −2 | −2 | | | |
| 18361−0647 | 18 38 50.54 | −06 44 49.6 | −32 | 14 | −34 | 14 | 025.4948−00.2879 |
| 18432−0149 | 18 45 52.40 | −01 46 42.5 | 6 | 0 | 6 | 0 | 030.7147+00.4264 |
| 18460−0254 | 18 48 41.97 | −02 50 25.4 | −23 | −10 | −24 | −6 | 030.0908−00.6866 |
| 18475−1428 | 18 50 22.90 | −14 24 30.7 | −6 | −3 | | | |
| 18488−0107 * | 18 51 26.02 | −01 03 56.0 | −3 | 2 | −6 | −2 | 031.9844−00.4849 |
| 19069+1335 | 19 09 16.61 | +13 40 27.9 | −6 | −3 | −6 | −3 | 047.1168+02.3242 |
| 19122−0230 | 19 14 54.84 | −02 25 28.8 | −7 | −2 | | | |

*Note:* *: tentative identification.

The identification strategy provided in 45 cases a plausible near-infrared counterpart to the GLMP OH/IR stars. In 13 cases only a tentative near-infrared counterpart is provided. These 58 sources are tabulated in Table 3.2. The Table lists the IRAS name, astrometric position from the 2MASS-PSC (RA and DEC, respectively), a comparison with the coordinates provided originally by IRAS and with the ones derived from the MSX6C, and the MSX name, when available. The objects with tentative identification have been labeled with an asterisk.

All the objects without a 2MASS counterpart but with an MSX one are shown in Table 3.3. This Table includes the MSX coordinates, a comparison with the original IRAS coordinates, and the associated MSX object name. Only IRAS 18479–2514 and IRAS 18195-2804 had neither MSX nor 2MASS counterpart. For these two sources no improvement to the IRAS coordinates was possible. Their IRAS coordinates have also been tabulated in Table 3.3.

### 3.3.3 Search for optical counterparts

In order to search for the optical counterparts of those GLMP sources for which we found a near-infrared counterpart, we inspected the corresponding accurate astrometric

**Table 3.3**: MSX coordinates of the subsample of OH/IR stars in the ‘GLMP sample’ without near-infrared counterpart detected, compared to IRAS coordinates.

| IRAS | MSX Coordinates (J2000) | | IRAS−MSX | | MSX6C_G |
|---|---|---|---|---|---|
| | | | Δα [″] | Δδ [″] | |
| 09024−5019 | 09 04 03.3 | −50 31 32 | 0 | 4 | 270.7424−02.4384 |
| 15198−5625 | 15 23 42.7 | −56 36 08 | 1 | 1 | 322.7729+00.2860 |
| 15327−5400 | 15 36 35.9 | −54 10 29 | −5 | 1 | 325.6578+01.2432 |
| 16236−5332 | 16 27 39.3 | −53 39 04 | −13 | 2 | 331.6587−03.3024 |
| 17055−3753 | 17 08 57.3 | −37 56 50 | 6 | 0 | 348.2670+01.3225 |
| 17128−3528 | 17 16 12.9 | −35 32 12 | −1 | 0 | 351.0725+01.5639 |
| 17207−3632 | 17 24 07.4 | −36 35 39 | 5 | −3 | 351.1189−00.3517 |
| 17251−2821 | 17 28 18.5 | −28 23 57 | 3 | −4 | 358.4140+03.4923 |
| 17292−2727 | 17 32 23.4 | −27 29 58 | 4 | −3 | 359.6629+03.2315 |
| 17323−2424 | 17 35 26.0 | −24 26 32 | −6 | 2 | 002.6111+04.3084 |
| 17361−2358 | 17 39 15.0 | −23 59 55 | 3 | −3 | 003.4525+03.8089 |
| 17367−2722 | 17 39 52.4 | −27 23 32 | −4 | −4 | 000.6467+01.8893 |
| 17368−3515 | 17 40 12.9 | −35 16 41 | 2 | −3 | 354.0019−02.3600 |
| 17411−3154 | 17 44 24.0 | −31 55 40 | −17 | 1 | 357.3108−01.3371 |
| 17418−2713 | 17 44 58.8 | −27 14 43 | −1 | −2 | 001.3690+01.0025 |
| 17521−2938 | 17 55 21.8 | −29 39 13 | 0 | 1 | 000.4720−02.1918 |
| 17545−3056 | 17 57 48.4 | −30 56 25 | 0 | −2 | 359.6212−03.2926 |
| 17584−3147 | 18 01 41.8 | −31 47 56 | −4 | −2 | 359.2842−04.4385 |
| 18007−1841 | 18 03 39.0 | −18 41 10 | 21 | 4 | 010.9257+01.6294 |
| 18019−3121 | 18 05 12.1 | −31 21 45 | −1 | 2 | 000.0313−04.8783 |
| 18040−2726 | 18 07 09.0 | −27 25 52 | −5 | −4 | 003.6860−03.3459 |
| 18040−2953 | 18 07 18.3 | −29 53 10 | −9 | −3 | 001.5478−04.5617 |
| 18091−0855 | 18 11 56.5 | −08 54 46 | −3 | −3 | 020.4676+04.5958 |
| 18092−2347 | 18 12 20.5 | −23 46 57 | −17 | −3 | 007.4526−02.6149 |
| 18092−2508 | 18 12 21.9 | −25 07 21 | −4 | −1 | 006.2765−03.2604 |
| 18100−1915 | 18 13 03.2 | −19 14 19 | −6 | −1 | 011.5218−00.5826 |
| 18195−2804* | 18 22 40.2 | −28 03 08 | | | |
| 18198−1249 | 18 22 43.1 | −12 47 42 | −12 | −2 | 018.2955+00.4291 |
| 18257−1000 | 18 28 31.0 | −09 58 15 | −35 | −3 | 020.6796+00.0841 |
| 18268−1117 | 18 29 35.6 | −11 15 54 | 3 | 0 | 020.4328−00.3439 |
| 18361−0036 | 18 38 45.1 | −00 33 22 | 2 | 1 | 030.9892+02.5686 |
| 18479−2514* | 18 51 00.9 | −25 11 06 | | | |
| 18518+0558 | 18 54 17.4 | +06 02 34 | −1 | −2 | 038.6366+02.1198 |
| 19087+1006 | 19 11 09.9 | +10 11 38 | −28 | −8 | 044.2404+00.3090 |
| 19112+1220 | 19 13 37.4 | +12 25 38 | −16 | −8 | 046.4992+00.8092 |
| 19254+1724 | 19 27 41.1 | +17 30 36 | 1 | −1 | 052.5814+00.2014 |

*Note:* * IRAS coordinates

**Table 3.4**: Median and mean separation (and standard deviation) between 2MASS and IRAS coordinates and between 2MASS and MSX coordinates.

| | N | $\Delta\alpha$ median | $\Delta\alpha$ ($\sigma_{\Delta\alpha}$) mean | $\Delta\delta$ median | $\Delta\delta$ ($\sigma_{\Delta\delta}$) mean |
|---|---|---|---|---|---|
| 2MASS–IRAS | 58 | 4.6″ | 8.1″ (9.3″) | 1.5″ | 2.0″ (2.4″) |
| 2MASS–MSX | 48 | 0.9″ | 1.2″ (1.1″) | 1.0″ | 1.3″ (1.1″) |

positions in the optical images extracted from the DSS2 (Djorgovski et al. 2001) in the red filter, which covers the spectral range 6 000 – 7 000 Å with a maximum efficiency around 6 700 Å. Using a 1″ × 1″ box centered on the nominal 2MASS source position.

The majority (88%) of the objects with near-infrared counterparts did not show any optical counterpart, and only 7 objects had a faint optical counterpart. This confirmed our preliminary expectation that the sources in the 'GLMP sample' belong all them to the group of variable OH/IR stars with redder colours and optically thick CSE.

### 3.3.4 Consistency checks

Here we present a number of consistency checks involving positional correlations between IRAS, MSX and 2MASS which can be made to validate the reliability of the near-infrared counterparts selected and to single out exceptional objects.

For this we have compared the new coordinates taken from 2MASS with those listed originally in the IRAS Point Source Catalogue and with those given by the MSX6C. In Table 3.4 we list the median and the mean separation (in arcsec) in Right Ascension ($\alpha$) and Declination ($\delta$) between 2MASS coordinates and the IRAS and MSX ones, together with the associated standard deviations.

There are 48 sources with near-infrared counterparts and available MSX coordinates in our 'GLMP sample'. The median angular separation between our new coordinates and the MSX ones is of $\approx 1.7''$, which is coincident with that found for the Arecibo sources in Chapter 2. In Figure 3.2, we have plotted in a histogram the angular separation distribution between 2MASS and MSX coordinates. The internal consistency between the 2MASS and MSX coordinates is very good (within 2.5″ in most cases).

As expected, much larger deviations are found when we compare 2MASS coordinates with the original IRAS coordinates. Misidentifications are in this case more difficult to determine, especially if MSX coordinates are not available to support our choice of a given counterpart. Figure 3.3 shows the histograms of these deviations. While in declination they are in most cases within 6″ with just two exceptions, in right ascension we find

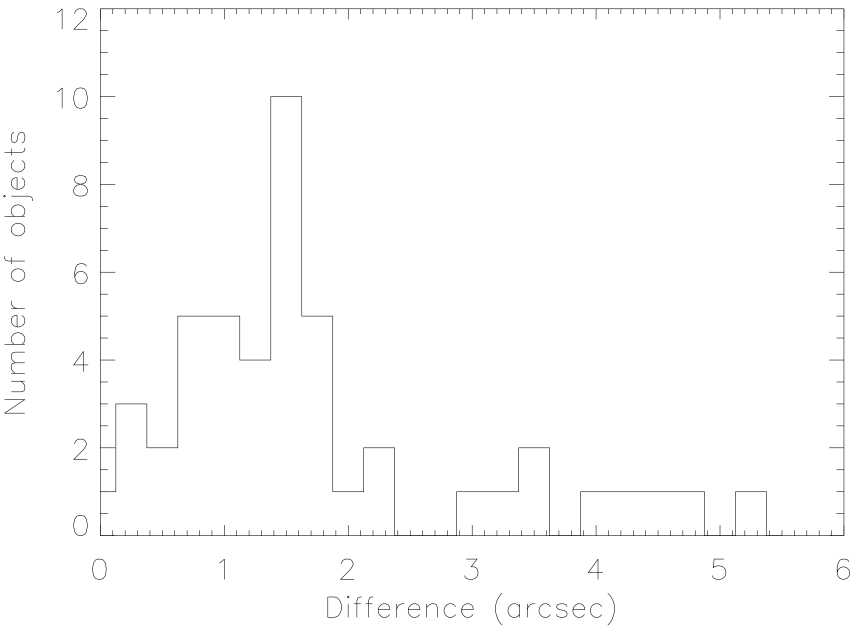

**Figure 3.2**: Angular separation between 2MASS and MSX coordinates for the 48 objects in common for which a near-infrared counterpart was found.

a considerable number of objects showing deviations larger than 10″. This result is in agreement with that found in Chapter 2 for the Arecibo sources. The larger errors in RA are a well known feature of the IRAS Point Source Catalogue (Herman et al. 1986; Bowers & Knapp 1989; Lewis et al. 1990b). The problem is related with the differential accuracy of the IRAS survey in the cross-scan and in-scan directions (Beichman et al. 1988).

As part of our quality checks we verified also that the differences found between 2MASS and IRAS coordinates were similar to those found between MSX and IRAS coordinates (for the objects with MSX data available). Large but consistent deviations can be attributed to the large errors associated to the IRAS coordinates. For the remaining GLMP sources (those with no MSX counterparts) it is more difficult to verify that large coordinate deviations are not due to a misidentification.

In Table 3.2 there are 9 sources with extremely large differences in RA ($\geq 20''$). All of them but IRAS 18298–2111 have MSX coordinates showing very similar deviations with respect to the original IRAS coordinates. IRAS 18298–2111 is a bright IRAS source and its near-infrared counterpart has one of the reddest colours (H–K = 4.69) in our sample. Moreover, this source is located at galactic latitudes $|b| > 5°$, where confusion is unlikely. We conclude therefore that the identification of this counterpart is correct. Similar very large astrometric errors (up to $\approx 60''$ in same cases; see Chapter 2) have been observed in

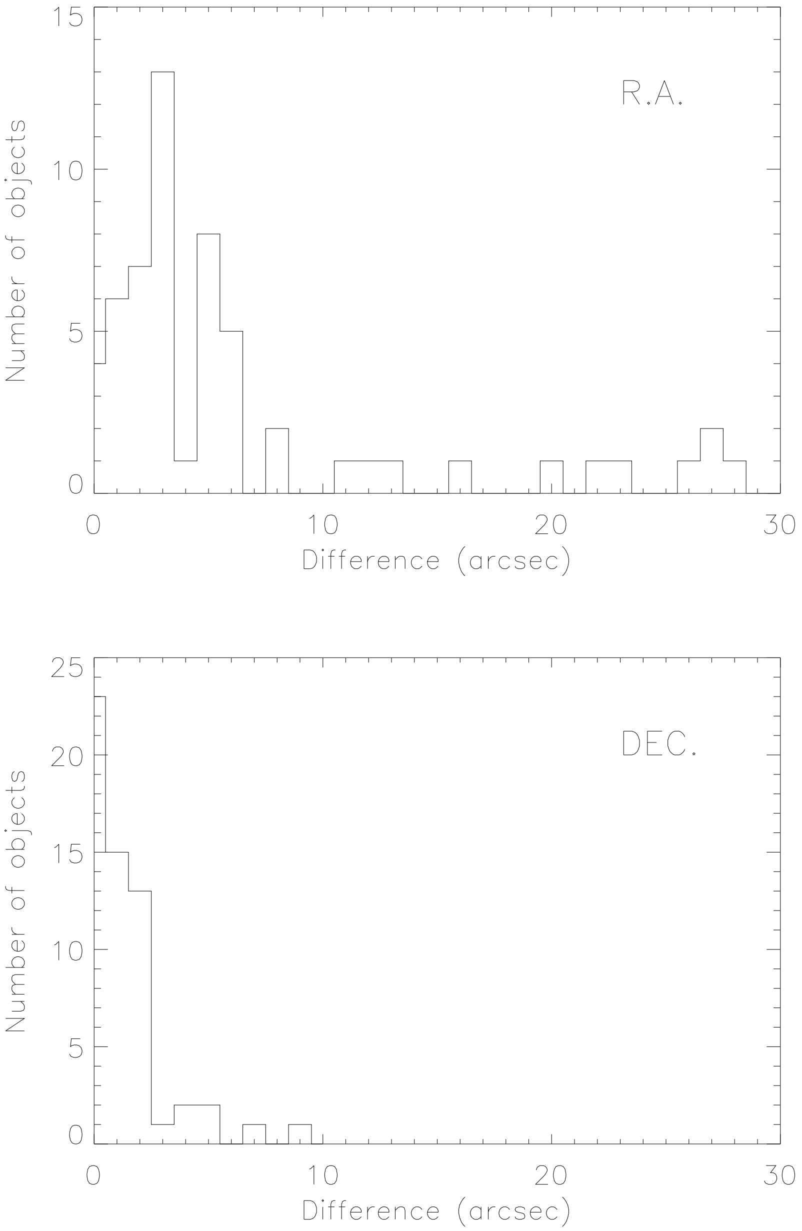

**Figure 3.3**: Angular separation in right ascension (upper panel) and declination (lower panel) between 2MASS and IRAS coordinates for the 58 OH/IR stars for which a near-infrared counterpart was found. Not included is one source with $|\Delta\alpha| = 41''$.

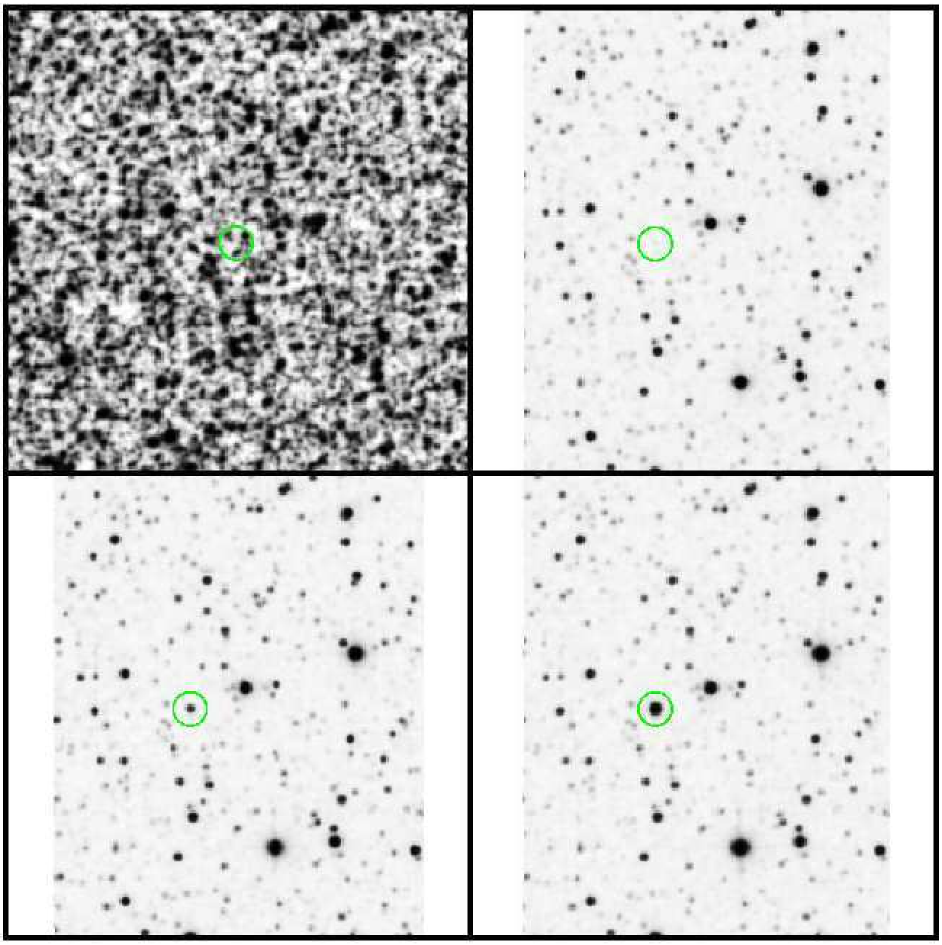

**Figure 3.4**: Atlas images for IRAS 18201–2549. The upper panel shows the optical DSS2 R band (left) and the 2MASS J band (right) images, and the lower panel shows the H-band (left) and K-band (right) images. The adopted counterpart is indicated by a circle.

other IRAS sources occasionally.

### 3.3.5 The atlas of optical and near-infrared counterparts

The results from our search are displayed as an atlas of finding charts. An example of the atlas images is given in Figure 3.4. For each source in our 'GLMP sample' (not already included in the 'Arecibo sample') a chart was put together as a mosaic of 4 frames containing the optical image taken from the DSS2 in the upper left panel, and the J, H and K images from the 2MASS in the upper right, lower left and lower right panels, respectively. The size of the field showed in each filter is $4.6' \times 4.6'$. For each source we marked the position of the proposed optical/near infrared counterpart with a circle in each of the available frames. In those cases where an optical/near-infrared counterpart was not found the circle was drawn at the position where the source should be located according to the best astrometric coordinates available (IRAS or MSX). The complete atlas can be accessed electronically at:

http://www.hs.uni-hamburg.de/DE/Ins/Per/Engels/engels/irext_catalogue/finding_charts.html

## 3.4 Near-infrared photometry

In Table 3.5 we present the J, H and K near-infrared 2MASS magnitudes (or lower limits) for all sources with a plausible or tentative near-infrared identification, including the 5 objects which have been identified only in the 2MASS images but have no associated entry in the 2MASS-PSC. 74% of the GLMP sources were not detected in the J-band, and 65% were not detected in the H band. As already mentioned in Section 3.3.2, for 39 sources (41% of the sample) the K-band counterpart was too weak to derive an accurate photometric measurement.

**Table 3.5**: 2MASS JHK band photometry of the OH/IR stars in the 'GLMP sample'

| IRAS | 2MASS photometry [mag] | | |
|---|---|---|---|
| | J | H | K |
| 08425−5116 | 13.79 ± 0.03 | 12.19 ± 0.03 | 10.83 ± 0.02 |
| 11438−6330 | > 17.39 ——— | 14.96 ± 0.09 | 9.05 ± 0.02 |
| 12158−6443 | 12.77 ± 0.02 | 10.96 ± 0.02 | 9.77 ± 0.02 |
| 12358−6323 | > 14.67 ——— | > 13.59 ——— | 12.06 ± 0.04 |
| 14247−6148 | 13.34 ± 0.03 | 10.27 ± 0.02 | 8.12 ± 0.02 |
| 14562−5637 | 15.20 ± 0.07 | * 13.73 ——— | * 13.20 ——— |
| 15471−4634 | > 16.74 ——— | 15.60 ± 0.16 | 11.95 ± 0.03 |
| 15514−5323 | 15.11 ± 0.04 | 11.62 ± 0.03 | 10.04 ± 0.02 |
| 16040−4708 | 15.87 ± 0.09 | 14.18 ± 0.09 | 12.75 ± 0.04 |
| 16219−4823 | > 15.31 ——— | > 14.05 ——— | 11.33 ± 0.04 |
| 16582−3059 | > 16.98 ——— | > 16.06 ——— | 13.56 ± 0.05 |
| 17004−4119 | 15.89 ± 0.10 | 13.23 ± 0.05 | * 11.52 ——— |
| 17030−3053 | > 17.48 ——— | > 16.88 ——— | 12.50 ± 0.03 |
| 17107−3330 | > 16.51 ——— | 13.86 ± 0.05 | 10.10 ± 0.03 |
| 17151−3642 | > 12.54 ——— | > 10.07 ——— | > 9.00 ——— |
| 17171−2955 | 14.71 ± 0.08 | 13.68 ± 0.09 | * 11.22 ——— |

*Continue in the next page.*

*Table 3.5: 2MASS photometry for the ‘GLMP sample’ (continued)*

| IRAS | 2MASS photometry [mag] | | |
|---|---|---|---|
| | J | H | K |
| 17242−3859 | > 13.59 ——— | > 12.67 ——— | 11.70 ± 0.04 |
| 17276−2846 | 10.89 ± 0.04 | * 9.47 ——— | * 8.79 ——— |
| 17316−3523 | > 16.89 ——— | > 14.58 ——— | 13.01 ± 0.06 |
| 17317−3331 | > 16.14 ——— | > 14.82 ——— | 10.24 ± 0.03 |
| 17341−3529 | 14.62 ± 0.06 | 11.28 ± 0.03 | 9.06 ± 0.02 |
| 17350−2413 | > 14.42 ——— | > 13.20 ——— | 11.01 ± 0.03 |
| 17351−3429 | > 14.46 ——— | > 13.27 ——— | 11.98 ± 0.04 |
| 17367−3633 | > 14.28 ——— | > 13.05 ——— | 12.52 ± 0.03 |
| 17392−3020 | 14.02 ± 0.06 | 11.60 ± 0.05 | * 9.12 ——— |
| 17417−1630 | > 17.85 ——— | 14.32 ± 0.04 | 10.41 ± 0.02 |
| 17428−2438 | > 15.17 ——— | > 13.72 ——— | > 13.24 ——— |
| 17467−4256 | > 17.98 ——— | 15.07 ± 0.08 | 11.35 ± 0.02 |
| 17495−2534 | > 13.29 ——— | > 12.12 ——— | > 11.29 ——— |
| 17504−3312 | > 15.45 ——— | 12.91 ± 0.02 | 11.26 ± 0.02 |
| 17545−3317 | > 15.48 ——— | > 14.63 ——— | 12.92 ± 0.07 |
| 17577−1519 | 14.41 ± 0.05 | 12.43 ± 0.03 | 10.38 ± 0.02 |
| 17583−3346 | > 15.33 ——— | 13.55 ± 0.05 | 10.27 ± 0.02 |
| 18000−2835 | 6.94 ± 0.03 | 5.75 ± 0.02 | 5.05 ± 0.02 |
| 18006−1734 | 13.30 ± 0.04 | 11.79 ± 0.03 | 10.48 ± 0.03 |
| 18015−1608 | > 14.93 ——— | 12.38 ± 0.04 | 9.39 ± 0.02 |
| 18081−0338 | 12.41 ± 0.03 | 10.55 ± 0.03 | 9.32 ± 0.02 |
| 18091−2437 | > 15.28 ——— | > 13.90 ——— | > 13.73 ——— |
| 18107−0710 | 15.60 ± 0.08 | 11.07 ± 0.03 | 7.87 ± 0.02 |
| 18152−0919 | > 16.02 ——— | > 15.17 ——— | 14.00 ± 0.08 |
| 18182−1504 | > 10.99 ——— | > 10.64 ——— | > 10.35 ——— |
| 18187−0208 | 13.61 ± 0.03 | 12.00 ± 0.02 | 10.78 ± 0.02 |
| 18201−2549 | 15.39 ± 0.06 | 11.25 ± 0.03 | 8.28 ± 0.02 |
| 18211−1712 | > 11.96 ——— | 11.94 ± 0.11 | 8.80 ± 0.09 |
| 18257−1052 | 11.70 ± 0.03 | 8.82 ± 0.04 | 7.47 ± 0.03 |
| 18262−0735 | > 16.07 ——— | 12.34 ± 0.03 | 8.70 ± 0.02 |
| 18266−1239 | 14.05 ± 0.02 | 12.74 ± 0.03 | 11.07 ± 0.02 |
| 18277−1059 | > 16.25 ——— | > 14.03 ——— | 9.76 ± 0.03 |
| 18298−2111 | > 16.64 ——— | 15.28 ± 0.09 | 10.59 ± 0.02 |
| 18299−1705 | 8.23 ± 0.02 | 6.56 ± 0.03 | 5.31 ± 0.02 |

*Continue in the next page.*

*Table 3.5: 2MASS photometry for the 'GLMP sample' (continued)*

| IRAS | 2MASS photometry [mag]<br>J | <br>H | <br>K |
|---|---|---|---|
| 18310−2834 | $> 16.20$ —— | $> 15.84$ —— | $11.77 \pm 0.03$ |
| 18361−0647 | $> 16.25$ —— | $> 15.93$ —— | $11.36 \pm 0.03$ |
| 18432−0149 | $> 16.07$ —— | $> 15.01$ —— | $13.60 \pm 0.05$ |
| 18460−0254 | $> 17.90$ —— | $> 15.76$ —— | $14.26 \pm 0.09$ |
| 18475−1428 | $11.52 \pm 0.02$ | $8.55 \pm 0.04$ | $6.52 \pm 0.02$ |
| 18488−0107 | $> 16.30$ —— | $> 13.87$ —— | $13.05 \pm 0.06$ |
| 19069+1335 | $> 17.29$ —— | $> 16.68$ —— | $14.18 \pm 0.08$ |
| 19122−0230 | $12.94 \pm 0.03$ | $10.11 \pm 0.03$ | $8.12 \pm 0.03$ |

Note: * The accuracy of the photometry is affected by deblending problems.

Figure 3.5 shows the J, H, and K magnitude distribution of all the GLMP sources with a near-infrared counterpart for which a photometric measurement is available at least in one band. Most of the sources observed have faint near-infrared counterparts with the magnitude distribution peaking around $10^m$ in K, $12^m$ in H, and $15^m$ in J. The distributions are not strongly peaked and are clearly limited by the 2MASS sensibility, especially in the J band. As it was also discussed for the sources in the 'Arecibo sample', the observed magnitude distribution can in principle be attributed to three main reasons:

i) the different intrinsic brightness of the sources in the sample;

ii) the different apparent luminosity expected from sources located at a wide range of distances, and

iii) the different CSE optical thickness of the sources in the sample.

Comparing the histogram shown in Figure 3.5 with the equivalent one obtained for the 'Arecibo sample' (Figure 2.5 of Chapter 2), we can immediately notice the fainter mean near-infrared brightness of the sources in the 'GLMP sample', and at the same time, the redder colours. The sources in the 'GLMP sample' are not expected to be intrinsically less luminous than the ones in the 'Arecibo sample' (actually we would expect the contrary, since they are suspected to represent a higher mass population). Thus, unless the sources in the 'GLMP sample' are preferentially found at larger distances than those in the 'Arecibo sample', the most probable explanation for the systematic fainter brightness and redder colours found seems to be the large optical thickness of their CSE, in comparison with the optically thinner shells of the bluer Arecibo sources.

In Figure 3.6 we have plotted the near-infrared colour H–K as a function of the K magnitude for all OH/IR stars in the 'GLMP sample' with near-infrared photometry available in the 2MASS-PSC. The objects in common with the 'Arecibo sample' have been plotted with a different symbol, and the rest of Arecibo OH/IR stars have also been

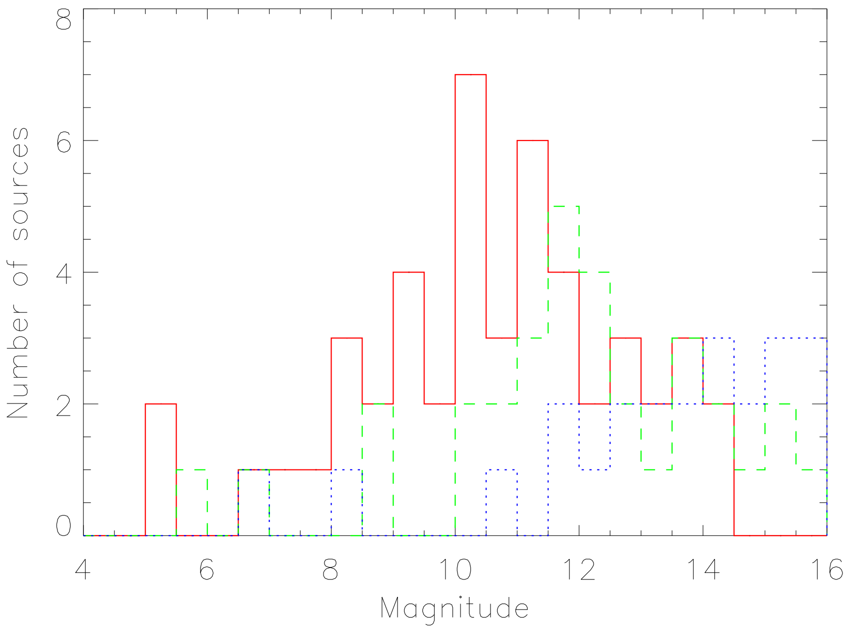

**Figure 3.5**: J band (*blue dotted line*), H band (*green dashed line*), and K band (*red solid line*) magnitude distribution of the sources included in the ‘GLMP sample’.

plotted for comparison. For the sources not detected in H, lower limits for the H–K colour were calculated and marked with vertical arrows. The objects with deblending problems have not been included. In addition we also indicate the reddening vector corresponding to $A_V = 10^m$, for reference.

Although a clear correlation exists between the H–K colour and the K magnitude as it is shown in Figure 3.6, there is a very large scatter in both axes, specially for large values of the K magnitude. This scattering can not be attributed to the intrinsic errors associated to the photometric measurements, which are in most cases negligible.

In Figure 3.6 there are clearly two different types of behaviour, one associated to the sources belonging to the ‘Arecibo sample’, and the other one associated to the sources belonging to the ‘GLMP sample’.

The correlation followed by the ‘Arecibo sample’ sources shows that an increase in CSE thickness (increase in H–K colour) goes accompanied by a proportional obscuration of the source in the near-infrared (decrease in K band brightness). The scatter in the horizontal axis can also be the result of the combination of several other minor effects as we have just discussed: i) the large variability of these sources, with typically $1^m \lesssim \Delta K \lesssim 2^m$ raising in the most extreme cases up to $4^m$; and ii) the wide range of distances at which these sources are located. Most of the Arecibo sources are at $1-5$ kpc (see Chapter 4),

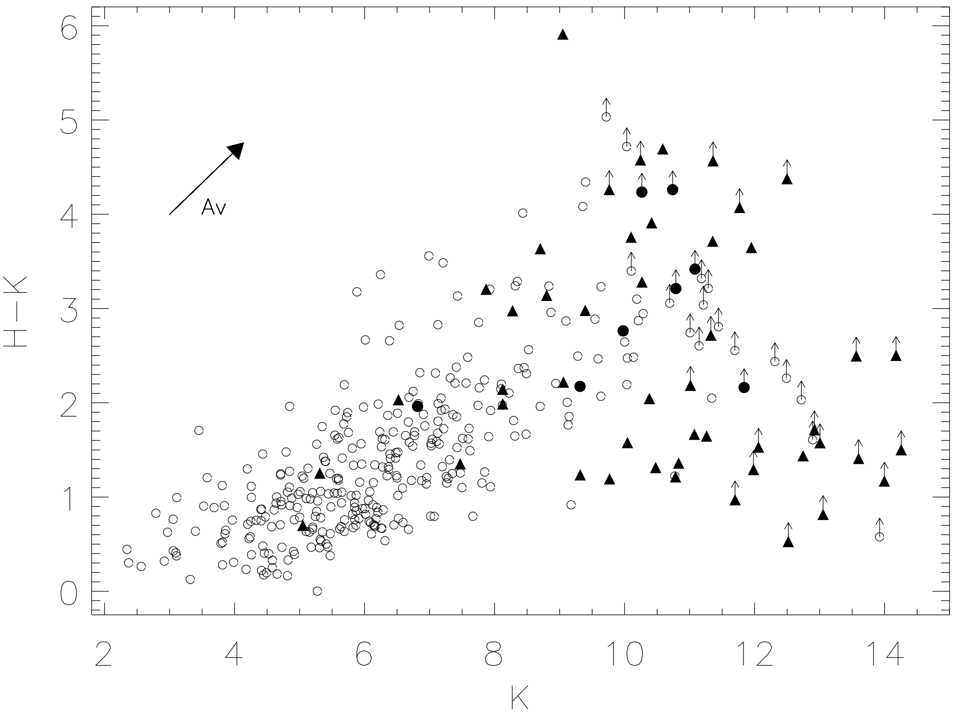

**Figure 3.6**: H–K vs. K magnitude diagram of all OH/IR stars in the 'GLMP sample' (filled triangles) with photometry in the H and K bands. The position of the OH/IR stars in the 'Arecibo sample' is also shown for comparison (open circles). Filled circles for the few objects in common. H–K lower limits are represented by vertical arrows. In addition we also indicate the reddening vector corresponding to $A_V = 10^m$.

which implies a scatter of $\approx 3.5^m$. The H–K colour, represented in the vertical axis can also change slightly as a function of the pulsation phase, the bluer colours corresponding to the maximum of luminosity (Harvey et al. 1974; Engels et al. 1983; Chapter 5). The amplitude in the variation of the H–K colour could reach in the most extreme cases a value of $\Delta$(H–K) $\gtrsim 1^m$.

The same correlation (i.e. increase in CSE thickness / H–K colour, accompanied by obscuration of the central star / decrease in K brightness) is observed by a considerable number of sources in our 'GLMP sample' but other sources in this sample show unexpected blue colours. The range of distances for the 'GLMP sample' (with the exceptions of those in the Galactic Bulge) is similar to that of the 'Arecibo sample' (see Chapter 4), which implies a similar ($\approx 3.5^m$) scattering in the horizontal axis. Probably these objects are more evolved than those of the 'Arecibo sample' and have also slightly larger amplitudes ($\Delta$K $> 2^m$). However, these two factors are not able to explain the dispersion of colours

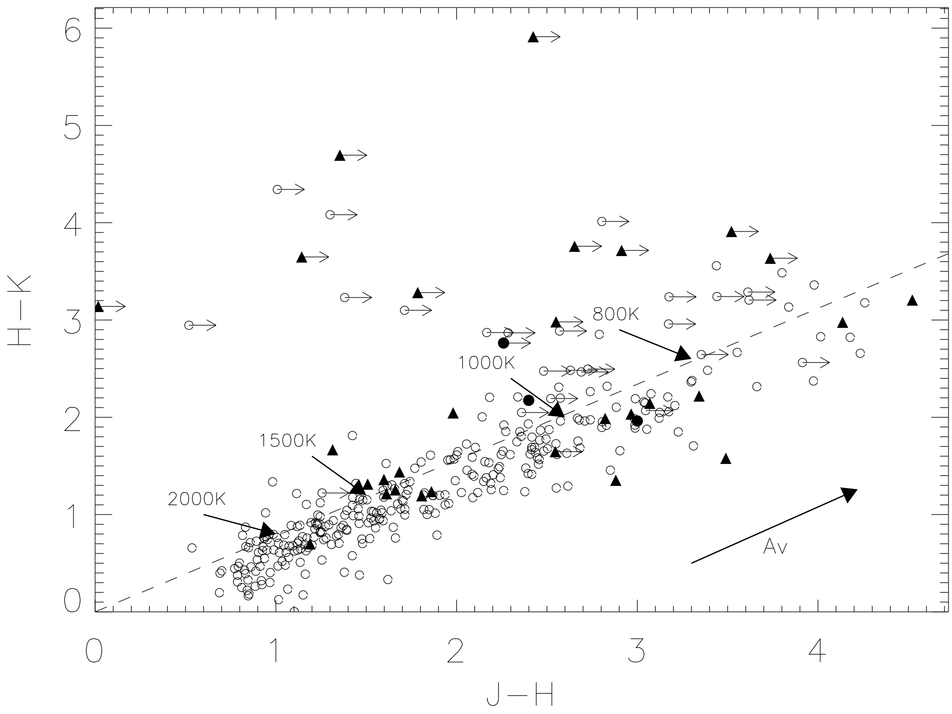

.

**Figure 3.7**: Near-infrared J–H vs. H–K colour-colour diagram of all the sources belonging to the 'GLMP sample' (filled triangles). For comparison, the near-infrared colours of the sources in the 'Arecibo sample' are also shown (open circles; filled circles for objects in common). J–H lower limits are indicated by horizontal arrows. The location of black-bodies of different temperatures and the reddening corresponding to $A_V = 10^m$ are also indicated.

observed in Figure 3.6. For this reason we believed that many of the blue colours associated to the fainter stars in our sample are just the consequence of these stars being field stars misidentified as the right counterparts of some of the most heavily obscured stars in the 'GLMP sample'. Alternatively, the may be extremely luminous OH/IR stars located at very long distances.

### 3.4.1 The J–H vs. H–K colour-colour diagram

In Figure 3.7 we have plotted the near-infrared colour-colour diagram J−H vs. H−K of all the sources belonging to the 'GLMP sample' with at least data available in the H and K bands. For objects not detected in J, lower limits for the J−H colours were calculated and these are indicated with horizontal arrows in this diagram. The objects with deblending problems have not been included. For comparison, we have also plotted the colours of the sources in the 'Arecibo sample'.

The near-infrared colours of the OH/IR stars in the 'GLMP sample' follow the same correlation shown by the more standard OH/IR stars of the 'Arecibo sample', extending from the blue part of the distribution (J–H ≈ 1.2; H–K ≈ 0.7) up to the reddest, more extreme colours (J$-$H ≈ 4.5; H$-$K ≈ 5.9). Again, the unexpected blue colours displayed by a fraction of stars in the 'GLMP sample' could be an indication of a wrong identification of the near-infrared counterpart. On the other hand, the limited sensitivity of 2MASS, especially in the J band, inhibits the full exploration of the red end of the distribution. Extrapolating the linear correlation of both colours, the reddest object (IRAS 11438–6330) with H–K = 5.91 should have an expected colour J–H ≈ 8 well beyond the limit of J$-$H ≈ 4.5 plotted in Figure 3.7.

In Chapter 2 we showed that in average the redder an object is in the far-infrared the redder its near-infrared counterpart (see Figure 2.8). Thus, the results obtained for the 'GLMP sample' are consistent with those obtained for the 'Arecibo sample' in the sense that the sources in our 'GLMP sample' are in average redder than those in the 'Arecibo sample', especially if we consider the blue sources above mentioned as a contamination. This suggests that the GLMP OH/IR stars have thicker CSE in average than those of the 'Arecibo sample', at it was expected.

Remarkably, the bluest GLMP source in the J$-$H vs. H$-$K diagram (IRAS 18000–2835, with J–H = 1.2; H–K = 0.7), which is also the brightest source in the near-infrared (K = $5.05^m$), does not show any optical counterpart in the DSS2 images. This indicates that despite the blue colours, this source may have an optically thick shell. However, even if it was observed in a deep minimum of the optical light curve, it is still very difficult to explain such a extremely blue colours in association with the absence of an optical counterpart. The extreme brightness of this source also in comparison with the IRAS measurement at 12 $\mu$m (see Figure 3.8) suggests, as an alternative explanation, that the source may have experience a sudden increase of brightness in the near-infrared in the last few years. Other explanations, like a the identification of this source as a post-AGB star seems very unlikeky according to the extreme brightness of the near-infrared counterpart (which is not expected for an unrelated field star) and to the strong variability index quoted by IRAS (which suggest that the star was at least 20 years ago still in the AGB).

### 3.4.2 K$-$[12] vs. [12]$-$[25] colour-colour diagram

Another way to visualize the near- and mid-infrared properties of the sources in the GLMP sample is to study their distribution in the K$-$[12] vs. [12]$-$[25] colour-colour diagram (Figure 3.8). The K$-$[12] colour provides information on the relative contribution of the near-infrared emission, dominated by the central star and by the hot dust surrounding it, and of the mid-infrared emission, mainly coming from the cool dust

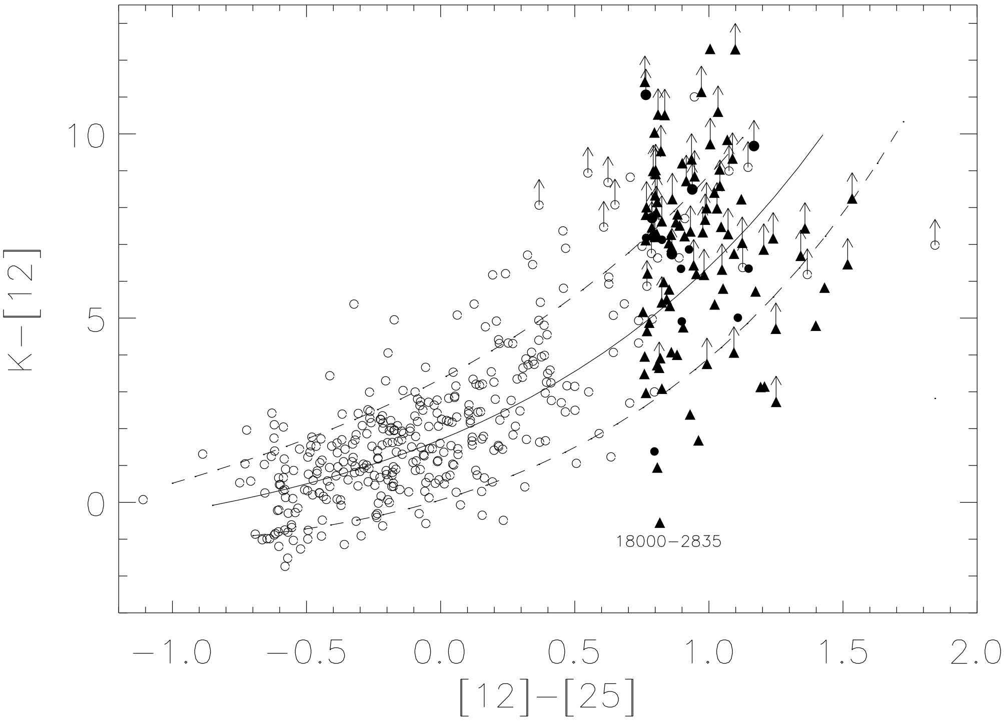

**Figure 3.8**: K−[12] vs. [12]−[25] colour-colour diagram of all GLMP OH/IR stars with K band photometry (filled triangles) together with those of the 'Arecibo sample' (open circles; filled circles for objects in common). Upper limits in K were converted to lower limits in K−[12] colour (arrows). The continuous line corresponds to the best fit to the observed data (see text). The dashed lines correspond to the dispersion expected from the variability of the sources in the K and at 12 $\mu$m band, and from the intrinsic errors associated to the photometric measurements. The position of the peculiar source IRAS 18000–2835 is indicated with a label

in the circumstellar shell, to the overall spectral energy distribution. As we showed in Chapter 2, the correlation of the K−[12] with the IRAS [12]−[25] colour showed by the Arecibo OH/IR stars could be interpreted as an additional indicator of the optical thickness of the CSE for a given source. In Figure 3.8 we have plotted the position in this diagram of all GLMP OH/IR stars together with those in the 'Arecibo sample'. For those sources with no photometric measurement in K, upper limits were converted to lower limits in the K−[12] colour. To calculate the K−[12] colour we adopted a zero-magnitude flux in the K band of 667 Jy (Cohen et al. 2003).

In Chapter 2 we also showed how the scatter in the [12]−[25] colour could be at least partly explained by the intrinsic error in the IRAS fluxes measurements, and how the main reason for the large scatter observed in the K–[12] colour was the strong variability of the sources and the non-contemporaneous nature of the near- and mid-infrared observations. This dispersion has been indicated in Figure 3.8 with dashed lines. However, the variability effect is not enough to explain the scatter observed in the 'GLMP sample'.

The 'GLMP sample' of OH/IR stars does confirm the colour trend showed by the 'Arecibo sample' of OH/IR stars. Using both samples we have fitted an exponential function to the observational data, weighting each data point according to the associated errors in each colour, obtaining the following equation:

$$\mathrm{K}-[12] = 3.44\,\mathrm{e}^{0.86([12]-[25])} - 1.74$$

This equation represents the sequence of colours that a source would show as it evolves along the 'O-rich AGB sequence'. This sequence of colours has been plotted in Figure 3.8 with a solid line. Note that in the reddest part of this diagram, the majority of data are lower limits in the K−[12] colour.

In general, the position of all GLMP OH/IR stars in the K−[12] vs. [12]−[25] colour-colour diagram can be explained as an extension toward redder colours of the sequence of colours associated to the Arecibo sources although with a much larger scatter.

## 3.5 Conclusions

We have presented an atlas of optical/near-infrared finding charts and near-infrared photometric data for 94 OH/IR stars taken from the GLMP catalogue, considered to be an extension toward redder colours and thicker shells of the sources in the 'Arecibo sample'. We successfully identified their near-infrared counterparts in the 2MASS-PSC and determined new positions for 58 sources in the sample with an accuracy of $\approx 0.2''$. The identifications were possible in many cases with the help of improved positional information taken from the MSX6C (accuracy $\approx 1.8''$) as an intermediate step, and confirmed through the analysis of their near- and mid-infrared colours. The 36 sources for which no near-infrared counterpart was found in the 2MASS-PSC were identified as heavily obscured variable OH/IR stars.

The most probable explanation for the systematic fainter brightness and redder colours found, in comparison with their bluer Arecibo counterparts, seem to be the larger optical thickness of their CSE. The wide dispersion observed in the JHK magnitudes measured is mainly attributed to the different optical thickness of the CSE, rather than to the different apparent luminosity expected from sources located at a wide range of distances, or to the different intrinsic luminosities of the sources in the sample.

The distribution of the GLMP sources in the near-infrared J−H vs. H−K colour-colour diagram follow the same correlation shown by the population of OH/IR stars in the 'Arecibo sample', which is interpreted once more as a sequence of increasing optical thickness of their circumstellar envelopes. However, the sources in the 'GLMP sample' are in average redder than those in the 'Arecibo sample'. This suggests again that the GLMP OH/IR stars have thicker CSE in average than those of the 'Arecibo sample'. A significant number of sources with unexpected 'blue colours' in the H–K vs. K diagram and in the J–H vs. H–K are suggested to be the result of possible misidentification with field stars.

The 'GLMP sample' of OH/IR stars follows the trend already showed by the 'Arecibo sample' of OH/IR stars in the K−[12] vs. [12]−[25] colour-colour diagram. Using both samples we have fitted an exponential function to the observational data. However, the large scatter observed cannot be explained in all cases as produced by the intrinsic variability of the sources in the K-band combined with that expected at 12 $\mu$m.

**Acknowledgements:**

This research has made use of the SIMBAD database, operated at CDS, Strasbourg, France. We acknowledge also the use of the Digitized Sky Survey, based on photographic data obtained using the UK Schmidt Telescope. The UK Schmidt Telescope was operated by the Royal Observatory Edinburgh, with funding from the UK Science and Engineering Research Council, until 1988 June, and thereafter by the Anglo-Australian Observatory. Original plate material is copyright (c) of the Royal Observatory Edinburgh and the Anglo-Australian Observatory. The plates were processed into the present compressed digital form with their permission. The Digitized Sky Survey was produced at the Space Telescope Science Institute under US Government grant NAG W-2166. This publication makes also use of data products from the Two Micron All Sky Survey, which is a joint project of the University of Massachusetts and the Infrared Processing and Analysis Center/California Institute of Technology, funded by the National Aeronautics and Space Administration and the National Science Foundation.

# Chapter 4

# The ‘O-rich AGB sequence’

## Abstract

In the previous chapters (2 and 3) we have presented a compilation of photometric data for a total of 457 OH/IR stars covering a wide range of different colours along what we have called the ‘O-rich AGB sequence’. We use now this large sample of OH/IR stars to try to interpret this sequence in terms of evolutionary stage and/or progenitor mass. For this we present here an innovative approach which is based on the selection of an adimensional parameter ($\lambda$) to describe the position of a star in the ‘O-rich AGB sequence’. Using a combination of optical and infrared data we confirm that the ‘O-rich AGB sequence’ can be explained as a sequence of increasing circumstellar optical depth.

With the photometric data collected from $1.25\,\mu$m to $100\,\mu$m we estimate the bolometric observed flux for all the sources in the sample. The characteristic OH/IR star luminosity ($L_{OH/IR}$) is determine from the analysis of the luminosity distribution of a subsample of very red OH/IR stars which are assumed to be located in the Galactic Bulge at a common distance of 8 kpc. We find that this distribution is strongly peaked at $L_{OH/IR} \approx 3\,500\,L_{\odot}$, in close agreement with the values previously obtained by other authors.

Assuming a common and constant luminosity for all the remaining OH/IR stars in the sample we explore both their distance and galactic height distribution. We find that the galactic scale height (H) along the ‘O-rich AGB sequence’ is clearly correlated with the value of the $\lambda$ parameter, decreasing with the redder colours, suggesting that only the most massive progenitor stars reach the upper end of the sequence.

## 4.1 Introduction

One of the most fundamental questions that still remains open in the understanding of AGB stellar evolution is the interpretation of the ‘O-rich AGB sequence’, reported for the first time by Olnon et al. in 1984. It has been shown by several authors (e.g Bedijn 1987; Volk & Kwok 1988) that this sequence reflects the increase of optical thickness of the CSE, the objects with the thinnest CSE (variable OH/IR stars with bright optical counterparts) being placed in the bluest part of the sequence and those with the thickest CSE (variable OH/IR stars without optical counterparts) in the reddest part of this sequence.

The first author who successfully modeled the ‘O-rich AGB sequence’ was Bedijn 1987. Bedijn reproduced the ‘O-rich AGB sequence’, by solving the radiative transfer equation corresponding to dust shells with increasing optical thickness.

However, this variation of the CSE thickness along the ‘O-rich AGB sequence’ can be interpreted in two different ways. The first interpretation assumes that the ‘O-rich AGB sequence’ represents an **evolutionary sequence** (e.g. van der Veen & Habing 1988) with the mass-loss rate increasing with time. Then, every star would start the AGB phase at the blue end of this sequence ([12]–[25] $\approx -1$), with a low mass-loss rate and a thin CSE, and would later move forward along the sequence while increasing its mass-loss rate until reaching the red extreme of the sequence ([12]–[25] $\approx 1.5$) at the end of the AGB. If the previous evolutionary scenario is correct, the relative percentage of stars of low and high mass in the blue and red part of the ‘O-rich AGB sequence’ should be the same.

The second interpretation is that the ‘O-rich AGB sequence’ is mainly a **mass sequence** (e.g. Ortiz & Maciel 1994; Lepine et al. 1995). In this case their different location in the IRAS two-colour diagram would be just a consequence of their different initial mass, which would determine the mass-loss rate (assumed to be constant) experienced in the AGB.

However, it has been shown that only objects with high expansion velocities are found at the highest values of [12]–[25], which suggests that only objects with massive progenitor stars reach the upper of this sequence if we assume that the expansion velocity is a distance independent mass indicator (Baud & Habing 1983). This would be consistent with larger initial mass (luminosity) stars driving a larger mass-loss rate.

For this reason, a third interpretation of the ‘O-rich AGB sequence’ was proposed, which is a combination of the previous ones. All AGB stars would move towards redder colours as they increase their mass-loss rate (and with it, the optical depth of the CSE), but only the more massive stars would be able to reach the reddest end of the sequence (García-Lario 1992).

This third interpretation first was proposed by Likkel (1989), who analyzed a sample of 135 OH/IR stars, including a part of those in the ‘Arecibo sample’. Using a simple bolometric correction (van der Veen & Habing 1989) she estimated the scale height and the progenitor mass of the bluer and redder objects in her sample. An iterative procedure was used until she got a satisfactory and consistent result between luminosities and scale heights. The result was that the bluer OH/IR stars were found to be both less massive and less luminous than the redder ones.

But, the interpretation of the 'O-rich AGB sequence' still remains controversial. For example, recently Jackson et al. (2002) concluded that there are no statistically significant differences in the galactic distribution of AGB stars with different IRAS colours.

In the previous chapters we have shown that we have a more numerous sample of OH/IR stars under analysis than the one used by Likkel, and with a better coverage of the whole 'O-rich AGB sequence'. In particular, we have the largest subsample of extremely red OH/IR stars ever studied. We also have photometric information not only in the mid- and far-infrared but also in the near-infrared where the bluer objects have the maximum of their spectral energy distribution. Thus, we should be able to derive more accurate bolometric fluxes by integrating the actual flux measurements over a wide spectral range instead of using an uncertain bolometric correction. In our following analysis, we will use this unique sample of OH/IR stars (which include all OH/IR stars available in both the 'Arecibo sample' studied in Chapter 2 and the sample of extremely red OH/IR stars taken from the GLMP catalogue analysed in Chapter 3; the 'extended OH/IR sample' in the following) to improve our knowledge on the main properties of the stars populating the 'O-rich AGB sequence' and derive our own conclusions.

## 4.2 The 'extended OH/IR sample'

From the 371 objects belonging to the 'Arecibo sample' we removed the 8 sources which were pointed out in Chapter 2 to be candidate post-AGB stars. In the 'GLMP sample' there was only one object that was pointed out to be a possible post-AGB star. However, because of the lack of additional evidences apart from the outlier position in the K–[12] vs. [12]–[25] diagram, we have maintained this source in the following analysis. Thus,what we have called the 'extended OH/IR sample' (of *variable OH/IR stars*) is formed by 457 sources, 324 of which have a counterpart in the MSX6C Point Source Catalogue, and 395 have NIR photometric data available in the standard JHK bands (either from our own observations or from 2MASS).

Despite both samples consist only of variable OH/IR stars, both are intrinsically different as they were created with completely different selection criteria.

76% (16 out of 21) of the fraction of variable OH/IR stars belonging to the GLMP catalogue visible at the Arecibo sky were actually detected and included in the 'Arecibo sample'. Out of the 5 objects not included in the 'Arecibo sample' 4 have never been detected in OH (IRAS 19087+1006 and IRAS 19069+1335 were tried by Lewis et al. (1987), IRAS 19112+1220 and IRAS 19254+1724 by Lewis et al. (1990b) but were classified as variable OH/IR stars in the GLMP catalogue, the remaining one (IRAS 18518+0558) did not fulfill the IRAS colour-colour constrains imposed in the ‘Arecibo sample’ (Chengalur et al. 1993). However, this last source was later detected in the OH maser by te Lintel-Hekkert et al. (1991) confirming that this star is actually an OH/IR star.

On the other hand, 16 out of 35 (46%) of the Arecibo sources which can be considered as red sources ([12]–[25] $\geq 0.75$) satisfy the selection criteria which define the ‘GLMP sample’. 9 of these objects were not well detected by the IRAS satellite in the 12, 25 and 60 $\mu$m bands, mainly they were not detected at 60 $\mu$m (78% of them), and thus they were not included in the GLMP catalogue. One object (IRAS 18498–0017) had [12]–[60] $> 1.13$ that was exactly the colour limit imposed by García-Lario. Another 12 sources had an associated IRAS variability index VAR $< 50$, which is the additional constraint that we have imposed to the sources in value that the GLMP catalogue imposed in order to avoid any possible contamination from post-AGB stars. The remaining 18 objects fulfilled all constraints imposed by García-Lario for the inclusion in the GLMP catalogue. However, IRAS 19071+0946 was not included in this catalogue, probably because of a change in the updated photometry quoted in the most recent version of the IRAS catalogue, which implied that the resulting colours are now non-consistent with the initial selection criteria used. Finally, IRAS 19254+1631 appears in the GLMP catalogue as a post-AGB star, and not as a variable OH/IR star.

Thus, despite, both samples are intrinsically different, and although they are not directly comparable, they are somehow complementary and useful for our analysis for the following reasons:

i) The ‘Arecibo sample’ is mainly formed by objects in the bluer part of the ‘O-rich AGB sequence’, with a small contribution from very red sources. On the other side, the ‘GLMP sample’ contains exclusively sources in the redder part of this sequence.

ii) The ‘Arecibo sample’ is a survey restricted to a well defined area of the sky (see Figure 4.1) that does not include the Galactic Center. However, the ‘GLMP sample’ includes sources all over the sky, with a large number of sources (32%) being located in the direction of the Galactic Bulge.

In Figure 4.1 we can also see the first evidence of mass segregation in the ‘extended OH/IR sample’ as in the common area all the objects with redder colors (the ‘GLMP sample’) are mainly located very close to the Galactic Plane, whereas the majority of bluer objects (those in the ‘Arecibo sample’) are distributed over a much larger range of Galactic latitudes.

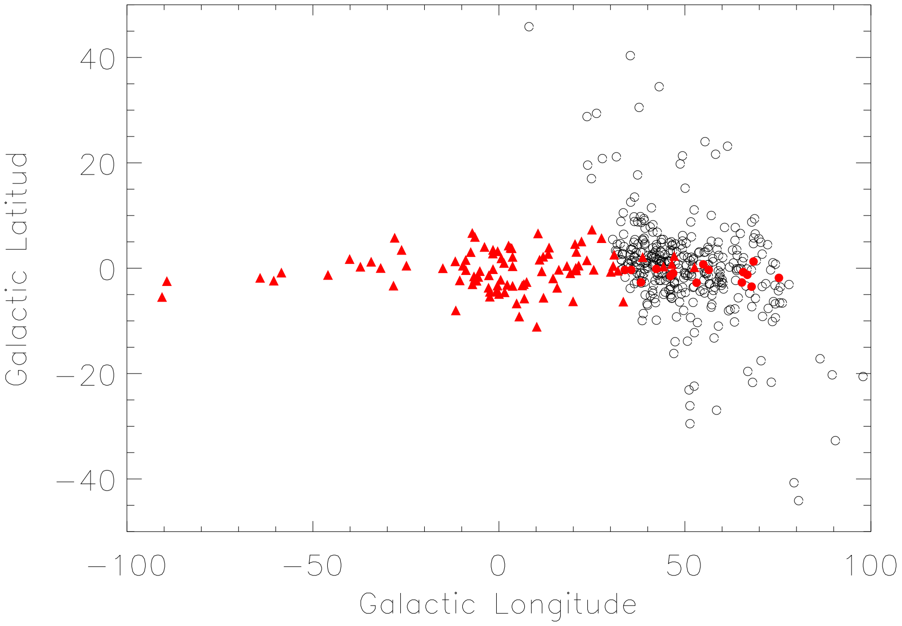

**Figure 4.1**: The position in the Galaxy of the sources taken from the 'Arecibo sample' (open circles) and of those taken from the GLMP catalogue (filled triangles). Sources in common are marked with filled circles. Together they form what we have called the 'extended OH/IR sample'.

## 4.3 Parametrization of the 'O-rich AGB sequence'

The IRAS colour-colour diagram [12]–[25] vs. [25]–[60] has been proved to be an efficient and simple tool for discussing the properties of AGB stars. However, none of the two IRAS colours [12]–[25] or [25]–[60], alone considered, are adequate to describe the full range of positions in this diagram covered by the 'O-rich AGB sequence'. This is because the [12]–[25] colour is a good descriptor of the position in this diagram for stars in the blue part of it. However, it is totally inadequate to indicate the position of the redder sources. Similarly, the [25]–[60] colour is a better descriptor for the sources located in the redder part of the diagram, but a very bad one for the blue sources. Thus, in order to have a good descriptor for the whole 'O-rich AGB sequence', we have used the parametrization introduced by García-Lario (1992) as it is shown in the following equations:

$$\left.\begin{aligned}[12]-[25] &= 0.912\,\mathrm{Ln}\lambda \\ [25]-[60] &= -2.42+0.72\lambda\end{aligned}\right\}$$

Each point of the 'O-rich AGB sequence' can then be associated with a given value of $\lambda$. According to these equations each star in the IRAS two colours diagram is then assigned a $\lambda$ value which corresponds to the nearest point in the 'O-rich AGB sequence'. Thus, low values of $\lambda$ would correspond with objects situated in the blue part of the sequence and high values with those situated in the redder part of it. The range of $\lambda$ values associated to stars in our 'extended OH/IR sample' goes from $\approx 0.3$ to $\approx 4.7$. Two objects (IRAS 18498–0017 and IRAS 20149+3440) have even larger $\lambda$ due to a bad quality measurement in the 60 $\mu$m IRAS band. In Table C.1 we have tabulated the value of the $\lambda$ parameter for each of the sources in the 'extended OH/IR sample'.

## 4.4 The circumstellar optical depth

During the AGB phase, the stars experience large mass-loss rates which will be reflected in the gradual obscuration of the central star first in the optical range and later also in the near-infrared. According to our current knowledge of the 'O-rich AGB sequence' we would expect to find the bluer sources with optically thin shells located in the region of the IRAS two-colour diagram associated to low values of $\lambda$, while the redder sources will occupy the red end of this sequence associated to high values of $\lambda$.

In order to check for this, in Figure 4.2 we have plotted the fraction of AGB stars with optically identified counterparts on the DSS2 images as a function of the $\lambda$ parameter. For this we have used only the objects with good quality IRAS fluxes at 12, 25 and 60 $\mu$m (IRAS-FQual $> 1$) (Beichman et al. 1988). As expected, this fraction decreases with $\lambda$. For the bluest sources ($\lambda \lesssim 0.9$) the detection rate is larger than 80%, quickly falling down to less than 20% for sources with $\lambda \gtrsim 1.8$. At $\lambda \approx 1.2$ the number of objects with and without optical counterpart are comparable. This confirms that the circumstellar optical depth is strongly correlated with the $\lambda$ parameter, as predicted by the models.

A few sources with very high $\lambda$, like IRAS 17004–4119 ($\lambda = 3.5$), show a faint optical counterpart on the DSS2 images. It could happen that these objects are extremely variable and that the DSS2 survey data corresponds to observations performed just during a maximum of the luminosity. However, their positions in the IRAS two colour diagram, usually well separated from the 'O-rich AGB squence', can only be explained as the consequence of the termination of the mass-loss, and the subsequent detachment of the CSE (van der Veen & Habing 1989). This means that they should be better classified as candidate post-AGB stars.

There are other observational characteristics which can be used as indicators of the thickness of the CSE in the 'O-rich AGB sequence', like the detection of the amorphous silicate dust features at 9.7 $\mu$m and 18 $\mu$m in emission or in absorption. The silicate dust feature at 9.7 $\mu$m was observed for first time in the CSE of O-rich AGB stars by Woolf

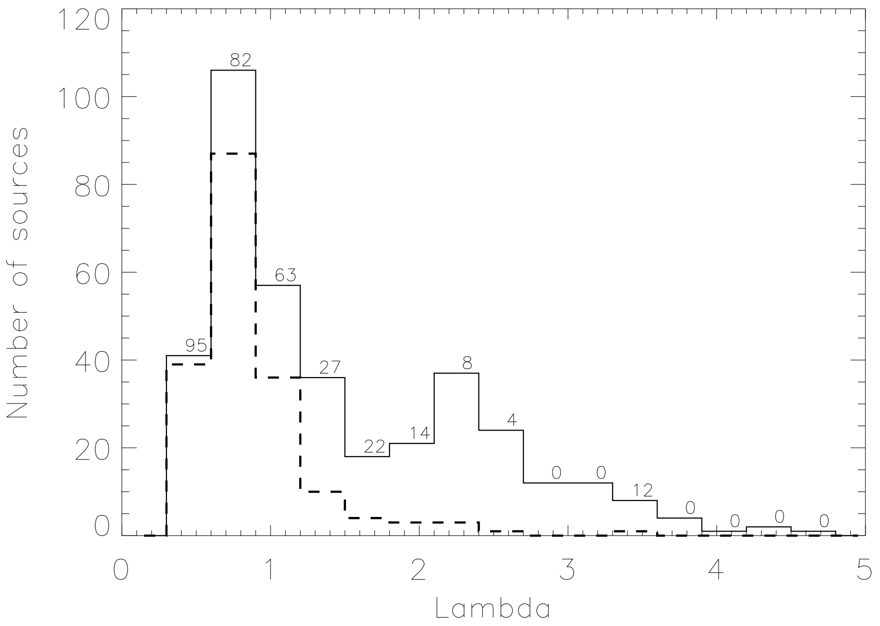

**Figure 4.2**: Sources with optical counterpart detection on the DSS2 images as a function of the $\lambda$ parameter. The total number of sources in the 'extended OH/IR sample' (*solid line*) is compared with the subsample of sources with optical counterpart (*dashed line*). In the figure the rate is given in percentage on top of each bin.

& Ney (1969). This feature and the accompanying one at 18 $\mu$m are detected in emission if the star has an optically thin CSE, and in absorption if the star has an optically thick CSE. The IRAS satellite provided Low Resolution Spectra covering the wavelength range from 7.5 to 23 $\mu$m for the brighter sources in the sky (F $\gtrsim$ 5 Jy at 12 $\mu$m and F $\gtrsim$ 10 Jy at 25 $\mu$m). In addition, Kwok et al. (1997) reclassified 11 224 IRAS LRS on the basis of the presence of emission and absorption features and on the shape of the continuum.

In our sample there were 140 sources included in the original atlas of LRS (Olnon et al. 1986) where sources with the silicate features detected in emission were classified as 2n (n increases from 1 to 9 indicating the strength of the emission) while sources where the silicate features were found in absorption were classified as 3n (n increases from 1 to 9 indicating the strength of the absorption). The number of sources for which information on these features is available increases up to 253 objects with the updated LRS classification of Kwok. 204 of them show a silicate dust feature at 9.7 $\mu$m, 149 in emission (LRS-type E) and 55 in absorption (LRS-type A). In addition, 8 objects showed a featureless continuum, flatter than that expected for a stellar photosphere (LRS-type F). They probably represent O-rich AGB stars with very thin CSE. 4 other sources showed a red continuum, with either

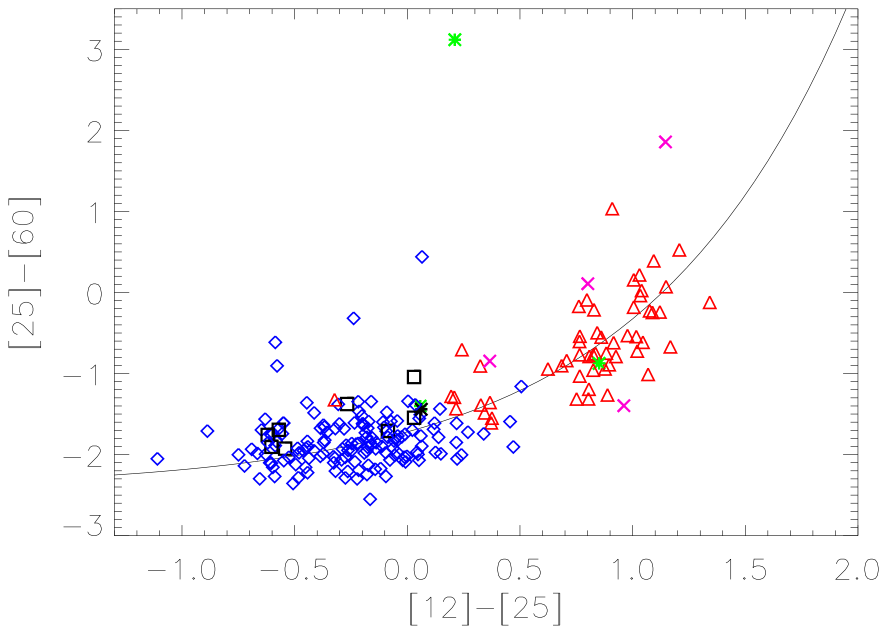

**Figure 4.3**: IRAS colour-colour diagram of all sources in the ‘extended OH/IR sample’ with LRS-type classification (Kwok et al. 1997). LRS-type F: black squares; LRS-type E: blue diamonds; LRS-type A: red triangles; LRS-type P: green asterisks; LRS-type H: pink crosses; LRS-type C: black asterisks.

(this is not clear) the 9.7 $\mu$m silicate absorption or the 11.3 $\mu$m PAH feature (LRS-type H). 3 stars showed a relative red continuum from 13 to 23 $\mu$m and a sharp rise at the blue end of the LRS range which could be interpreted in some cases as due to the presence of the 11.3 or 12.5 $\mu$m emission features that are attributed to PAH molecules (LRS-type P). 20 objects showed spectra with a flat continuum and unusual features (LRS-type U). Finally, 13 sources had noisy or incomplete spectra (LRS-type I), and 1 source showed a spectrum with circumstellar 11 $\mu$m SiC dust emission (LRS-type C). This latter source is expected to be an evolved carbon star undergoing heavy mass-loss.

In Figure 4.3 we have plotted in an IRAS colour-colour diagram all the sources in the sample for which LRS classification was available with the exception of those with LRS-type U and I. In this figure we can see how the objects with optically thin envelope in the mid-infrared (LRS-types F, E & P) have all [12]–[25] $\lesssim$ 0.5 (which correspond to $\lambda \lesssim 1.7$) with the only exception of IRAS 18310-2834 which has [12]–[25] = 0.85 (i.e. $\lambda = 2.54$) and LRS-type P, and thus, it is possibly a C-rich source.

On the other hand the objects with optically thick envelopes in the mid-infrared (LRS-type A and H) have all of them [12]–[25] $\gtrsim$ 0.2 (i.e. $\lambda \gtrsim 1.2$) with the exception of

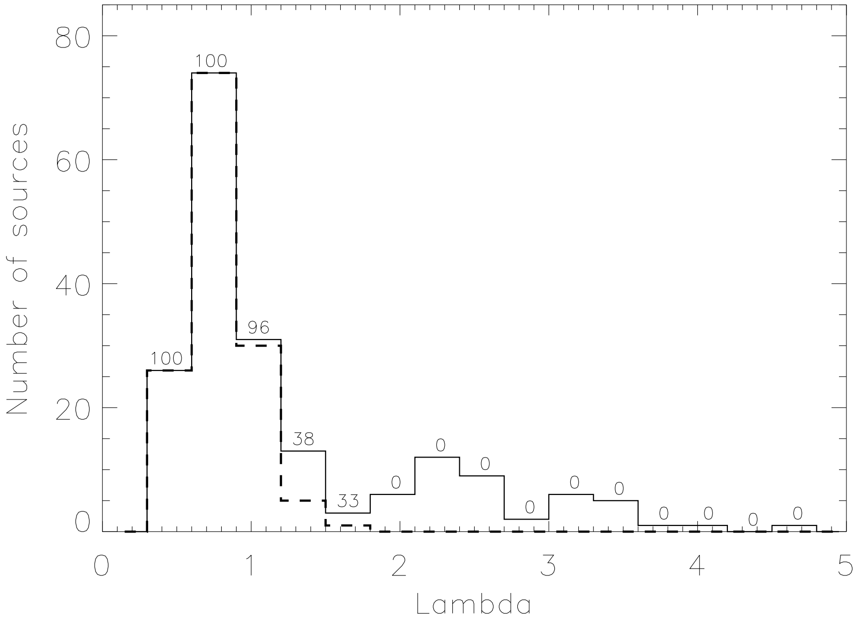

**Figure 4.4**: The total number of sources in the 'extended OH/IR sample' with LRS-type available (*solid line*) is compared with the number of sources showing the dust silicate feature at 9.7 $\mu$m in emission (dashed line) as a function of the $\lambda$ parameter. In the figure the rate is given in percentage on top of each bin.

the peculiar source IRAS 20547+0247 (Barnbaum et al. 1996) which has [12]–[25] = –0.32 (i.e. $\lambda = 0.70$) and LRS-type A. This source has almost lost its OH maser since 1988 when it was detected with 540 mJy during the Arecibo survey (Chengalur et al. 1993). It was later observed 5 times between 1999 April and 2001 August and was never detected above the 2.55 mJy level (Lewis 2002). The interpretation is that this source may be already a post-AGB star or it may be have experienced a very recent thermal pulse.

In Figure 4.4 we have plotted the fraction of sources with the dust silicate feature at 9.7 $\mu$m in emission as a function of the $\lambda$ parameter. For this we have used only the objects with good quality fluxes at 12, 25 and 60 $\mu$m (IRAS-FQual > 1). Again, as expected, this fraction decreases with $\lambda$. The distribution of sources with the feature detected in emission is similar to those for which an optical counterpart was found, with a sharp fall down starting at arround $\lambda \approx 1.2$, the same value derived for the abrupt decrease in optical detectability rate, with the dust silicate feature turning from emission into absorption at $\lambda \approx 1.8$.

Figures 4.2 and 4.4 corroborate the idea that the 'O-rich AGB sequence' represents a sequence of increasing circumstellar optical depth. However, this does not clarify whether the observed sequence is mainly an evolutionary sequence or whether it can also be interpreted as a 'progenitor mass sequence'.

Volk & Kwok (1988) and later Chen et al. (2001) found that OH/IR stars with silicate absorption features (LRS-type A) tend to lie very close to the Galactic Plane, while OH/IR stars showing silicate emission (LRS-type E) were found at higher galactic latitudes. These studies conclude that LRS-type A stars must be statistically considered more massive than the LRS-type E stars, and that the different LRS types are somehow correlated with the progenitor mass.

In order to check for this, we analyzed the galactic distribution of sources located in different regions of the 'O-rich AGB sequence'. In Figure 4.5 we can see that the sources with optically thin CSE in the visible range or in the mid-IR show a larger dispersion in galactic latitude, compared to the one observed in the objects with optically thick CSE, which are more strongly concentrated towards the galactic plane. The natural interpretation of this result is that the objects with thick CSE have larger progenitor masses, at least from the statistical point of view, than those with thin CSE. This result is again in agreement with those previously reported by other authors (e.g. Volk & Kwok (1988); Likkel 1989; Chen et al. 2001).

## 4.5 The observed bolometric flux

For all the objects in the 'extended OH/IR sample' we have collected: J (1.25 $\mu$m), H (1.65 $\mu$m) and K (2.2 $\mu$m) photometric data from our own observations or from the 2MASS-PSC; A (8.28 $\mu$m), C (12.13 $\mu$m), D (14.65 $\mu$m) and E (21.3 $\mu$m) flux densities from the MSX6C Point Source Catalogue; and 12, 25, 60 and 100 $\mu$m photometry from the IRAS Point Source Catalogue. This way, we have been able to determine their *Spectral Energy Distribution* (SED) from the near-infrared to the far-infrared domain, the wavelength range where these objects radiate the majority of their energy.

Then, we have estimated the bolometric flux from these data for each source in the sample by integrating $F_\nu$ as a function of $\nu$ applying the trapezium integrating rule. We used only IRAS and MSX photometric measurements with very good quality (IRAS-FQual $=3$ and MSX-FQual $>2$) unless upper limits were also useful to impose further constraints to the observed SED. The same was done with the near-infrared data. In the case of the objects initially included in the 'Arecibo sample' we considered only those measurements corresponding to good detections (at least $3\sigma$ above the background) and/or not affected by any other instrumental problem. In the case of the objects taken from the 'GLMP sample' we did the same for 2MASS data. Upper limits were again only used if they were useful to impose further constraints to the blue end of the observed SED. To transform the J, H and K magnitudes into flux densities we adopted zero-magnitude fluxes

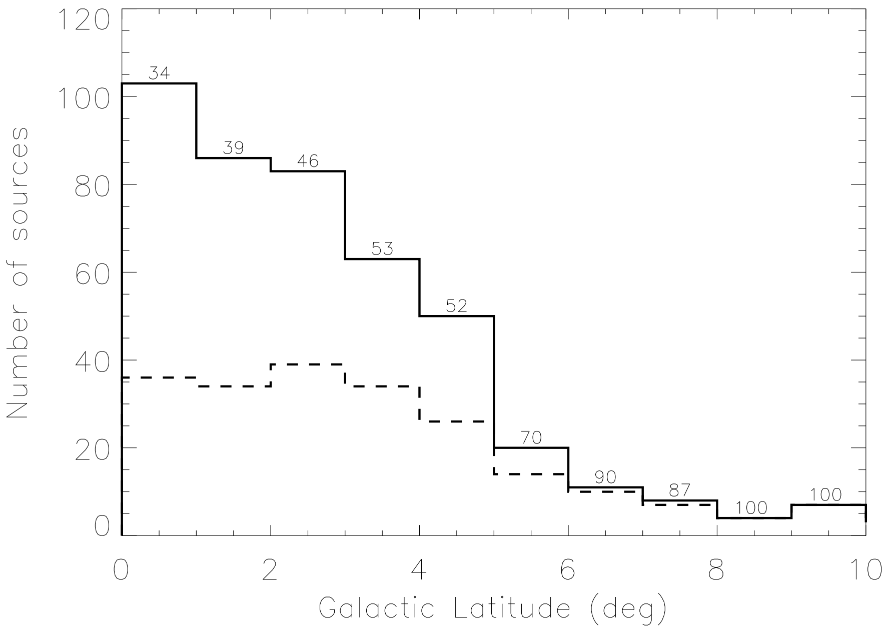

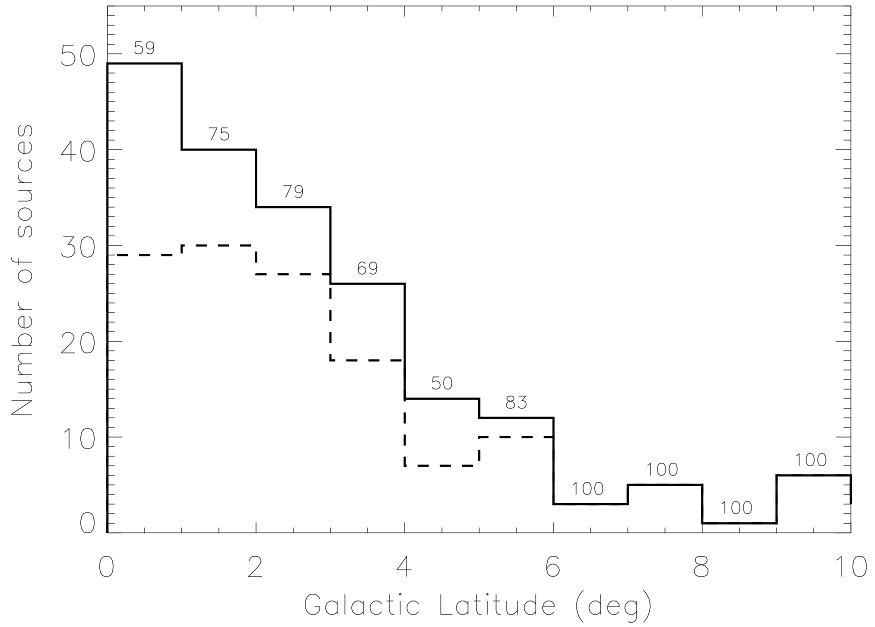

**Figure 4.5**: Upper panel: The distribution of sources as a function of the galactic latitude in the ‘extended OH/IR sample’ (solid line) is compared with the subsample of those for which an optical counterpart has been detected (dashed line). The rate is given as a percentage on the top of each bin.
Lower panel: The distribution of sources in the ‘extended OH/IR sample’ (solid line) with LRS available as a function of the galactic latitude is compared with the subsample of those for which the silicate dust feature at 9.7 $\mu$m is seen in emission (dashed line). The rate is given again as a percentage on the top of each bin.

of 1635 Jy, 1090 Jy and 665 Jy respectively for the 'Arecibo sample' (Koornneef 1983a), and 1594 Jy, 1024 Jy and 667 Jy respectively for the 'GLMP sample' (Cohen et al. 2003) according to the different photometric systems used.

To calculate the flux contribution at shortest wavelengths beyond the available data, we extrapolated a straight line joining the two bluest reliable photometric data. At longer wavelengths we have assumed zero flux at zero frequency and then we have integrated under the line that joined the flux density corresponding to the reddest photometric band with good quality and zero.

The MSX satellite covered the mid-infrared wavelength range with four photometric bands covering the wavelength range from 6.0 to 26.8 $\mu$m. IRAS covered approximately the same wavelength range with its 12 and 25 $\mu$m bands, overlapping with the MSX satellite, but extended its coverage to the far-infrared with two other bands centered at 60 and 100 $\mu$m. Although both satellites have a band centered at $\approx 12\,\mu$m, they are not directly comparable. The MSX C band covered the range $11.1-13.2\,\mu$m, while the 12 $\mu$m IRAS band covered a wider range $8.5-15.5\,\mu$m. Actually, the MSX A and D bands are almost entirely included in the 12 $\mu$m IRAS band. Similarly, the MSX E band and the 25 $\mu$m IRAS band are also different; although both have their peak between 21 and 25 $\mu$m, the MSX E band is actually completely included within the 25 $\mu$m IRAS band. Both IRAS and MSX data have been used in our calculation when available. However, we could not use both IRAS and MSX data simultaneously as our OH/IR stars are expected to be large amplitude variable objects and both missions were not simultaneous.

We first calculated the observed bolometric fluxes ($F_{bol}$) for almost all (97%) objects in our 'extended OH/IR sample' using a combination of near-infrared and IRAS photometry ($F_{bol-IRAS}$). Only three sources did not have near-infrared photometry available (See Section 2.4), and 12 more had either a bad quality 12 $\mu$m or 25 $\mu$m IRAS band measurement, or both. As the most important contribution to the emitted energy is in this near and mid-infrared range, we were not able to estimate a reliable ($F_{bol}$) for these 15 sources. In the case of sources with only upper limits in the J and H bands (6%) we used the flux density at 12 $\mu$m and in the K band for the extrapolation to shorter wavelengths. In the most extreme cases when only an upper limit flux in the K band is available (12%), we calculated the contribution from the extrapolated flux at the blue end of the SED joining the measurements at 12 and 25 $\mu$m. For $\approx$9% of the objects we used the flux density at 100 $\mu$m to calculate the contribution from the extrapolated flux at longer wavelengths end of the SED, for $\approx$66% we used the flux density at 60 $\mu$m, and for $\approx$22% we extrapolated from 25 $\mu$m.

Second, we calculated again the observed bolometric fluxes ($F_{bol}$) following the same strategy for all objects with good quality fluxes in all MSX bands using this time a combination of near-infrared, MSX and the 60 $\mu$m and 100 $\mu$m IRAS band fluxes. We calculated the integrated $F_{bol}$ for all objects in the 'extended OH/IR sample', with the exception of 5 sources (IRAS 18549+0208, IRAS 19029+0933 and IRAS 20149+3440, without near-infrared photometry; and IRAS 19035+0801 and IRAS 20529+3013, because of the bad IRAS photometry and lack of MSX data). For the rest of objects with bad IRAS fluxes we were able to obtain $F_{bol}$ using the MSX photometry.

This means that, in summary, we ended up with an estimation of $F_{bol}$ for 452 objects: 192 calculated using IRAS data ($F_{bol_{IRAS}}$); 10 using MSX data ($F_{bol_{MSX}}$); and 250 using both IRAS and MSX data. Typically, the differences found between $F_{bol_{IRAS}}$ and $F_{bol_{MSX}}$ were of the order of $\Delta m_{bol} \approx 0.3^m$; however in 20 cases (4% of the 'extended OH/IR sample') one of the two values of $F_{bol}$ was more than double, the difference raising up to $\Delta m_{bol} \approx 1.4^m$ in the most extreme cases. Differences in $F_{bol}$ are expected as a consequence of the intrinsic variability of OH/IR stars (van der Veen and Habing 1990; Engels et al. 1983; Blommaert 2003) and the non-simultaneous nature of the observations made by of MSX and IRAS. Thus, for the objects with both $F_{bol_{IRAS}}$ and $F_{bol_{MSX}}$, we averaged the integrated fluxes and the mean value is the one quoted in Table C.1. After studying the mean differences found between $F_{bol_{IRAS}}$ and $F_{bol_{MSX}}$ we roughly estimate that an uncertainty of $\approx 35\%$ is introduced by the variability in the determination of the total $F_{bol}$.

On the other hand, OH/IR stars are usually very red sources and, thus, the contribution of the extrapolated flux at shorter wavelengths to the total $F_{bol}$ is found to be lower than 10% for $\approx 86\%$ of the objects. Then, the error introduced in the extrapolation toward bluer wavelengths is expected to be almost negligible for the majority of the sources. However, there was a small (3% of the total) group of OH/IR objects (belonging to the 'Arecibo sample') with very blue colors, and therefore thin CSE, that emitted an important fraction ($> 20\%$) of their energy below $1.25\,\mu$m. In the near-infrared their SED's are dominated by the emission coming from the cool central star. If we assume a $T_{\rm eff} \approx 2\,500$ K for the central star, the fraction of energy emitted below $1.25\,\mu$m raises up to $\approx 30\%$ of the total energy. In the two more extreme cases (IRAS 20440+0412 and IRAS 21062+0058) the contribution of the extrapolated flux at the blue end of the SED to the total bolometric flux was found to be of 53% and 78%, respectively.

Regarding the contribution of the extrapolated flux at the red end of the SED to the integrated bolometric flux we found that this was lower than 10% of the total $F_{bol}$ for $\approx 88\%$ of the objects, and then that the error introduced in the extrapolation toward longer wavelengths is also negligible for the majority of the sources. However, there was a small group (2% of the total) of objects among the ones with redder colours, and therefore thick CSE, for which the situation was more complicated because only bad photometric measurements were available beyond $25\,\mu$m, for which the extrapolated flux at longer wavelengths can represent more than 20% of the total $F_{bol}$. In a thick CSE

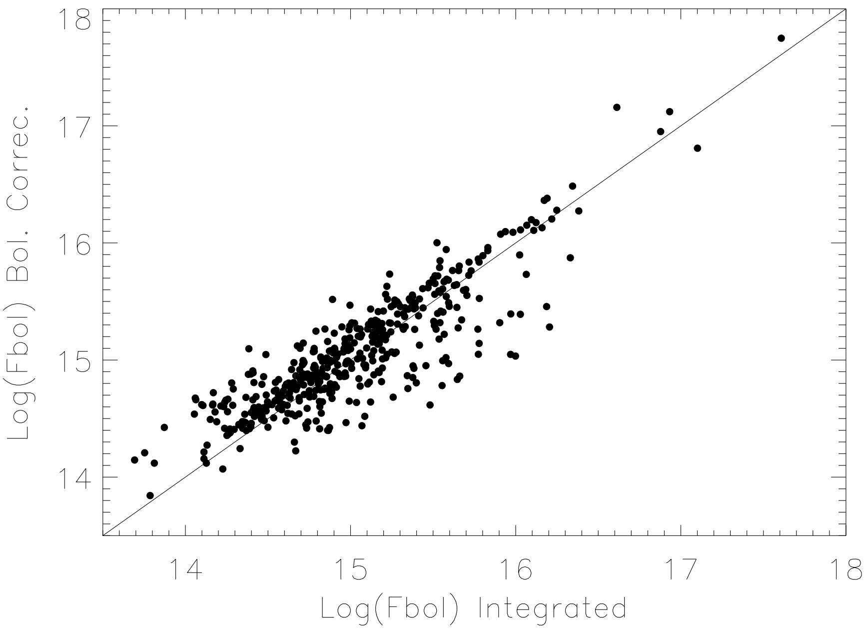

**Figure 4.6**: $F_{bol_{BC}}$ obtained using the bolometric correction of van der Veen & Breukers (1989) versus the $F_{bol_{Int}}$ obtained by us with the integration method describe in the text.

the far-infrared region of the spectrum will be dominated by the thermal emission of the dust in the CSE. If we assume a $T \approx 200\,K$ for this dust component the fraction of energy emitted beyond $25\,\mu$m would raise up to $\approx 37\%$ of the total energy. In our sample the contribution from this extrapolated flux at the red end of the SED is of $\approx 40\%$, in the most extreme cases, very consistent with this reasoning.

In summary, although the error in the extrapolation both towards the blue and the red ends of our SEDs could be large, these only affect a minority of sources. This means that, in most cases, the main source of uncertainty will still be their intrinsic variability. Adding up the two effects, we could roughly estimate the typical uncertainty of our $F_{bol}$ estimation to be of $\lesssim 40\%$ in most cases.

The bolometric flux can also be computed from the measured $12\,\mu$m flux using the more simple IR-bolometric correction suggested by van der Veen & Breukers (1989) for O-rich AGB stars. This correction is based on the use of the [12]–[25] IRAS colour as a temperature indicator. In Figure 4.6 the results obtained using this bolometric correction ($F_{bol_{BC}}$) are compared with the bolometric fluxes calculated by us with the above integration method ($F_{bol_{Int}}$). For comparison we have also plotted the line corresponding to a perfect match between both estimations. As this figure shows, the bolometric correction performed by van der Veen & Breukers usually produce slighter larger $F_{bol}$ than those obtained with our integration method. Typically, $F_{bol_{BC}}$ are $\approx 23\%$ larger than $F_{bol_{Int}}$, although with a large scatter. Van der Veen & Breukers roughly estimated that the expected uncertainty in the determination of the IR-bolometric correction following their method was $\approx 30\%$, larger for the bluer sources ($40-50\%$) and smaller (15%) for the redder ones. However, they did not take into account the contribution due to the intrinsic variability of these stars that, as we have seen, is actually the main source of uncertainty.

## 4.6 Absolute bolometric luminosity of the Galactic Bulge OH/IR stars

The absolute luminosity of OH/IR stars is still subject to debate since different authors provide a different estimation of the mean luminosity of stars in this short transition phase. In addition, there is not also a common opinion on the evolutionary connection between OH/IR stars with different luminosities and PNe, as well as there is not yet any definitive conclusion reached regarding the connection between stellar luminosity, progenitor mass and galactic height.

One of the main problems to deal with when determining the absolute bolometric luminosity of OH/IR stars, as it also happens with the PNe, is the determination of the distance.

In order to avoid or at least diminish the effect of this uncertainty we selected the subgroup of sources in our sample detected in the direction of the Galactic Bulge and assumed a common distance to all these sources equivalent to the generally assumed distance to the Galactic Center of $\approx 8\,\mathrm{kpc}$ (Reid 1993). Statistically, we know that this will be true for at least $\approx 80\%$ of the sources located at an angular distance of $\leq 10^\circ$ from the Galactic Center, which in our sample are 41 sources, all of them belonging to the 'GLMP sample'. These sources have been labeled accordingly in Table C.1.

Assuming a size of the Galactic Bulge of $\pm 2\,\mathrm{kpc}$ around the Galactic Center this translates into uncertainties of the order of 20% in the determination of the distances to these sources.

With our derived value of $F_{bol}$ and assuming that the distances (D) are known it is straightforward to calculate the absolute bolometric luminosity ($L_{bol}$) of the OH/IR stars in our Galactic Bulge sample:

$$L_{bol} = 4\,\pi\,D^2\,F_{bol}$$

Figure 4.7 shows a histogram of the absolute luminosity of the OH/IR stars in our Galactic Bulge sample. Our sample of OH/IR stars in the Galactic Bulge is strongly biased to the reddest sources, as it only contains sources taken from the 'GLMP sample' (see Figure 4.1).

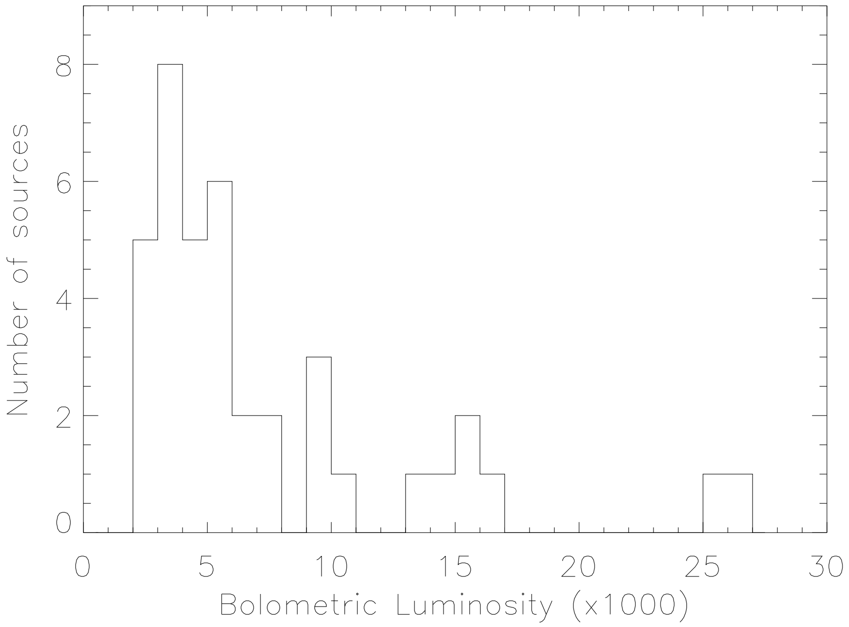

**Figure 4.7**: Absolute bolometric luminosity in thousands of $L_\odot$ of the OH/IR stars belonging to the Galactic Bulge population

The range of luminosities found goes from $\approx 2\,500$ to $\approx 26\,000\,L_\odot$ ($-3.5^m > M_{bol} > -6.3^m$), strongly peaked around $3\,500 - 4\,000\,L_\odot$ ($M_{bol} \approx -4.2^m$). There are two sources (IRAS 17317–3331 and IRAS 17411–3154) which show unrealistically high $L_{bol} > 10^5\,L_\odot$. Clearly these two stars must be foreground sources belonging to the disk population and not to the bulge. They must be part of the expected 20% contamination above mentioned. The two other objects with the largest luminosities found were IRAS 18000–2835 and IRAS 17418–2713, with $L_{bol} > 25\,000\,L_\odot$. IRAS 18000–2835 is the brightest near-infrared source in the ‘GLMP sample’ ($K = 5.05^m$). As we have discussed in Chapter 3, the extreme brightness of this source, its extremely blue colours and the absence of an optical counterpart suggest that IRAS 18000–2835 may have experienced a sudden increase of brightness in the last few years. On the other hand, IRAS 17418–2713 was identified by Ratag & Pottasch (1991) as a possible planetary nebula (PN), on the basis of the detection of radio continuum emission at 6 cm. If confirmed, this would suggest that this source could be classified among the rare class of ‘OHPNe’ (Zijlstra et al. 1989). These are young PNe with OH maser emission, which have been proposed to be massive stars evolving so fast that the central star would be already hot enough to produce ionization in the envelope while the CSE is still optically thick. Thus, they would only be detectable as ‘infrared PNe’.

The peak of our distribution is in very good agreement with that previously determined by other authors who studied OH/IR stars in the Galactic Bulge in the past (Habing et al. 1985; Rowan-Robinson & Chester 1987; Jones et al. 1994; Blommaert et al. 1998; Wood et al. 1998). Van der Veen & Habing (1990), using the bolometric correction suggested by van der Veen & Breukers (1989), found a similar peak at slightly larger luminosities for the distribution of OH/IR stars in the Galactic Bulge between 5 000 and 5 500 $L_\odot$. This discrepancy could be attributed to the systematic differences in their $F_{bol}$ estimation with respect to ours, as we have seen in the previous section. García-Lario (1992) found that the luminosity distribution for non-variable OH/IR stars in the Galactic Bulge was also strongly peaked at 4 000 $L_\odot$, a result that supports the idea that both kind of objects are evolutionary connected. More recently, Jackson et al. (2002) calculated the absolute luminosity of a group of OH/IR stars in the Galactic Bulge with bluer colours ($\lambda \lesssim 1$) and they also found an absolute luminosity of 3 500 $L_\odot$, exactly the same result we obtain, suggesting that the luminosity function for OH/IR bulge stars is not dependent on the colours of the selected sources.

In addition, others works centered on AGB stars in the solar neighbourhood based on Hipparcos data suggest a luminosity distribution peaking again at around $\approx$3 000 $L_\odot$ (Knauer et al. 2001). Since this is very similar to the luminosity peak that we obtained for the bulge stars, it appears that the luminosity function may be similar throughout the Galaxy, as previously suggested by Jackson et al. (2002).

Both the population of stars in the solar neighbourhood and in the Galactic Bulge are expected to be dominated by low mass stars ($\approx 1\,M_\odot$). This means that the narrow peak found at 3 500 $L_\odot$ in the luminosity distribution of our sample of bulge OH/IR stars must also correspond to one solar mass stars. But if this is the case, they must be in a much more advanced stage of their evolution as AGB stars, in order to explain the redder colours observed.

However, Likkel (1989), found using a large sample of OH/IR stars belonging to the Galactic Disk population, that the reddest sources in her sample (equivalent to our group of Galactic Bulge OH/IR stars) are much more luminous according to their low galactic scale height (up to 20 000 $L_\odot$), while the bluer ones would have a luminosity of only 2 500 $L_\odot$, only slightly lower to the value found in the Galactic Bulge.

## 4.7 The distance to the ‘extended OH/IR sample’

Based on the strongly peaked luminosity function of the OH/IR stars in the Galactic Bulge and on the similar results provided by Hipparcos for AGB stars in the solar neighbourhood, we can tentatively determine the distance to the rest of OH/IR stars in our extended sample by simply assuming a common and constant luminosity of

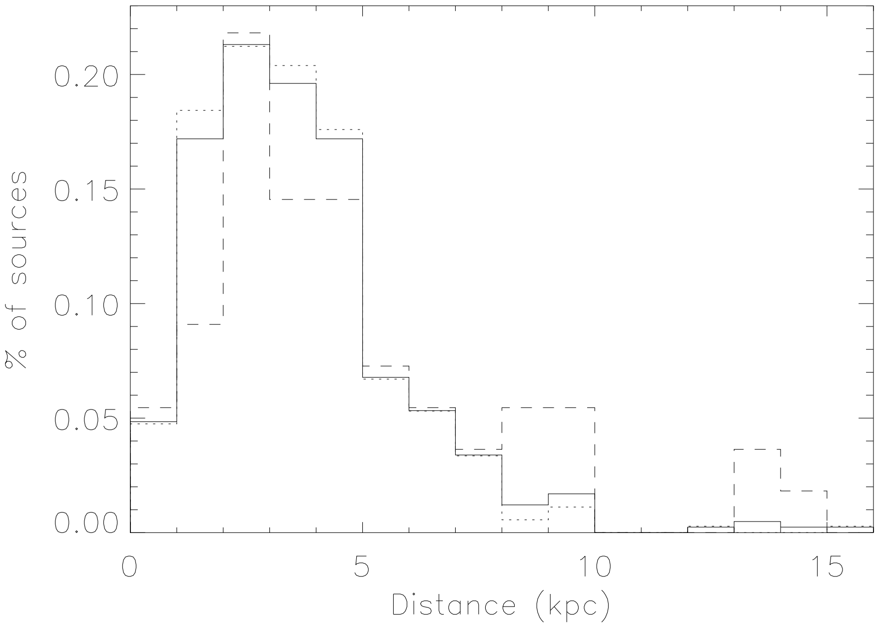

**Figure 4.8**: Distance distribution of the sources in the 'extended OH/IR sample' (solid line), in the 'Arecibo sample' (dotted line) and in the 'GLMP sample' (dashed line), once the subsample of Galactic Bulge sources has been excluded (assuming $L_{OH/IR} = 3\,500\,L_{\odot}$). Each distribution has been normalized with respect to the total number of sources in each subsample. Not included is one source with $D \approx 21$ kpc.

$L_{OH/IR} = 3\,500\,L_{\odot}$ for all them.

This way, we will explore the spatial distribution of our sample of stars not located in the direction of the Galactic Bulge, although we are conscious that this would give us just a rough approximation to the actual distribution.

Then, taking the value of $F_{bol}$ listed in Table C.1 we can derive the distance D from the following equation:

$$D = \sqrt{\frac{L_{OH/IR}}{4\,\pi\,F_{bol}}}$$

In Table C.1 we have tabulated the value of the distance derived from the above equation for all the objects belonging to the 'extended OH/IR sample' for which we were able to determine $F_{bol}$, with the exception of those located in the direction of the Galactic Bulge for which we have assumed a distance of 8 kpc. We have also calculated the distance (assuming $L_{OH/IR} = 3\,500\,L_{\odot}$) to the two foreground sources identified as such in the previous section in the Galactic Bulge sample.

In Figure 4.8 we have plotted the distance distribution of all objects belonging to the ‘extended OH/IR sample’ once the subsample of Galactic Bulge sources has been excluded. Most of them are found to be located at distances between $1-5$ kpc with the peak of the distribution in the $2-3$ kpc range. In addition, we have plotted the distance distribution of the sources in the ‘Arecibo sample’ and of the subsample of disk sources in the ‘GLMP sample’. Each distribution has been normalized with respect to the total number of sources of each subsample.

As we can see, the distance distribution of both the ‘Arecibo sample’ and the subsample of disk sources of the ‘GLMP sample’ are very similar at least up to a distance of 8 kpc. This implies that in general both subsamples must be very similar. However, beyond 8 kpc, we mainly find sources belonging to the ‘GLMP sample’, which can be explained as the consequence of a large fraction of high luminous stars in the ‘GLMP sample’ compared to the ‘Arecibo sample’.

Only 6 objects ($\approx 1\%$ of the sample) have distance estimates larger than 10 kpc. The object with the largest distance determination ($\approx 21$ kpc) is IRAS 18091–0855. This source was detected by IRAS just above the detection limit ($F_{12} = 0.52$ Jy), and by MSX, although only in the A-band ($F_A = 0.26$ Jy), also close to the MSX detection limit but it was not detected in the near-infrared with 2MASS. The other 5 objects (IRAS 18569+0553, IRAS 18518+0558, IRAS 18187–0208, IRAS 18361–0036, IRAS 18475+0353) have distance estimates between 12 and 15 kpc. All of them were detected by IRAS and MSX with flux densities of only a few Jy, and only IRAS 18187–0208 was detected in the near-infrared, although with a faint counterpart ($K = 10.8^m$). Apart from these exceptions, the distance estimates obtained for the rest of sources in the ‘extended OH/IR sample’ are quite reasonable. Thus, these will be the distances assumed in the rest of our discussion.

## 4.8 The Galactic Height of the ‘O-rich AGB sequence’

Once the distance D has been estimated for each source in the sample as described in Section 4.7, we can now use the galactic latitude $b$ to estimate the galactic height Z:

$$Z = D \sin(b)$$

In Table C.1 we have tabulated the value of the galactic height resulting from the above equation for all the OH/IR stars in the sample for which we were able to derive a value of $F_{bol}$, with the exception of those belonging to the Galactic Bulge[1].

In Figure 4.9 we have plotted the galactic height distribution (in absolute value) of the objects in the ‘extended OH/IR sample’, assumed to be part of the galactic disk population.

---

[1] The Galactic Bulge is a spheroidal component of our Galaxy for which the concept of galactic height as an indicator of mass does not apply

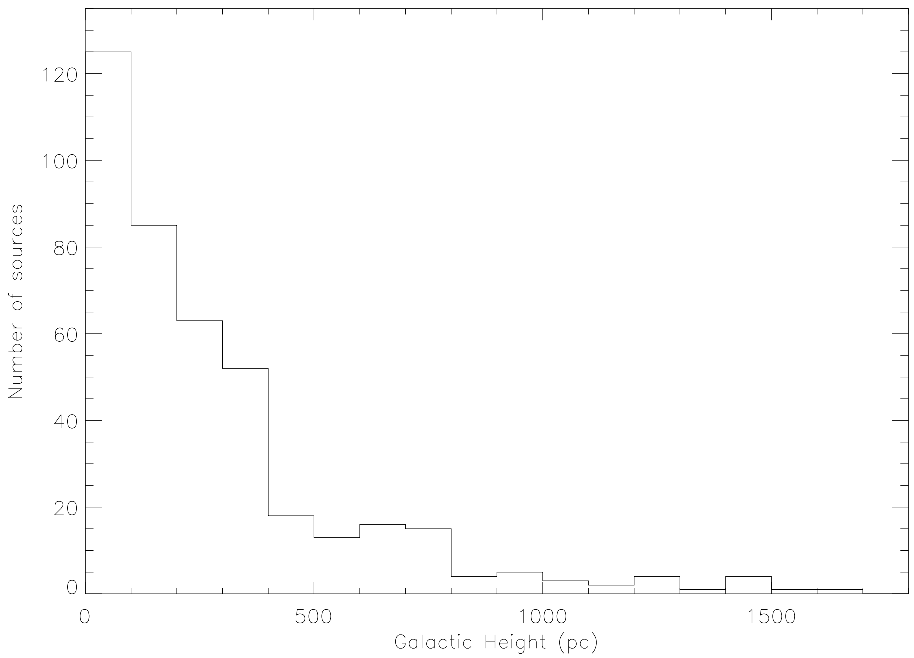

**Figure 4.9**: Galactic height distribution of the disk sources in the 'extended OH/IR sample' ($L_{OH/IR} = 3\,500\,L_{\odot}$ assumed).

Almost all (98%) the sources in the sample have a galactic height below 1 kpc, with the majority of the objects located very close to the Galactic Plane. There is only one object with $Z > 1.8$ kpc: IRAS 21100+2205 ($Z \approx -2.5$ kpc) which might be a nearby source with a very low luminosity.

## 4.9 Interpretation of the 'O-rich AGB sequence'

It has been suggested by several authors (e.g. Likkel 1989; García-Lario 1992) that the redder OH/IR stars (i.e. those with optically thick CSE and no optical counterpart) are intrinsically more luminous than the bluer ones (i.e. those with optically thin CSE and relatively bright optical counterparts). This idea comes from the interpretation of the 'O-rich AGB sequence' as a **mass sequence**, where the redder objects are the more massive ones. Thus, in the literature typically a $L_{bol} \approx 10\,000\,L_{\odot}$, or even higher, has been assumed for the redder OH/IR stars in many cases.

However, in Section 4.6 we have shown that the luminosity distribution of the subsample of OH/IR stars in the 'GLMP sample' belonging to the Galactic Bulge is strongly peaked at $L \approx 3\,500\,L_{\odot}$. Very similar low luminosities were also found by other authors, for other samples of galactic bulge OH/IR stars, as we have already reported. The difference is that the bulge OH/IR stars that we have used in this work, in contrast with previous studies, are all very red OH/IR stars ($1.6 > \lambda > 4.4$) and, despite of this, we have obtained exactly the same result e.g. of Jackson et al. (2002) that used exclusively blue OH/IR stars ($\lambda < 1.0$). Our interpretation is that our sample of red OH/IR stars do not represent a different population of higher mass stars, but the same population of typically $\approx 1\,\mathrm{M}_{\odot}$ stars in a much more evolved stage (i.e. with thicker shells) as AGB stars. The consequence is a $\mathrm{L}_{OH/IR} = 3\,500\,\mathrm{L}_{\odot}$ seems to be a more plausive approximation to the actual bolometric luminosity for any OH/IR star in the Galaxy than the higher value of $\approx 10\,000\,\mathrm{L}_{\odot}$ frecuently used in the literature, regardless of whether the star is located in the blue or red part of hte 'O-rich AGB sequence' and this will be the value assumed in the rest of the discussion.

The agreement with Jackson et al. (2002) is not surprising since the Galactic Bulge is a region dominated by a homogeneous population of low mass stars (typically $\approx 1\,\mathrm{M}_{\odot}$). Thus, our sample of red OH/IR stars in the Galactic Bulge could simply be identified as the most evolved sample of OH/IR stars in the Galactic Bulge. The surprising result is that if most of them are actually $\approx 1\,\mathrm{M}_{\odot}$ stars, as their associated mean luminosity suggest, this would imply that even the less massive OH/IR stars are able to create optically thick CSEs at least at the very end of their AGB lifetime.

Therefore, the red part of the 'O-rich AGB sequence' ($\lambda \gtrsim 1.5$) would not only be populated by the more massive OH/IR stars in the Galaxy, but also by a significant fraction of less massive stars in an extremely evolved stage as OH/IR stars.

Figure 4.10 shows the galactic height (in absolute value) derived as a function of the $\lambda$ parameter for the whole 'extended OH/IR sample', excluding the Galactic Bulge subsample, assuming $\mathrm{L}_{OH/IR} = 3\,500\,\mathrm{L}_{\odot}$ for all sources as a first approach. Despite of the low number of objects with high $\lambda$ value, we found a very clear trend in the sense that sources with low values of $\lambda$ are found to show a wider distribution in galactic height, whereas sources associated to large values of $\lambda$ are found much more concentrated towards the Galactic Plane. This implies that the redder part of the 'O-rich AGB sequence' must be populated mainly with objects of higher mass. Note that assuming a larger luminosity of $10\,000\,\mathrm{L}_{\odot}$ for all sources in the sample would just change the scale of the y-axis and considering e.g. a linear increase of the L towards higher values of $\lambda$ would just make the range of galactic scale heights narrower (i.e. the progenitor stars of the high luminous sources would be of smaller mass).

We have divided the distribution of OH/IR stars plotted in Figure 4.10 according to the value of the $\lambda$ parameter in several bins of width $\Delta\lambda = 0.3$ to obtain their 'galactic scale height' (H), defined as the distance above the galactic plane where the number density of stars has dropped to 1/e, assuming an exponential distribution above the plane. Thus, for each bin of $\lambda$ we have fitted an exponential function to the galactic height distribution:

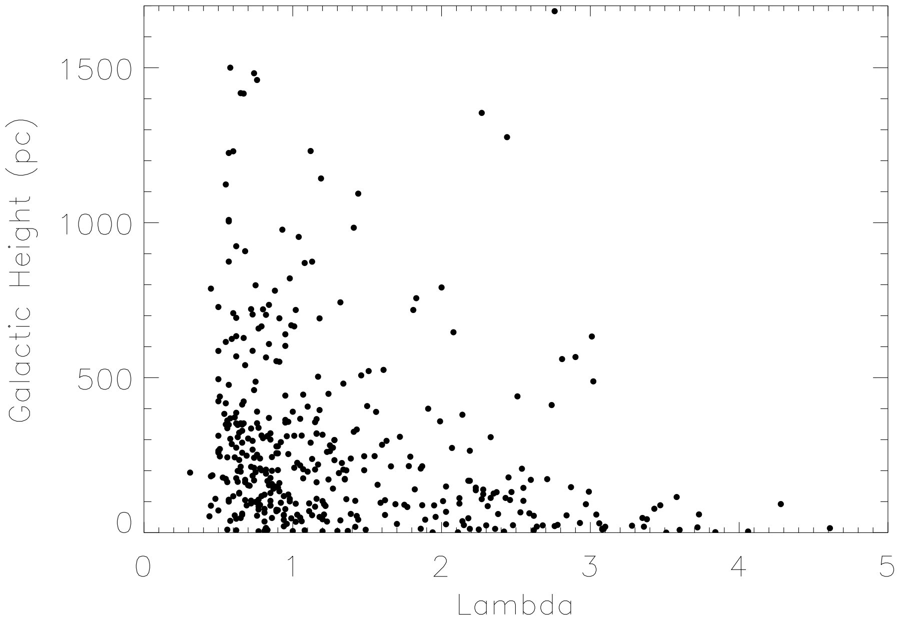

**Figure 4.10**: Galactic height distribution as a function of $\lambda$ derived for all the sources in the 'extended OH/IR sample', excluding the Galactic Bulge OH/IR stars ($L_{OH/IR} = 3\,500\,L_{\odot}$ assumed).

$$N(Z) = N_0\, e^{-Z/H}$$

where N is the number of sources as a function of Z and $N_0$ the number of sources corresponding to Z=0. For this calculation we have not considered the obvious outliers in Figure 4.10. The galactic scale height distribution as a function of $\lambda$ has been plotted in Figure 4.11. As it was expected, this distribution shows more clearly the general behaviour already observed in Figure 4.10. In Figure 4.11 we have put together in the last bin all the sources with $\lambda > 3.6$ because of the low number of stars in this region of the 'O-rich AGB sequence'.

In the remaining discussion we will divide the whole sample in up to five smaller subsamples to facilitate our subsequent analysis. In Table 4.1 these subsamples are defined as a function of the values of their associated $\lambda$ parameter. For each subsample we have derived its mean galactic scale height H and the associated progenitor mass suggested.

The *'extremely blue subsample'* of OH/IR stars is defined as the one formed by the stars located at the blue end of the 'O-rich AGB sequence', with $\lambda \leq 0.6$. This subsample has the largest galactic scale height H = 536 pc, remarkably similar to that found by Jura (1994) for optically bright Miras variables with short periods ($P < 300^d$). Maciel & Dutra (1992) studied the space distribution and the kinematics of PNe in the Galaxy. According

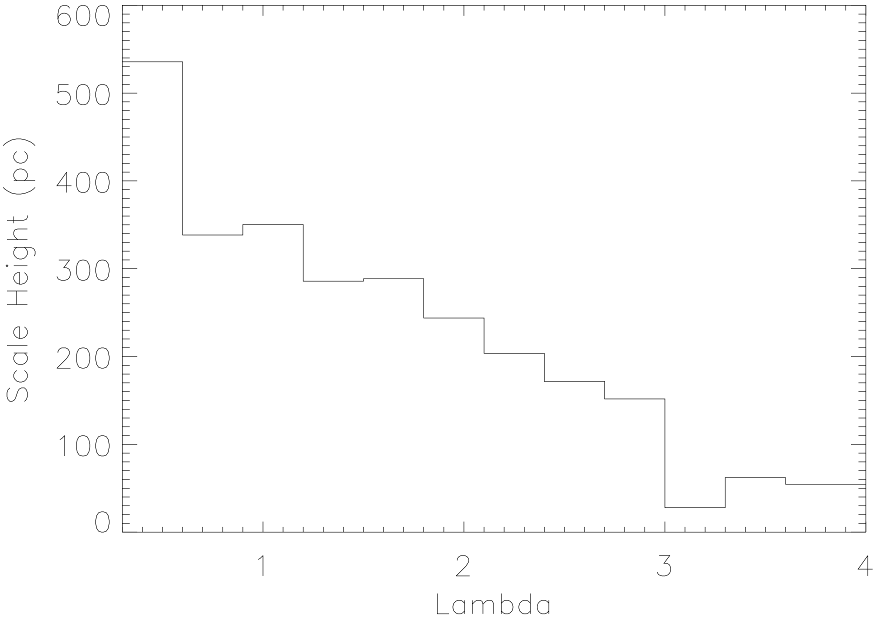

**Figure 4.11**: Galactic scale height distribution as a function of the $\lambda$ parameter for all the sources in the 'extended OH/IR sample', excluding the Galactic Bulge.

**Table 4.1**: Galactic scale heights, and estimated progenitor masses for the different sub-samples identified in our study.

| Sample | $\lambda$ range | N of stars | H [pc] | M [$M_\odot$] |
|---|---|---|---|---|
| All | | 403 | 260 | |
| Extremely Blue | $\lambda \leq 0.6$ | 43 | 536 | $0.8-1.0$ |
| Blue | $0.6 < \lambda \leq 1.2$ | 193 | 344 | $1.0-1.5$ |
| Transition | $1.2 < \lambda \leq 1.8$ | 58 | 287 | $1.5-2.5$ |
| Red | $1.8 < \lambda \leq 3.0$ | 66 | 193 | $2.5-4.0$ |
| Extremely Red | $3.0 < \lambda$ | 22 | 48 | $> 4.0$ |

**Table 4.2**: Galactic scale height estimations for different samples compiled from the literature.

| Sample | H [pc] | Reference |
|---|---|---|
| Miras | 315 | Wood & Cahn (1977) |
| Short-period Miras | 600 | Jura (1994) |
| Intermediate-period Miras | 240 | Jura & Kleinmann (1992) |
| Long-period Miras | 240 | Jura et al. (1993) |
| OH/IR | 330 | Ortiz & Maciel (1996) |
| OH/IR LRS 2n | 210 | Likkel (1989) |
| OH/IR LRS 3n | 140 | Likkel (1989) |
| Carbon stars | 200 | Claussen et al. (1987) |
| Carbon stars | 155-290 | Groenewegen et al. (1992) |
| Planetary Nebulae I | 150* | Maciel & Dutra (1992) |
| Planetary Nebulae II | 350* | Maciel & Dutra (1992) |
| Planetary Nebulae III | 660* | Maciel & Dutra (1992) |

*Note:* The values from Maciel & Dutra (1992) correspond actually to values of the mean galactic height <Z>.

to their results only type III PNe (very low mass O-rich PNe belonging to the thick disk population) with $<Z> = 660$ pc show a galactic height which corresponds very well with the one found in our ‘extremely blue subsample’. If this subsample of OH/IR stars are evolutionary connected with type III PNe they must represent the group of OH/IR stars with the lowest progenitor masses ($M \lesssim 1.0\,M_\odot$).

The *‘blue subsample’* is the following group in the sequence represented by those OH/IR stars with $0.6 < \lambda \leq 1.2$. This subsample has an associated value of the galactic scale height $H = 344$ pc, which is similar to that found by Ortiz & Maciel (1996) for their sample of OH/IR stars in the solar neighborhood, and with that obtained by Wood & Cahn (1977) for their sample of Mira variables near the Galactic Plane, which combine both short and long period Miras. These coincident results suggest that the large majority of the OH/IR stars with optically thin shells in this subsample represent just a more evolved stage in the evolution of normal Miras. Type II PNe (mixed population of O-rich and C-rich PNe belonging to the disk population) have a $<Z> = 350$ pc according to Maciel & Dutra (1992), which fits very well with the galactic scale height found for our ‘blue subsample’. According to Miller & Scalo (1979) this stellar population would correspond to progenitor masses in the range $1.0 - 1.5\,M_\odot$.

The region of the 'O-rich AGB sequence' associated to the values of $\lambda$ between 1.2 and 1.8 is populated by what we have called the 'transition subsample'. This is the transition region in which OH/IR stars become optically thick. The percentage of them not showing any optical counterpart increases with $\lambda$ and the LRS class turn also from type E (emission) into type A (absorption), as expected for an optically thick shell. Thus, in this region OH/IR stars with both optically thin CSE and optically thick CSE coexist. The OH/IR stars belonging to this *'transition subsample'* have a galactic scale height $H = 287\,pc$, which is consistent with the value obtained by Jura & Kleinmann (1992) and Jura et al. (1993) for intermediate- and long-period Mira variables, and by Groenewegen et al. (1992) for a small group of low mass optically bright carbon stars. This region of the 'O-rich AGB sequence' must then be populated by stars with progenitor masses in the range $1.5 - 2.5\,M_\odot$. The galactic scale height H that we obtain for the 'transition subsample' is remarkably higher than the one derived by Likkel (1989) for her sample of OH/IR stars with LRS class 2n (LRS 2n corresponds to the LRS-Type E used in this work). This discrepancy must be due to the use of the bolometric correction of van der Veen & Breukers (1989) which, as we have shown in Section 4.5, overestimates $F_{bol}$, which would cause an underestimation of the H derived.

The *'red subsample'* is formed by all the OH/IR stars with associated values of $\lambda$ between 1.8 and 3.0. This region is populated exclusively by OH/IR stars with optically thick CSE (LRS 3n or LRS-Type A). The estimated value of the galactic scale height in this case is $H = 193$. This value is very similar to the one obtained by Claussen et al. (1987) and by Groenewegen et al. (1992) for two independent large samples of galactic carbon stars, both including a significant fraction of infrared carbon stars. This region of the diagram should then be populated by OH/IR stars with similar masses to these carbon stars (between $2.5 - 3.0\,M_\odot$). Some of them may actually change their chemical composition from O-rich to C-rich during their evolution in the AGB phase as a consequence of the dredge-up processes that the theory predicts for intermediate mass stars. Type I PNe (O-rich PNe belonging to the thin disk population with high He and N/O abundances) have a mean galactic height $<Z> = 150\,pc$ (Maciel & Dutra 1992) which is only slightly lower than the galactic scale height of our 'red subsample' and very similar to the value of $H = 140\,pc$ derived by Likkel for LRS class 3n sources. These PNe are probably the result of the evolution of Hot Bottom Burning AGB stars, as indicated by their peculiar chemical composition. Stellar models (D'Antona & Mazzitelli 1996) predict the production of $^{7}Li$ as well as low values of $^{12}C/^{13}C$ in these stars and the activation of Hot Bottom Burning (HBB) mechanism in our Galaxy for progenitor masses $M \gtrsim 3\,M_\odot$. We believe that a significant number of type I PNe with masses slightly higher than $3\,M_\odot$ may also be part of our 'red sample'.

The last subsample with $\lambda > 3.0$ is defined as the *'extremely red subsample'* in

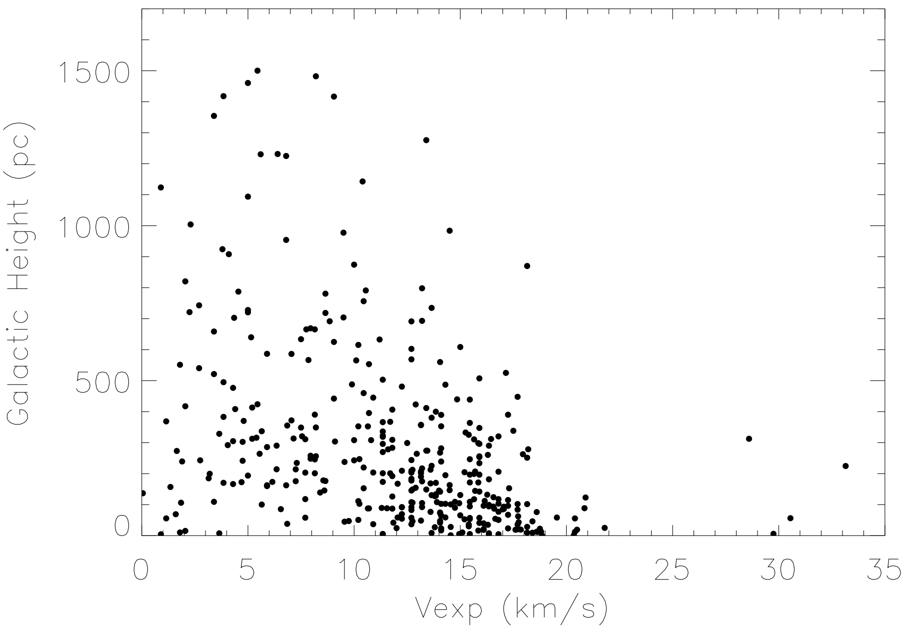

**Figure 4.12**: Galactic height distribution as a function of $v_{exp}$ for all the sources in the ‘extended OH/IR sample’, excluding the Galactic Bulge sources ($L_{OH/IR} = 3\,500\,L_{\odot}$ assumed).

Table 4.1 and it is formed by the reddest OH/IR stars in our sample, all of them with optically thick CSE and a extremely low galactic scale height of only H = 48 pc. These objects should then represent the most massive OH/IR stars in our Galaxy. Probably these OH/IR stars are massive enough to activate the HBB. Spectroscopic observations to search for signatures of HBB, as the ones mentioned above, would be desirable in order to confirm this hypothesis. However, this may be difficult in practice, considering that they must be extremely obscured by their optically thick CSE. Note that there are no known PN class which can be associated to our ‘extremely red subsample’ with only 48 pc of galactic scale height. It is possible that these massive OH/IR stars evolve so quickly that when the central star reaches the necessary temperature to ionize the envelope, this would still be thick enough to prevent the detection of the PN in the optical. And when the CSE would have dissipated enough to see the central star again in the optical this would already be a white dwarf. Thus, these massive OH/IR stars would never form visible PNe. Rather they would evolve as ‘infrared PNe’ and might be related with the rare group of so-called ‘OHPNe’ (Zijlstra et al. 1989), heavily obscured sources which show both OH maser and radio continuum emission.

In order to check the consistency of the scenario proposed above, other observational parameters associated to galactic OH/IR stars have been inspected, like the ex-

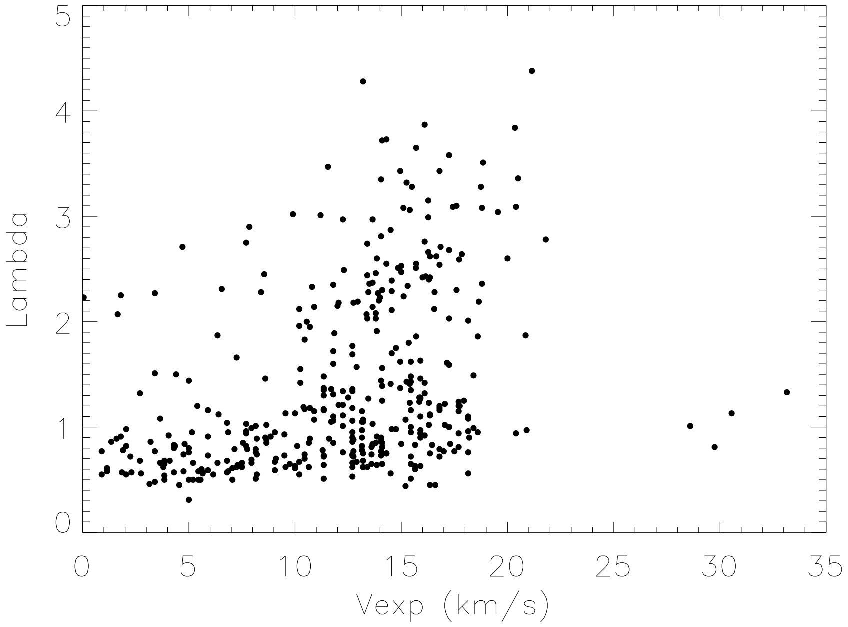

**Figure 4.13**: $v_{exp}$ distribution as a function of the $\lambda$ parameter for all the sources in the 'extended OH/IR sample' ($L_{OH/IR} = 3\,500\,L_{\odot}$ assumed).

pansion velocity ($v_{exp}$), which has been proposed in several occasions to be a distance independent mass indicator (Baud & Habing 1983; García-Lario 1992). The $v_{exp}$ can be derived from the OH maser measurements for all the objects in the 'extended OH/IR sample' with a double peaked maser. Figure 4.12 shows that there is also a very clear correlation between the galactic height and $v_{exp}$ in the sense that there is a deficit of OH/IR stars with high $v_{exp}$ at high galactic heights and that there is a systematic trend to find a higher $v_{exp}$ in sources located at lower galactic heights. This can be interpreted as an additional evidence which supports the initial suggestion that $v_{exp}$ in OH/IR stars can be taken as a distance independent mass indicator.

If the $\lambda$ parameter is correlated with the galactic height (Figure 4.10), and the latter is correlated with $v_{exp}$ (Figure 4.12), then the $\lambda$ parameter should also be correlated with $v_{exp}$. In Figure 4.13 we have plotted the $\lambda$ parameter as a function of the $v_{exp}$. In this figure we can clearly see that the objects with the lower $v_{exp}$ are associated to low values of $\lambda$, while those with the higher values of $\lambda$ are predominantly high $v_{exp}$ OH/IR stars.

In view of the last three figures, we can easily conclude that the red part of the 'O-rich AGB sequence' (high $\lambda$) is mainly populated by both higher progenitor mass (see Figure 4.10) and higher $v_{exp}$ sources (see Figure 4.13).

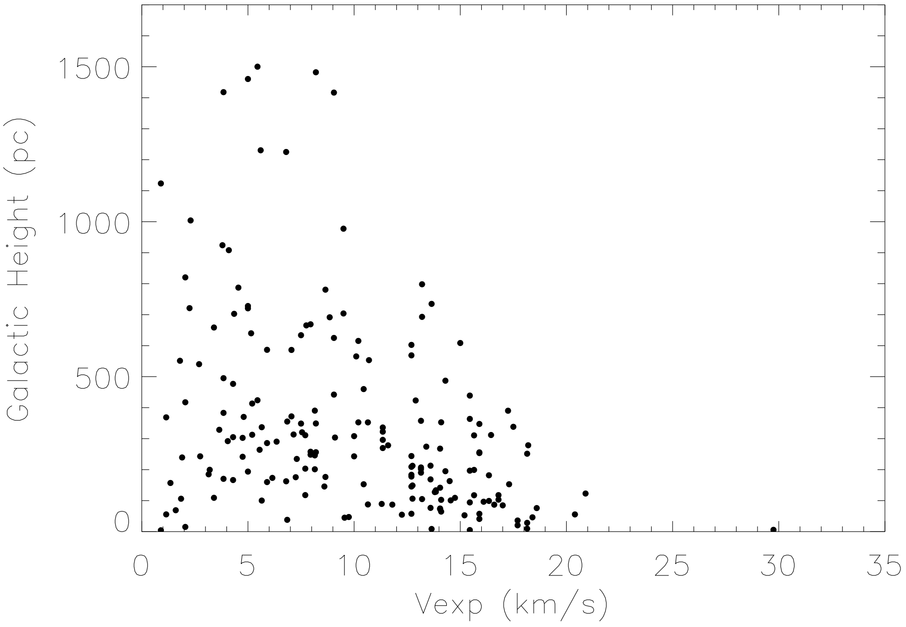

**Figure 4.14**: Galactic height distribution as a function of $v_{exp}$ for the bluer ($\lambda < 1$) OH/IR stars in the 'extended OH/IR sample' ($L_{OH/IR} = 3\,500\,L_\odot$ assumed).

However, the OH/IR stars placed in the blue part of the 'O-rich AGB sequence' (low $\lambda$) cover the whole range of $v_{exp}$ (see Figure 4.13), which corresponds to the whole range of possible galactic heights (see Figure 4.12). This would mean that the blue part of the 'O-rich AGB sequence' is populated not only by OH/IR stars of low progenitor mass and low $v_{exp}$ but also by OH/IR stars of high progenitor mass and high $v_{exp}$. Furthermore, the objects with low progenitor mass and low $v_{exp}$ are predominantly found only at low $\lambda$ values (see Figure 4.13), which implies that they must abandon the AGB phase without reaching the red end of the 'O-rich AGB sequence'.

These conclusions are also supported by Figure 4.14, where we show $v_{exp}$ as a function of the galactic height only for the bluer objects ($\lambda < 1$) in our sample. In this plot we see how the bluer OH/IR stars display the full range of possible $v_{exp}$ which should correspond to the full range of possible progenitor masses. Actually there is only one source with $v_{exp} \approx 30\,\mathrm{km\,s^{-1}}$ among them, but this may be a blue SG with OH maser emission and not an AGB star, as the rest of other outliers shown in Figure 4.13.

Another distance independent observational parameter which could be considered a mass indicator is the period but, unfortunately, this is unknown in the most cases. This analysis will have to wait until the end of our long term monitoring program.

According to the above conclusions, we propose an evolutionary scenario in which all OH/IR stars would start the AGB phase, independent of their progenitor mass (0.8 – 8 $M_\odot$), in the bluer part of the ‘O-rich AGB sequence’, with a $v_{exp}$ probably proportional to their mass, and then they would evolve toward redder colors, although only the more massive stars would reach the very end of the ‘O-rich AGB sequence’.

## 4.10 Conclusions

The bolometric fluxes ($F_{bol}$) of most of the sources included in the so-called ‘extended OH/IR sample’ (a combination of OH/IR stars taken from the ‘Arecibo sample’ and from the ‘GLMP sample’ to cover a wide range of infrared colours) have been determined after integrating the photometric data available from the near infrared to the far infrared domain (JHK, MSX and IRAS data) and extrapolating both toward shorter and longer wavelengths.

Whenever possible, we have used the non-simultaneous MSX and IRAS photometry to derive a mean value of the bolometric flux as a better approach to the actual value considering the strong variability of the sources under study. We estimate that this intrinsic variability is the main source of uncertainty in our calculations rather than the extrapolations made. Typically we estimate that the accuracy of our bolometric flux estimations is of the order of $\approx 40\%$.

We have determined the absolute luminosity distribution of a sample of 41 sources belonging to the ‘GLMP subsample’ located in the direction of the Galactic Center by adopting a common distance of 8 kpc, assuming that they are all part of the Galactic Bulge population of OH/IR stars. The luminosities found range from $\approx 2\,500$ to $\approx 26\,000\,L_\odot$ ($-3.5^m > M_{bol} > -6.3^m$) but they are strongly peaked around $3\,500 - 4\,000\,L_\odot$ ($M_{bol} \approx -4.2^m$). This result is in agreement with those found by other authors using different OH/IR star samples in the bulge with very different (bluer) colours or using samples located in different parts of the Galaxy. Then we conclude that the luminosity function may be similar throughout the Galaxy and not very dependent on the colours of the stars selected. This result is in disagreement with the general assumption that ‘red’ OH/IR stars are typically $\approx 10\,000\,L_\odot$ sources, generally used in the literature. Our interpretation is that our sample of red OH/IR stars in the Galactic Bulge is dominated by relative low mass ($\approx 1\,M_\odot$) stars and do not differ significantly from the rest of galactic samples used by other authors in terms of progenitor mass but they are probably in a more evolved stage as AGB stars (i.e with thicker shells). If our interpretation is correct this would imply that relatively low mass OH/IR stars can also reach the red part of the ‘O-rich AGB sequence’ at the very end of their AGB lifetime. And because they are much more numerous than massive stars they can still be the dominant population of the red part of the ‘O-rich AGB sequence’, even at considerably high values of $\lambda$.

Based on the narrow luminosity distribution shown by our red sample of Galactic Bulge OH/IR stars we have been able to explore the galactic height distribution of the rest of stars in our sample belonging to the disk population. Assuming a common and constant luminosity of $L_{OH/IR} = 3\,500\,L_\odot$ for all them, as a first guess to their true luminosity, we found a clear correlation between $\lambda$ and galactic height, indicating that the fraction of high mass stars do increases with $\lambda$. In addition, we found a similar correlation between $v_{exp}$ and $\lambda$.

Based on of the results mentioned above we propose an evolutionary scenario in which all OH/IR stars would start their life as AGB stars in the bluer part of the 'O-rich AGB sequence', with a $v_{exp}$ probably proportional to their mass, and then evolve toward redder colours as their CSE increases its optical depth. Even relatively low-mass OH/IR stars ($\approx 1\,M_\odot$) would be able to create at least for a short time an optically thick CSE enough to prevent their detection in the optical range just at the very end of the AGB phase, appearing as considerable red sources in the IRAS two-colour diagram. However, only the most massive stars would reach the upper end of the 'O-rich AGB sequence' ($\lambda \gtrsim 3$).

We have divided the 'O-rich AGB sequence' in bins of $\lambda$ and determined the galactic scale height associated to stars within each of the resulting bins. Then we have classified all the OH/IR stars in our 'extended sample' in 5 main groups as a function of their galactic scale height, and we have established evolutionary connections between each of these groups and other samples taken from the literature, including all kind of AGB stars and PNe.

Our results suggest that the 'extremely blue subsample' ($\lambda < 0.6$; $H = 536$ pc) is dominated by OH/IR stars that can be identified as the result of the evolution of low mass ($\lesssim 1\,M_\odot$) optically bright short period ($\lesssim 300^d$) Miras. These OH/IR stars could be the progenitors of type III PNe.

The 'blue subsample' ($0.6 < \lambda \leq 1.2$; $H = 344$ pc) is mainly formed by OH/IR stars identified as the result of the evolution of intermediate period ($\approx 300^d$) Miras, with typical progenitor masses of $1.0 - 1.5\,M_\odot$. These OH/IR stars would be the progenitor of low mass type II PNe.

The 'transition subsample' ($1.2 < \lambda \leq 1.8$; $H = 287$ pc) of OH/IR stars is identified as the result of the evolution of intermediate period ($300 - 500^d$) Miras. We suggest a wide progenitor mass range between 1.5 and $2.5\,M_\odot$. These OH/IR stars must be the progenitors of high mass type II PNe.

The mean galactic scale height of the 'red subsample' ($1.8 < \lambda \leq 3.0$; $H = 193$ pc) of OH/IR stars is found to be consistent with stars with masses in the range $2.5 - 4.0\,M_\odot$. This is only slightly larger than the value taken from the literature for type I PNe. If type I PNe are the result of the evolution of HBB AGB stars, they should have progenitor masses $\gtrsim 3\,\mathrm{M}_{\odot}$ (i.e. within this 'red subsample').

Some of the stars in these three intermediate groups (blue, transition and red) may turn into C-rich AGB stars at some point during their evolution in the AGB as a consequence of the dredge-up of C-rich processed material to the surface after a few thermal pulses. Their progenitor masses would then cover a wide range between $1.0-3.0\,\mathrm{M}_{\odot}$, with an increasing number of 'infrared carbon stars' (with optically thick shells) as they approach the upper limit in mass expected for galactic carbon stars ($2.0-3.0\,\mathrm{M}_{\odot}$).

Finally, the 'extremely red subsample' ($3.0 < \lambda$; $\mathrm{H} = 48\,\mathrm{pc}$) of OH/IR stars is identified as the group containing the most massive OH/IR stars that would evolve all along the 'O-rich AGB sequence', and may be also during the whole PNe phase, as infrared sources with no optical counterpart. We identify this group of very massive AGB stars ($\gtrsim 4\,\mathrm{M}_{\odot}$) as the precursors of the so-called 'OHPNe', heavily obscured OH/IR stars with radiocontinuum emission that have been proposed to be 'infrared PNe'. They are fast evolving sources that will evolve toward the white dwarf stage without having shown themselves in the optical as PNe.

**Acknowledgements:**

Based on observations collected at the German-Spanish Astronomical Centre, Calar Alto, operated jointly by Max-Planck-Institut für Astronomie and Instituto de Astrofísica de Andalucía (CSIC). This work has been supported by the Deutsche Forschungsgemeinschaft through travel grants (En 176/24-1 and 25-1) and by the Spanish Ministerio de Ciencia y Tecnología through grant AYA2003−09499. Part of the data reduction was supported by a grant of the Deutscher Akademischer Auslandsdienst (DAAD) to FJE. This research has made use of the SIMBAD database, operated at CDS, Strasbourg, France. This publication makes also use of data products from the Two Micron All Sky Survey, which is a joint project of the University of Massachusetts and the Infrared Processing and Analysis Center/California Institute of Technology, funded by the National Aeronautics and Space Administration and the National Science Foundation.

# Chapter 5

# A near-infrared monitoring of a selected sample of OH/IR stars

## Abstract

We present in this chapter the results of a near-infrared monitoring campaign centred on a sample of 25 galactic sources selected from the IRAS Point Source Catalogue as candidate long-period variable stars in the late-AGB phase.

All IRAS fields were imaged in the JHK photometric bands in order to identify the near-infrared counterparts. Then the astrometric coordinates were derived using 2MASS data. Only in the case of IRAS 18092–2347 it was not possible to find any near-infrared counterpart.

JHK near-infrared photometry was then performed in several epochs using a combination of dedicated runs and service time at the 1.5 m Carlos Sánchez Telescope of the Observatorio del Teide, and at the 1.23 m telescope at Calar Alto Observatory, both in Spain, over a period of 10 years, starting in 1991.

As a result of these observations, we have been able to determine their mean JHK magnitudes, J−H, H−K colours and study the overall variability properties. Accurate periods ranging from $365^d$ to $1\,176^d$ have been determined for 8 sources in the sample, and tentative values are given for 5 additional sources.

The detailed analysis of some of the light curves derived shows that in many cases they are far from symmetric and show secular variations which are yet unexplained. The results obtained are discussed in the context of stellar evolution.

## 5.1 Introduction

Asymptotic Giant Branch (AGB) stars are low and intermediate mass stars ($0.8\,\mathrm{M}_\odot < \mathrm{M} < 8\,\mathrm{M}_\odot$) at the end of their evolution. During this phase they experience a heavy mass loss (up to $10^{-4} - 10^{-4}\,\mathrm{M}_\odot\mathrm{year}^{-1}$) which results in the formation of cool circumstellar envelopes (CSE) of gas and dust emiting very strongly at infrared wavelengths. If the mass loss rate surpasses $10^{-6}\,\mathrm{M}_\odot\mathrm{year}^{-1}$the CSE eventually becomes optically thick to visible light (Habing 1996). Stars st the end of the AGB appear as large amplitudes long period variables (LALPV) some of them heavily obscured in the optical. Many of these invisible stars at optical wavelengths were called 'OH/IR stars', because they were discovered by their strong OH maser emission (1612 MHz) and were only later identified in the infrared. These are expected to be O-rich AGB stars associated either with a massive progenitor star and/or at a well advanced evolutionary stage in the AGB. This phase suddenly finishes with the total ejection of the most external atmospheric layers. At that moment the variability stops and the effective temperature of the central star raises until the star turns into a Planetary Nebula.

With the advent of the IRAS satellite the number of OH/IR stars in our Galaxy increased up to ≈ 2 000, being easily discovered by their strong infrared radiation over the full sky. Other surveys were made at radio frequencies, in the 1612 MHz OH maser line. The largest surveys were those made using Arecibo (Eder et al. 1988; Lewis et al. 1990b), Nançay (Sivagnanam et al. 1990; David et al. 1993), and Parkes (te Lintel Hekkert et al. 1991) radiotelescopes.

Nowadays, the better known objects are the less massive ones, typically optically bright variable OH/IR stars, with periods shorter than $400^d$ and amplitudes lower than $1^m$ in the K band. These objects are not expected to develop an optically thick CSE capable of completely obscuring the central star at optical wavelengths (at least until the very end of their AGB lifetime). For this reason these objects can still be studied through optical photometry and spectroscopy in most cases.

The periods of 'genuine' OH/IR stars are considerably longer than those of optical Miras. Herman and Habing (1985b) found that the periods derived from the monitoring of the OH maser emission in a small sample of bright OH/IR stars ranged from 500 to $2\,000^d$. Observing in the infrared, Engels et al. (1983) also derived the periods of 17 objects monitored during 4 years, finding similar periods and very large amplitudes ($\approx 4^m$) in the K band. They represent in general an extension towards more extreme values of the characteristics observed in optical Mira variables. More recently, some authors (Nakashima et al. 2000; Blommaert et al. 1998; Wood et al. 1998; Wood 1998; Jones et al. 1994; Van Langevelde et al. 1993, 1990; Le Bertre 1988) provided new data for a few more OH/IR stars both in the near-infrared and in the OH maser emission as a result of several monitoring programs. However, the amount of data available at the present time is still clearly insufficient to properly analyse in detail the photometric properties of individual sources and to derived statistical conclusions on the overall variability properties of OH/IR stars.

In this chapter we present data from an IR monitoring program carried out over 10 years on a sample of galactic OH/IR stars in order to enlarge the small sample of OH/IR stars with known periods and light curves. In Section 5.2 we describe the selection of the sample; the observations and the data reduction are explained in Section 5.3; the main results (including photometry and light curves) are in Section 5.4 while in Section 5.5 the overall properties and some individual sources with peculiar light curves are analysed. Finally, the main conclusions are given in Section 5.6.

## 5.2 Sample selection

The sample we present in this chapter includes 25 possible OH/IR stars, selected from the IRAS Point Source Catalogue with a variety of infrared and OH maser luminosities, $\lambda$ parameter values and LRS types, as can be seen in Table 5.1. They all have been detected in OH at 1612 MHz (te Lintel Hekkert et al., 1989, 1991; te Lintel Hekkert, P., 1990; Zijlstra et al., 1989; David et al., 1993), with the exception of IRAS 18576+0341 that was never tried. IRAS 18576+0341 was selected because of its properties observed in the infrared: high IRAS variability index, near-infrared variability, presence of the silicate absorption feature in a red-continuum spectrum (Volk and Cohen 1989), and its peculiar position in the IRAS two-colour diagram in the region of the PPNe (Chapter 2). On the other hand, te Lintel Hekkert (1990) classified IRAS 02095−2355 and IRAS 23492+0846 as sources detected in OH, with fluxes near the detection limit, whereas in a later publication te Lintel Hekkert et al., 1991 considered them as 'non detected'.

The position of the sources included in our sample in the IRAS two-colour diagram is shown in Figure 5.1, together with those included in what we have called the 'extended OH/IR sample' (Chapter 4). In this Figure the solid line corresponds to the so-called 'O-rich AGB sequence'. They all are well detected sources in the IRAS photometric bands centred at 12, 25 and 60 $\mu$m. The objects of the sample are located at different positions along the 'O-rich AGB sequence', in most cases very close to it with the exception of two of them, IRAS 17347–3139 and IRAS 18576+0341, which are placed in the region of the IRAS two-colour diagram corresponding to sources with detached shells (like post-AGB stars or planetary nebulae). Our objetive was to monitor and characterize a wide variety of sources showing OH maser emission: a subsample of sources with optically thin CSE (small $\lambda$ values; see Section 4.3 for a definition of $\lambda$ parameter), another subsample with optically thick CSE (large $\lambda$ values) (Section 4.4), and, finally some sources suspected to be in a more evolved stage (those labeled in Figure 5.1) but still showing the

**Table 5.1**: IRAS sources included in the monitoring program.

| IRAS name | $\lambda$ | $F_{12}$(Jy) | [12] − [25] | [25] − [60] | Other names |
|---|---|---|---|---|---|
| 02095−2355 | 0.457 | 16.3 | −0.75 | −1.98 | IRC −20029, AFGL 4168 |
| 03293+6010 | 1.560 | 37.3 | 0.68 | −1.51 | OH 141.7+3.5, AFGL 5097 |
| 04130+3918 | 0.286 | 53.6 | −1.27 | −1.63 | AFGL 6312S, CGCS 645 |
| 05131+4530 | 1.691 | 27.8 | 0.61 | −1.29 | AFGL 712 |
| 06297+4045 | 0.960 | 103.0 | −0.09 | −1.65 | OH 174.7+13.5, IRC +40156, AFGL 955 |
| 07222−2005 | 0.386 | 24.9 | −0.74 | −2.58 | |
| 16029−3041 | 1.767 | 141.7 | 0.69 | −1.27 | OH 345.0+15.7, AFGL 1822 |
| 16037+4218 | 0.558 | 12.3 | −0.55 | −1.97 | |
| 16437−3140 | 1.652 | 11.0 | 0.61 | −1.32 | |
| 17103−0559 | 0.519 | 96.5 | −0.54 | −2.18 | |
| 17105−2804 | 0.523 | 15.8 | −0.61 | −1.97 | |
| 17313−1531 | 0.799 | 62.6 | −0.12 | −1.96 | OH 10.0+9.3 |
| 17347−3139 | 3.940 | 19.0 | 1.81 | 0.24 | PN RPZM 28 |
| 17411−3154 | 2.361 | 1262.0 | 0.83 | −0.75 | OH 357.3−1.3, AFGL 5379 |
| 18025−2113 | 0.991 | 177.6 | −0.17 | −1.50 | IRC −20427, AFGL 2062 |
| 18092−2347 | 3.078 | 11.0 | 0.93 | −0.15 | |
| 18299−1705 | 1.417 | 23.6 | 0.96 | −1.40 | |
| 18314−1131 | 0.633 | 147.5 | −0.53 | −1.74 | |
| 18327−0715 | 3.363 | 44.4 | 0.66 | 0.17 | OH 24.7−0.2 |
| 18429−1721 | 0.557 | 64.9 | −0.53 | −1.89 | V 3952 Sgr, IRC −20514, RAFGL 5288 |
| 18454−1226 | 0.439 | 18.0 | −0.69 | −2.28 | IRC −10463 |
| 18576+0341 | 3.280 | 58.5 | 2.15 | −0.47 | RAFGL 2298 |
| 19129+2803 | 0.557 | 15.4 | −0.52 | −2.03 | |
| 19147+5004 | 0.468 | 13.7 | −0.66 | −2.16 | TZ Cyg, IRC +50290 |
| 23492+0846 | 0.489 | 27.4 | −0.71 | −1.90 | RAFGL 3163 |

characteristic OH maser usually associated to stars in the AGB.

## 5.3 Observations and data reduction

Considering the characteristic long period variability associated to OH/IR stars a real ‘long-term’ monitoring program was started in 1991. The observations here presented were performed over a period of 10 years from 1991 March to 2001 July. During the first years we used mainly service time at the infrared 1.5 m Carlos Sánchez Telescope (CST) at the Observatorio del Teide (Tenerife, Spain). More recently we completed the monitoring program with punctual observations of the different objects, using either the CST or the 1.23 m telescope at Calar Alto observatory. Some of the objects presented in this work

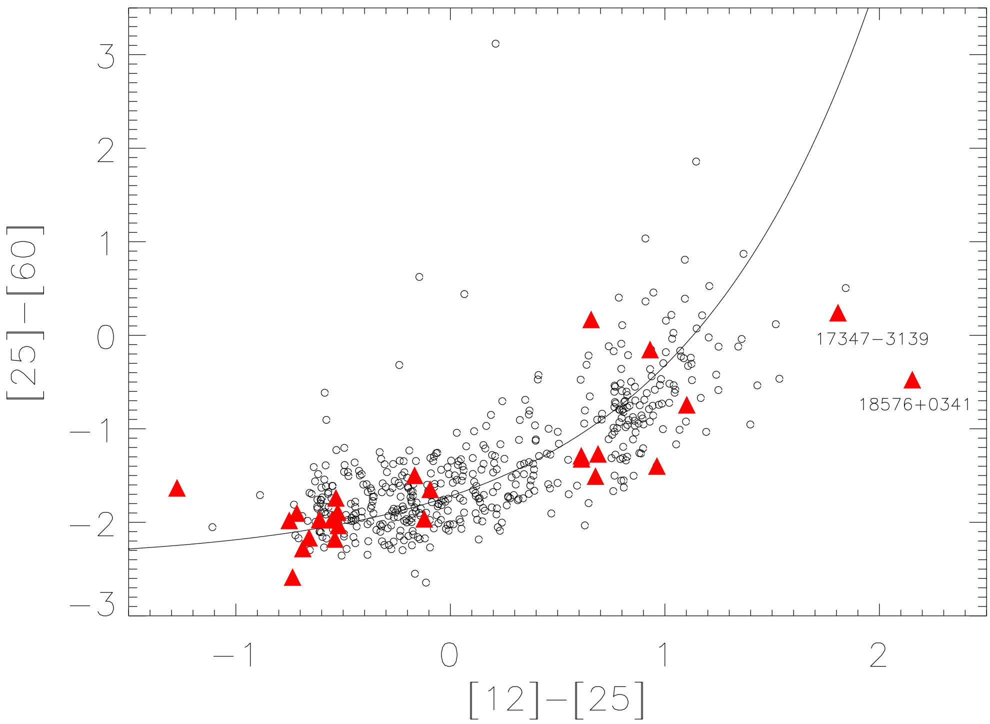

**Figure 5.1**: The position in the IRAS colour-colour diagram of the stars included in the monitoring program (filled triangles), together with those in the 'extended OH/IR sample' (open circles). The continuous line is the 'O-rich AGB sequence', and the IRAS colours are defined as: $[12]-[25] = -2.5\log\frac{F_\nu(12)}{F_\nu(25)}$ and $[25]-[60] = -2.5\log\frac{F_\nu(25)}{F_\nu(60)}$.

had never been observed before in the near-infrared, or only exceptionally in the K band. For these sources, we provide identification of the counterpart in the near-infrared and photometric data at this wavelength range for the first time.

### 5.3.1 Aperture photometry

As already mentioned, this monitoring program was carried out using mainly service time at the infrared 1.5 m CST operated by the Instituto de Astrofíca de Canarias, at the spanish Observatorio del Teide. We used a CVF infrared spectrometer equipped with an InSb photometric detector, operating at the temperature of liquid nitrogen with a photometric aperture of 15″ and a chopper throw of 30″ in right ascension to subtract the the contribution from the background sky, to derive the JHKL' photometry. For the photometric calibration we used the list of standard stars in Koornneef (1983a), observing at least two of these standard stars several times during the night at different air masses. The service observations were solicited imposing a minimum S/N ratio of 50 in the K band.

The Teide photometric system as well as its relations with other standard photometric systems are described in Arribas & Martínez Roger (1987).

### 5.3.2 Infrared images

With the initial aim of determining the accurate astrometry of the near-infrared counterparts found, we also took images in the J, H and K bands of all the stars in the sample in two dedicated observing runs, in 1996 October and 1997 June, using the same telescope (CST) equipped this time with the IR camera CAIN, which uses a NICMOS array of $256 \times 256$ pixels as detector. The pixel scale was $0.4''$, resulting in an image size of $1.7' \times 1.7'$.

In addition, in the final years of the monitoring program we also used in three different runs the 1.23 m telescope of Calar Alto Observatory (Almería, Spain) equipped with the IR camera MAGIC (Herbst et al. 1993) to obtain new photometric data. This camera uses a $256 \times 256$ NICMOS3 HgCdTe detector array with a pixel scale of $1.2''$ which provides an approximate field of $5' \times 5'$. Several standard stars of the list of Elias et al. (1982) were observed during each night of observation at different airmasses in order to calculate the atmospheric extinction.

The main difficulty to observe in the IR is the high sky background level and its fast temporal and spatial variation. For the accurate determination of the background we took at both telescopes for each object and every filter 5 images with the object centered at different positions in the frame (dithering or ‘moving sky’ technique). Thus, each measurement consist actually of a set of 5 individual images. Taking the median average of the 5 images we obtained a temporally and spatially well determined sky frame which is them subtracted from the object frame. Flat-field images were taken every night for each individual filter to correct for pixel-to-pixel sensitivity variations during the data reduction process.

In all cases data reduction was performed using standard routines within the IRAF[1] software package. First, all individual images were corrected with a detector mask in order to remove bad pixels from the frame. Then they were divided by the appropriate flat-field images and, subsequently, the sky was subtracted. The sky images were obtained by median averaging the five-image set associated to each measurement. Finally, the sky-subtracted images were then inspected for cosmic ray hits and cleaned appropriately by interpolating over the neighbouring pixels to yield the final near-infrared science images.

---

[1] IRAF is distributed by the National Optical Astronomy Observatories, which are operated by the Association of Universities for Research in Astronomy, Inc., under cooperative agreement with the National Science Foundation.

## 5.4 Results

### 5.4.1 Identification of the near-infrared counterparts

In order to determine the near-infrared counterpart for each of the sources in the sample we first compared our near-infrared images with the optical ones extracted from the Second Digitized Sky Survey (DSS2) (Djorgovski et al. 2001) in the red filter, which covers the spectral range 6 000 – 7 000 Å with the maximum efficiency around 6 700 Å. Finding the right counterpart is not a simple task, for the extremely crowded fields close to the Galactic Centre and especially for sources showing a very faint near-infrared counterpart as we will show later with some examples.

To avoid this problem it was necessary to use other stars in the field as reference stars to identify first that the telescope pointing was correct, and later look for the precise counterpart of the IRAS source in a small area (usually $30'' \times 30''$), centred at the nominal IRAS position. Usually only one source showing typical AGB colours was found close to the expected coordinates (usually the target source was actually the reddest in the field) but sometimes more than one candidate counterpart was found with similar colours and the only way to determine which was the right one was by inspecting images corresponding to the same field observed in a different epoch and search for variability, since most OH/IR stars are expected to be strongly variable in the near-infrared.

Sometimes the near-infrared counterpart found was so bright that the integration times were too short (if we wanted to avoid saturation) that it was not possible to detect any reference star in the field with high enough S/N ratio. In these cases (20%) we have assumed that our source is just the brightest one.

In most cases (84%), the counterpart was found to be the brightest source in the K-band near the IRAS position, and then it was easily recognizable. However, four sources (IRAS 17347–3139, IRAS 17411–3154, IRAS 18092–2347 and IRAS 18327–0715) did not show any clear near-infrared counterpart, with the adecuate colours, among several candidates, usually all them very faint.

With the recent publication of the MSX Point Source Catalogue (MSX6C) (Egan et al. 2003) we had the possibility to improve the astrometric information associated to many of the sources in the sample. Searching for the MSX6C counterparts of the 12 objects of the sample which were contained in the area of the sky surveyed by MSX ($|b| < 6^o$), we found that all but one had an MSX counterpart in the MSX6C. This object (IRAS 03293+6010), although it was observed with MSX and showed a bright counterpart in the MSX image (at least in A band), does not appear in the MSX6C. The MSX6C names are tabulated in Table 5.2. In Chapter 2 we determined the near-infrared and MSX counterparts for a group of 249 OH/IR stars detected by IRAS and found that 99% of the near-infrared counterparts were located within $10''$ from the MSX coordinates. We

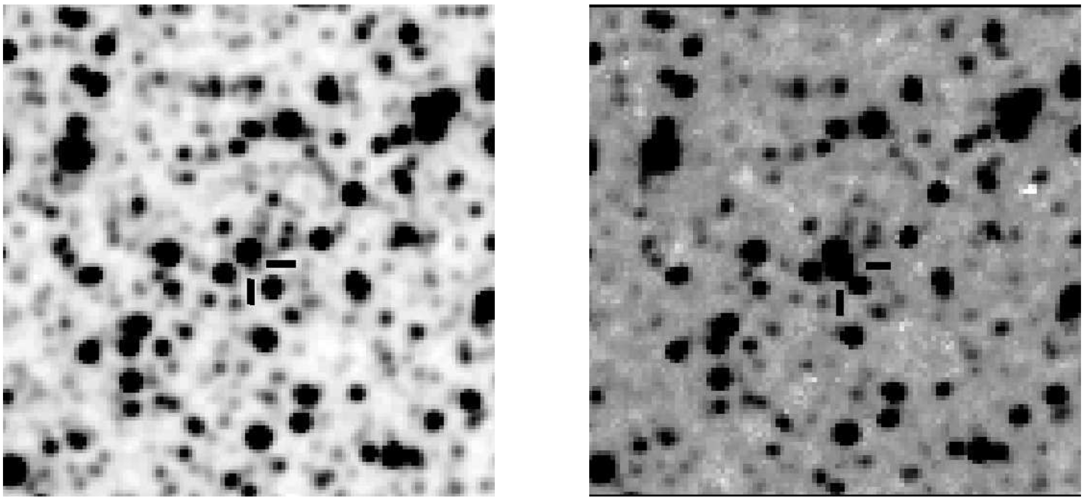

**Figure 5.2**: K-band images of IRAS 17411–3154 in two different epochs: 1998 (2MASS) in the left panel and 2001 (MAGIC) in the right panel.

reduced, therefore, the search area to a radius of 10″ around the MSX position for the 4 unidentified objects in the near-infrared above mentioned. This allowed us to identify the near-infrared counterpart of two additional sources, IRAS 17347–3139 and IRAS 18327–0715, but for IRAS 18092–2347 and IRAS 17411–3154 there were still more than one candidate source even within this smaller area. At a later stage, we were able to identify also the right counterpart of one of these two remaining sources by searching for variability between two different observing epochs. IRAS 17411–3154 was observed in the framework of the 2-Micron All-Sky Survey (2MASS) in August of 1998, and by us with the MAGIC camera in May of 2001. In Figure 5.2 we show the K-band images corresponding to both epochs. The object marked as the right counterpart was clearly visible in the image taken in 2001, while it was only barely visible close to a brighter nearby source in the left image, taken in 1998. This object was of course identified as the right near-infrared counterpart of the IRAS source. For the remaining source (IRAS 18092–2347), despite the fact that we had NIR images available from three different epochs, June 1999 and May 2001 taken with the MAGIC camera and May 1998 obtained from 2MASS, we did not find any variable source around the MSX position. Considering that this source is among the reddest ones in the sample (with $\lambda > 3$) we believe that it is so heavily obscured that the near-infrared counterpart is below our detection limit.

We have also used the 2MASS Point Source Catalog (2MASS-PSC) to improve the accuracy of the astronomical coordinates of all the sources in the sample for which a near-infrared counterpart was found (actually all but IRAS 18092–2347). 2MASS provides an astrometric accuracy of $\approx 0.2''$. In the case of IRAS 17411–3154, for which the very faint counterpart shown in the left panel of Figure 5.2 is not in the 2MASS-PSC, we used a group of three field stars visible in both 2MASS and MAGIC near-infrared images to improve its astronomical coordinates. Using the relative distances between our source and these reference stars in the MAGIC images, we have derived the astrometric position of this source in the 2MASS image with an accuracy of $\approx 0.1$ pixels which, from the pixel scale of the 2MASS images, is equivalent to an accuracy of $\approx 0.2''$, both in RA and DEC.

The complete list of improved astrometric positions is shown in Table 5.2. Columns 2 and 3 give the 2MASS coordinates (RA and DEC, respectively). For IRAS 18092–2347, the only star without a near-infrared counterpart in the sample, we give the MSX coordinates, as they are for the moment the most accurate ones. In this table we also give in Columns 4 and 5 the differences in RA and DEC with respect to the original IRAS coordinates quoted in the PSC for each source. In columns 6 and 7 we have tabulated the differences in RA and DEC between the MSX position and the original IRAS coordinates for each source in the sample with an MSX counterpart, but IRAS 18092–2347. The relative differences between 2MASS coordinates and both IRAS and MSX ones are in good agreement with the results already shown in Chapter 2 and 3 for a similar comparison.

The selected counterparts are displayed in Figure D.1 as an atlas of finding charts. For each source we have put together 3 frames containing the near-infrared images in the J, H and K bands taken from 2MASS. The size of the field showed in each filter is $2' \times 2'$. In those cases where our source was not the brightest in the K-band frame, or it was considerably shifted from the center of the field, we have marked the position of the selected near-infrared counterpart in each frame. For IRAS 18092–2347 we have marked the MSX position.

### 5.4.2 Near infrared photometry

The near-infrared JHKL' photometric data together with their associated errors for all the sources for which a near-infrared counterpart was found are listed in Table E.1 with the only exception of IRAS 17411–3154. This Table contains a total of 999 new measurements, collected during 119 observing nights. The typical accuracy is in the range $0.01-0.1^m$ in the majority of cases. As most of the observations were made using the 1.5 m CST telescope at the Observatorio del Teide, those made using the 1.23 m telescope at Calar Alto Observatory equipped with the MAGIC camera are indicated in the table.

For the observations not taken with the CVF we had to use the SEXtractor Software package (Bertin and Arnouts 1996) in combination with IDL routines to perform aperture photometry on the selected near-infrared counterpart following the method already described in Chapter 2. The associated errors in this case are typically $\approx 0.03^m$ for ‘well-detected’ sources in the three filters considered.

In case we had more than one epoch of observations with the MAGIC camera for a given source available, and if the IRAS source was at least observed once under

**Table 5.2**: Astrometric data for the sources included in the ‘ monitoring sample’

| | 2MASS | | 2MASS–IRAS | | MSX–IRAS | | |
|---|---|---|---|---|---|---|---|
| IRAS | Coordinates | | $\Delta\alpha$ | $\Delta\delta$ | $\Delta\alpha$ | $\Delta\delta$ | MSX6C_G |
| | (J2000) | | [″] | [″] | [″] | [″] | |
| 02095−2355 | 02 11 48.02 | −23 41 43.8 | −7 | −4 | | | |
| 03293+6010 | 03 33 30.59 | +60 20 09.4 | 0 | 0 | | | |
| 04130+3918 | 04 16 24.21 | +39 25 45.1 | −4 | 1 | | | |
| 05131+4530 | 05 16 47.47 | +45 34 04.1 | 4 | 0 | 9 | 0 | 162.9514+04.3336 |
| 06297+4045 | 06 33 15.79 | +40 42 51.4 | 10 | 2 | | | |
| 07222−2005 | 07 24 24.43 | −20 11 56.0 | 2 | −1 | 1 | −2 | 234.5808−02.1602 |
| 16029−3041 | 16 06 08.36 | −30 49 34.0 | 1 | 0 | | | |
| 16037+4218 | 16 05 28.91 | +42 10 29.4 | 6 | −1 | | | |
| 16437−3140 | 16 46 58.83 | −31 46 13.0 | −1 | 1 | | | |
| 17103−0559 | 17 12 58.13 | −06 02 57.1 | −16 | 2 | | | |
| 17105−2804 | 17 13 42.01 | −28 07 49.9 | 6 | 0 | | | |
| 17313−1531 | 17 34 11.30 | −15 33 01.5 | 7 | 0 | | | |
| 17347−3139 | 17 38 00.61 | −31 40 55.2 | −8 | 3 | −10 | 2 | 356.8001−00.0547 |
| 17411−3154* | 17 44 23.89 | −31 55 39.5 | 15 | 0 | 17 | −1 | 357.3103−01.3368 |
| 18025−2113 | 18 05 35.50 | −21 13 42.3 | −1 | −3 | 1 | −2 | 008.9338−00.0150 |
| 18092−2347** | 18 12 20.79 | −23 46 58.4 | 18 | 3 | 18 | 3 | 007.4526−02.6160 |
| 18299−1705 | 18 32 50.75 | −17 02 48.5 | 4 | 0 | 4 | 1 | 015.6623−03.7102 |
| 18314−1131 | 18 34 16.40 | −11 29 29.2 | 18 | 4 | 17 | 4 | 020.7618−01.4660 |
| 18327−0715 | 18 35 29.22 | −07 13 11.0 | −11 | −1 | −12 | −1 | 024.6919+00.2345 |
| 18429−1721 | 18 45 51.33 | −17 17 59.4 | −0 | 2 | | | |
| 18454−1226 | 18 48 17.53 | −12 22 43.2 | 7 | 0 | 8 | −2 | 021.5331−04.9234 |
| 18576+0341 | 19 00 10.89 | +03 45 47.1 | −4 | 1 | −4 | 2 | 037.2776−00.2260 |
| 19129+2803 | 19 14 59.10 | +28 09 14.1 | −8 | −1 | | | |
| 19147+5004 | 19 16 04.03 | +50 09 36.6 | 4 | 5 | | | |
| 23492+0846 | 23 51 47.89 | +09 03 23.4 | 1 | 1 | | | |

*Notes:* * Coordinates derived from our near-infrared MAGIC images. ** Coordinates taken from the MSX6C Point Source Catalogue photometric weather conditions, we performed differential photometry using field stars when the observations were made under non-photometric conditions. Measurements made under non-photometric conditions are marked in Table E.1 with an asterisk.

At the beginning of the monitoring program in 1991 no near-infrared images of the regions of the sky where our objects are located were available. Thus, we assumed by default that our objects were the brightest sources in the field in the near-infrared, at least in the K-band. That resulted to be true for most of the sources in the sample (see Appendix D). But in some cases this assumption turned out to be totally wrong, and only after we had the possibility to obtain near-infrared images of the IRAS fields we could identify them. Even in the more complicated cases, only after we had the possibility to get better coordinates from the MSX satellite or or near-infrared images from 2MASS, we were able to identify the right counterparts, as we have just shown. Thus, for a few cases, we have reliable photometric data only from the MAGIC images. In the case of IRAS 16437–3140, for instance, we found that this source was strongly blended with another one having similar brightness in the J-band, but which is fainter in the H and K bands. Thus, the photometry in the J filter for this source has been removed from Table E.1, because it is highly unreliable.

All our observational data for the K-band is shown in Appendix F for all objects for which we have measurements made at more than two different epochs. The data obtained using the CST equipped with the CVF photometer have been plotted together with the data obtained using the 1.23 m telescope equipped with the MAGIC camera using different symbols. Whenever a light curve has been fitted to the observational data this is also plotted. The different kind of light curves and the process followed to obtain them is explained in the next subsection.

In the Table 5.3 we present for each source in the sample the mean near-infrared properties derived from the full set of photometric data available, together with the number of measurements (N) used in the calculations. In Column 2 we list the estimated K mean magnitude calculated from the average of all the observed values. In Columns 3, 4 and 5 the mean near-infrared colours J − K, H − K and K − L' are also listed, respectively. We have used K as the reference wavelength in all our subsequent calculations and plots because it is the best monitored band where the sources are usually brighter. Figure 5.3 shows the evolution of the H–K color as a function of the Julian date for IRAS 05131+4530. The variation of the near-infrared colour with the variability phase is clearly evident from this figure. Thus, colours have been also averaged in Table 5.3. Similar variations of the near-infrared colour with the pulsation phase in OH/IR stars were previously reported by Harvey et al. (1974) and Engels (1983). The near-infrared colours tend to be bluer at maximum brightness and redder at the minimun of a pulsation cycle, and the amplitude of these variations in colour are larger for those sources with the larger variability amplitudes.

**Table 5.3**: Mean photometric properties of the sources in the 'monitoring sample'.

| IRAS name | Near-IR Colours [Mag]<br>K (N) | J–K (N) | H–K (N) | K–L' (N) |
|---|---|---|---|---|
| 02095-2355 | 2.1 (19) | 1.2 (19) | 0.3 (19) | 0.2 ( 7) |
| 03293+6010 | 7.4 (12) | 6.0 ( 9) | 2.8 (11) | 4.0 ( 2) |
| 04130+3918 | 3.4 (19) | 3.7 (19) | 1.6 (19) | 2.0 ( 6) |
| 05131+4530 | 6.8 (27) | 6.2 (21) | 2.7 (27) | 3.6 ( 2) |
| 06297+4045 | 2.9 (25) | 3.0 (25) | 1.3 (25) | 1.5 ( 6) |
| 07222-2005 | 4.6 (17) | 2.0 (17) | 0.8 (17) | 1.1 ( 5) |
| 16029-3041 | 6.9 (14) | 6.8 ( 8) | 3.7 (10) | 5.5 ( 1) |
| 16037+4218 | 3.6 (37) | 1.3 (36) | 0.5 (36) | 0.8 ( 7) |
| 16437-3140 | 8.5 ( 8) | ——— | 3.3 ( 8) | 4.1 ( 1) |
| 17103-0559 | 3.5 (20) | 2.4 (20) | 1.0 (20) | 1.5 ( 2) |
| 17105-2804 | 4.8 (12) | 1.8 (12) | 0.8 (12) | ——— |
| 17313-1531 | 4.9 (11) | 3.6 (10) | 1.7 (10) | ——— |
| 17347-3139 | 10.1 ( 1) | ——— | ——— | ——— |
| 18025-2113 | 2.6 (14) | 1.8 (13) | 0.8 (13) | ——— |
| 18299-1705 | 5.2 ( 8) | 2.9 ( 7) | 1.3 ( 7) | ——— |
| 18314-1131 | 3.5 (10) | 2.8 ( 9) | 1.1 ( 9) | 1.7 ( 1) |
| 18327-0715 | 8.5 ( 2) | ——— | ——— | ——— |
| 18429-1721 | 3.2 ( 7) | 1.7 ( 7) | 0.7 ( 7) | 1.3 ( 1) |
| 18454-1226 | 2.0 ( 8) | 1.4 ( 8) | 0.4 ( 8) | 0.4 ( 2) |
| 18576+0341 | 6.9 (14) | 5.3 ( 9) | 1.9 (12) | ——— |
| 19129+2803 | 5.1 (23) | 2.1 (23) | 0.9 (23) | 1.1 ( 2) |
| 19147+5004 | 2.5 (19) | 1.2 (19) | 0.3 (19) | 0.3 ( 9) |
| 23492+0846 | 1.4 ( 6) | 1.3 ( 6) | 0.4 ( 6) | 0.3 ( 2) |

### 5.4.3 Light curves

In order to characterize the variability properties of all the sources in the 'monitoring sample' for which enough observational data are available, we have tried to fit light curves of several types to the photometric data. As a first approximation, we have adopted a sinusoidal light curve (Type 1):

$$m(t_i) \,=\, \overline{m} \,+\, A\,sin(2\,\pi\,(\tfrac{t_i}{P} + \varphi))$$

where $m(t_i)$ is the observational magnitude at the epoch $t_i$, $\overline{m}$ the mean magnitude, $A$ the amplitude of the oscillation, $t_i$ the Julian date, $P$ the period of the light curve, and $\varphi$ the initial phase. We have fitted the observational data to sinusoidal light curves using the Least Mean Square (LMS) method, for a range of periods that go from

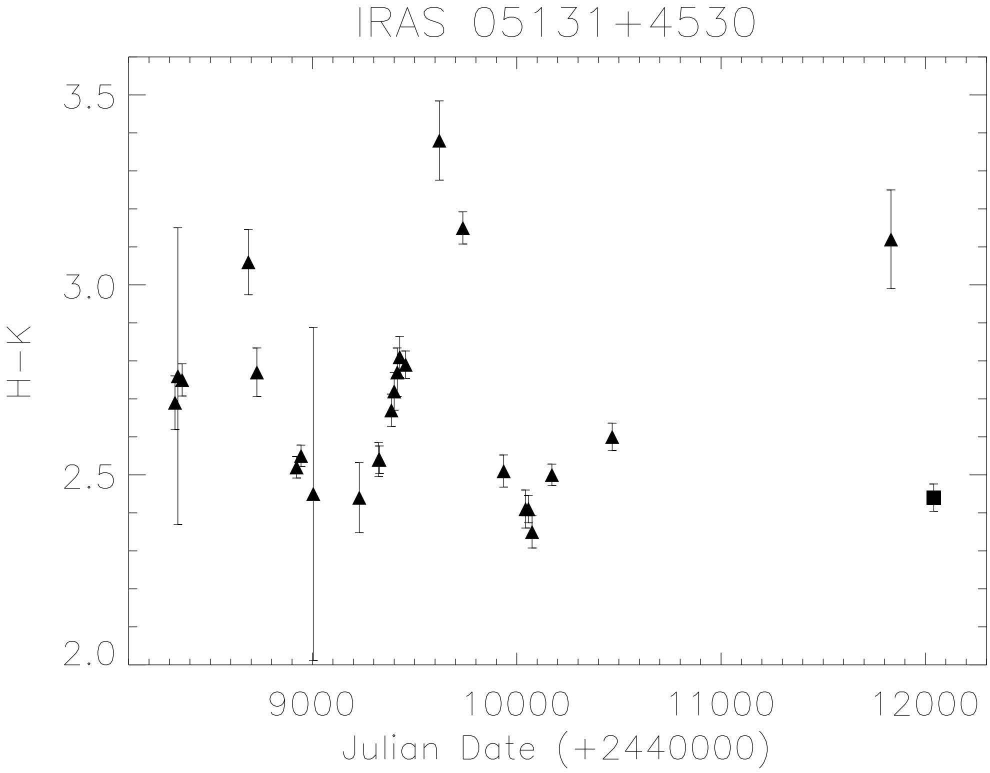

**Figure 5.3**: Variation of the H–K near-infrared colour with the Julian date for IRAS 05131+4530.

$200^d$ to $3\,000^d$. The goodness of the fit has been studied with the $\chi^2$ test, weighting each observational data with the square of the observational error. In a plot of $\chi^2$ versus P it is easy to find the period which best fits the data (van Langevelde et al. 1993). It also allows to identify those cases where there is more than one period that could fit the data reasonably well. As an example, Figure 5.4 shows the behaviour of $\chi^2$ in two cases: a well determined period (IRAS 04130+3918) and a failed determination (IRAS 18454–1226). When the primary minimum of $\chi^2$ is twice or more deeper than the secondary minimum, the period associated to the primary minimum is considered to be reliable.

Usually, the periods were better derived using K band data, but estimates made using data obtained at J and H bands always confirmed the K band periods, when they were well determined, confirming that periods are independent on the wavelength considered (Le Bertre 1993; Hjalmarson & Olofsson 1979; Alcolea et al. 1999).

Because: i) our objects are only visible during half of the year; ii) sometimes the observations were not possible because of bad weather or technical problems; iii) the monitoring program was depending on the irregular schedule of the service time at the Teide Observatory, our photometric points are not regularly spaced in time. For this

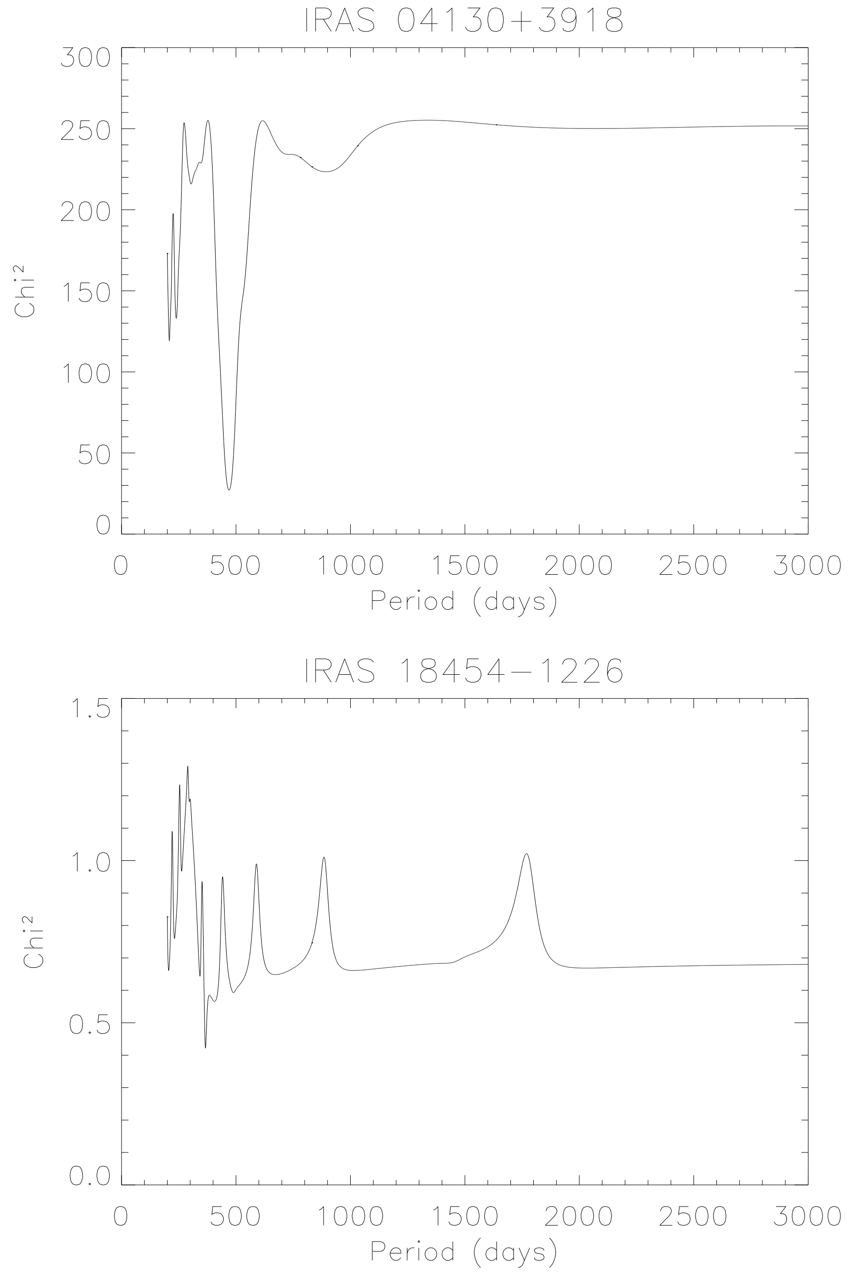

**Figure 5.4**: The upper figure shows an example of a well determined period using the $\chi^2$ test method for IRAS 04130+3918 and the lower figure the impossibility to predict any period for IRAS 18454−1226 using the same method.

reason we have verified the validity of our results by comparing the results obtained with the LMS method with the results obtained using the Period Dispersion Minimization (PDM) method (Stellingwerf 1978). The PDM method does not assume any shape for the light curve and is well suited to the case in which the time variation of a physical magnitude is covered by only a few irregularly spaced observations. We have checked all objects with more than 10 observational points available in our sample, finding that both methods agree in all cases within the errors. So, we can conclude that the results obtained assuming a sinusoidal light curve are reliable at least as a first approximation, although, in some cases, the assumption of a symmetric sinusoidal variation and a constant mean magnitude is clearly not adequate as we will see later. As both LMS and PDM provide the same solutions for the period estimates, we have considered the width FWHM of the parabola that draw the line profile near the minimum in the PDM method as a good estimation of the uncertainty ΔP in our period determination. This ΔP is given approximately by

$$\Delta \mathrm{P} \simeq \frac{P^2}{2T}$$

where P is the trial period at the primary minimum, and T is the time baseline of the observations (Nakashima et al. 2000; and references therein).

A deeper analysis of the best sinusoidal light curves fitted to the observational data clearly indicates that in some cases, the assumption of a symmetric sinusoidal and constant mean magnitude behaviour is clearly not the best choice. Some objects, like IRAS 17103−0559 (See Appendix F), show large secular variations in the mean brightness at all near infrared filters. And this is not the only case in the sample. Thus, as a second approximation for the light curve fitting we have tried a sinusoidal curve with mean magnitude linearly variable in time (Type 2):

$$m(t_i) \,=\, A\, sin(2\,\pi\,(\tfrac{t_i}{P} + \varphi)) \,+\, \dot{m}\, t_i \,+\, m_o$$

where $\dot{m}$ is the slope of the mean magnitude, and $m_o$ is the mean magnitude for the Julian Date 2 440 000. We have used this light curve to fit all objects, and we have assigned this type of light curve to a source in the sample only when the new choice increased strongly the quality of the fitting, with a value of $\chi^2$ at least 30% smaller than the one derived from the fitting of a Type 1 light curve.

A third kind of light curve has also been used, this time assuming a constant mean magnitude but with an asymmetric sine (Type 3) (van Langevelde et al. 1993). This light curve follows the equation:

$$m(t_i) \,=\, \overline{m} \,+\, A\, cos(2\,\pi\,\phi(t_i))$$

where:

$$\phi(t_i) = \begin{cases} \frac{\omega}{2f} & \text{when } 0 \leq \omega < \text{f, decrease} \\ \frac{\omega-1}{2\,(1-f)} + 1 & \text{when f} \leq \omega < 1\text{, increase} \end{cases}$$

being ($\omega$) the phase:

$$\omega = \frac{t_i - \varphi}{P}$$

and f is an asymmetric factor which can get values from 0 to 1, 0.5 corresponding to a symmetric curve. A good example is IRAS 05131+4530 (See Figure F.1). As we did for Type 2 light curves, we tried to fit this type of curve to all the sources in the sample, and this Type 3 light curve was only assigned to a given source in the sample if the value of $\chi^2$ was found to be at least 30% smaller than for a Type 1 light curve with the new choice.

In Table 5.4 we show the results derived from this fitting exercise. For each source in the sample we have selected the best fit possible and the sources have been classified according to the type of light curve that best fits the observational data. In the second column we show the number of observational data that have been used to fit the light curve; in the third column the estimated period with its error; the fourth column shows the amplitude calculated from the fitted light curve as the difference between the maximum and minimum brightness; in the fifth column we show the mean magnitude ($\overline{K}$) for Type 1 and 3 light curves, or the slope of the mean magnitude ($\dot{K}$) in case of a light curve of Type 2; in the following column we show the mean magnitude ($K_o$) for the Julian Date 2 440 000 for Type 2 light curves, or the asymmetric factor for Type 3 light curves; and in the last column we show the Julian Date of the first maximum of luminosity after the beginning of the monitoring program.

Appendix G shows the variation of the K magnitude against the pulsation phase for each target once a specific kind of curve has been assumed.

## 5.5 Discussion

For 3 objects in the sample we do not have any data to perform any photometric analysis: IRAS 18092–2347, the source without a near-infrared counterpart; IRAS 17411–3154, with a very faint near-infrared counterpart not always visible in a crowded field and, thus, without reliable photometric data; and IRAS 17347–3139, with a faint near-infrared counterpart and just one photometric measurement from MAGIC (see Appendix D).

For the remaining objects, with the exception of IRAS 16437–3140, because of the contaminated photometry in the J-band above mentioned, and IRAS 18327–0715, with only two measurements in the K-band, we have plotted in Figure 5.5 the mean near-infrared colours derived from Table 5.3. Together with the colours of our sources and their errors, we have also plotted the near-infrared colours of the sources in the ‘extended

**Table 5.4**: Periods and light curve types derived for each object in the ‘monitoring sample (from K-band data).

Type 1 light curves

| IRAS name | N | Period (day) | Amplitude (mag) | $\overline{K}$ (mag) | | JD Maximum (+2 440 000) |
|---|---|---|---|---|---|---|
| 03293+6010 | 12 | 1776 ± 454 | 1.09 ± 0.14 | 7.420 ± 0.009 | | 9190 ± 212 |
| 04130+3918 | 19 | 470 ± 32 | 0.93 ± 0.02 | 3.554 ± 0.005 | | 8525 ± 11 |
| 17105−2804* | 12 | 415 ± 28 | 1.08 ± 0.02 | 4.712 ± 0.006 | | 8631 ± 20 |

Type 2 light curves

| IRAS name | N | Period (day) | Amplitude (mag) | $\dot{K}$ ($\mathrm{mag\,yr^{-1}}$) | $K_o$ (mag) | JD Maximum (+2 440 000) |
|---|---|---|---|---|---|---|
| 06297+4045 | 25 | 536 ± 39 | 1.22 ± 0.01 | $(-45 \pm 1)\cdot 10^{-3}$ | 3.149 ± 0.006 | 8402 ± 8 |
| 07222−2005 | 17 | 1245 ± 221 | 1.11 ± 0.02 | $(53 \pm 3)\cdot 10^{-3}$ | 4.562 ± 0.008 | 8377 ± 15 |
| 16037+4218 | 37 | 365 ± 18 | 0.73 ± 0.01 | $(522 \pm 8)\cdot 10^{-4}$ | 3.563 ± 0.004 | 8363 ± 4 |
| 16437−3140* | 8 | 2215 ± 665 | 3.48 ± 0.02 | $(239 \pm 3)\cdot 10^{-3}$ | 7.21 ± 0.02 | 9551 ± 360 |
| 17103−0559* | 21 | 425 ± 34 | 1.15 ± 0.01 | $(253 \pm 2)\cdot 10^{-3}$ | 2.980 ± 0.006 | 8497 ± 14 |
| 17313−1531 | 11 | 487 ± 39 | 1.39 ± 0.03 | $(92 \pm 2)\cdot 10^{-3}$ | 4.244 ± 0.007 | 8697 ± 30 |
| 18429−1721* | 8 | 1508 ± 527 | 1.29 ± 0.02 | $(41 \pm 3)\cdot 10^{-3}$ | 2.13 ± 0.01 | 10879 ± 449 |

Type 3 light curves

| IRAS name | N | Period (day) | Amplitude (mag) | $\overline{K}$ (mag) | f | JD Maximum (+2 440 000) |
|---|---|---|---|---|---|---|
| 05131+4530 | 27 | 1058 ± 151 | 2.49 ± 0.02 | 6.730 ± 0.005 | 0.65 | 9004 ± 96 |
| 18299−1705* | 8 | 1303 ± 336 | 0.44 ± 0.02 | 5.124 ± 0.006 | 0.29 | 9346 ± 30 |
| 19129+2803 | 23 | 423 ± 25 | 1.14 ± 0.01 | 5.194 ± 0.004 | 0.33 | 8884 ± 23 |

*Notes:* Type 1: symmetric light curve with constant mean magnitude. Type 2: symmetric light curve with linear variation of the mean magnitude. Type 3: asymmetric light curve with constant mean magnitude. *: tentative fit.

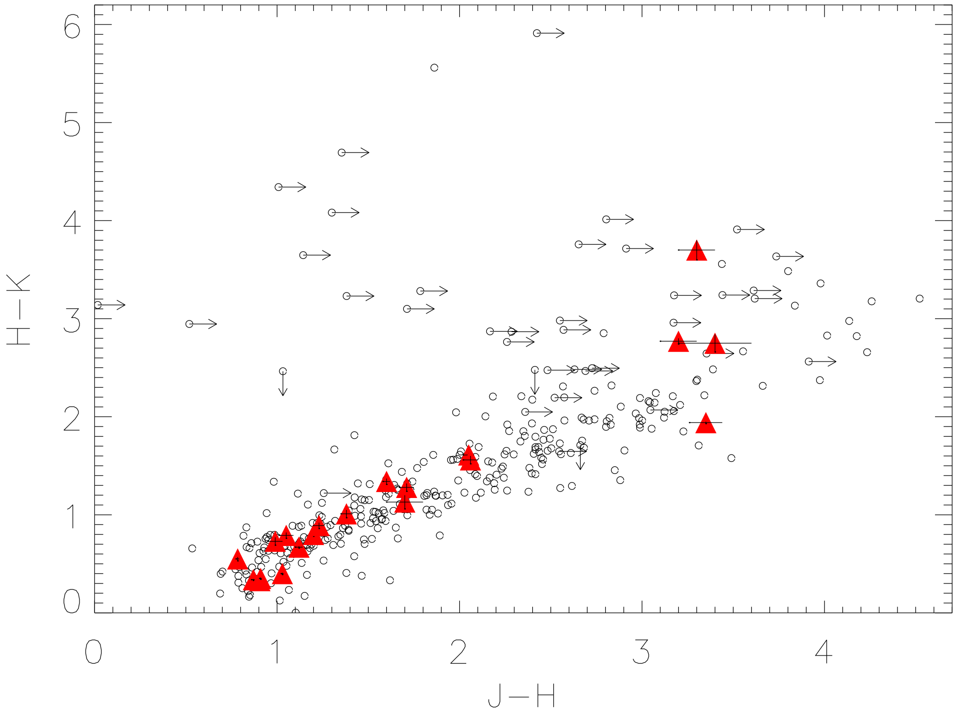

**Figure 5.5**: Near-infrared colour-colour diagram with the J–H vs. H–K colours of the sources in the 'monitoring sample' (red filled triangles) with their associated errors (bars) for which photometric measurements in all bands are available. For comparison, we also show the colours of the OH/IR stars included in the 'extended OH/IR sample' (open circles) (see Chapters 2 and 3)

OH/IR sample' analysed in Chapters 2 to 4. The near-infrared colours of the sources in our sample match perfectly with the colours derived for the OH/IR stars sources in our 'extended OH/IR sample'.

OH/IR stars are expected to be variable stars with periods typically longer than $300^d$ and amplitudes $\Delta K \gtrsim 0.7^m$. These properties are expected to be even more extreme in some OH/IR stars if they are either more massive or in a more evolved stage. Keeping this in mind we have analyzed the infrared properties of our objects, in order to determine whether their behaviour was the expected for OH/IR stars. Despite of our sources having all them near-infrared colours of OH/IR stars, we have found that our sample is contaminated by several kind of objects which are not OH/IR stars. The objects without a typical behaviour of OH/IR stars are listed in Table 5.5, together with the amplitude shown in the K-band and their possible classification.

Sources in the sample were classified as non-variable if the difference between

**Table 5.5**: IRAS objects without the typical variability properties of an OH/IR star.

| IRAS name | Number of obs. | Amplitude (Mag) | Classification |
|---|---|---|---|
| 02095−2355 | 19 | 0.16 ± 0.03 | M-type SG? |
| 18025−2113 | 14 | 0.60 ± 0.20 | M-type SG? / Semi-regular variable? |
| 18454−1226 | 8 | 0.08 ± 0.07 | M-type SG |
| 18576+0341 | 14 | 1.06 ± 0.02 | LBV |
| 19147+5004 | 19 | 0.43 ± 0.10 | M-type SG? / Semi-regular variable? |
| 23492+0846 | 6 | 0.05 ± 0.04 | M-type SG |

the maximum and the minimum magnitude at K-band was lower than $0.1^m$. Thus 2 sources (IRAS 18454–1226 and IRAS 23492+0846) were found to be not variable at all with photometric amplitudes of the order of the photometric errors. These two objects have both very bright near-infrared counterparts (see Appendix D), they are both placed in the blue extreme of the near-infrared colour diagram, which implies a thin CSE, confirmed by their bright optical counterpart in the DSS2 (Djorgovski et al. 2001), and have M spectral type. More probably both sources are bright galactic M-type Supergiants (SG). In the case of IRAS 23492+0846, the tentative OH detection reported by te Lintel Hekkert 1990, showing a extremely high expansion velocity of $25\,\mathrm{km\,s^{-1}}$, would confirm the SG nature of this star.

Other objects showing amplitudes larger than $0.1^m$ but still lower than $0.7^m$ as it should be expected for normal OH/IR stars, and for which we were not able to find any regular periodicity are also listed in Table 5.5. One of these objects (IRAS 02095–2355) is one of the tentative OH detections reported by te Lintel Hekkert. This object shows a non-regular variability with very low amplitude ($\Delta\mathrm{K} \approx 0.16^m$; see Figure F.1), and is also placed in the bluest part of the near-infrared colour-colour diagram; again it has both a very bright near-infrared and optical counterpart, and M-spectral type. Two other sources, IRAS 18025–1213 and IRAS 19147+5004, share the same near-infrared and optical characteristics than the previous one, although this time with considerably larger amplitudes ($\Delta\mathrm{K} \approx 0.6^m$ and $\Delta\mathrm{K} \approx 0.43^m$, respectively). We suggest that these two sources must be either M-type supergiants or semiregular variables, and as such are listed in Table 5.5.

IRAS 18576+0341 has been included in Table 5.5 despite it has amplitude $\Delta\mathrm{K} \approx 1.06^m$ typical of an OH/IR star, but we were not able to fit any period for it, and forthermore it has been classified as a *Luminous Blue Variable* (LBV) with extensive dust emission by several authors (Clark et al., 2003; and references therein). This source shows redder near-infrared colours, signature of a thick CSE.

For IRAS 18327–0715 we were only able to check that this is a variable source with amplitude $\Delta\mathrm{K} \gtrsim 0.79^m$, and then probably a true OH/IR star.

No period determination was possible for 2 sources, despite there were observations in more than 10 different epochs: IRAS 16029–3041 and IRAS 18314–1131. IRAS 16029–3041 shows a strong variability with one of the largest amplitude ($\Delta\mathrm{K} \approx 2.75^m$) of our sample. This object currently shows the reddest near-infrared colours of our sample, but these have been changing during the 10 years of monitoring. In Figure 5.6 we show its H–K infrared colours versus Julian Date. It is clear that the H–K colour has increased by $\approx 1^m$ in the last 10 years. This object has a very thick CSE as derived from its large near-infrared colours and its lack of optical counterpart, which suggests a large mass-loss in the recent past. The increase of its near-infrared colours suggest a continuous increase in the thickness of its CSE which is still not finished, probably due to a very recent episode of high mass-loss.

IRAS 18314–1131 shows a very large amplitude ($\Delta\mathrm{K} \approx 1.81^m$) too although in this case the near-infrared colours indicate a moderate optical thickness of the CSE. OH/IR stars are erratic pulsators in the sense that their light curves do not exactly repeat from one cycle to the next at visual or infrared wavelengths. Wood et al. (1998) used light curves consisting of a combination of the fundamental period and the first harmonic to analyse the photometric behaviour of a sample of galactic OH/IR stars. Maybe these objects are pulsating with more than one period but it is clear that we would need a more extensive and better sampled light curve to be able to test this possibility.

As we have already mentioned, the number of photometric data points available in some cases were not enough to obtain a reliable light curve. Thus, from the 13 remaining objects, only 8 additional periods were found, and for the rest plausible although not definitive periods have been suggested. The reason for the non-definitive period determination for IRAS 16437–3140, IRAS 18299–1705 and IRAS 18429–1721 is the small number of measurements, and for IRAS 17103–0559 and IRAS 17105–2804 is that the primary minimum of $\chi^2$ is less than twice deeper than the secondary minimum.

For the 3 types of light curves studied in this work we have found that 7 objects improve their fit to the observational data when we tried a light curve with linear variation of the mean magnitude (Type 2), 3 objects showed better fit when the light curve used was an asymmetric one (Type 3), and 3 objects did not show any significant improvement with respect to a Type 1 light curve. Only for IRAS 19129+2803 both Type 2 and 3 light curves show significant improvement with respect to the Type 1 light curve. We have selected the Type 3 light curve because it is slightly better. Probably in some cases, especially in those with a small number of data, the improvement in the fit is a logical consequence of introducing a new variable in the light curve.

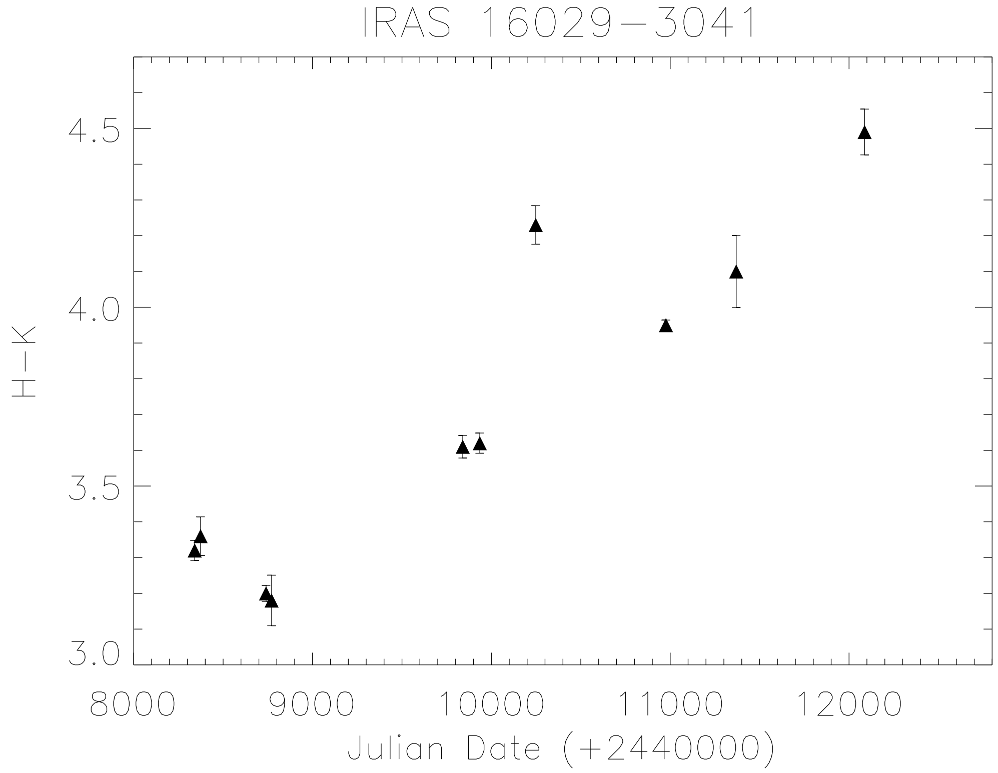

**Figure 5.6**: Variation of the H–K colour with time for IRAS 16029–3041

These secular variations in luminosity have previously been observed and reported only in a few other long period variables, predominantly among C-rich stars rather than in O-rich stars. Whitelock et al. (2000, 2003) found long term trends for carbon stars, oxygen-rich Mira and semi-regular variables in both our Galaxy and in the Large Magellanic Cloud. All the curves fitted to the data assume a main pulsation period and, overimposed on it, a significantly longer period more adequate to reproduce the long term trend. Olivier et al. (2001) reported a variation over a more than $6\,000^d$ cycle of V Hya as the result of orbital variations in a binary system. Winters et al. (1994) predicted periodic mass-loss variation on time scales of a few times the pulsation period for carbon stars. If this is true for carbon stars it would be reasonable to think that this could happen to O-rich stars too. It seems likely that the regular variations showed by several objects are caused by small mass-loss variations. A better sampled long term monitoring is necessary to characterize these light curves sufficiently well.

In Figure 5.7 we have plotted the K amplitude ($\Delta$K) as a function of the period for the objects of our sample for which a period was derived. Together with them we have plotted the data for several OH/IR stars obtained from the bibliography (Olivier et al. 2001; Wood et al. 1998; Whitelock et al. 1994; Le Bertre 1993; Engels et al. 1983). Up to a

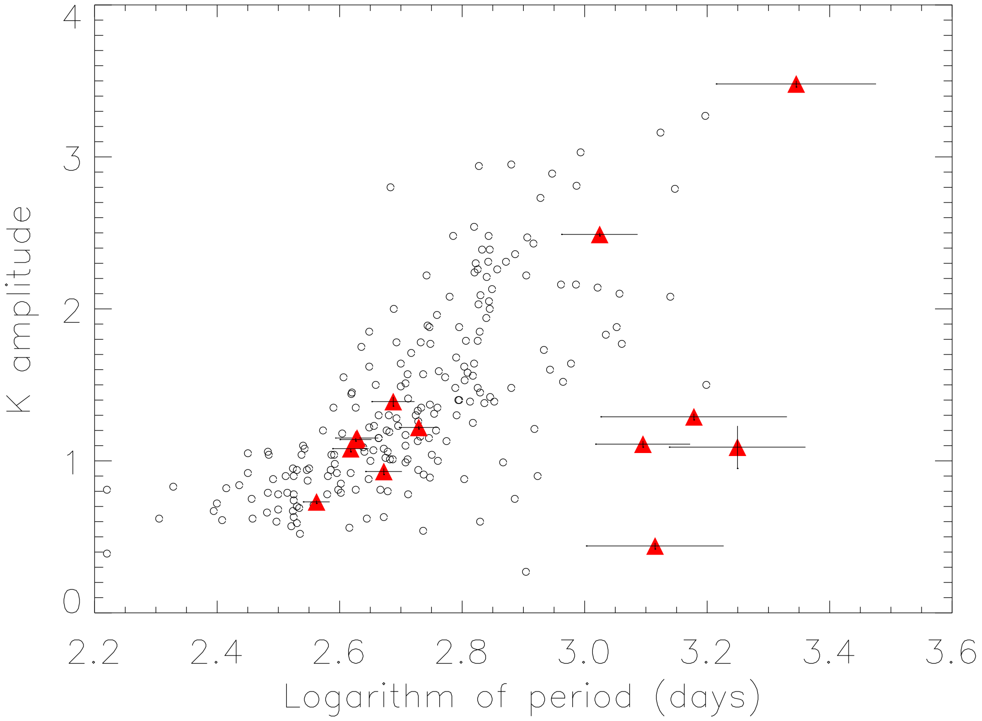

**Figure 5.7**: The K amplitude (ΔK) as a function of the period. We have plotted our data (filled triangles) together with data extracted from the bibliography (open circles).

value of $log\,\mathrm{P} \approx 2.6$ we can see that the periods are not correlated with the amplitude, which covers the range $0.5^m < \Delta\mathrm{K} < 1.1^m$. However, the amplitudes increase with the period for $log\,\mathrm{P} \gtrsim 2.6$, the largest amplitudes corresponding to values of $log\,\mathrm{P} \gtrsim 2.8$. However, there is a handful of objects which present very low amplitudes and large periods.

IRAS 16437–3140 has the largest amplitude and period reported for the moment in an OH/IR star ($\Delta\mathrm{K} = 3.48^m$ and $\mathrm{P} = 2\,215^d$), although the variability parameters for this source are not yet totally determined because of the small number of measurements available. The type of light curve that better fits the data is a Type 2 curve with a decrease of the luminosity with time at a rate of $1^m$ in 4 years, although this result could be an artifact of the low number of measurements. This source has very red near-infrared colours which implies a very thick CSE, and probably it is in a very evolved stage, close to departure from the AGB phase.

The other object with a not yet definitive value of the period and the amplitude is IRAS 18299–1705. For this object we have been able to fit a period of $1\,303^d$ but with an amplitude of only $0.44^m$. This amplitude is typical of a Mira variable, but the period is typical of an OH/IR star.

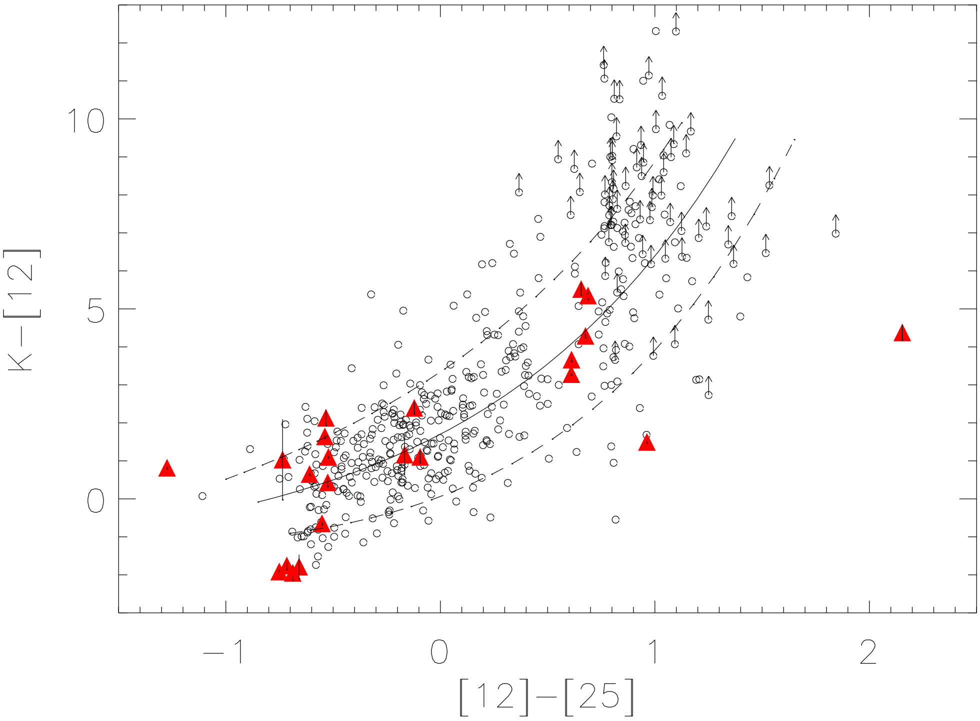

**Figure 5.8**: IRAS-NIR colour-colour diagram K−[12] vs. [12]−[25] of all stars of the sample with K band photometry. The continuous line correspond to the best fit to the observed data derived for the 'extended OH/IR sample' discussed in previous chapters. The dashed lines correspond to the dispersion expected from the variability of the sources at the K and 12 $\mu$m bands, and from the intrinsic errors associated to the photometric measurements (see Chapter 3).

In Figure 5.8 we have plotted the K−[12] vs. [12]−[25] diagram for the sources in our 'monitoring sample'. To calculate the K−[12] colour we used the mean K magnitude and adopted a zero-magnitude flux at K of 665 Jy (Koornneef 1983a). Together with our objects we have plotted again the location of the sources included in the 'extended OH/IR sample' analysed in this thesis for comparison.

Two objects are placed in the region where Proto Planetary Nebulae (PPN) are expected to be found (see Chapter 2). One of these objects is the known Luminous Blue Variable IRAS 18576+0341, one of the sources included in Table 5.5. The other object is IRAS 18299–1705. The low amplitude and the large period found for this source could be consistent with the source being already in a PPN evolutionary phase, and this is what we suggest.

## 5.6 Conclusions

We have presented the result of a near-infrared monitoring program of a small sample of 25 galactic sources selected from the IRAS Point Source Catalogue including an atlas of near-infrared finding charts for all the stars in the sample. Except for one source (IRAS 18092–2347), we successfully identified the near-infrared counterparts and determined improved astrometric coordinates for each source in the sample with an accuracy of $\approx 0.2''$. The correctness of the identifications was carefully assessed using improved positional information from the MSX satellite and, in some cases, checking for variability.

The distribution of the monitoring objects in the near-infrared J–H vs. H–K colour-colour diagram was found to be consistent with the colours of the OH/IR stars in the 'extended OH/IR sample' analysed in this thesis. However, on the basis of their variability and photometric properties 6 (24% of the sample) sources were identified either as M-type Supergiants, or as semiregular variables, or as Luminous Blue Variables, and are contaminating our OH/IR sample.

With the photometric data collected during the monitoring program, we have analyzed the light curves of all objects in the sample with enough observational data, using 3 types of light curves. 8 periods were found, and for 5 sources plausible although not definitive periods have tentatively been suggested. In 7 cases we found a secular variation of the mean brightness and in 3 cases asymmetries in the light curves.

The range of periods found goes from $365^d$ to $2\,215^d$, with 6 objects with periods over $1\,000^d$. The range of amplitudes found goes from $0.44^m$ to $3.48^m$, with the majority of the sources around $1^m$. IRAS 16437–3140 has the longest period ($\mathrm{P} = 2\,215^d$) and one of the largest amplitudes ($\Delta\mathrm{K} = 3.48^m$) reported for the moment in an OH/IR star, although the variability parameters for this source are not yet totally determined because of the small number of measurements available.

We have presented evidence for an on-going obscuration process in IRAS 16029–3041. This source shows a strong variability with one of the largest amplitude ($\Delta\mathrm{K} \approx 2.75^m$) in our sample, and very red colours that have been changing at least during the last 10 years. The H–K colour has increased by $\approx 1^m$ during this period of time. However, no period determination was yet possible for IRAS 16029–3041 with the available data.

In the K–[12] vs. [12]–[25] colour-colour diagram we found that IRAS 18299-1705 is located in the region mainly populated by PPN. Such an evolutionary stage could explain its low variability amplitude and the long period derived for this source.

**Acknowledgements:**

Based on service time observations made with the Carlos Sánchez telescope of the Observatorio del Teide (Tenerife, Spain), operated by the Instituto de Astrofísica de Canarias, and on observations collected at the German-Spanish Astronomical Centre, Calar Alto, operated jointly by Max-Planck-Institut für Astronomie and the Instituto de Astrofísica de Andalucía (CSIC). This work has partially been funded through grant PB94−1274 from the Spanish Dirección General de Investigación Científica y Técnica (DGICYT). This publication makes use of data products from the Two Micron All Sky Survey, which is a joint project of the University of Massachusetts and the Infrared Processing and Analysis Center/California Institute of Technology, funded by the National Aeronautics and Space Administration and the National Science Foundation.

# Chapter 6

# Main conclusions

In this thesis we have presented a detailed study of the infrared photometric properties of a large sample of galactic OH/IR stars, which includes atlas of optical/near-infrared finding charts corresponding to two different samples:

i) the 'Arecibo sample', formed by 371 objects, in the bluer part of the 'O-rich AGB sequence', with a small contribution from very red sources, and restricted to a well defined area of the sky.

ii) the 'GLMP sample', exclusively formed by 94 sources in the redder part of the 'O-rich AGB sequence', including sources all over the sky, 32% of them being located in the direction of the Galactic Bulge.

Firstly, we have presented near-infrared photometric observations for 371 objects taken from the 'Arecibo sample of OH/IR stars'. Except for 8 sources, we successfully identified their near-infrared counterparts and determined new positions for each source in the sample with an accuracy of $\approx 1''$. The correctness of the identifications was carefully assessed using improved positional information (MSX, VLA), analyzing the near- and mid-infrared colour measurements, and in some cases checking for variability. The few sources for which no near-infrared counterparts were found were identified either as heavily obscured variable OH/IR stars at the very end of the AGB or as non-variable OH/IR stars in a very early post-AGB stage.

Secondly, we have presented near-infrared photometric observations for 94 OH/IR stars taken from the GLMP catalogue. We successfully identified their near-infrared counterparts and determined new positions for 58 sources in the sample with an accuracy of $\approx 0{,}2''$. The correctness of the identifications was carefully assessed using also improved positional information (MSX) and analyzing the near- and mid-infrared colour measurements. The 36 sources for which no near-infrared counterparts were found were again identified as heavily obscured variable OH/IR stars.

The wide dispersion observed in the JHK magnitudes measured for the sources in both the 'Arecibo sample' and the 'GLMP sample' is mainly attributed to the different optical thickness of their CSE, rather than to the different apparent luminosity expected from sources located at a wide range of distances, or to the different intrinsic luminosities of the sources in the sample. The most probable explanation for the systematic fainter brightness and redder colours found for the GLMP sources, in comparison with the bluer Arecibo sources, seems to be the larger optical thickness of their CSE.

The distribution of the Arecibo sources in the near-infrared J−H vs. H−K colour-colour diagram is also interpreted as a sequence of increasing optical thickness of their CSE, where Mira-like variables with still optically thin shells are placed in the blue part of this diagram while the more extreme OH/IR stars with thicker shells are located in the redder part of the diagram. Their near-infrared colours can be reproduced with the combination of the emission coming from a cool central star ($T \approx 2\,500\,K$) and a much cooler dust shell ($T < 800\,K$). The dispersion of colours observed along the sequence can be explained as differential circumstellar and/or interstellar reddening. The distribution of the GLMP sources in this diagram follow the same correlation shown by the population of OH/IR stars in the 'Arecibo sample'. However, the sources in the 'GLMP sample' are in average redder than those in the 'Arecibo sample'. This suggests again that the GLMP OH/IR stars have thicker CSE in average than those of the 'Arecibo sample'.

This interpretation was confirmed by determining the detection rate of optical counterparts as a function of the H−K colour. We found that most of the sources with $H-K < 1.0$ are detected in the optical range while those with $H-K > 2.0$ are heavily obscured sources with no optical counterpart on the DSS2 images. These sources are also located in different regions of the IRAS [12]−[25] vs. [25]−[60] colour-colour diagram, suggesting that both near- and mid-infrared colours are good indicators of the optical thickness of the shell.

The connection between the near- and the mid-infrared data was analyzed with the help of the K−[12] vs. [12]−[25] colour-colour diagram. We found that there is also a clear correlation between these two colours which can also be interpreted as an indication of the increasing contribution of the mid-infrared component (emission from the cool dust in the circumstellar shell) with respect to the near-infrared component (emission from the central star plus the hot dust surrounding it) to the overall spectral energy distribution as these stars evolve along the 'O-rich AGB sequence'. However, the scatter of this correlation is found to be very large, partly because of the strong variability of these sources in the near- and mid-infrared and the non-simultaneity of the observations under comparison. The expected variability goes from $0.5^m$ to more than $4^m$ in the K band and from $0.5^m$ to $1.8^m$ at $12\,\mu$m, both increasing towards redder [12]−[25] colours. Once these uncertainties are considered, the distribution of the Arecibo sources observed in the K−[12] vs. [12]−[25] diagram can be explained as a consequence of the different optical thicknes of their CSE, with the exception of a few outliers which are found to be much brighter than expected in the near-infrared according to their [12]−[25] colour. However, the large scatter observed for the sources in the 'GLMP sample' cannot be fully explained as produced by the intrinsic variability of the sources in the K-band combined with that expected at 12 $\mu$m unless this variability is underestimated in these very red OH/IR stars. Putting together both samples we have fitted the good quality observational data to an exponential function.

A few Arecibo sources showing very red [12]−[25] colours in combination with unusually blue near-infrared counterparts as well as a few outliers in the K−[12] vs. [12]−[25] diagram have been identified as candidate post-AGB stars, proto-planetary nebulae or even as planetary nebulae.

We have also presented in this thesis the first results of a long-term infrared and optical monitoring program started in 1999, which is aimed at determining the variability properties of all the sources in the 'Arecibo sample of OH/IR stars' and combine the information collected in the near-infrared with data available at other wavelengths in order to study the nature of these stars in the context of stellar evolution. As part of this thesis work, a semi-automated reduction procedure was developed combining a self-written IDL (Interactive Data Language; Research Systems Inc.) routine with pre-existing routines within the IRAF software package to deal with the huge amount of data which is being produced by this long-term monitoring program.

Using all OH/IR stars compiled from both the 'Arecibo sample' and the 'GLMP sample' (457 in total; the so-called 'extended OH/IR sample') we have studied the 'O-rich AGB sequence' of infrared colours showed in the IRAS two colour-colour diagram by these stars in terms of evolutionay stage and progenitor masses.

The bolometric fluxes ($F_{bol}$) of most of the sources included in the so-called 'extended OH/IR sample' (a combination of OH/IR stars taken from the Arecibo sample and from the GLMP sample to cover a wide range of infrared colours) have been determined after integrating the photometric data available from the near infrared to the far infrared domain (JHK, MSX and IRAS data) and extrapolating both toward shorter and longer wavelengths.

Whenever possible, we have used the non-simultaneous MSX and IRAS photometry to derive a mean value of the bolometric flux as a better approach to the actual value considering the strong variability of the sources under study. We estimate that this intrinsic variability is the main source of uncertainty in our calculations rather than the extrapolations made. Typically we estimate that the accuracy of our bolometric flux estimations is of the order of $\approx$ 40%.

We have determined the absolute luminosity distribution of a sample of 41 sources belonging to the 'GLMP subsample' located in the direction of the Galactic Center by adopting a common distance of 8 kpc, assuming that they are all part of the Galactic Bulge population of OH/IR stars. The range of luminosities found range from $\approx$ 2 500 to $\approx 26\,000\,\mathrm{L}_\odot$ $(-3.5^m > \mathrm{M}_{bol} > -6.3^m)$ but it is strongly peaked around $3\,500-4\,000\,\mathrm{L}_\odot$ $(\mathrm{M}_{bol} \approx -4.2^m)$. This result is in agreement with those found by other authors using different OH/IR samples in the bulge with very different (bluer) colours or using samples located in different parts of the Galaxy. Then we conclude that the luminosity function may be similar throughout the Galaxy and not very dependent on the colours of the stars selected. This result is in disagreement with the general assumption that 'red' OH/IR stars are typically $\approx 10\,000\,\mathrm{L}_\odot$ sources, generally used in the literature. Our interpretation is that our sample of red OH/IR stars in the Galactic Bulge is dominated by relative low mass ($\approx 1\,\mathrm{M}_\odot$) stars and do not differ significantly from the rest of galactic samples used by other authors in terms of progenitor mass but they are probably in a more evolved stage as AGB stars (i.e. with thicker shells). If our interpretation is correct this would imply that relatively low mass OH/IR stars can also reach the red part of the 'O-rich AGB sequence' at the very end of their AGB lifetime. And because they are much more numerous than massive stars they can still be the dominant population of the red part of the 'O-rich AGB sequence' even at considerably high values of $\lambda$.

Based on the narrow luminosity distribution shown by our red sample of Galactic Bulge OH/IR stars we have been able to explore the galactic height distribution of the rest of stars in our sample belonging to the disk population. Assuming a common and constant luminosity of $\mathrm{L}_{OH/IR} = 3\,500\,\mathrm{L}_\odot$ for all them, as a first guess to their true luminosity, we found a clear correlation between $\lambda$ and galactic height indicating that the fraction of high mass stars do increases with $\lambda$. In addition, we found the same correlation between $\mathrm{v}_{exp}$ and $\lambda$.

Based on of the results mentioned above we propose an evolutionary scenario in which all OH/IR stars would start their life as AGB stars in the bluer part of the 'O-rich AGB sequence', with a $\mathrm{v}_{exp}$ probably proportional to their mass, and then evolve toward redder colours as their CSE increases its optical depth. Even relatively low-mass OH/IR stars ($\approx 1\,\mathrm{M}_\odot$) would be able to create at least for a short time an optically thick CSE enough to prevent their detection in the optical range just at the very end of the AGB phase, appearing as considerable red sources in the IRAS two-colour diagram. However, only the most massive stars would reach the upper end of the 'O-rich AGB sequence' $(\lambda \gtrsim 3)$.

We have divided the 'O-rich AGB sequence' in bins of $\lambda$ and determined the galactic scale height associated to stars within each of the resulting bins. Then we have classified all the OH/IR stars in our 'extended sample' in 5 main groups as a function of their galactic scale height, and we have established evolutionary connections between each of these groups and other samples taken from the literature, including all kind of AGB stars and PNe.

Our results suggest that the 'extremely blue subsample' $(\lambda < 0.6;\ \mathrm{H} = 536\,\mathrm{pc})$ is dominated by OH/IR stars that can be identified as the result of the evolution of low mass ($\lesssim 1\,\mathrm{M}_\odot$) optically bright short period ($\lesssim 300^d$) Miras. These OH/IR stars could be the progenitors of type III PNe.

The 'blue subsample' ($0.6 < \lambda \leq 1.2$; $\mathrm{H} = 344\,\mathrm{pc}$) is mainly formed by OH/IR stars identified as the result of the evolution of intermediate period ($\approx 300^d$) Miras, with typical progenitor masses of $1.0 - 1.5\,\mathrm{M}_\odot$. These OH/IR stars would be the progenitor of low mass type II PNe.

The 'transition subsample' ($1.2 < \lambda \leq 1.8$; $\mathrm{H} = 287\,\mathrm{pc}$) of OH/IR stars is identified as the result of the evolution of intermediate period ($300 - 500^d$) Miras. We suggest a wide progenitor mass range between 1.5 and $2.5\,\mathrm{M}_\odot$. These OH/IR stars must be the progenitors of high mass type II PNe.

The mean galactic scale height of the 'red subsample' ($1.8 < \lambda \leq 3.0$; $\mathrm{H} = 193\,\mathrm{pc}$) of OH/IR stars is found to be consistent with stars with masses in the range $2.5 - 4.0\,\mathrm{M}_\odot$. This is only slightly larger than the value taken from the literature for type I PNe. If type I PNe are the result of the evolution of HBB AGB stars, they should have progenitor masses $\gtrsim 3\,\mathrm{M}_\odot$ (i.e. within this 'red subsample').

Some of the stars in these three intermediate groups (blue, transition and red) may turn into C-rich AGB stars at some point during their evolution in the AGB as a consequence of the dredge-up of C-rich processed material to the surface after a few thermal pulses. Their progenitor masses would then cover a wide range between $1.0 - 3.0\,\mathrm{M}_\odot$, with an increasing number of 'infrared carbon stars' (with optically thick shells) as they approach the upper limit in mass expected for galactic carbon stars ($2.0 - 3.0\,\mathrm{M}_\odot$).

Finally, the 'extremely red subsample' ($3.0 < \lambda$; $\mathrm{H} = 48\,\mathrm{pc}$) of OH/IR stars is identified as the group containing the most massive OH/IR stars that would evolve all along the AGB sequence, and may be also during the whole PNe phase, as infrared sources with no optical counterpart. We identify this group of very massive AGB stars ($\gtrsim 4\,\mathrm{M}_\odot$) as the precursors of the so-called 'OHPNe', heavily obscured OH/IR stars with radiocontinuum emission that have been proposed to be 'infrared PNe'. They are fast evolving sources that will evolve toward the white dwarf stage without having shown themselves in the optical as PNe.

To finish this thesis work, we have presented the result of a near-infrared monitoring program of a small sample of 25 galactic sources selected from the IRAS Point Source Catalogue including an atlas of near-infrared finding charts for all the stars in the sample. Except for one source (IRAS 18092–2347), we successfully identified the near-infrared counterparts and determined improved astrometric coordinates for each source in the sample with an accuracy of $\approx 0.2''$. The correctness of the identifications was carefully assessed using improved positional information from the MSX satellite and, in some cases, checking for variability.

The distribution of the monitored objects in the near-infrared J–H vs. H–K colour-colour diagram was found to be consistent with the colours of the OH/IR stars in the 'extended OH/IR sample' analysed in this thesis. However, on the basis of their variability and photometric properties 6 (24% of the sample) sources were identified either as M-type Supergiants, or as semiregular variables, or as Luminous Blue Variables, and are contaminating our OH/IR sample.

With the photometric data collected during the monitoring program, we have analyzed the light curves of all objects in the sample with enough observational data, using 3 types of light curves. 8 periods were found, and for 5 sources plausible although not definitive periods have tentatively been suggested. In 7 cases we found a secular variation of the mean brightness and in 3 cases asymmetries in the light curves.

The range of periods found goes from $365^d$ to $2\,215^d$, with 6 objects with periods over $1\,000^d$. The range of amplitudes found goes from $0.44^m$ to $3.48^m$, with the majority of the sources around $1^m$. IRAS 16437–3140 has the longest period ($P = 2\,215^d$) and one of the largest amplitudes ($\Delta K = 3.48^m$) reported for the moment in an OH/IR star, although the variability parameters for this source are not yet totally determined because of the small number of measurements available.

We have presented evidence for an on-going obscuration process in IRAS 16029–3041. This source shows a strong variability with one of the largest amplitude ($\Delta K \approx 2.75^m$) in our sample, and very red colours that have been changing at least during the last 10 years. The H–K colour has increased by $\approx 1^m$ during this period of time. However, no period determination was yet possible for IRAS 16029–3041 with the available data.

In the K–[12] vs. [12]–[25] colour-colour diagram we found that IRAS 18299-1705 is located in the region mainly populated by PPN. Such an evolutionary stage could explain its low variability amplitude and the long period derived for this source.

# Appendix A

# Astrometric data for the sources in the ‘Arecibo sample‘

**Table A.1**: Astrometric information derived for the sources belonging to the ‘Arecibo sample’ for which an optical/near-infrared counterpart was found.

| IRAS | Calar Alto | | CA–IRAS | | MSX–IRAS | | VLA–IRAS | | MSX6C_G |
|---|---|---|---|---|---|---|---|---|---|
| | Coordinates | | $\Delta\alpha$ | $\Delta\delta$ | $\Delta\alpha$ | $\Delta\delta$ | $\Delta\alpha$ | $\Delta\delta$ | |
| | (J2000) | | [”] | [”] | [”] | [”] | [”] | [”] | |
| 01037+1219 | 01 06 26.0 | +12 35 53 | 1 | −1 | | | | | |
| 01085+3022 | 01 11 15.9 | +30 38 06 | 0 | 1 | | | | | |
| 02404+2150 | 02 43 16.5 | +22 03 35 | −3 | 1 | | | | | |
| 02420+1206 | 02 44 45.5 | +12 19 03 | 7 | 3 | | | | | |
| 02547+1106 | 02 57 27.5 | +11 18 06 | 4 | 2 | | | | | |
| 03507+1115 | 03 53 28.9 | +11 24 22 | 4 | 2 | | | | | |
| 12562+2324 | 12 58 38.9 | +23 08 21 | 3 | −2 | | | | | |
| 15060+0947 | 15 08 25.7 | +09 36 18 | 0 | 1 | | | | | |
| 15262+0400 | 15 28 43.7 | +03 49 43 | −1 | 0 | | | −1 | 0 | |
| 16235+1900 | 16 25 47.5 | +18 53 33 | −1 | 3 | | | | | |
| 16503+0529 | 16 52 48.2 | +05 24 27 | 6 | 0 | | | | | |
| 16523+0745 | 16 54 46.5 | +07 40 27 | 0 | 0 | | | | | |
| 16560+2252 | 16 58 12.1 | +22 47 50 | −6 | 2 | | | | | |
| 17050+1714 | 17 07 17.6 | +17 10 22 | 1 | 1 | | | | | |
| 17230+0113 | 17 25 36.6 | +01 11 05 | 3 | 1 | | | 2 | 1 | |
| 17256+0504 | 17 28 08.3 | +05 02 18 | 0 | 1 | | | 0 | 1 | |
| 17308+0822 | 17 33 13.9 | +08 20 41 | 4 | 3 | | | 4 | 1 | |
| 17338+0051 | 17 36 26.8 | +00 49 34 | 3 | 0 | | | | | |

*Continue in the next page.*

*Table A.1: Astrometric data for the sources belonging to the ‘Arecibo sample’ (continued)*

| IRAS | Calar Alto Coordinates (J2000) | | CA–IRAS Δα ["] | CA–IRAS Δδ ["] | MSX–IRAS Δα ["] | MSX–IRAS Δδ ["] | VLA–IRAS Δα ["] | VLA–IRAS Δδ ["] | MSX6C_G |
|---|---|---|---|---|---|---|---|---|---|
| 17528+1144 | 17 55 13.8 | +11 43 46 | 1 | 0 | | | 0 | 0 | |
| 17554+2946 | 17 57 19.7 | +29 46 29 | 0 | 0 | | | | | |
| 17579+2335 | 18 00 04.0 | +23 35 37 | 3 | 1 | | | 1 | 1 | |
| 18033+2229 | 18 05 26.6 | +22 30 04 | 29 | 6 | | | | | |
| 18069+0911 | 18 09 18.5 | +09 12 16 | 0 | 0 | | | 0 | −1 | |
| 18076+3445 | 18 09 24.7 | +34 46 20 | 2 | 3 | | | | | |
| 18085+0752 | 18 10 58.5 | +07 53 09 | −10 | 1 | | | | | |
| 18095+2704 | 18 11 30.8 | +27 05 14 | 3 | 0 | | | | | |
| 18099+3127 | 18 11 47.5 | +31 28 20 | −7 | 2 | | | | | |
| 18123+0511 | 18 14 49.4 | +05 12 56 | 0 | 1 | | | | | |
| 18170+0353 | 18 19 33.6 | +03 54 50 | 5 | 2 | | | 3 | 1 | |
| 18203+0723 | 18 22 44.0 | +07 24 55 | 3 | 1 | | | | | |
| 18223+1217 | 18 24 36.6 | +12 19 16 | −10 | −2 | | | | | |
| 18231+0855 | 18 25 33.3 | +08 56 47 | −7 | −1 | | | | | |
| 18236+0706 | 18 26 06.8 | +07 08 33 | −4 | −3 | | | | | |
| 18237+2150 | 18 25 51.1 | +21 52 14 | 15 | 3 | | | | | |
| 18251+0023 | 18 27 44.0 | +00 25 12 | 2 | −1 | | | | | |
| 18254+0750 | 18 27 50.9 | +07 52 21 | 3 | 2 | | | 1 | 2 | |
| 18262+0934 | 18 28 37.0 | +09 36 50 | 4 | 3 | | | | | |
| 18270+0326 | 18 29 34.6 | +03 28 12 | 2 | 0 | | | 1 | 0 | |
| 18276+0839 | 18 30 03.5 | +08 41 26 | 2 | 2 | | | | | |
| 18278+0931 | 18 30 12.1 | +09 33 44 | 0 | 2 | | | | | |
| 18307+0102 | 18 33 15.3 | +01 04 39 | 9 | 3 | 6 | 0 | 8 | 4 | 031.8158+04.5372 |
| 18318+0150 | 18 34 20.6 | +01 53 12 | 11 | −1 | 5 | −4 | | | 032.6625+04.6642 |
| 18333+0903 | 18 35 42.5 | +09 05 39 | −3 | 1 | | | −5 | −2 | |
| 18341+0005 | 18 36 40.8 | +00 08 03 | −3 | 1 | −6 | −5 | | | 031.3652+03.3445 |
| 18347+1113 | 18 37 08.6 | +11 16 16 | −2 | 1 | | | | | |
| 18349+1023 | 18 37 19.3 | +10 25 42 | −3 | 1 | | | | | |
| 18353+0020 | 18 37 55.8 | +00 23 32 | −2 | 1 | −2 | −3 | | | 031.7390+03.1839 |
| 18355+0227 | 18 38 06.8 | +02 29 58 | 19 | 1 | 13 | 2 | | | 033.6401+04.1048 |
| 18362+0538 | 18 38 42.5 | +05 41 29 | 7 | 2 | | | | | |
| 18375+0510 | 18 39 59.7 | +05 13 14 | −3 | 2 | −3 | 4 | | | 036.2878+04.9180 |
| 18381+0020 | 18 40 44.1 | +00 23 42 | −9 | 3 | −9 | −1 | | | 032.0617+02.5609 |
| 18395+0130 | 18 42 03.2 | +01 33 14 | 9 | 2 | 4 | 2 | 8 | 3 | 033.2453+02.7975 |
| 18397+0758 | 18 42 09.2 | +08 01 18 | 11 | 6 | | | | | |
| 18398+0728 | 18 42 15.8 | +07 31 29 | 5 | −1 | | | 5 | 2 | |
| 18398+1035 | 18 42 10.0 | +10 38 55 | 0 | 1 | | | | | |
| 18400+0123 | 18 42 36.8 | +01 26 04 | 0 | 1 | −3 | 1 | | | 033.2027+02.6181 |

*Continue in the next page.*

*Table A.1: Astrometric data for the sources belonging to the ‘Arecibo sample’ (continued)*

| IRAS | Calar Alto Coordinates (J2000) | | CA–IRAS $\Delta\alpha$ [”] | CA–IRAS $\Delta\delta$ [”] | MSX–IRAS $\Delta\alpha$ [”] | MSX–IRAS $\Delta\delta$ [”] | VLA–IRAS $\Delta\alpha$ [”] | VLA–IRAS $\Delta\delta$ [”] | MSX6C_G |
|---|---|---|---|---|---|---|---|---|---|
| 18407+0350 | 18 43 15.5 | +03 53 09 | 3 | 1 | 4 | 7 | | | 035.4648+03.5886 |
| 18407+0601 | 18 43 09.9 | +06 04 47 | 7 | 0 | 6 | 2 | | | 037.4142+04.6027 |
| 18408+0730 | 18 43 19.2 | +07 33 13 | 3 | −1 | | | | | |
| 18409+0431 | 18 43 28.2 | +04 34 16 | 2 | −1 | 5 | 4 | | | 036.1008+03.8519 |
| 18415+0404 | 18 44 05.0 | +04 07 19 | 3 | −1 | 3 | 4 | | | 035.7688+03.5128 |
| 18420+1137 | 18 44 24.6 | +11 40 12 | 0 | 2 | | | | | |
| 18430+0039 | 18 45 38.3 | +00 42 44 | 10 | 0 | 9 | 1 | | | 032.9047+01.6156 |
| 18433+0039 | 18 45 55.0 | +00 42 23 | −2 | 3 | −4 | 1 | | | 032.9303+01.5511 |
| 18435+0745 | 18 46 00.4 | +07 48 26 | 1 | 0 | −2 | 1 | | | 039.2799+04.7523 |
| 18441+0311 | 18 46 37.6 | +03 14 56 | 0 | 2 | 3 | 9 | | | 035.2792+02.5502 |
| 18441+2216 | 18 46 13.5 | +22 20 09 | 8 | 1 | | | | | |
| 18444+0734 | 18 46 49.4 | +07 38 14 | 4 | 3 | 3 | 3 | | | 039.2193+04.4947 |
| 18455+0448 | 18 48 02.4 | +04 51 31 | 3 | 2 | 3 | 4 | | | 036.8738+02.9676 |
| 18476+0555 | 18 50 04.8 | +05 59 32 | −4 | 4 | −6 | 1 | −5 | 1 | 038.1146+03.0292 |
| 18477+0243 | 18 50 13.5 | +02 47 12 | 1 | 0 | −1 | 1 | | | 035.2742+01.5406 |
| 18481+0405 | 18 50 37.8 | +04 09 09 | 6 | 3 | 4 | 5 | 5 | 3 | 036.5373+02.0723 |
| 18487+0152 | 18 51 15.7 | +01 56 20 | 3 | 2 | 6 | 1 | | | 034.6378+00.9222 |
| 18487+0617 | 18 51 14.1 | +06 21 35 | 1 | 2 | −1 | 2 | | | 038.5735+02.9411 |
| 18490+0302 | 18 51 35.8 | +03 05 55 | −1 | −1 | −4 | −1 | | | 035.7079+01.3778 |
| 18490+1158 | 18 51 25.2 | +12 02 08 | 9 | 4 | | | | | |
| 18497+0200 | 18 52 15.2 | +02 03 44 | −1 | −6 | 0 | −2 | | | 034.8615+00.7590 |
| 18499+1224 | 18 52 18.4 | +12 28 38 | −1 | 3 | | | | | |
| 18501+1019 | 18 52 32.8 | +10 23 32 | 2 | 4 | −1 | 4 | 1 | 3 | 042.3245+04.4752 |
| 18506+0912 | 18 53 02.7 | +09 16 38 | −5 | 4 | −5 | 2 | −3 | 4 | 041.3824+03.8617 |
| 18511+1141 | 18 53 32.2 | +11 45 01 | 3 | 2 | 1 | 6 | | | 043.6522+04.8700 |
| 18512+2029 | 18 53 26.2 | +20 33 27 | −6 | −2 | | | | | |
| 18518+0358 | 18 54 16.1 | +04 02 32 | −24 | −3 | −26 | −3 | | | 036.8520+01.2139 |
| 18520+0533 | 18 54 31.8 | +05 37 11 | 7 | 2 | 6 | 2 | 6 | 4 | 038.2863+01.8746 |
| 18520+1014 | 18 54 26.2 | +10 18 02 | 9 | 2 | 6 | 3 | | | 042.4531+04.0195 |
| 18525+0210 | 18 55 05.2 | +02 14 42 | 4 | 1 | 4 | 2 | | | 035.3458+00.2124 |
| 18530+0507 | 18 55 30.3 | +05 11 40 | 9 | 2 | 8 | 1 | | | 038.0183+01.4646 |
| 18535+0726 | 18 55 57.0 | +07 30 32 | 3 | 4 | 2 | 0 | | | 040.1297+02.4195 |
| 18540+0302 | 18 56 36.4 | +03 06 50 | 25 | 4 | 25 | 7 | | | 036.2927+00.2711 |
| 18542+0940 | 18 56 35.7 | +09 43 60 | −6 | −1 | −4 | 0 | | | 042.1880+03.2879 |
| 18548+0823 | 18 57 13.1 | +08 27 44 | −4 | 1 | −4 | 2 | | | 041.1238+02.5738 |
| 18549+0208 | 18 57 27.5 | +02 12 16 | 13 | 5 | 13 | 7 | | | 035.5804−00.3330 |
| 18549+0905 | 18 57 20.9 | +09 09 40 | 0 | 0 | 0 | −1 | | | 041.7611+02.8626 |
| 18551+0159 | 18 57 37.9 | +02 03 45 | 0 | 7 | −3 | 3 | | | 035.4720−00.4364 |

*Continue in the next page.*

*Table A.1: Astrometric data for the sources belonging to the 'Arecibo sample' (continued)*

| IRAS | Calar Alto Coordinates (J2000) | | CA–IRAS Δα ["] | CA–IRAS Δδ ["] | MSX–IRAS Δα ["] | MSX–IRAS Δδ ["] | VLA–IRAS Δα ["] | VLA–IRAS Δδ ["] | MSX6C_G |
|---|---|---|---|---|---|---|---|---|---|
| 18551+0323 | 18 57 37.4 | +03 27 25 | 13 | 1 | 12 | 2 | | | 036.7131+00.2022 |
| 18554+0231 | 18 57 56.7 | +02 35 17 | 2 | 2 | 2 | 3 | 3 | 9 | 035.9769−00.2664 |
| 18554+1333 | 18 57 43.7 | +13 37 17 | −6 | 1 | −7 | 4 | −7 | 1 | 045.7906+04.7991 |
| 18556+0811 | 18 58 04.3 | +08 15 30 | 4 | 2 | 4 | 2 | | | 041.0380+02.2929 |
| 18556+1409 | 18 57 59.2 | +14 13 20 | −1 | 1 | −4 | 4 | | | 046.3572+05.0141 |
| 18560+0638 | 18 58 30.0 | +06 42 58 | 0 | 2 | 1 | −1 | | | 039.7125+01.4946 |
| 18563+0816 | 18 58 43.9 | +08 20 10 | 4 | 1 | 4 | 1 | | | 041.1817+02.1830 |
| 18567+0003 | 18 59 21.2 | +00 07 27 | 4 | 2 | 3 | 1 | | | 033.9447−01.7042 |
| 18567+1046 | 18 59 08.2 | +10 50 59 | 10 | 2 | 9 | 3 | | | 043.4681+03.2379 |
| 18568+0550 | 18 59 20.8 | +05 54 42 | 12 | 3 | 12 | 1 | | | 039.0925+00.9408 |
| 18568+2554 | 18 58 50.5 | +25 58 50 | −1 | 1 | | | | | |
| 18569+0553 | 18 59 22.2 | +05 57 13 | 9 | −3 | 6 | −2 | | | 039.1331+00.9557 |
| 18569+1722 | 18 59 10.9 | +17 27 03 | 0 | 2 | | | | | |
| 18571+0611 | 18 59 36.1 | +06 15 37 | 6 | 1 | 4 | 1 | | | 039.4320+01.0442 |
| 18572+0618 | 18 59 40.4 | +06 23 04 | 2 | 2 | 2 | 1 | | | 039.5505+01.0846 |
| 18577+1047 | 19 00 08.9 | +10 52 15 | 3 | 1 | 0 | 1 | 0 | 2 | 043.5997+03.0266 |
| 18578+0831 | 19 00 17.5 | +08 35 29 | −1 | −2 | −3 | 1 | | | 041.5856+01.9568 |
| 18581+1405 | 19 00 28.1 | +14 09 54 | 3 | 3 | 0 | 3 | | | 046.5775+04.4508 |
| 18585+0900 | 19 00 53.9 | +09 05 02 | 3 | 1 | 1 | 2 | | | 042.0920+02.0478 |
| 18588+1400 | 19 01 07.2 | +14 05 13 | 10 | 3 | 9 | 4 | | | 046.5795+04.2746 |
| 18592+1455 | 19 01 32.3 | +15 00 22 | 6 | 3 | 6 | 3 | | | 047.4476+04.5997 |
| 18593+1009 | 19 01 44.2 | +10 14 00 | 5 | 2 | 2 | 1 | | | 043.2094+02.3885 |
| 19007+1652 | 19 03 01.5 | +16 56 31 | 6 | 2 | 4 | 1 | | | 049.3428+05.1551 |
| 19008+0907 | 19 03 17.0 | +09 12 10 | 4 | 0 | 1 | 3 | | | 042.4673+01.5794 |
| 19010+0526 | 19 03 33.6 | +05 31 31 | 1 | 2 | −2 | 1 | | | 039.2285−00.1670 |
| 19010+1307 | 19 03 21.5 | +13 12 02 | 6 | 3 | 6 | 1 | | | 046.0351+03.3867 |
| 19012+1128 | 19 03 36.8 | +11 33 03 | 4 | 1 | 3 | 1 | | | 044.5936+02.5796 |
| 19017+0412 | 19 04 14.4 | +04 17 01 | −5 | 2 | −3 | −1 | | | 038.2026−00.8881 |
| 19017+0608 | 19 04 09.9 | +06 13 15 | 10 | 4 | 6 | 5 | | | 039.9159+00.0185 |
| 19023+0745 | 19 04 43.5 | +07 50 19 | 7 | 2 | 4 | 2 | | | 041.4170+00.6369 |
| 19024+1923 | 19 04 36.4 | +19 28 28 | 3 | 3 | | | | | |
| 19026+0336 | 19 05 09.8 | +03 41 00 | 0 | 2 | 0 | 0 | | | 037.7748−01.3674 |
| 19026+1300 | 19 04 56.0 | +13 05 07 | 3 | 1 | 3 | −1 | | | 046.1075+02.9931 |
| 19027+1341 | 19 05 04.2 | +13 45 43 | 2 | −1 | 2 | 0 | | | 046.7264+03.2726 |
| 19028+1613 | 19 05 04.0 | +16 18 11 | 0 | 2 | −3 | 2 | | | 048.9932+04.4304 |
| 19029+0933 | 19 05 22.1 | +09 38 23 | 3 | 0 | 4 | 1 | 3 | 1 | 043.0914+01.3211 |
| 19035+0451 | 19 05 59.0 | +04 55 46 | 4 | 3 | 4 | 2 | | | 038.9764−00.9774 |
| 19035+0801 | 19 05 56.5 | +08 05 57 | 3 | 1 | 2 | 2 | | | 041.7873+00.4886 |

*Continue in the next page.*

*Table A.1: Astrometric data for the sources belonging to the 'Arecibo sample' (continued)*

| | Calar Alto | | CA–IRAS | | MSX–IRAS | | VLA–IRAS | | |
|---|---|---|---|---|---|---|---|---|---|
| IRAS | Coordinates | | $\Delta\alpha$ | $\Delta\delta$ | $\Delta\alpha$ | $\Delta\delta$ | $\Delta\alpha$ | $\Delta\delta$ | MSX6C_G |
| | (J2000) | | ["] | ["] | ["] | ["] | ["] | ["] | |
| 19035+1010 | 19 05 55.5 | +10 14 41 | 4 | 2 | 4 | 5 | | | 043.6925+01.4772 |
| 19041+0952 | 19 06 31.2 | +09 57 17 | −3 | 0 | −5 | 0 | | | 043.5012+01.2140 |
| 19041+1734 | 19 06 24.2 | +17 39 32 | 0 | 3 | −4 | 4 | | | 050.3508+04.7613 |
| 19043+1009 | 19 06 43.0 | +10 14 32 | −4 | −2 | −7 | −1 | | | 043.7789+01.3037 |
| 19047+0924 | 19 07 07.5 | +09 29 29 | −7 | −5 | −9 | −4 | | | 043.1584+00.8690 |
| 19052+0922 | 19 07 39.2 | +09 27 15 | 1 | 0 | −1 | 2 | | | 043.1852+00.7364 |
| 19052+1431 | 19 07 34.0 | +14 36 47 | 2 | 2 | 0 | 4 | | | 047.7616+03.1238 |
| 19054+0419 | 19 07 55.9 | +04 23 51 | 10 | 4 | 10 | 4 | | | 038.7272−01.6528 |
| 19055+0225 | 19 08 03.2 | +02 30 30 | 5 | 2 | 5 | 2 | 3 | 2 | 037.0617−02.5474 |
| 19057+0141 | 19 08 18.4 | +01 46 28 | 1 | 2 | 0 | 1 | | | 036.4375−02.9402 |
| 19060+1612 | 19 08 15.9 | +16 17 21 | −4 | 3 | −4 | 3 | | | 049.3316+03.7402 |
| 19061+1041 | 19 08 31.3 | +10 46 47 | 15 | 4 | 15 | 6 | | | 044.4608+01.1564 |
| 19065+0832 | 19 08 58.8 | +08 37 45 | 6 | −2 | 2 | 2 | | | 042.6040+00.0666 |
| 19067+0811 | 19 09 08.3 | +08 16 32 | 15 | 1 | 13 | 3 | | | 042.3083−00.1324 |
| 19068+0016 | 19 09 22.5 | +00 21 17 | 3 | 2 | 3 | 2 | | | 035.2962−03.8278 |
| 19068+1127 | 19 09 11.7 | +11 32 43 | 10 | −2 | 10 | 3 | | | 045.2175+01.3627 |
| 19069+0916 | 19 09 19.4 | +09 21 13 | 4 | 3 | 1 | 2 | | | 043.2849+00.3241 |
| 19071+0946 | 19 09 32.0 | +09 51 49 | 7 | 2 | 4 | 3 | | | 043.7619+00.5138 |
| 19074+0336 | 19 09 54.9 | +03 41 28 | 16 | 3 | 18 | 2 | | | 038.3267−02.4172 |
| 19075+1147 | 19 09 54.1 | +11 52 48 | 4 | 3 | 4 | 3 | | | 045.5930+01.3627 |
| 19076+1247 | 19 09 56.8 | +12 52 59 | 4 | 6 | 7 | 3 | | | 046.4881+01.8144 |
| 19079+1143 | 19 10 19.5 | +11 49 04 | 0 | 8 | 0 | 3 | | | 045.5843+01.2414 |
| 19081+0322 | 19 10 36.8 | +03 27 01 | 3 | −2 | 1 | −1 | | | 038.1933−02.6817 |
| 19083+0851 | 19 10 47.4 | +08 56 22 | 9 | 2 | 6 | 3 | | | 043.0853−00.1878 |
| 19085+0755 | 19 10 59.7 | +08 00 23 | 61 | 11 | 59 | 14 | | | 042.2819−00.6638 |
| 19087+0323 | 19 11 17.0 | +03 28 26 | 0 | 3 | 0 | 1 | 1 | 3 | 038.2907−02.8202 |
| 19088+1129 | 19 11 11.4 | +11 34 38 | 4 | 2 | 4 | 4 | | | 045.4704+00.9437 |
| 19097+0411 | 19 12 13.2 | +04 16 54 | 3 | 1 | 3 | 1 | | | 039.1169−02.6552 |
| 19112+0819 | 19 13 37.3 | +08 24 53 | −22 | −3 | −24 | −5 | | | 042.9437−01.0519 |
| 19115+0752 | 19 13 59.7 | +07 57 21 | −3 | 2 | −2 | −1 | | | 042.5799−01.3470 |
| 19116+1511 | 19 13 58.5 | +15 16 57 | 3 | 2 | 3 | 1 | | | 049.0691+02.0573 |
| 19117+1558 | 19 14 01.2 | +16 03 36 | −1 | 1 | 0 | 4 | | | 049.7649+02.4077 |
| 19128+0910 | 19 15 16.2 | +09 15 46 | −3 | 2 | 0 | 1 | | | 043.8846−01.0195 |
| 19128+1310 | 19 15 08.0 | +13 16 00 | 3 | 3 | 3 | 3 | 3 | 3 | 047.4137+00.8732 |
| 19129+2803 | 19 14 59.1 | +28 09 15 | −8 | 0 | | | | | |
| 19131+1157 | 19 15 29.2 | +12 02 39 | 0 | 2 | 0 | 2 | | | 046.3713+00.2284 |
| 19140+0652 | 19 16 29.5 | +06 57 30 | 6 | 3 | 4 | 1 | | | 041.9834−02.3578 |
| 19147+1349 | 19 17 00.6 | +13 55 22 | −12 | 0 | −10 | −2 | | | 048.2064+00.7747 |

*Continue in the next page.*

*Table A.1: Astrometric data for the sources belonging to the ‘Arecibo sample’ (continued)*

| | Calar Alto | | CA–IRAS | | MSX–IRAS | | VLA–IRAS | | |
|---|---|---|---|---|---|---|---|---|---|
| IRAS | Coordinates | | $\Delta\alpha$ | $\Delta\delta$ | $\Delta\alpha$ | $\Delta\delta$ | $\Delta\alpha$ | $\Delta\delta$ | MSX6C_G |
| | (J2000) | | ["] | ["] | ["] | ["] | ["] | ["] | |
| 19149+1638 | 19 17 11.6 | +16 43 55 | 4 | 4 | 3 | 5 | | | 050.7133+02.0461 |
| 19160+0755 | 19 18 26.8 | +08 00 38 | −1 | 3 | 1 | 2 | | | 043.1418−02.2973 |
| 19161+2343 | 19 18 14.7 | +23 49 28 | 1 | 2 | −4 | 3 | 0 | 2 | |
| 19162+0607 | 19 18 41.8 | +06 13 14 | 10 | 4 | 7 | 5 | | | 041.5849−03.1849 |
| 19167+1733 | 19 19 00.0 | +17 38 52 | 0 | 2 | 0 | 2 | | | 051.7253+02.0913 |
| 19168+0814 | 19 19 14.9 | +08 19 57 | −12 | −1 | −9 | −1 | | | 043.5199−02.3224 |
| 19172+1956 | 19 19 28.7 | +20 01 39 | 6 | 1 | 3 | 1 | | | 053.8847+03.1025 |
| 19175+0958 | 19 19 54.9 | +10 04 15 | 1 | 2 | 1 | 1 | | | 045.1337−01.6542 |
| 19175+1042 | 19 19 57.2 | +10 48 09 | 7 | 4 | 7 | 3 | | | 045.7847−01.3197 |
| 19176+1939 | 19 19 48.1 | +19 45 34 | 1 | −1 | 0 | 1 | | | 053.6832+02.9102 |
| 19177+1333 | 19 20 04.8 | +13 39 24 | 6 | 5 | 7 | 4 | | | 048.3202−00.0084 |
| 19178+1206 | 19 20 14.0 | +12 12 20 | −1 | −2 | −1 | 2 | | | 047.0573−00.7213 |
| 19183+1148 | 19 20 42.5 | +11 54 05 | −2 | 2 | 0 | 1 | | | 046.8421−00.9678 |
| 19184+1055 | 19 20 45.9 | +11 00 59 | 2 | 3 | 0 | 2 | | | 046.0668−01.3950 |
| 19186+0315 | 19 21 11.7 | +03 20 58 | 9 | 4 | 4 | −3 | | | 039.3240−05.0707 |
| 19186+1657 | 19 20 51.8 | +17 03 30 | 2 | 2 | 0 | 2 | | | 051.4124+01.4225 |
| 19187+2221 | 19 20 50.2 | +22 27 24 | 3 | 3 | 4 | 2 | | | 056.1858+03.9540 |
| 19188+1057 | 19 21 11.8 | +11 02 49 | 15 | 5 | 15 | 5 | | | 046.1439−01.4743 |
| 19189+1758 | 19 21 08.3 | +18 03 55 | −1 | 1 | −1 | 0 | | | 052.3327+01.8371 |
| 19190+1128 | 19 21 26.7 | +11 33 59 | 4 | 5 | 3 | 3 | | | 046.6305−01.2838 |
| 19190+3035 | 19 20 59.2 | +30 41 30 | 1 | 3 | | | | | |
| 19192+0922 | 19 21 36.7 | +09 27 57 | 3 | 6 | 1 | 6 | | | 044.7950−02.3066 |
| 19195+0522 | 19 22 03.3 | +05 28 27 | −6 | 2 | −9 | 5 | | | 041.3138−04.2713 |
| 19195+1747 | 19 21 44.1 | +17 53 10 | 3 | 2 | 3 | 2 | | | 052.2414+01.6277 |
| 19200+1035 | 19 22 24.8 | +10 40 51 | −6 | −4 | −6 | −3 | | | 045.9614−01.9099 |
| 19200+1536 | 19 22 17.9 | +15 41 50 | 3 | 2 | 1 | 1 | 2 | 2 | 050.3728+00.4784 |
| 19201+1040 | 19 22 29.2 | +10 46 19 | 7 | 2 | 6 | 4 | | | 046.0504−01.8826 |
| 19201+2101 | 19 22 17.4 | +21 07 23 | −46 | −11 | −49 | −8 | | | 055.1632+03.0337 |
| 19206+2121 | 19 22 48.5 | +21 26 56 | 3 | 1 | 3 | 0 | | | 055.5075+03.0788 |
| 19206+2216 | 19 22 44.9 | +22 22 05 | 3 | 2 | 1 | 2 | | | 056.3142+03.5227 |
| 19206+2517 | 19 22 43.8 | +25 22 56 | 0 | 1 | −5 | 6 | | | |
| 19214+0513 | 19 23 57.5 | +05 19 02 | −6 | 1 | −12 | 1 | | | 041.3954−04.7632 |
| 19218+0425 | 19 24 21.4 | +04 31 02 | 6 | 1 | | | | | |
| 19229+1708 | 19 25 12.5 | +17 14 50 | −9 | 1 | −9 | 2 | | | 052.0691+00.5964 |
| 19231+3555 | 19 24 59.1 | +36 01 42 | 1 | 2 | | | | | |
| 19237+1430 | 19 26 02.2 | +14 36 39 | −10 | −4 | −9 | −3 | −10 | −5 | 049.8435−00.8307 |
| 19241+3457 | 19 26 02.1 | +35 03 04 | 2 | −2 | | | | | |
| 19248+1122 | 19 27 14.5 | +11 29 05 | 6 | 2 | 6 | 2 | | | 047.2304−02.5739 |

*Continue in the next page.*

*Table A.1: Astrometric data for the sources belonging to the ‘Arecibo sample’ (continued)*

| IRAS | Calar Alto Coordinates (J2000) | | CA–IRAS Δα [”] | CA–IRAS Δδ [”] | MSX–IRAS Δα [”] | MSX–IRAS Δδ [”] | VLA–IRAS Δα [”] | VLA–IRAS Δδ [”] | MSX6C_G |
|---|---|---|---|---|---|---|---|---|---|
| 19248+1441 | 19 27 07.3 | +14 47 21 | −15 | −2 | −15 | −2 | | | 050.1250−00.9764 |
| 19252+2420 | 19 27 18.0 | +24 26 59 | 0 | 3 | 0 | 3 | | | 058.6469+03.5816 |
| 19253+1114 | 19 27 40.1 | +11 20 20 | −19 | −4 | −19 | −4 | | | 047.1518−02.7351 |
| 19254+1631 | 19 27 42.1 | +16 37 24 | 6 | 2 | 6 | 3 | | | 051.8042−00.2247 |
| 19256+0254 | 19 28 08.3 | +03 00 26 | 3 | 2 | | | | | |
| 19258+1111 | 19 28 14.0 | +11 17 31 | 12 | 2 | 10 | 1 | | | 047.1762−02.8792 |
| 19259+0510 | 19 28 22.3 | +05 16 29 | 1 | 2 | | | | | |
| 19261+1003 | 19 28 33.9 | +10 10 11 | 12 | 2 | 9 | 2 | | | 046.2259−03.4839 |
| 19261+1435 | 19 28 28.5 | +14 41 52 | −1 | 1 | −1 | 1 | | | 050.2004−01.3076 |
| 19261+1849 | 19 28 23.8 | +18 55 18 | 7 | 4 | 7 | 4 | | | 053.9025+00.7271 |
| 19265+3116 | 19 28 31.2 | +31 22 24 | 1 | 1 | | | | | |
| 19268+0254 | 19 29 21.6 | +03 01 04 | −6 | 0 | | | | | |
| 19268+1539 | 19 29 11.7 | +15 45 53 | 20 | 5 | 17 | 4 | | | 051.2204−00.9497 |
| 19269+0813 | 19 29 21.5 | +08 19 23 | −5 | 1 | −3 | −2 | | | 044.6893−04.5339 |
| 19271+1354 | 19 29 30.2 | +14 00 49 | −1 | 2 | −1 | 2 | | | 049.7184−01.8535 |
| 19274+0919 | 19 29 51.5 | +09 25 26 | 1 | 0 | 0 | 0 | | | 045.7202−04.1191 |
| 19276+0739 | 19 30 04.8 | +07 46 03 | 27 | 5 | 28 | 1 | | | 044.2832−04.9545 |
| 19276+1500 | 19 29 53.9 | +15 06 48 | 7 | 2 | 7 | 3 | | | 050.7304−01.4106 |
| 19277+0947 | 19 30 08.4 | +09 53 56 | 6 | 2 | 6 | 1 | | | 046.1718−03.9544 |
| 19283+1944 | 19 30 29.4 | +19 50 41 | −4 | 1 | −4 | 1 | | | 054.9492+00.7354 |
| 19288+2923 | 19 30 50.3 | +29 29 57 | 0 | 0 | | | 1 | 0 | |
| 19290+1600 | 19 31 20.7 | +16 07 19 | 3 | 3 | 4 | 5 | | | 051.7831−01.2321 |
| 19291+0502 | 19 31 36.1 | +05 08 35 | −10 | −1 | | | | | |
| 19295+2228 | 19 31 39.0 | +22 35 16 | 3 | 0 | 3 | 1 | 2 | 2 | 057.4854+01.8171 |
| 19302+0110 | 19 32 49.4 | +01 16 35 | 4 | 2 | | | | | |
| 19303+1553 | 19 32 35.9 | +15 59 41 | 1 | 3 | 3 | 4 | | | 051.8163−01.5574 |
| 19305+2410 | 19 32 39.9 | +24 16 54 | 0 | 0 | 3 | 5 | | | 059.0848+02.4279 |
| 19310+2044 | 19 33 11.7 | +20 51 30 | −3 | 1 | −1 | 2 | | | 056.1433+00.6681 |
| 19312+1130 | 19 33 34.5 | +11 37 03 | 0 | 1 | 0 | 0 | | | 048.0894−03.8734 |
| 19314+2059 | 19 33 34.7 | +21 06 13 | −1 | −2 | −1 | −2 | | | 056.4010+00.7090 |
| 19316+0919 | 19 34 02.8 | +09 26 06 | 6 | 1 | 3 | 1 | | | 046.2241−05.0211 |
| 19319+2214 | 19 34 03.8 | +22 21 16 | 6 | 2 | 2 | 2 | | | 057.5494+01.2169 |
| 19323+1952 | 19 34 36.9 | +19 59 44 | 35 | 13 | 34 | 13 | | | 055.5493−00.0404 |
| 19327+0903 | 19 35 11.0 | +09 10 01 | 3 | 1 | | | | | |
| 19330+1245 | 19 35 20.1 | +12 52 13 | 1 | 1 | 3 | 4 | | | 049.3983−03.6463 |
| 19333+1918 | 19 35 30.8 | +19 25 08 | −3 | 3 | −3 | 1 | | | 055.1476−00.5059 |
| 19343+0912 | 19 36 45.0 | +09 18 53 | −3 | 0 | | | | | |
| 19343+2926 | 19 36 18.9 | +29 32 50 | 4 | 2 | 5 | 2 | | | 064.0964+04.2563 |

*Continue in the next page.*

*Table A.1: Astrometric data for the sources belonging to the 'Arecibo sample' (continued)*

| | Calar Alto | | CA–IRAS | | MSX–IRAS | | VLA–IRAS | | |
|---|---|---|---|---|---|---|---|---|---|
| IRAS | Coordinates | | $\Delta\alpha$ | $\Delta\delta$ | $\Delta\alpha$ | $\Delta\delta$ | $\Delta\alpha$ | $\Delta\delta$ | MSX6C_G |
| | (J2000) | | ["] | ["] | ["] | ["] | ["] | ["] | |
| 19344+0016 | 19 36 59.6 | +00 23 10 | 5 | 2 | | | | | |
| 19344+2457 | 19 36 32.1 | +25 04 13 | 0 | −1 | −1 | −1 | | | 060.1997+02.0410 |
| 19346+0913 | 19 36 59.3 | +09 20 22 | −27 | −4 | | | | | |
| 19347+2755 | 19 36 44.6 | +28 01 59 | −4 | 2 | −5 | 1 | | | 062.8140+03.4410 |
| 19352+1914 | 19 37 26.1 | +19 20 54 | 0 | 2 | 1 | 2 | | | 055.3079−00.9358 |
| 19352+2030 | 19 37 24.0 | +20 36 58 | 6 | 3 | 6 | 3 | | | 056.4095−00.3083 |
| 19359+1936 | 19 38 12.6 | +19 43 08 | 14 | 4 | 13 | 4 | | | 055.7201−00.9129 |
| 19360+3442 | 19 37 57.9 | +34 49 33 | 16 | 4 | | | 13 | 7 | |
| 19366+1149 | 19 39 01.8 | +11 56 46 | 0 | 1 | 0 | 1 | | | 049.0248−04.8833 |
| 19368+1935 | 19 39 04.3 | +19 43 05 | 30 | 12 | 31 | 11 | | | 055.8191−01.0910 |
| 19371+2855 | 19 39 07.8 | +29 02 39 | 4 | 2 | 3 | 2 | | | 063.9547+03.4762 |
| 19378+1256 | 19 40 13.4 | +13 03 11 | 3 | 3 | 2 | 2 | | | 050.1371−04.5985 |
| 19382+3400 | 19 40 08.0 | +34 07 18 | 4 | 3 | | | | | |
| 19386+1513 | 19 40 55.2 | +15 20 16 | −15 | −3 | −15 | −4 | −14 | −3 | 052.2174−03.6271 |
| 19387+1527 | 19 41 03.3 | +15 34 19 | 3 | 4 | −1 | 3 | | | 052.4371−03.5393 |
| 19395+1827 | 19 41 44.6 | +18 34 27 | 0 | 2 | −1 | 1 | | | 055.1339−02.2030 |
| 19395+1949 | 19 41 43.6 | +19 56 33 | 3 | 4 | 0 | 3 | | | 056.3217−01.5227 |
| 19396+2338 | 19 41 47.2 | +23 45 54 | −5 | 0 | −5 | 0 | | | 059.6502+00.3581 |
| 19412+0337 | 19 43 45.3 | +03 44 30 | 1 | 2 | | | | | |
| 19412+1042 | 19 43 36.7 | +10 49 18 | 3 | 1 | | | | | |
| 19413+2829 | 19 43 24.7 | +28 36 34 | −3 | −1 | −4 | 0 | | | 064.0387+02.4458 |
| 19414+2237 | 19 43 34.0 | +22 44 59 | 10 | 2 | 11 | 2 | | | 058.9725−00.5012 |
| 19422+3506 | 19 44 07.1 | +35 14 07 | 2 | 0 | | | | | |
| 19425+3323 | 19 44 30.0 | +33 30 38 | 8 | 4 | 11 | 2 | | | 068.4192+04.6717 |
| 19448+2653 | 19 46 54.4 | +27 00 33 | 7 | 3 | 5 | 3 | | | 063.0385+00.9765 |
| 19451+1628 | 19 47 26.6 | +16 35 36 | 0 | 3 | 0 | 3 | | | 054.0893−04.3667 |
| 19453+1917 | 19 47 36.2 | +19 24 54 | 18 | 5 | 16 | 5 | | | 056.5549−02.9845 |
| 19454+2536 | 19 47 30.7 | +25 43 32 | 1 | 2 | 1 | 1 | | | 061.9978+00.2122 |
| 19456+1927 | 19 47 49.7 | +19 35 24 | 7 | 4 | 9 | 3 | | | 056.7335−02.9435 |
| 19459+1716 | 19 48 10.5 | +17 24 06 | 3 | 2 | 1 | 1 | | | 054.8786−04.1132 |
| 19462+2232 | 19 48 26.4 | +22 39 55 | 10 | 0 | 7 | 1 | | | 059.4631−01.5148 |
| 19464+3514 | 19 48 16.0 | +35 22 06 | −2 | 2 | −10 | 4 | | | 070.4238+04.9252 |
| 19467+2213 | 19 48 52.6 | +22 21 18 | 10 | 3 | 7 | 4 | | | 059.2463−01.7586 |
| 19471+2944 | 19 49 10.5 | +29 52 33 | 0 | 1 | 0 | 1 | | | 065.7659+01.9926 |
| 19479+2111 | 19 50 07.4 | +21 19 04 | 1 | 1 | 0 | 4 | | | 058.4986−02.5337 |
| 19488+1346 | 19 51 09.5 | +13 54 37 | 2 | 2 | | | | | |
| 19488+1719 | 19 51 07.2 | +17 26 53 | 4 | 0 | 4 | 1 | | | 055.2740−04.6969 |
| 19490+1049 | 19 51 24.9 | +10 57 22 | 3 | 0 | | | | | |

*Continue in the next page.*

*Table A.1: Astrometric data for the sources belonging to the 'Arecibo sample' (continued)*

| IRAS | Calar Alto Coordinates (J2000) | | CA–IRAS | | MSX–IRAS | | VLA–IRAS | | MSX6C_G |
|---|---|---|---|---|---|---|---|---|---|
| | | | $\Delta\alpha$ ["] | $\Delta\delta$ ["] | $\Delta\alpha$ ["] | $\Delta\delta$ ["] | $\Delta\alpha$ ["] | $\Delta\delta$ ["] | |
| 19493+2905 | 19 51 21.2 | +29 13 01 | −16 | −1 | −16 | −1 | | | 065.4392+01.2497 |
| 19495+0835 | 19 51 57.7 | +08 42 55 | −3 | −1 | | | | | |
| 19499+2141 | 19 52 07.6 | +21 49 28 | −4 | −2 | −7 | 0 | −7 | 0 | 059.1720−02.6766 |
| 19500+2239 | 19 52 12.0 | +22 47 34 | −3 | 0 | −3 | −1 | | | 060.0139−02.1976 |
| 19508+2014 | 19 53 03.0 | +20 22 17 | 6 | 0 | 6 | 0 | | | 058.0311−03.6046 |
| 19508+2659 | 19 52 57.9 | +27 07 45 | 5 | 3 | 5 | 3 | | | 063.8275−00.1242 |
| 19516+2217 | 19 53 49.6 | +22 25 38 | −1 | −1 | −4 | 0 | | | 059.8920−02.7063 |
| 19520+2729 | 19 54 08.7 | +27 37 02 | 4 | 1 | 4 | 0 | | | 064.3806−00.0977 |
| 19522+1935 | 19 54 29.0 | +19 43 44 | 11 | 3 | 11 | 2 | 8 | 2 | 057.6498−04.2227 |
| 19522+2653 | 19 54 17.1 | +27 01 42 | 6 | 4 | 6 | 2 | | | 063.8919−00.4282 |
| 19527+2231 | 19 54 52.5 | +22 39 29 | 0 | 0 | −3 | 1 | | | 060.2147−02.7951 |
| 19529+3634 | 19 54 44.4 | +36 42 14 | 2 | 0 | 2 | 2 | | | 072.2449+04.4707 |
| 19534+2802 | 19 55 30.1 | +28 10 48 | 1 | 1 | 0 | −2 | 1 | 0 | 065.0168−00.0636 |
| 19535+2157 | 19 55 41.2 | +22 05 29 | −5 | 0 | −7 | 1 | | | 059.8256−03.2486 |
| 19547+1848 | 19 56 56.3 | +18 56 05 | −1 | 0 | 1 | −1 | | | 057.2650−05.1280 |
| 19565+3140 | 19 58 30.3 | +31 48 16 | 6 | 3 | 5 | 4 | | | 068.4510+01.2679 |
| 19566+3423 | 19 58 32.4 | +34 31 34 | 5 | 2 | 4 | 2 | | | 070.7766+02.6836 |
| 19573+2204 | 19 59 29.3 | +22 13 05 | 1 | 1 | −1 | −1 | | | 060.3907−03.9352 |
| 19575+1143 | 19 59 56.4 | +11 51 45 | 2 | 1 | | | | | |
| 19576+2814 | 19 59 39.3 | +28 23 06 | 6 | −1 | 8 | 3 | | | 065.6705−00.7365 |
| 19579+2926 | 19 59 55.8 | +29 34 32 | 5 | 2 | 7 | 3 | | | 066.7142−00.1623 |
| 19579+3223 | 19 59 51.3 | +32 32 09 | 4 | 1 | 4 | 2 | | | 069.2240+01.4077 |
| 19588+2541 | 20 00 54.4 | +25 49 54 | 7 | 4 | 7 | 4 | | | 063.6437−02.3167 |
| 20011+1752 | 20 03 25.0 | +18 00 28 | −10 | −4 | | | | | |
| 20015+3019 | 20 03 38.5 | +30 28 09 | 45 | 14 | 45 | 14 | | | 067.8975−00.3708 |
| 20023+2855 | 20 04 20.7 | +29 04 08 | 2 | 3 | 4 | 2 | | | 066.7943−01.2472 |
| 20024+1727 | 20 04 40.4 | +17 35 57 | 2 | 1 | | | 0 | 1 | |
| 20043+2653 | 20 06 22.9 | +27 02 09 | −1 | −2 | −3 | 0 | | | 065.3169−02.7141 |
| 20047+1248 | 20 07 05.4 | +12 57 06 | 3 | 2 | | | | | |
| 20052+0554 | 20 07 43.1 | +06 03 11 | −3 | −2 | | | | | |
| 20095+2726 | 20 11 36.2 | +27 35 58 | 15 | 4 | 13 | 3 | | | 066.4198−03.3844 |
| 20097+1107 | 20 12 09.2 | +11 16 51 | 3 | 1 | | | | | |
| 20110+3555 | 20 12 59.0 | +36 05 03 | 0 | 2 | −2 | −1 | | | 073.6728+01.0322 |
| 20115+0844 | 20 13 58.5 | +08 53 23 | 6 | 0 | | | 6 | 1 | |
| 20123+0429 | 20 14 50.3 | +04 38 55 | 1 | −1 | | | | | |
| 20127+2430 | 20 14 57.0 | +24 39 23 | 24 | 5 | | | | | |
| 20137+2838 | 20 15 47.7 | +28 47 55 | 4 | 3 | 4 | 2 | | | 067.9320−03.4954 |
| 20140+3620 | 20 15 54.1 | +36 30 05 | −1 | 0 | −1 | 0 | | | 074.3470+00.7740 |

*Continue in the next page.*

*Table A.1: Astrometric data for the sources belonging to the ‘Arecibo sample’ (continued)*

| IRAS | Calar Alto Coordinates (J2000) | | CA–IRAS | | MSX–IRAS | | VLA–IRAS | | MSX6C_G |
|---|---|---|---|---|---|---|---|---|---|
| | | | $\Delta\alpha$ [”] | $\Delta\delta$ [”] | $\Delta\alpha$ [”] | $\Delta\delta$ [”] | $\Delta\alpha$ [”] | $\Delta\delta$ [”] | |
| 20149+3440 | 20 16 50.6 | +34 49 27 | 1 | 4 | 6 | 6 | | | 073.0636−00.3219 |
| 20153+2057 | 20 17 36.8 | +21 07 10 | 11 | 3 | | | | | |
| 20156+2130 | 20 17 48.9 | +21 40 04 | 4 | 0 | | | | | |
| 20160+2734 | 20 18 05.9 | +27 44 04 | 1 | 4 | 0 | 3 | | | 067.3287−04.5088 |
| 20171+2732 | 20 19 11.1 | +27 42 12 | 1 | 2 | 3 | 2 | | | 067.4383−04.7259 |
| 20181+2234 | 20 20 21.9 | +22 43 47 | 0 | 0 | | | | | |
| 20194+1707 | 20 21 42.7 | +17 17 18 | −27 | −7 | | | | | |
| 20211+3100 | 20 23 08.6 | +31 10 08 | 0 | 3 | 0 | 2 | | | 070.7921−03.4769 |
| 20215+3205 | 20 23 36.2 | +32 15 11 | 13 | 5 | 13 | 4 | | | 071.7392−02.9375 |
| 20246+1456 | 20 26 56.7 | +15 06 02 | −2 | 0 | | | | | |
| 20246+2813 | 20 26 46.6 | +28 23 59 | 10 | 6 | | | 9 | 7 | |
| 20267+2105 | 20 28 57.3 | +21 15 39 | 4 | 3 | | | | | |
| 20272+3535 | 20 29 08.4 | +35 45 44 | 5 | 5 | 6 | 3 | | | 075.2679−01.8424 |
| 20280+2631 | 20 30 08.6 | +26 41 37 | 9 | 5 | | | | | |
| 20296+3355 | 20 31 40.2 | +34 05 37 | 4 | 4 | 3 | 4 | | | 074.2214−03.2416 |
| 20351+3450 | 20 37 08.0 | +35 01 11 | 6 | 3 | 7 | 3 | | | 075.6383−03.5936 |
| 20363+3401 | 20 38 19.9 | +34 12 21 | 0 | 0 | −1 | −1 | | | 075.1358−04.2808 |
| 20403+3143 | 20 42 20.6 | +31 54 29 | 3 | 0 | | | | | |
| 20403+3700 | 20 42 18.5 | +37 11 41 | −1 | 1 | −1 | −1 | | | 078.0039−03.1009 |
| 20410+2949 | 20 43 06.8 | +30 00 38 | 3 | 1 | | | | | |
| 20423+2742 | 20 44 29.5 | +27 53 04 | 3 | 1 | | | | | |
| 20432+3151 | 20 45 20.7 | +32 02 41 | 5 | 4 | | | | | |
| 20440+0412 | 20 46 33.2 | +04 23 35 | −3 | −3 | | | | | |
| 20444+0540 | 20 46 53.9 | +05 51 28 | −3 | −3 | | | | | |
| 20460+3253 | 20 48 03.4 | +33 05 02 | −2 | 0 | | | | | |
| 20482+3325 | 20 50 18.0 | +33 36 33 | −3 | 1 | | | −2 | 1 | |
| 20529+3013 | 20 55 05.6 | +30 24 51 | 3 | 2 | | | | | |
| 20531+2909 | 20 55 17.8 | +29 20 49 | 0 | 0 | | | −1 | 2 | |
| 20547+0247 | 20 57 16.4 | +02 58 44 | 0 | −2 | | | | | |
| 21062+0058 | 21 08 47.7 | +01 10 14 | 3 | 1 | | | | | |
| 21074+1812 | 21 09 46.6 | +18 24 50 | 3 | 4 | | | | | |
| 21100+2205 | 21 12 16.7 | +22 17 55 | −4 | −2 | | | | | |
| 21120+0736 | 21 14 29.6 | +07 48 35 | 6 | 2 | | | 6 | 2 | |
| 21174+1747 | 21 19 45.0 | +18 00 30 | −3 | −3 | | | −2 | −7 | |
| 21305+2118 | 21 32 53.7 | +21 32 00 | 38 | 18 | | | | | |
| 21576+3259 | 21 59 50.4 | +33 13 59 | 16 | 11 | | | | | |
| 22180+3225 | 22 20 20.1 | +32 40 28 | −14 | −11 | | | | | |
| 22402+1045 | 22 42 47.2 | +11 00 53 | 6 | 2 | | | | | |

*Continue in the next page.*

*Table A.1: Astrometric data for the sources belonging to the 'Arecibo sample' (continued)*

| IRAS | Calar Alto Coordinates (J2000) | | CA–IRAS Δ$\alpha$ ["] | CA–IRAS Δ$\delta$ ["] | MSX–IRAS Δ$\alpha$ ["] | MSX–IRAS Δ$\delta$ ["] | VLA–IRAS Δ$\alpha$ ["] | VLA–IRAS Δ$\delta$ ["] | MSX6C_G |
|---|---|---|---|---|---|---|---|---|---|
| 22510+3614 | 22 53 20.4 | +36 30 26 | 0 | 2 | | | | | |
| 22516+0838 | 22 54 11.5 | +08 54 07 | −6 | −5 | | | −6 | −5 | |
| 22517+2223 | 22 54 12.0 | +22 39 34 | −6 | −1 | | | | | |

# Appendix B

# NIR photometry of the sources in the ‘Arecibo sample’

**Table B.1**: Calar Alto photometry of the 371 Arecibo OH/IR stars measured.

| IRAS | Julian Date | Calar Alto photometry [mag] | | |
|---|---|---|---|---|
| | (2450000+) | J | H | K |
| 01037+1219 | 1747 | 8.47 ± 0.02 | 5.16 ± 0.01 | 3.45 ± 0.12 |
| 01085+3022 | 1744 | 4.88 ± 0.03 | 3.50 ± 0.05 | 3.10 ± 0.12 |
| 02404+2150 | 1747 | 5.02 ± 0.04 | 4.09 ± 0.04 | 3.81 ± 0.05 |
| 02420+1206 | 1750 | 5.02 ± 0.13 | 4.03 ± 0.10 | 3.40 ± 0.15 |
| 02547+1106 | 1750 | 5.48 ± 0.01 | 4.41 ± 0.01 | 4.18 ± 0.16 |
| 03507+1115 | 1752 | 2.46 ± 0.14 | 0.87 ± 0.07 | −0.15 ± 0.07 |
| 12562+2324 | 1745 | 5.48 ± 0.02 | 4.64 ± 0.02 | 4.41 ± 0.04 |
| 15060+0947 | 1746 | 6.38 ± 0.31 | 5.28 ± 0.04 | 5.27 ± 0.10 |
| 15262+0400 | 1746 | 4.31 ± 0.05 | 3.49 ± 0.06 | 3.06 ± 0.13 |
| 16235+1900 | 1747 | 1.69 ± 0.04 | 0.80 ± 0.02 | 0.38 ± 0.04 |
| 16503+0529 | 1744 | 4.16 ± 0.04 | 3.24 ± 0.03 | 2.92 ± 0.04 |
| 16523+0745 | 1745 | 6.15 ± 0.01 | 5.31 ± 0.01 | 4.92 ± 0.03 |
| 16560+2252 | 1745 | 5.38 ± 0.20 | 4.69 ± 0.04 | 4.49 ± 0.21 |
| 17050+1714 | 1745 | 5.64 ± 0.10 | 4.83 ± 0.09 | 4.58 ± 0.14 |
| 17230+0113 | 1745 | 5.77 ± 0.07 | 4.62 ± 0.16 | 4.45 ± 0.14 |
| 17256+0504 | 1745 | 5.69 ± 0.32 | 4.84 ± 0.10 | 4.66 ± 0.12 |
| 17308+0822 | 1744 | 11.57 ± 0.04 | 9.17 ± 0.01 | 7.24 ± 0.01 |
| 17338+0051 | 1362 | 6.56 ± 0.01 | 5.65 ± 0.11 | 5.18 ± 0.03 |

*Continue in the next page.*

*Table B.1: Near-IR photometry of the sources in the 'Arecibo sample' (continued)*

| IRAS | Julian Date (2450000+) | Calar Alto photometry [mag] J | H | K |
|---|---|---|---|---|
| 17528+1144 | 1745 | 7.96 ± 0.01 | 6.84 ± 0.01 | 6.14 ± 0.02 |
| 17554+2946 | 1745 | 3.71 ± 0.07 | 2.83 ± 0.04 | 2.56 ± 0.12 |
| 17579+2335 | 1746 | 3.56 ± 0.03 | 2.79 ± 0.05 | 2.34 ± 0.12 |
| 18033+2229 | 1746 | 5.08 ± 0.04 | 4.29 ± 0.05 | 3.98 ± 0.11 |
| 18069+0911 | 1746 | 7.16 ± 0.01 | 5.26 ± 0.01 | 4.47 ± 0.18 |
| 18076+3445 | 1744 | 7.34 ± 0.02 | 5.68 ± 0.01 | 4.92 ± 0.28 |
| 18085+0752 | 1744 | 5.76 ± 0.01 | 4.91 ± 0.02 | 4.58 ± 0.10 |
| 18095+2704 | 1747 | 7.43 ± 0.04 | 6.74 ± 0.02 | 6.48 ± 0.03 |
| 18099+3127 | 1363 | 5.83 ± 0.02 | 4.86 ± 0.01 | 4.46 ± 0.11 |
| 18123+0511 | 1744 | 7.87 ± 0.02 | 7.33 ± 0.01 | 6.68 ± 0.01 |
| 18170+0353 | 1367 | 13.36 ± 0.11 | 10.80 ± 0.02 | 8.49 ± 0.02 |
| 18203+0723 | 1747 | 7.12 ± 0.49 | 5.86 ± 0.01 | 5.33 ± 0.03 |
| 18223+1217 | 1368 | 7.71 ± 0.02 | 6.82 ± 0.02 | 6.09 ± 0.01 |
| 18231+0855 | 1368 | 8.15 ± 0.01 | 6.94 ± 0.01 | 6.18 ± 0.02 |
| 18236+0706 | 1369 | 7.76 ± 0.01 | 6.93 ± 0.02 | 6.25 ± 0.01 |
| 18237+2150 | 1367 | 6.63 ± 0.02 | 5.77 ± 0.02 | 5.31 ± 0.02 |
| 18251+0023 | 1744 | 10.54 ± 0.01 | 8.28 ± 0.01 | 6.63 ± 0.02 |
| 18254+0750 | 1368 | 9.94 ± 0.02 | 8.20 ± 0.01 | 6.86 ± 0.01 |
| 18262+0934 | 1744 | 7.83 ± 0.02 | 6.89 ± 0.37 | 5.87 ± 0.01 |
| 18270+0326 | 1744 | 6.86 ± 0.02 | 5.64 ± 0.06 | 4.72 ± 0.07 |
| 18276+0839 | 1368 | 7.86 ± 0.02 | 6.93 ± 0.01 | 6.27 ± 0.01 |
| 18278+0931 | 1744 | 7.67 ± 0.02 | 6.38 ± 0.38 | 5.48 ± 0.08 |
| 18307+0102 | 1744 | 10.78 ± 0.03 | 8.70 ± 0.02 | 7.11 ± 0.01 |
| 18318+0150 | 1368 | 10.88 ± 0.01 | 8.46 ± 0.01 | 6.77 ± 0.01 |
| 18333+0903 | 1368 | 7.97 ± 0.01 | 6.74 ± 0.01 | 5.85 ± 0.02 |
| 18341+0005 | 1363 | 9.78 ± 0.01 | 7.33 ± 0.01 | 5.81 ± 0.02 |
| 18347+1113 | 1369 | 7.75 ± 0.01 | 6.85 ± 0.02 | 6.31 ± 0.02 |
| 18349+1023 | 1750 | 3.60 ± 0.09 | 2.22 ± 0.10 | 1.22 ± 0.10 |
| 18353+0020 | 1744 | > 15.25 ——— | > 14.75 ——— | 12.49 ± 0.11 |
| 18355+0227 | 1744 | 7.81 ± 0.01 | 6.24 ± 0.01 | 5.28 ± 0.02 |
| 18362+0538 | 1744 | 7.50 ± 0.01 | 6.11 ± 0.02 | 5.26 ± 0.02 |
| 18375+0510 | 1744 | 9.76 ± 0.03 | 7.99 ± 0.01 | 6.51 ± 0.01 |
| 18381+0020 | 1363 | 8.65 ± 0.01 | 6.27 ± 0.01 | 4.79 ± 0.01 |
| 18395+0130 | 1744 | > 15.25 ——— | > 14.50 ——— | >13.50 ——— |

*Continue in the next page.*

*Table B.1: Near-IR photometry of the sources in the 'Arecibo sample' (continued)*

| IRAS | Julian Date | Calar Alto photometry [mag] | | |
|---|---|---|---|---|
| | (2450000+) | J | H | K |
| 18397+0758 | 1366 | 7.09 ± 0.02 | 6.04 ± 0.01 | 5.24 ± 0.01 |
| 18398+0728 | 1366 | 11.29 ± 0.04 | 8.93 ± 0.02 | 7.13 ± 0.01 |
| 18398+1035 | 1367 | < 5.37 ——— | 4.78 ± 0.10 | 3.58 ± 0.10 |
| 18400+0123 | 1744 | 9.64 ± 0.01 | 7.70 ± 0.01 | 6.50 ± 0.01 |
| 18407+0350 | 1368 | 7.44 ± 0.02 | 6.32 ± 0.01 | 5.69 ± 0.03 |
| 18407+0601 | 1367 | 8.69 ± 0.31 | 6.80 ± 0.02 | 5.79 ± 0.01 |
| 18408+0730 | 1746 | 9.09 ± 0.01 | 7.53 ± 0.01 | 6.51 ± 0.01 |
| 18409+0431 | 1745 | 6.77 ± 0.02 | 5.15 ± 0.01 | 4.82 ± 0.18 |
| 18415+0404 | 1745 | 8.55 ± 0.03 | 6.70 ± 0.02 | 5.65 ± 0.01 |
| 18420+1137 | 1369 | 10.77 ± 0.02 | 9.11 ± 0.01 | 7.85 ± 0.01 |
| 18430+0039 | 1745 | 11.99 ± 0.03 | 9.55 ± 0.01 | 7.91 ± 0.02 |
| 18433+0039 | 1745 | 13.07 ± 0.03 | 9.40 ± 0.03 | 7.09 ± 0.02 |
| 18435+0745 | 1369 | > 14.75 ——— | 12.23 ± 0.08 | 10.03 ± 0.03 |
| 18441+0311 | 1365 | 9.74 ± 0.11 | 7.72 ± 0.07 | 6.49 ± 0.08 |
| 18441+2216 | 1369 | 8.15 ± 0.34 | 6.84 ± 0.02 | 6.15 ± 0.01 |
| 18444+0734 | 1369 | 7.90 ± 0.03 | 6.58 ± 0.01 | 5.64 ± 0.01 |
| 18455+0448 | 1365 | > 15.75 ——— | 13.39 ± 0.10 | 11.34 ± 0.08 |
| 18475+0353 | 1745 | > 14.25 ——— | > 14.00 ——— | >13.25 ——— |
| 18476+0555 | 1745 | 8.22 ± 0.01 | 5.96 ± 0.02 | 4.71 ± 0.09 |
| 18477+0243 | 1367 | 10.72 ± 0.03 | 8.27 ± 0.02 | 6.69 ± 0.02 |
| 18481+0405 | 1745 | > 15.25 ——— | > 13.50 ——— | >12.50 ——— |
| 18487+0152 | 1746 | 13.53 ± 0.11 | 9.35 ± 0.01 | 6.53 ± 0.02 |
| 18487+0617 | 1367 | 11.31 ± 0.04 | 8.80 ± 0.02 | 7.13 ± 0.01 |
| 18490+0302 | 1367 | 12.08 ± 0.06 | 8.87 ± 0.01 | 6.75 ± 0.01 |
| 18490+1158 | 1367 | 7.22 ± 0.05 | 5.85 ± 0.03 | 4.96 ± 0.10 |
| 18497+0200 | 1746 | > 15.75 ——— | > 14.50 ——— | 12.89 ± 0.51 |
| 18498−0017 | 1746 | > 14.50 ——— | > 13.75 ——— | >12.75 ——— |
| 18499+1224 | 1367 | 7.37 ± 0.02 | 6.32 ± 0.03 | 5.64 ± 0.01 |
| 18501+0013 | 1746 | > 13.00 ——— | > 12.75 ——— | >12.25 ——— |
| 18501+1019 | 1746 | 11.89 ± 0.03 | 9.34 ± 0.01 | 7.61 ± 0.01 |
| 18506+0912 | 1366 | 8.08 ± 0.02 | 6.26 ± 0.01 | 5.06 ± 0.02 |
| 18511+1141 | 1747 | 10.92 ± 0.41 | 8.73 ± 0.03 | 7.47 ± 0.03 |
| 18512+2029 | 1746 | 11.49 ± 0.05 | 8.82 ± 0.10 | 6.83 ± 0.03 |
| 18517+0037 | 1369 | > 14.50 ——— | > 13.75 ——— | >12.50 ——— |

*Continue in the next page.*

*Table B.1: Near-IR photometry of the sources in the 'Arecibo sample' (continued)*

| IRAS | Julian Date (2450000+) | Calar Alto photometry [mag] J | H | K |
|---|---|---|---|---|
| 18518+0358 | 1746 | 10.89 ± 0.05 | 8.47 ± 0.01 | 6.67 ± 0.02 |
| 18520+0533 | 1746 | 12.69 ± 0.37 | 11.16 ± 0.03 | 10.23 ± 0.06 |
| 18520+1014 | 1746 | 7.55 ± 0.02 | 6.09 ± 0.02 | 5.10 ± 0.01 |
| 18525+0210 | 1365 | > 15.50 ——— | > 14.75 ——— | 12.72 ± 0.15 |
| 18530+0507 | 1746 | 10.80 ± 0.03 | 7.57 ± 0.01 | 5.72 ± 0.01 |
| 18535+0726 | 1363 | 12.69 ± 0.03 | 9.86 ± 0.02 | 7.94 ± 0.01 |
| 18540+0302 | 1746 | 13.27 ± 1.03 | 9.04 ± 0.04 | 6.38 ± 0.01 |
| 18542+0940 | 1368 | 7.44 ± 0.02 | 6.11 ± 0.01 | 5.33 ± 0.01 |
| 18548+0823 | 1367 | 12.83 ± 0.05 | 10.09 ± 0.05 | 8.12 ± 0.02 |
| 18549+0208 | | no photometric measurement | | |
| 18549+0905 | 1746 | 6.61 ± 0.01 | 5.09 ± 0.01 | 4.33 ± 0.02 |
| 18551+0159 | 1369 | > 15.00 ——— | 12.17 ± 0.08 | 10.51 ± 0.05 |
| 18551+0323 | 1363 | 14.40 ± 0.14 | 10.56 ± 0.07 | 7.43 ± 0.01 |
| 18554+0231 | 1363 | 8.74 ± 0.01 | 5.89 ± 0.01 | 4.43 ± 0.04 |
| 18554+1333 | 1368 | 7.89 ± 0.03 | 6.63 ± 0.01 | 5.81 ± 0.01 |
| 18556+0811 | 1363 | 6.97 ± 0.01 | 5.25 ± 0.04 | 4.26 ± 0.13 |
| 18556+1409 | 1369 | 11.62 ± 0.01 | 9.27 ± 0.01 | 7.42 ± 0.01 |
| 18560+0638 | 1751 | 13.32 ± 0.09 | 9.06 ± 0.10 | 5.88 ± 0.05 |
| 18563+0816 | 1366 | > 15.00 ——— | 12.52 ± 0.04 | 10.04 ± 0.01 |
| 18567+0003 | 1746 | 9.95 ± 0.04 | 7.45 ± 0.05 | 5.68 ± 0.01 |
| 18567+1046 | 1746 | 7.02 ± 0.03 | 5.47 ± 0.02 | 4.61 ± 0.01 |
| 18568+0550 | 1367 | > 15.25 ——— | > 14.75 ——— | >13.25 ——— |
| 18568+2554 | 1369 | 8.83 ± 0.01 | 7.86 ± 0.01 | 7.07 ± 0.02 |
| 18569+0553 | 1367 | > 15.00 ——— | > 14.25 ——— | >12.00 ——— |
| 18569+1722 | 1369 | 6.69 ± 0.01 | 5.74 ± 0.02 | 5.10 ± 0.03 |
| 18571+0611 | 1367 | > 15.25 ——— | 13.08 ± 0.10 | 10.21 ± 0.03 |
| 18572+0618 | 1367 | 9.01 ± 0.02 | 6.77 ± 0.03 | 5.39 ± 0.01 |
| 18577+1047 | 1746 | 9.16 ± 0.02 | 7.81 ± 0.01 | 7.01 ± 0.01 |
| 18578+0831 | 1366 | 10.87 ± 0.05 | 7.88 ± 0.04 | 5.69 ± 0.01 |
| 18581+1405 | 1366 | 8.15 ± 0.01 | 7.17 ± 0.40 | 5.83 ± 0.01 |
| 18585+0900 | 1363 | 12.23 ± 0.18 | 8.68 ± 0.03 | 6.01 ± 0.01 |
| 18588+1400 | 1366 | 10.08 ± 0.02 | 8.28 ± 0.02 | 6.74 ± 0.02 |
| 18592+1455 | 1745 | 5.81 ± 0.01 | 4.65 ± 0.04 | 4.26 ± 0.17 |
| 18593+1009 | 1367 | 10.01 ± 0.02 | 7.80 ± 0.01 | 6.39 ± 0.01 |

*Continue in the next page.*

*Table B.1: Near-IR photometry of the sources in the 'Arecibo sample' (continued)*

| IRAS | Julian Date | Calar Alto photometry [mag] | | |
|---|---|---|---|---|
| | (2450000+) | J | H | K |
| 18596+0315 | 1752 | > 13.75 ——— | > 12.50 ——— | >13.00 ——— |
| 19006+0624 | 1746 | > 14.50 ——— | > 13.75 ——— | >13.00 ——— |
| 19007+1652 | 1749 | 8.44 ± 0.01 | 7.04 ± 0.02 | 6.20 ± 0.02 |
| 19008+0907 | 1368 | 10.69 ± 0.02 | 8.22 ± 0.01 | 6.36 ± 0.01 |
| 19010+0526 | 1750 | > 15.25 ——— | 12.45 ± 0.14 | 8.43 ± 0.04 |
| 19010+1307 | 1749 | 11.38 ± 0.07 | 8.40 ± 0.01 | 6.51 ± 0.02 |
| 19012+1128 | 1367 | 8.55 ± 0.02 | 7.02 ± 0.03 | 6.06 ± 0.02 |
| 19017+0412 | 1363 | > 14.75 ——— | 11.13 ± 0.08 | 7.93 ± 0.03 |
| 19017+0608 | 1362 | > 14.75 ——— | 13.74 ± 0.09 | 9.40 ± 0.01 |
| 19023+0745 | 1746 | 13.09 ± 0.26 | 9.79 ± 0.03 | 7.41 ± 0.01 |
| 19024+1923 | 1746 | 9.49 ± 0.02 | 7.07 ± 0.02 | 5.66 ± 0.02 |
| 19026+0336 | 1747 | > 14.25 ——— | > 13.75 ——— | 11.01 ± 0.08 |
| 19026+1300 | 1749 | > 16.00 ——— | 12.65 ± 0.10 | 10.00 ± 0.07 |
| 19027+1341 | 1368 | 13.24 ± 0.11 | 10.66 ± 0.02 | 8.70 ± 0.05 |
| 19028+1613 | 1362 | 10.56 ± 0.03 | 8.95 ± 0.36 | 7.42 ± 0.03 |
| 19029+0933 | | No photometry: Blended | | |
| 19035+0451 | 1747 | 8.67 ± 0.05 | 6.12 ± 0.01 | 4.85 ± 0.05 |
| 19035+0801 | 1365 | > 15.00 ——— | > 14.00 ——— | >13.25 ——— |
| 19035+1010 | 1366 | 8.70 ± 0.01 | 6.79 ± 0.01 | 5.59 ± 0.01 |
| 19041+0952 | 1366 | 12.96 ± 0.29 | 9.92 ± 0.02 | 7.76 ± 0.01 |
| 19041+1734 | 1362 | 9.10 ± 0.01 | 7.68 ± 0.06 | 6.58 ± 0.03 |
| 19043+1009 | 1363 | 9.43 ± 0.01 | 7.09 ± 0.03 | 5.35 ± 0.02 |
| 19047+0924 | 1366 | > 15.00 ——— | 13.29 ± 0.16 | 10.19 ± 0.04 |
| 19052+0922 | 1749 | 10.74 ± 0.09 | 7.94 ± 0.03 | 5.98 ± 0.02 |
| 19052+1431 | 1369 | 9.80 ± 0.02 | 8.09 ± 0.01 | 6.95 ± 0.03 |
| 19054+0419 | 1369 | > 14.50 ——— | 11.77 ± 0.06 | 9.28 ± 0.02 |
| 19055+0225 | 1747 | > 14.75 ——— | 11.70 ± 0.05 | 9.64 ± 0.05 |
| 19057+0141 | 1368 | 10.19 ± 0.03 | 8.60 ± 0.01 | 7.35 ± 0.03 |
| 19060+1612 | 1369 | 5.66 ± 0.02 | 4.72 ± 0.05 | 3.96 ± 0.08 |
| 19061+1041 | 1362 | 10.90 ± 0.03 | 8.42 ± 0.03 | 6.77 ± 0.03 |
| 19065+0832 | 1363 | 9.42 ± 0.01 | 7.66 ± 0.02 | 6.96 ± 0.01 |
| 19067+0811 | 1750 | > 15.50 ——— | > 14.75 ——— | >13.25 ——— |
| 19068+0016 | 1368 | 10.18 ± 0.02 | 7.95 ± 0.02 | 6.48 ± 0.01 |
| 19068+1127 | 1752 | 9.19 ± 0.01 | 6.79 ± 0.03 | 5.37 ± 0.01 |

*Continue in the next page.*

*Table B.1: Near-IR photometry of the sources in the 'Arecibo sample' (continued)*

| IRAS | Julian Date | Calar Alto photometry [mag] | | |
|---|---|---|---|---|
| | (2450000+) | J | H | K |
| 19069+0916 | 1366 | > 15.25 ——— | 11.64 ± 0.11 | 8.35 ± 0.04 |
| 19071+0946 | 1749 | > 15.50 ——— | > 14.25 ——— | 11.44 ± 0.05 |
| 19074+0336 | 1368 | 11.35 ± 0.03 | 9.11 ± 0.01 | 7.62 ± 0.01 |
| 19075+1147 | 1362 | > 14.25 ——— | > 13.75 ——— | 11.15 ± 0.01 |
| 19076+1247 | 1368 | 10.65 ± 0.03 | 8.95 ± 0.01 | 7.80 ± 0.02 |
| 19079+1143 | 1366 | 11.54 ± 0.09 | 9.13 ± 0.02 | 7.51 ± 0.01 |
| 19081+0322 | 1747 | > 14.50 ——— | > 14.00 ——— | 11.84 ± 0.07 |
| 19083+0851 | 1363 | 8.32 ± 0.02 | 5.94 ± 0.02 | 4.71 ± 0.06 |
| 19085+0755 | 1366 | > 15.50 ——— | > 14.75 ——— | 9.72 ± 0.01 |
| 19087+0323 | 1747 | 12.32 ± 0.22 | 9.58 ± 0.02 | 7.32 ± 0.03 |
| 19088+1129 | 1366 | 8.00 ± 0.02 | 6.47 ± 0.02 | 5.44 ± 0.01 |
| 19097+0411 | 1365 | 10.45 ± 0.11 | 7.89 ± 0.07 | 6.27 ± 0.08 |
| 19112+0819 | 1749 | > 14.75 ——— | > 13.75 ——— | 10.69 ± 0.13 |
| 19115+0752 | 1366 | 10.71 ± 0.05 | 8.52 ± 0.01 | 7.20 ± 0.02 |
| 19116+1511 | 1368 | 8.07 ± 0.01 | 6.83 ± 0.01 | 6.01 ± 0.01 |
| 19117+1558 | 1362 | 11.00 ± 0.02 | 8.94 ± 0.38 | 7.22 ± 0.01 |
| 19128+0910 | 1366 | > 15.00 ——— | > 14.25 ——— | 11.70 ± 0.17 |
| 19128+1310 | 1366 | 13.97 ± 0.03 | 9.95 ± 0.01 | 7.13 ± 0.01 |
| 19129+2803 | 1746 | 7.97 ± 0.01 | 6.58 ± 0.01 | 5.53 ± 0.01 |
| 19131+1157 | 1363 | 10.44 ± 0.02 | 7.64 ± 0.04 | 5.74 ± 0.01 |
| 19140+0652 | 1366 | 13.29 ± 0.45 | 10.24 ± 0.05 | 8.10 ± 0.03 |
| 19147+1349 | 1365 | 11.92 ± 0.11 | 8.74 ± 0.07 | 6.68 ± 0.08 |
| 19149+1638 | 1752 | 10.28 ± 0.06 | 7.67 ± 0.01 | 6.37 ± 0.06 |
| 19160+0755 | 1367 | > 15.00 ——— | 11.09 ± 0.05 | 8.52 ± 0.04 |
| 19161+2343 | 1366 | 13.58 ± 0.08 | 9.60 ± 0.04 | 6.24 ± 0.01 |
| 19162+0607 | 1368 | 10.72 ± 0.01 | 9.05 ± 0.02 | 7.94 ± 0.01 |
| 19167+1733 | 1368 | 8.07 ± 0.03 | 6.43 ± 0.36 | 5.13 ± 0.01 |
| 19168+0814 | 1750 | 5.49 ± 0.01 | 4.73 ± 0.03 | < 4.11 ——— |
| 19172+1956 | 1752 | > 15.25 ——— | 12.07 ± 0.03 | 8.84 ± 0.02 |
| 19175+0958 | 1368 | 13.21 ± 0.04 | 10.32 ± 0.02 | 8.22 ± 0.02 |
| 19175+1042 | 1752 | 12.11 ± 0.03 | 9.77 ± 0.02 | 7.56 ± 0.01 |
| 19176+1939 | 1368 | 8.38 ± 0.02 | 6.78 ± 0.01 | 5.84 ± 0.02 |
| 19177+1333 | 1752 | > 13.75 ——— | 13.23 ± 0.50 | 10.28 ± 0.05 |
| 19178+1206 | 1368 | > 14.75 ——— | 14.19 ± 0.18 | 13.54 ± 0.88 |

*Continue in the next page.*

*Table B.1: Near-IR photometry of the sources in the 'Arecibo sample' (continued)*

| IRAS | Julian Date | Calar Alto photometry [mag] | | |
|---|---|---|---|---|
| | (2450000+) | J | H | K |
| 19183+1148 | 1368 | > 14.75 ——— | > 13.50 ——— | >12.50 ——— |
| 19184+1055 | 1750 | > 15.00 ——— | 11.83 ± 0.23 | 8.87 ± 0.01 |
| 19186+0315 | 1365 | 9.78 ± 0.11 | 7.92 ± 0.07 | 6.31 ± 0.09 |
| 19186+1657 | 1363 | 7.24 ± 0.01 | 5.66 ± 0.02 | 4.71 ± 0.03 |
| 19187+2221 | 1368 | 10.14 ± 0.03 | 8.05 ± 0.01 | 6.88 ± 0.02 |
| 19188+1057 | 1750 | > 15.00 ——— | > 14.00 ——— | >12.75 ——— |
| 19189+1758 | 1361 | 6.22 ± 0.01 | < 6.05 ——— | 4.30 ± 0.04 |
| 19190+1128 | 1363 | 14.49 ± 0.11 | 10.69 ± 0.41 | 7.21 ± 0.02 |
| 19190+3035 | 1368 | 13.36 ± 0.13 | 10.90 ± 0.05 | 9.13 ± 0.03 |
| 19192+0922 | 1752 | 11.18 ± 0.03 | 8.20 ± 0.02 | 6.21 ± 0.01 |
| 19195+0522 | 1752 | 6.46 ± 0.34 | 5.26 ± 0.11 | 4.57 ± 0.09 |
| 19195+1747 | 1747 | 6.92 ± 0.01 | 5.27 ± 0.01 | 4.40 ± 0.04 |
| 19200+1035 | 1361 | 9.55 ± 0.02 | 8.00 ± 0.01 | 7.18 ± 0.01 |
| 19200+1536 | 1368 | > 14.75 ——— | > 14.25 ——— | 11.21 ± 0.06 |
| 19201+1040 | 1367 | 13.40 ± 0.03 | 10.61 ± 0.05 | 7.76 ± 0.03 |
| 19201+2101 | 1745 | > 15.25 ——— | > 14.75 ——— | 10.03 ± 0.01 |
| 19206+2121 | 1744 | 10.73 ± 0.02 | 8.57 ± 0.02 | 7.02 ± 0.01 |
| 19206+2216 | 1368 | 10.58 ± 0.03 | 8.59 ± 0.01 | 7.02 ± 0.01 |
| 19206+2517 | 1368 | 7.89 ± 0.03 | 6.61 ± 0.01 | 5.85 ± 0.02 |
| 19214+0513 | 1367 | 8.63 ± 0.01 | 6.76 ± 0.02 | 5.57 ± 0.02 |
| 19218+0425 | 1369 | 7.94 ± 0.02 | 6.72 ± 0.02 | 5.87 ± 0.01 |
| 19229+1708 | 1363 | 6.69 ± 0.02 | < 5.15 ——— | < 4.36 ——— |
| 19231+3555 | 1750 | 5.34 ± 0.01 | 4.11 ± 0.01 | 3.11 ± 0.06 |
| 19237+1430 | 1362 | 8.94 ± 0.01 | 6.78 ± 0.03 | 5.40 ± 0.05 |
| 19241+3457 | 1750 | 5.37 ± 0.07 | 4.34 ± 0.03 | 3.82 ± 0.09 |
| 19248+1122 | 1750 | 5.66 ± 0.05 | 4.43 ± 0.06 | 3.52 ± 0.09 |
| 19248+1441 | 1752 | 7.68 ± 0.01 | 5.87 ± 0.02 | 4.81 ± 0.01 |
| 19252+2420 | 1368 | 10.35 ± 0.05 | 8.48 ± 0.01 | 7.29 ± 0.04 |
| 19253+1114 | 1363 | 8.08 ± 0.01 | 6.81 ± 0.02 | 6.07 ± 0.01 |
| 19254+1631 | 1747 | > 14.75 ——— | > 14.25 ——— | >13.00 ——— |
| 19256+0254 | 1752 | 9.88 ± 0.04 | 8.16 ± 0.03 | 6.96 ± 0.02 |
| 19258+1111 | 1363 | 7.62 ± 0.01 | 6.45 ± 0.02 | 5.69 ± 0.02 |
| 19259+0510 | 1367 | 5.66 ± 0.02 | 4.57 ± 0.07 | 3.68 ± 0.17 |
| 19261+1003 | 1361 | 10.53 ± 0.04 | 8.60 ± 0.07 | 7.50 ± 0.02 |

*Continue in the next page.*

*Table B.1: Near-IR photometry of the sources in the ‘Arecibo sample’ (continued)*

| IRAS | Julian Date (2450000+) | Calar Alto photometry [mag] J | H | K |
|---|---|---|---|---|
| 19261+1435 | 1752 | 11.84 ± 0.21 | 8.78 ± 0.04 | 6.91 ± 0.01 |
| 19261+1849 | 1367 | > 14.25 ——— | 11.97 ± 0.02 | 9.10 ± 0.01 |
| 19265+3116 | 1749 | 5.82 ± 0.20 | 4.98 ± 0.33 | 4.81 ± 0.22 |
| 19268+0254 | 1749 | 13.26 ± 0.07 | 11.12 ± 0.08 | 9.12 ± 0.03 |
| 19268+1539 | 1368 | > 15.00 ——— | 12.43 ± 0.07 | 9.54 ± 0.02 |
| 19269+0813 | 1362 | > 14.75 ——— | 12.06 ± 0.03 | 9.59 ± 0.01 |
| 19271+1354 | 1369 | 5.85 ± 0.01 | 4.78 ± 0.12 | 4.22 ± 0.11 |
| 19274+0919 | 1361 | 8.51 ± 0.02 | 7.15 ± 0.06 | 6.28 ± 0.02 |
| 19276+0739 | 1368 | 9.31 ± 0.02 | 7.59 ± 0.01 | 6.28 ± 0.01 |
| 19276+1500 | 1368 | 9.65 ± 0.02 | 7.50 ± 0.01 | 6.16 ± 0.01 |
| 19277+0947 | 1361 | 8.05 ± 0.02 | 6.57 ± 0.06 | 5.87 ± 0.02 |
| 19283+1944 | 1363 | > 15.00 ——— | > 13.75 ——— | >13.25 ——— |
| 19288+2923 | 1363 | 13.99 ± 0.42 | 10.55 ± 0.42 | 6.99 ± 0.01 |
| 19290+1600 | 1362 | 9.98 ± 0.02 | 7.89 ± 0.02 | 6.48 ± 0.03 |
| 19291+0502 | 1753 | 7.55 ± 0.01 | 6.01 ± 0.02 | 4.98 ± 0.03 |
| 19295+2228 | 1746 | > 14.25 ——— | > 13.50 ——— | 10.10 ± 0.02 |
| 19302+0110 | 1369 | 8.17 ± 0.02 | 7.16 ± 0.01 | 6.45 ± 0.01 |
| 19303+1553 | 1367 | 12.24 ± 0.37 | 9.12 ± 0.01 | 7.13 ± 0.01 |
| 19305+2410 | 1746 | 8.45 ± 0.01 | 6.72 ± 0.01 | 5.47 ± 0.02 |
| 19310+2044 | 1368 | 11.74 ± 0.08 | 9.23 ± 0.01 | 7.36 ± 0.02 |
| 19312+1130 | 1367 | 8.37 ± 0.02 | 6.78 ± 0.02 | 5.60 ± 0.02 |
| 19314+2059 | 1749 | 14.80 ± 0.23 | 10.83 ± 0.01 | 8.45 ± 0.01 |
| 19316+0919 | 1753 | 8.56 ± 0.02 | 7.04 ± 0.01 | 6.13 ± 0.02 |
| 19319+2214 | 1361 | > 13.25 ——— | 11.99 ± 0.07 | 10.77 ± 0.04 |
| 19323+1952 | 1369 | > 14.74 ——— | 13.44 ± 0.24 | 9.36 ± 0.06 |
| 19327+0903 | 1368 | 6.71 ± 0.02 | 5.86 ± 0.02 | 5.20 ± 0.09 |
| 19330+1245 | 1368 | 7.39 ± 0.06 | 6.14 ± 0.01 | 5.16 ± 0.08 |
| 19333+1918 | 1366 | 10.10 ± 0.61 | 7.20 ± 0.01 | 5.54 ± 0.01 |
| 19343+0912 | 1368 | 6.60 ± 0.03 | 5.79 ± 0.07 | 5.00 ± 0.06 |
| 19343+2926 | 1369 | 9.56 ± 0.01 | 7.88 ± 0.02 | 6.09 ± 0.01 |
| 19344+0016 | 1369 | 7.96 ± 0.01 | 6.84 ± 0.01 | 5.97 ± 0.01 |
| 19344+2457 | 1367 | > 15.00 ——— | 11.56 ± 0.04 | 8.32 ± 0.01 |
| 19346+0913 | 1368 | 6.92 ± 0.02 | 5.90 ± 0.02 | 5.43 ± 0.07 |
| 19347+2755 | 1750 | 10.36 ± 0.05 | 7.92 ± 0.01 | 6.23 ± 0.01 |

*Continue in the next page.*

*Table B.1: Near-IR photometry of the sources in the 'Arecibo sample' (continued)*

| IRAS | Julian Date | Calar Alto photometry [mag] | | |
|---|---|---|---|---|
| | (2450000+) | J | H | K |
| 19352+1914 | 1749 | 12.09 ± 0.22 | 9.10 ± 0.02 | 7.18 ± 0.03 |
| 19352+2030 | 1363 | 13.89 ± 0.10 | 11.49 ± 0.02 | 9.31 ± 0.02 |
| 19359+1936 | 1367 | 13.33 ± 0.73 | 11.15 ± 0.02 | 8.94 ± 0.03 |
| 19360+3442 | 1366 | 12.77 ± 0.06 | 9.60 ± 0.01 | 7.39 ± 0.01 |
| 19366+1149 | 1368 | 6.71 ± 0.03 | 5.91 ± 0.01 | 5.41 ± 0.01 |
| 19368+1935 | 1366 | > 15.00 ——— | > 14.75 ——— | 12.31 ± 0.05 |
| 19371+2855 | 1750 | 6.18 ± 0.01 | 4.93 ± 0.09 | 3.81 ± 0.09 |
| 19374+1626 | 1368 | > 15.00 ——— | > 14.50 ——— | >13.25 ——— |
| 19378+1256 | 1369 | 5.95 ± 0.01 | 4.99 ± 0.01 | 4.25 ± 0.10 |
| 19382+3400 | 1750 | 7.14 ± 0.02 | 6.08 ± 0.01 | 5.47 ± 0.01 |
| 19386+1513 | 1363 | 6.63 ± 0.01 | 5.16 ± 0.01 | 4.41 ± 0.06 |
| 19387+1527 | 1363 | 8.26 ± 0.01 | 6.62 ± 0.01 | 5.58 ± 0.01 |
| 19395+1827 | 1368 | 9.30 ± 0.04 | 7.31 ± 0.01 | 5.96 ± 0.02 |
| 19395+1949 | 1367 | 7.76 ± 0.01 | 6.07 ± 0.01 | 5.01 ± 0.02 |
| 19396+2338 | 1368 | > 14.25 ——— | 12.87 ± 0.15 | 9.64 ± 0.02 |
| 19412+0337 | 1363 | 5.43 ± 0.01 | 4.30 ± 0.05 | 3.79 ± 0.04 |
| 19412+1042 | 1369 | 11.97 ± 0.01 | 9.96 ± 0.02 | 8.31 ± 0.01 |
| 19413+2829 | 1369 | 10.65 ± 0.02 | 8.65 ± 0.02 | 7.04 ± 0.01 |
| 19414+2237 | 1749 | 4.34 ± 0.07 | 3.27 ± 0.08 | < 3.36 ——— |
| 19422+3506 | 1363 | 7.42 ± 0.01 | 5.56 ± 0.02 | not obs. |
| 19425+3323 | 1363 | 7.30 ± 0.01 | 5.87 ± 0.02 | 4.88 ± 0.01 |
| 19440+2251 | 1366 | > 14.50 ——— | > 14.25 ——— | >12.75 ——— |
| 19448+2653 | 1363 | 12.35 ± 0.39 | 9.23 ± 0.03 | 7.18 ± 0.04 |
| 19451+1628 | 1368 | 7.83 ± 0.02 | 6.68 ± 0.01 | 5.91 ± 0.01 |
| 19453+1917 | 1368 | 9.59 ± 0.05 | 8.47 ± 0.01 | 7.26 ± 0.01 |
| 19454+2536 | 1367 | 7.22 ± 0.02 | 5.76 ± 0.01 | 4.85 ± 0.06 |
| 19456+1927 | 1367 | 11.51 ± 0.06 | 9.21 ± 0.01 | 7.59 ± 0.01 |
| 19459+1716 | 1368 | 14.03 ± 0.19 | 10.73 ± 0.01 | 8.36 ± 0.01 |
| 19462+2232 | 1749 | 9.97 ± 0.08 | 7.51 ± 0.02 | 5.95 ± 0.01 |
| 19464+3514 | 1366 | 13.46 ± 0.17 | 10.07 ± 0.01 | 7.59 ± 0.01 |
| 19467+2213 | 1367 | > 15.25 ——— | 12.62 ± 0.06 | 10.14 ± 0.04 |
| 19471+2944 | 1366 | 8.85 ± 0.04 | 7.14 ± 0.01 | 6.08 ± 0.01 |
| 19479+2111 | 1752 | 6.72 ± 0.01 | 5.48 ± 0.03 | < 4.72 ——— |
| 19488+1346 | 1368 | 6.80 ± 0.02 | 5.86 ± 0.01 | 5.32 ± 0.02 |

*Continue in the next page.*

*Table B.1: Near-IR photometry of the sources in the 'Arecibo sample' (continued)*

| IRAS | Julian Date | Calar Alto photometry [mag] | | |
|---|---|---|---|---|
| | (2450000+) | J | H | K |
| 19488+1719 | 1369 | 9.13 ± 0.02 | 7.69 ± 0.01 | 6.37 ± 0.01 |
| 19490+1049 | 1368 | 13.27 ± 0.09 | 11.00 ± 0.05 | 9.15 ± 0.05 |
| 19493+2905 | 1368 | 12.00 ± 0.06 | 9.17 ± 0.01 | 6.85 ± 0.02 |
| 19495+0835 | 1753 | 7.49 ± 0.06 | 5.65 ± 0.01 | 4.65 ± 0.15 |
| 19499+2141 | 1368 | 7.12 ± 0.01 | 5.57 ± 0.01 | 4.64 ± 0.12 |
| 19500+2239 | 1368 | 8.79 ± 0.02 | 7.29 ± 0.02 | 6.14 ± 0.01 |
| 19508+2014 | 1368 | 9.32 ± 0.02 | 7.90 ± 0.01 | 6.72 ± 0.01 |
| 19508+2659 | 1363 | 10.12 ± 0.02 | 7.43 ± 0.01 | 5.75 ± 0.09 |
| 19516+2217 | 1368 | 8.45 ± 0.01 | 7.32 ± 0.01 | 6.59 ± 0.01 |
| 19520+2729 | 1363 | > 14.75 ——— | > 14.50 ——— | 11.29 ± 0.15 |
| 19522+1935 | 1749 | 8.77 ± 0.02 | 6.82 ± 0.01 | 5.26 ± 0.02 |
| 19522+2653 | 1369 | 9.69 ± 0.02 | 7.57 ± 0.01 | 6.34 ± 0.01 |
| 19527+2231 | 1368 | 8.16 ± 0.02 | 6.88 ± 0.01 | 6.01 ± 0.01 |
| 19529+3634 | 1747 | 7.73 ± 0.02 | 6.71 ± 0.01 | 6.11 ± 0.01 |
| 19534+2802 | 1366 | > 15.75 ——— | > 14.50 ——— | 11.18 ± 0.11 |
| 19535+2157 | 1368 | 8.21 ± 0.01 | 7.07 ± 0.02 | 6.18 ± 0.01 |
| 19547+1848 | 1753 | 4.70 ± 0.05 | 3.60 ± 0.04 | 2.97 ± 0.10 |
| 19565+3140 | 1367 | > 15.00 ——— | 12.74 ± 0.06 | 9.98 ± 0.04 |
| 19566+3423 | 1747 | > 15.25 ——— | > 14.50 ——— | 13.92 ± 1.05 |
| 19573+2204 | 1368 | 12.57 ± 0.03 | 10.15 ± 0.03 | 8.48 ± 0.01 |
| 19575+1143 | 1367 | 6.97 ± 0.02 | 5.88 ± 0.02 | 5.20 ± 0.02 |
| 19576+2814 | 1366 | > 15.25 ——— | > 14.50 ——— | 11.08 ± 0.05 |
| 19579+2926 | 1368 | 6.76 ± 0.02 | 5.41 ± 0.01 | 4.70 ± 0.10 |
| 19579+3223 | 1366 | 5.51 ± 0.01 | 4.57 ± 0.06 | < 4.21 ——— |
| 19588+2541 | 1368 | 12.88 ± 0.02 | 10.30 ± 0.01 | 8.10 ± 0.01 |
| 20011+1752 | 1369 | 9.89 ± 0.01 | 8.41 ± 0.02 | 7.26 ± 0.02 |
| 20015+3019 | 1747 | 3.95 ± 0.05 | 2.82 ± 0.07 | < 2.64 ——— |
| 20023+2855 | 1366 | > 15.25 ——— | > 14.50 ——— | 10.27 ± 0.05 |
| 20024+1727 | 1752 | 7.11 ± 0.02 | 5.49 ± 0.03 | 4.20 ± 0.27 |
| 20043+2653 | 1366 | > 15.25 ——— | > 14.00 ——— | 10.79 ± 0.06 |
| 20047+1248 | 1753 | 4.82 ± 0.06 | 3.82 ± 0.06 | 3.06 ± 0.08 |
| 20052+0554 | 1753 | 4.86 ± 0.20 | 3.62 ± 0.15 | 2.79 ± 0.08 |
| 20095+2726 | 1366 | 9.84 ± 0.02 | 7.23 ± 0.01 | 5.60 ± 0.01 |
| 20097+1107 | 1369 | 9.90 ± 0.01 | 7.84 ± 0.02 | 6.39 ± 0.01 |

*Continue in the next page.*

*Table B.1: Near-IR photometry of the sources in the 'Arecibo sample' (continued)*

| IRAS | Julian Date | Calar Alto photometry [mag] | | |
|---|---|---|---|---|
| | (2450000+) | J | H | K |
| 20110+3555 | 1747 | 10.80 ± 0.02 | 8.70 ± 0.05 | 7.31 ± 0.03 |
| 20115+0844 | 1366 | 7.84 ± 0.01 | 6.38 ± 0.01 | 5.32 ± 0.01 |
| 20123+0429 | 1369 | 6.12 ± 0.01 | 5.29 ± 0.04 | 4.42 ± 0.07 |
| 20127+2430 | 1366 | 6.24 ± 0.01 | 4.82 ± 0.01 | 4.24 ± 0.06 |
| 20137+2838 | 1747 | 11.78 ± 0.02 | 8.77 ± 0.03 | 6.81 ± 0.02 |
| 20140+3620 | 1367 | 5.99 ± 0.08 | 4.75 ± 0.04 | 3.84 ± 0.15 |
| 20149+3440 | | No photometry: Blended | | |
| 20153+2057 | 1366 | 7.46 ± 0.01 | 6.28 ± 0.01 | 5.62 ± 0.01 |
| 20156+2130 | 1749 | 7.31 ± 0.02 | 5.85 ± 0.02 | 5.47 ± 0.20 |
| 20160+2734 | 1750 | 7.01 ± 0.03 | 6.41 ± 0.01 | 6.12 ± 0.01 |
| 20171+2732 | 1750 | 9.44 ± 0.02 | 7.20 ± 0.01 | 5.58 ± 0.01 |
| 20181+2234 | 1744 | 13.16 ± 0.12 | 10.09 ± 0.03 | 7.84 ± 0.01 |
| 20194+1707 | 1752 | 5.37 ± 0.04 | 4.46 ± 0.04 | 3.85 ± 0.06 |
| 20211+3100 | 1747 | 9.97 ± 0.03 | 7.79 ± 0.01 | 6.26 ± 0.01 |
| 20215+3205 | 1744 | 8.09 ± 0.01 | 6.26 ± 0.02 | 5.04 ± 0.02 |
| 20246+1456 | 1744 | 5.90 ± 0.01 | 5.18 ± 0.06 | < 4.57 ——— |
| 20246+2813 | 1366 | 11.29 ± 0.01 | 10.09 ± 0.01 | 9.18 ± 0.01 |
| 20267+2105 | 1744 | 9.52 ± 0.01 | 6.81 ± 0.01 | 4.85 ± 0.07 |
| 20272+3535 | 1362 | > 15.25 ——— | > 15.00 ——— | 10.74 ± 0.08 |
| 20280+2631 | 1366 | 10.24 ± 0.01 | 8.13 ± 0.01 | 6.44 ± 0.01 |
| 20296+3355 | 1368 | 6.95 ± 0.01 | 5.78 ± 0.01 | 5.15 ± 0.01 |
| 20351+3450 | 1744 | 5.65 ± 0.01 | 4.51 ± 0.03 | 3.86 ± 0.07 |
| 20363+3401 | 1746 | 5.97 ± 0.01 | 4.91 ± 0.02 | 4.43 ± 0.05 |
| 20403+3143 | 1744 | 11.35 ± 0.02 | 8.68 ± 0.03 | 6.93 ± 0.01 |
| 20403+3700 | 1366 | 7.33 ± 0.01 | 5.37 ± 0.01 | 4.26 ± 0.07 |
| 20410+2949 | 1369 | 7.57 ± 0.02 | 6.50 ± 0.02 | 5.82 ± 0.01 |
| 20423+2742 | 1746 | 7.83 ± 0.03 | 6.24 ± 0.01 | 5.20 ± 0.01 |
| 20432+3151 | 1746 | 10.68 ± 0.03 | 8.71 ± 0.02 | 7.15 ± 0.01 |
| 20440+0412 | 1744 | 4.66 ± 0.05 | not obs. | 3.47 ± 0.10 |
| 20444+0540 | 1744 | 7.11 ± 0.01 | 5.95 ± 0.01 | 4.84 ± 0.01 |
| 20460+3253 | 1369 | 6.91 ± 0.02 | 5.98 ± 0.04 | 5.35 ± 0.07 |
| 20482+3325 | 1368 | 8.55 ± 0.03 | 7.08 ± 0.01 | 5.93 ± 0.01 |
| 20529+3013 | 1745 | 3.64 ± 0.07 | 2.67 ± 0.04 | 2.37 ± 0.11 |
| 20531+2909 | 1746 | 12.40 ± 0.02 | 9.72 ± 0.03 | 7.74 ± 0.01 |

*Continue in the next page.*

*Table B.1: Near-IR photometry of the sources in the 'Arecibo sample' (continued)*

| IRAS | Julian Date (2450000+) | Calar Alto photometry [mag] J | H | K |
|---|---|---|---|---|
| 20547+0247 | 1363 | 11.53 ± 0.04 | 10.10 ± 0.02 | 8.29 ± 0.01 |
| 21062+0058 | 1744 | 5.12 ± 0.02 | < 4.77 ——— | < 4.26 ——— |
| 21074+1812 | 1746 | 5.61 ± 0.01 | 4.92 ± 0.06 | 4.53 ± 0.11 |
| 21100+2205 | 1369 | 9.45 ± 0.02 | 8.46 ± 0.02 | 7.67 ± 0.01 |
| 21120+0736 | 1744 | 5.77 ± 0.01 | 4.91 ± 0.06 | 4.20 ± 0.03 |
| 21174+1747 | 1745 | 8.02 ± 0.04 | 6.86 ± 0.02 | 6.16 ± 0.03 |
| 21305+2118 | 1362 | 9.73 ± 0.14 | 7.47 ± 0.02 | 5.55 ± 0.01 |
| 21576+3259 | 1369 | 8.24 ± 0.02 | 7.29 ± 0.01 | 6.52 ± 0.02 |
| 22180+3225 | 1745 | 5.05 ± 0.02 | < 4.72 ——— | 3.74 ± 0.06 |
| 22402+1045 | 1745 | 6.03 ± 0.01 | 5.33 ± 0.08 | 4.91 ± 0.05 |
| 22510+3614 | 1745 | 4.27 ± 0.05 | 3.48 ± 0.05 | 3.11 ± 0.10 |
| 22516+0838 | 1745 | 4.46 ± 0.15 | 3.44 ± 0.20 | 3.32 ± 0.16 |
| 22517+2223 | 1366 | 5.99 ± 0.01 | 5.20 ± 0.01 | 4.73 ± 0.01 |

# Appendix C

# Main observational parameters for the sources in the 'extended OH/IR sample'

**Table C.1**: Main observational parameters of the sources in the 'extended OH/IR sample'

| IRAS | $\lambda$ | V$_{exp}$ [km s$^{-1}$] | F$_{bol}$ [Wm$^{-2}$] | D [kpc] | Z [pc] | sample |
|---|---|---|---|---|---|---|
| 01037+1219 | 0.90 | 18.2 | 8.56e−10 | 0.36 | −278 | Arecibo |
| 01085+3022 | 0.67 | 12.9 | 1.77e−10 | 0.80 | −423 | Arecibo |
| 02404+2150 | 0.57 | | 4.59e−11 | 1.57 | −874 | Arecibo |
| 02420+1206 | 0.62 | 3.8 | 5.90e−11 | 1.38 | −924 | Arecibo |
| 02547+1106 | 0.93 | 9.5 | 5.07e−11 | 1.49 | −977 | Arecibo |
| 03507+1115 | 0.45 | 16.6 | 4.06e−09 | 0.17 | −86 | Arecibo |
| 08425−5116 | 1.81 | | 1.97e−12 | 7.56 | −718 | GLMP |
| 09024−5019 | 2.33 | | 1.63e−11 | 2.63 | −112 | GLMP |
| 11438−6330 | 2.03 | 13.8 | 1.55e−10 | 0.85 | −27 | GLMP |
| 12158−6443 | 2.45 | 8.5 | 5.98e−12 | 4.35 | −178 | GLMP |
| 12358−6323 | 2.62 | 16.6 | 7.84e−12 | 3.79 | −54 | GLMP |
| 12562+2324 | 0.58 | 5.4 | 4.99e−11 | 1.50 | 1500 | Arecibo |
| 14247−6148 | 2.23 | | 2.96e−12 | 6.18 | −136 | GLMP |
| 14562−5637 | 2.55 | 14.3 | 1.00e−11 | 3.36 | 102 | GLMP |
| 15060+0947 | 0.67 | 9.0 | 3.61e−11 | 1.77 | 1416 | Arecibo |
| 15198−5625 | 3.38 | | 1.55e−12 | 8.54 | 43 | GLMP |

*Continue in the next page.*

*Table C.1: Main observational parameters for the ‘extended OH/IR sample’ (continued)*

| IRAS | $\lambda$ | $V_{exp}$ [$\mathrm{km\,s^{-1}}$] | $F_{bol}$ [$\mathrm{Wm^{-2}}$] | D [kpc] | Z [pc] | sample |
|---|---|---|---|---|---|---|
| 15262+0400 | 0.60 | | 1.16e−10 | 0.99 | 708 | Arecibo |
| 15327−5400 | 1.78 | | 1.15e−12 | 9.92 | 214 | GLMP |
| 15471−4634 | 1.91 | 13.9 | 7.19e−12 | 3.96 | 399 | GLMP |
| 15514−5323 | 3.84 | 20.4 | 3.49e−11 | 1.80 | 1 | GLMP |
| 16040−4708 | 2.90 | 7.9 | 1.30e−12 | 9.34 | 566 | GLMP |
| 16219−4823 | 2.48 | | 1.44e−11 | 2.80 | 23 | GLMP |
| 16235+1900 | 0.31 | 5.0 | 1.26e−09 | 0.30 | 193 | Arecibo |
| 16236−5332 | 2.51 | 14.8 | 1.94e−12 | 7.64 | −439 | GLMP |
| 16503+0529 | 0.50 | 3.8 | 1.07e−10 | 1.03 | 495 | Arecibo |
| 16523+0745 | 0.57 | 6.8 | 1.81e−11 | 2.50 | 1225 | Arecibo |
| 16560+2252 | 0.57 | 2.3 | 3.58e−11 | 1.78 | 1004 | Arecibo |
| 16582−3059* | 2.28 | 13.4 | 2.31e−12 | 8 | | GLMP |
| 17004−4119 | 3.51 | 18.9 | 1.33e−10 | 0.92 | 0 | GLMP |
| 17030−3053* | 2.34 | 15.3 | 1.81e−12 | 8 | | GLMP |
| 17050+1714 | 0.57 | | 2.86e−11 | 1.99 | 1008 | Arecibo |
| 17055−3753 | 2.38 | | 1.66e−11 | 2.61 | 60 | GLMP |
| 17107−3330* | 2.15 | | 2.21e−12 | 8 | | GLMP |
| 17128−3528* | 3.68 | | 2.51e−12 | 8 | | GLMP |
| 17151−3642* | 2.95 | | 2.91e−12 | 8 | | GLMP |
| 17171−2955* | 1.82 | | 3.08e−12 | 8 | | GLMP |
| 17207−3632* | 3.87 | 16.1 | 2.98e−12 | 8 | | GLMP |
| 17230+0113 | 0.82 | 10.1 | 3.96e−11 | 1.69 | 565 | Arecibo |
| 17242−3859 | 2.19 | 13.0 | 2.61e−12 | 6.58 | −264 | GLMP |
| 17251−2821* | 2.42 | 16.0 | 1.46e−12 | 8 | | GLMP |
| 17256+0504 | 0.95 | 5.1 | 3.48e−11 | 1.80 | 640 | Arecibo |
| 17276−2846* | 3.28 | 15.5 | 3.00e−12 | 8 | | GLMP |
| 17292−2727* | 2.30 | 17.6 | 4.76e−12 | 8 | | GLMP |
| 17308+0822 | 1.12 | 6.4 | 9.69e−12 | 3.41 | 1231 | Arecibo |
| 17316−3523* | 2.49 | 12.3 | 8.40e−12 | 8 | | GLMP |
| 17317−3331 | 3.08 | 15.1 | 9.63e−11 | 1.08 | −10 | GLMP |
| 17323−2424* | 2.46 | 13.8 | 1.71e−12 | 8 | | GLMP |
| 17338+0051 | 0.45 | 4.6 | 1.56e−11 | 2.69 | 787 | Arecibo |
| 17341−3529* | 1.89 | | 7.00e−12 | 8 | | GLMP |
| 17350−2413* | 1.68 | | 3.13e−12 | 8 | | GLMP |

*Continue in the next page.*

*Table C.1: Main observational parameters for the 'extended OH/IR sample' (continued)*

| IRAS | $\lambda$ | V$_{exp}$ [km s$^{-1}$] | F$_{bol}$ [Wm$^{-2}$] | D [kpc] | Z [pc] | sample |
|---|---|---|---|---|---|---|
| 17351−3429* | 2.60 | 20.0 | 3.83e−12 | 8 | | GLMP |
| 17361−2358* | 2.20 | | 1.28e−12 | 8 | | GLMP |
| 17367−2722* | 2.75 | 7.7 | 1.73e−12 | 8 | | GLMP |
| 17367−3633* | 2.39 | 14.5 | 7.26e−12 | 8 | | GLMP |
| 17368−3515* | 2.36 | 13.5 | 1.76e−12 | 8 | | GLMP |
| 17392−3020* | 4.38 | 21.1 | 5.22e−12 | 8 | | GLMP |
| 17411−3154 | 2.36 | 18.8 | 4.10e−10 | 0.52 | −12 | GLMP |
| 17417−1630 | 2.08 | | 3.59e−12 | 5.61 | 646 | GLMP |
| 17418−2713* | 3.32 | 15.2 | 1.27e−11 | 8 | | GLMP |
| 17428−2438* | 2.08 | 13.8 | 2.41e−12 | 8 | | GLMP |
| 17467−4256 | 2.00 | 10.5 | 3.49e−12 | 5.68 | −791 | GLMP |
| 17495−2534* | 1.80 | 15.4 | 7.78e−12 | 8 | | GLMP |
| 17504−3312* | 3.65 | 15.7 | 2.68e−12 | 8 | | GLMP |
| 17521−2938* | 3.15 | 16.3 | 1.51e−12 | 8 | | GLMP |
| 17528+1144 | 0.60 | 5.6 | 6.90e−12 | 4.05 | 1230 | Arecibo |
| 17545−3056* | 3.43 | 15.0 | 1.80e−12 | 8 | | GLMP |
| 17545−3317* | 2.20 | 13.9 | 3.87e−12 | 8 | | GLMP |
| 17554+2946 | 0.66 | 7.5 | 1.54e−10 | 0.86 | 348 | Arecibo |
| 17577−1519 | 1.99 | | 4.09e−12 | 5.25 | 359 | GLMP |
| 17579+2335 | 0.50 | 5.6 | 2.14e−10 | 0.73 | 264 | Arecibo |
| 17583−3346* | 2.07 | 13.4 | 1.78e−12 | 8 | | GLMP |
| 17584−3147* | 2.71 | 16.8 | 2.56e−12 | 8 | | GLMP |
| 18000−2835* | 2.11 | | 1.32e−11 | 8 | | GLMP |
| 18006−1734 | 2.71 | 4.7 | 5.53e−12 | 4.52 | 172 | GLMP |
| 18007−1841 | 2.99 | 16.3 | 5.17e−12 | 4.67 | 132 | GLMP |
| 18015−1608 | 1.79 | | 4.20e−12 | 5.18 | 245 | GLMP |
| 18019−3121* | 2.19 | | 1.64e−12 | 8 | | GLMP |
| 18033+2229 | 0.68 | 2.7 | 4.43e−11 | 1.60 | 540 | Arecibo |
| 18040−2726* | 2.66 | 16.3 | 2.49e−12 | 8 | | GLMP |
| 18040−2953* | 2.47 | | 1.95e−12 | 8 | | GLMP |
| 18069+0911 | 0.83 | 16.5 | 6.33e−11 | 1.34 | 311 | Arecibo |
| 18076+3445 | 0.84 | 13.7 | 3.23e−11 | 1.87 | 734 | Arecibo |
| 18081−0338 | 2.07 | 1.7 | 2.46e−11 | 2.14 | 273 | GLMP |
| 18085+0752 | 0.54 | 3.8 | 3.63e−11 | 1.76 | 383 | Arecibo |

*Continue in the next page.*

*Table C.1: Main observational parameters for the 'extended OH/IR sample' (continued)*

| IRAS | $\lambda$ | $V_{exp}$ [$km\,s^{-1}$] | $F_{bol}$ [$Wm^{-2}$] | D [kpc] | Z [pc] | sample |
|---|---|---|---|---|---|---|
| 18091−0855 | 2.76 | | 2.57e−13 | 20.98 | 1682 | GLMP |
| 18091−2437* | 2.51 | 15.7 | 1.48e−12 | 8 | | GLMP |
| 18092−2347* | 3.09 | 17.4 | 4.95e−12 | 8 | | GLMP |
| 18092−2508* | 2.29 | 14.5 | 2.60e−12 | 8 | | GLMP |
| 18099+3127 | 0.59 | 9.1 | 3.93e−11 | 1.70 | 625 | Arecibo |
| 18100−1915 | 3.35 | 14.1 | 5.16e−12 | 4.68 | −47 | GLMP |
| 18107−0710 | 2.33 | 10.8 | 9.36e−12 | 3.47 | 308 | GLMP |
| 18123+0511 | 1.51 | 3.4 | 1.38e−11 | 2.86 | 521 | Arecibo |
| 18152−0919 | 2.23 | 14.0 | 1.56e−11 | 2.69 | 145 | GLMP |
| 18170+0353 | 0.75 | 13.2 | 4.21e−12 | 5.18 | 798 | Arecibo |
| 18182−1504 | 3.60 | | 3.80e−11 | 1.72 | −8 | GLMP |
| 18187−0208 | 2.27 | 3.4 | 6.11e−13 | 13.59 | 1354 | GLMP |
| 18195−2804* | 2.40 | 16.3 | 1.25e−12 | 8 | | GLMP |
| 18198−1249 | 3.06 | 15.4 | 7.00e−12 | 4.02 | 30 | GLMP |
| 18201−2549* | 1.63 | | 4.58e−12 | 8 | | GLMP |
| 18203+0723 | 0.73 | 5.9 | 9.39e−12 | 3.47 | 586 | Arecibo |
| 18211−1712 | 2.46 | | 1.14e−11 | 3.14 | −105 | GLMP |
| 18223+1217 | 0.50 | 5.0 | 8.42e−12 | 3.66 | 728 | Arecibo |
| 18231+0855 | 0.73 | 9.5 | 6.59e−12 | 4.14 | 703 | Arecibo |
| 18236+0706 | 0.82 | 4.4 | 5.42e−12 | 4.56 | 702 | Arecibo |
| 18237+2150 | 0.72 | 2.2 | 1.49e−11 | 2.75 | 721 | Arecibo |
| 18251+0023 | 0.73 | 11.3 | 1.17e−11 | 3.11 | 296 | Arecibo |
| 18254+0750 | 1.01 | 8.1 | 5.97e−12 | 4.35 | 665 | Arecibo |
| 18257−1000 | 3.28 | 18.8 | 1.72e−11 | 2.56 | 22 | GLMP |
| 18257−1052 | 4.06 | | 1.63e−11 | 2.63 | 3 | GLMP |
| 18262+0934 | 0.62 | 7.5 | 7.50e−12 | 3.88 | 633 | Arecibo |
| 18262−0735 | 2.27 | 13.9 | 6.70e−12 | 4.11 | 108 | GLMP |
| 18266−1239 | 2.59 | 17.7 | 7.97e−12 | 3.76 | −62 | GLMP |
| 18268−1117 | 2.68 | 17.2 | 7.26e−12 | 3.94 | −23 | GLMP |
| 18270+0326 | 0.64 | 7.3 | 2.58e−11 | 2.09 | 234 | Arecibo |
| 18276+0839 | 1.32 | 2.7 | 4.66e−12 | 4.92 | 743 | Arecibo |
| 18277−1059 | 2.64 | 17.8 | 1.53e−11 | 2.72 | −19 | GLMP |
| 18278+0931 | 0.62 | 10.6 | 2.24e−11 | 2.25 | 352 | Arecibo |
| 18298−2111 | 2.18 | 12.1 | 3.82e−11 | 1.72 | −167 | GLMP |

*Continue in the next page.*

*Table C.1: Main observational parameters for the 'extended OH/IR sample' (continued)*

| IRAS | $\lambda$ | $V_{exp}$ [km s$^{-1}$] | $F_{bol}$ [Wm$^{-2}$] | D [kpc] | Z [pc] | sample |
|---|---|---|---|---|---|---|
| 18299−1705 | 1.82 | | 2.42e−11 | 2.16 | −139 | GLMP |
| 18307+0102 | 1.16 | 11.4 | 5.27e−12 | 4.63 | 366 | Arecibo |
| 18310−2834* | 2.24 | 15.1 | 7.68e−12 | 8 | | GLMP |
| 18318+0150 | 0.97 | 13.1 | 5.85e−12 | 4.39 | 357 | Arecibo |
| 18333+0903 | 0.95 | 9.1 | 1.01e−11 | 3.34 | 442 | Arecibo |
| 18341+0005 | 0.71 | | 1.67e−11 | 2.60 | 151 | Arecibo |
| 18347+1113 | 0.77 | 3.4 | 5.36e−12 | 4.59 | 658 | Arecibo |
| 18349+1023 | 0.44 | 15.2 | 7.55e−10 | 0.39 | 52 | Arecibo |
| 18353+0020 | 1.56 | 14.1 | 2.29e−12 | 7.02 | 389 | Arecibo |
| 18355+0227 | 0.65 | 15.4 | 1.50e−11 | 2.75 | 196 | Arecibo |
| 18361−0036 | 3.01 | 11.2 | 5.67e−13 | 14.11 | 632 | GLMP |
| 18361−0647 | 4.61 | | 1.40e−11 | 2.84 | −14 | GLMP |
| 18362+0538 | 1.16 | 16.8 | 9.82e−12 | 3.39 | 320 | Arecibo |
| 18375+0510 | 0.65 | 13.6 | 1.83e−11 | 2.48 | 212 | Arecibo |
| 18381+0020 | 0.75 | 16.4 | 2.29e−11 | 2.22 | 99 | Arecibo |
| 18395+0130 | 1.63 | 15.9 | 3.07e−12 | 6.06 | 296 | Arecibo |
| 18397+0758 | 0.59 | 5.9 | 1.36e−11 | 2.88 | 285 | Arecibo |
| 18398+0728 | 1.05 | 11.7 | 7.55e−12 | 3.87 | 367 | Arecibo |
| 18398+1035 | 0.63 | | 6.01e−11 | 1.37 | 163 | Arecibo |
| 18400+0123 | 1.13 | 9.5 | 4.17e−12 | 5.20 | 237 | Arecibo |
| 18407+0350 | 1.55 | 10.2 | 7.26e−12 | 3.94 | 246 | Arecibo |
| 18407+0601 | 0.62 | 13.4 | 9.66e−12 | 3.42 | 274 | Arecibo |
| 18408+0730 | 0.55 | 8.2 | 7.70e−12 | 3.83 | 349 | Arecibo |
| 18409+0431 | 0.97 | 20.9 | 3.37e−11 | 1.83 | 122 | Arecibo |
| 18415+0404 | 0.75 | 14.3 | 1.11e−11 | 3.18 | 194 | Arecibo |
| 18420+1137 | 0.88 | 8.7 | 2.62e−12 | 6.57 | 780 | Arecibo |
| 18430+0039 | 0.81 | | 6.02e−12 | 4.33 | 122 | Arecibo |
| 18432−0149 | 3.10 | 17.6 | 1.76e−11 | 2.53 | 18 | GLMP |
| 18433+0039 | 1.11 | 16.4 | 9.27e−12 | 3.49 | 94 | Arecibo |
| 18435+0745 | 1.83 | 10.4 | 1.35e−12 | 9.14 | 756 | Arecibo |
| 18441+0311 | 0.90 | 8.6 | 1.05e−11 | 3.27 | 145 | Arecibo |
| 18441+2216 | 1.04 | 6.8 | 4.57e−12 | 4.97 | 954 | Arecibo |
| 18444+0734 | 0.66 | 6.4 | 8.21e−12 | 3.71 | 290 | Arecibo |
| 18455+0448 | 1.87 | 6.4 | 6.61e−12 | 4.13 | 214 | Arecibo |

*Continue in the next page.*

*Table C.1: Main observational parameters for the ‘extended OH/IR sample’ (continued)*

| IRAS | $\lambda$ | $V_{exp}$ [km s$^{-1}$] | $F_{bol}$ [Wm$^{-2}$] | D [kpc] | Z [pc] | sample |
|---|---|---|---|---|---|---|
| 18460−0254 | 3.09 | 20.4 | 1.07e−10 | 1.03 | −12 | GLMP |
| 18475+0353 | 2.81 | 14.1 | 4.93e−13 | 15.14 | 560 | Arecibo |
| 18475−1428 | 1.61 | 17.1 | 4.90e−12 | 4.80 | −525 | GLMP |
| 18476+0555 | 0.85 | 14.1 | 3.00e−11 | 1.94 | 102 | Arecibo |
| 18477+0243 | 0.98 | 14.6 | 8.01e−12 | 3.75 | 100 | Arecibo |
| 18479−2514 | 2.44 | 13.4 | 2.57e−12 | 6.63 | −1276 | GLMP |
| 18481+0405 | 1.48 | 15.5 | 2.42e−12 | 6.83 | 246 | Arecibo |
| 18487+0152 | 1.23 | 15.4 | 2.27e−11 | 2.23 | 35 | Arecibo |
| 18487+0617 | 1.25 | 14.1 | 3.74e−12 | 5.49 | 281 | Arecibo |
| 18488−0107 | 3.36 | 20.5 | 2.14e−11 | 2.29 | −19 | GLMP |
| 18490+0302 | 2.01 | 18.2 | 6.33e−12 | 4.22 | 101 | Arecibo |
| 18490+1158 | 0.90 | 15.9 | 1.56e−11 | 2.69 | 255 | Arecibo |
| 18497+0200 | 3.73 | 14.3 | 5.75e−12 | 4.43 | 58 | Arecibo |
| 18498−0017 | 5.80 | 15.9 | 1.32e−11 | 2.92 | −16 | Arecibo |
| 18499+1224 | 0.84 | 4.8 | 7.46e−12 | 3.89 | 370 | Arecibo |
| 18501+0013 | 3.72 | 14.1 | 2.33e−12 | 6.97 | −17 | Arecibo |
| 18501+1019 | 1.27 | 13.5 | 9.13e−12 | 3.52 | 274 | Arecibo |
| 18506+0912 | 1.15 | 10.9 | 1.23e−11 | 3.03 | 203 | Arecibo |
| 18511+1141 | 0.74 | 10.5 | 3.85e−12 | 5.42 | 459 | Arecibo |
| 18512+2029 | 0.83 | 15.7 | 2.73e−11 | 2.03 | 310 | Arecibo |
| 18517+0037 | 2.76 | 16.1 | 8.86e−12 | 3.57 | −21 | Arecibo |
| 18518+0358 | 1.03 | 7.7 | 1.50e−11 | 2.74 | 57 | Arecibo |
| 18518+0558 | 3.02 | 9.9 | 6.49e−13 | 13.19 | 488 | GLMP |
| 18520+1014 | 0.82 | 7.7 | 1.34e−11 | 2.90 | 203 | Arecibo |
| 18525+0210 | 2.19 | 18.6 | 1.02e−11 | 3.33 | 12 | Arecibo |
| 18530+0507 | 3.43 | 16.8 | 1.25e−11 | 3.00 | 77 | Arecibo |
| 18535+0726 | 0.95 | 18.6 | 3.48e−11 | 1.80 | 76 | Arecibo |
| 18540+0302 | 1.86 | 18.6 | 1.72e−11 | 2.56 | 12 | Arecibo |
| 18542+0940 | 0.62 | 7.2 | 1.21e−11 | 3.06 | 175 | Arecibo |
| 18548+0823 | 2.74 | 13.4 | 1.34e−12 | 9.18 | 411 | Arecibo |
| 18549+0208 | 2.97 | 13.7 |  |  |  | Arecibo |
| 18549+0905 | 0.78 | 11.3 | 3.52e−11 | 1.79 | 89 | Arecibo |
| 18551+0323 | 1.20 | 16.8 | 6.78e−11 | 1.29 | 4 | Arecibo |
| 18554+0231 | 1.08 | 3.7 | 4.51e−11 | 1.58 | −7 | Arecibo |

*Continue in the next page.*

*Table C.1: Main observational parameters for the 'extended OH/IR sample' (continued)*

| IRAS | $\lambda$ | $V_{exp}$ [km s$^{-1}$] | $F_{bol}$ [Wm$^{-2}$] | D [kpc] | Z [pc] | sample |
|---|---|---|---|---|---|---|
| 18554+1333 | 0.85 | 7.6 | 7.69e−12 | 3.83 | 320 | Arecibo |
| 18556+0811 | 0.65 | 9.8 | 8.11e−11 | 1.18 | 47 | Arecibo |
| 18556+1409 | 0.95 | 15.4 | 6.51e−12 | 4.17 | 363 | Arecibo |
| 18560+0638 | 1.42 | 16.1 | 2.21e−10 | 0.71 | 18 | Arecibo |
| 18563+0816 | 1.48 | 11.3 | 4.03e−12 | 5.29 | 201 | Arecibo |
| 18567+0003 | 0.81 | 14.1 | 2.38e−11 | 2.18 | −64 | Arecibo |
| 18567+1046 | 0.77 | 12.8 | 3.19e−11 | 1.88 | 106 | Arecibo |
| 18568+0550 | 2.35 | 11.8 | 1.91e−12 | 7.70 | 126 | Arecibo |
| 18568+2554 | 0.68 | 4.1 | 4.14e−12 | 5.22 | 908 | Arecibo |
| 18569+0553 | 2.54 | 16.8 | 7.45e−13 | 12.31 | 206 | Arecibo |
| 18569+1722 | 0.66 | 3.6 | 1.22e−11 | 3.04 | 328 | Arecibo |
| 18571+0611 | 2.87 | 14.5 | 1.73e−12 | 8.09 | 146 | Arecibo |
| 18572+0618 | 1.39 |  | 1.10e−11 | 3.20 | 60 | Arecibo |
| 18577+1047 | 1.20 | 5.4 | 3.16e−12 | 5.98 | 315 | Arecibo |
| 18578+0831 | 1.75 | 14.8 | 1.63e−11 | 2.63 | 89 | Arecibo |
| 18581+1405 | 0.85 |  | 7.54e−12 | 3.87 | 300 | Arecibo |
| 18585+0900 | 1.13 | 30.5 | 4.56e−11 | 1.57 | 56 | Arecibo |
| 18588+1400 | 0.86 | 12.7 | 1.06e−11 | 3.27 | 243 | Arecibo |
| 18592+1455 | 0.64 | 13.9 | 4.39e−11 | 1.60 | 128 | Arecibo |
| 18593+1009 | 1.17 | 10.5 | 4.06e−12 | 5.27 | 219 | Arecibo |
| 18596+0315 | 4.28 | 13.2 | 2.92e−12 | 6.21 | −92 | Arecibo |
| 19006+0624 | 2.53 | 15.0 | 1.16e−12 | 9.88 | 65 | Arecibo |
| 19007+1652 | 0.76 | 8.2 | 5.99e−12 | 4.34 | 390 | Arecibo |
| 19008+0907 | 0.98 | 14.8 | 7.23e−12 | 3.95 | 109 | Arecibo |
| 19010+0526 | 1.30 | 11.3 | 3.68e−11 | 1.75 | −5 | Arecibo |
| 19010+1307 | 1.28 | 15.9 | 7.22e−12 | 3.96 | 233 | Arecibo |
| 19012+1128 | 0.74 | 13.6 | 8.05e−12 | 3.75 | 168 | Arecibo |
| 19017+0412 | 1.20 | 17.8 | 1.46e−11 | 2.78 | −43 | Arecibo |
| 19017+0608 | 2.11 | 14.6 | 1.10e−11 | 3.21 | 1 | Arecibo |
| 19023+0745 | 1.44 | 14.1 | 8.03e−12 | 3.75 | 41 | Arecibo |
| 19024+1923 | 0.76 | 18.2 | 1.93e−11 | 2.42 | 251 | Arecibo |
| 19026+0336 | 1.42 | 10.2 | 6.12e−12 | 4.29 | −102 | Arecibo |
| 19026+1300 | 1.43 | 15.2 | 2.78e−12 | 6.38 | 332 | Arecibo |
| 19027+1341 | 1.24 | 17.7 | 1.83e−12 | 7.85 | 447 | Arecibo |

*Continue in the next page.*

*Table C.1: Main observational parameters for the ‘extended OH/IR sample’ (continued)*

| IRAS | $\lambda$ | $V_{exp}$ [km s$^{-1}$] | $F_{bol}$ [Wm$^{-2}$] | D [kpc] | Z [pc] | sample |
|---|---|---|---|---|---|---|
| 19028+1613 | 0.75 | 14.3 | 2.84e−12 | 6.31 | 487 | Arecibo |
| 19029+0933 | 1.10 | 18.1 | | | | Arecibo |
| 19035+0451 | 0.99 | 18.4 | 1.55e−11 | 2.70 | −46 | Arecibo |
| 19035+0801 | 4.56 | | | | | Arecibo |
| 19035+1010 | 1.22 | 17.1 | 1.02e−11 | 3.33 | 86 | Arecibo |
| 19041+0952 | 0.89 | | 9.26e−12 | 3.49 | 73 | Arecibo |
| 19041+1734 | 0.65 | 14.1 | 6.25e−12 | 4.25 | 352 | Arecibo |
| 19043+1009 | 0.94 | 15.9 | 3.46e−11 | 1.81 | 40 | Arecibo |
| 19047+0924 | 1.69 | 12.7 | 3.09e−12 | 6.05 | 91 | Arecibo |
| 19052+0922 | 0.96 | 18.1 | 2.35e−11 | 2.19 | 28 | Arecibo |
| 19052+1431 | 1.01 | 28.6 | 3.42e−12 | 5.74 | 312 | Arecibo |
| 19054+0419 | 1.86 | 15.7 | 2.19e−12 | 7.18 | −206 | Arecibo |
| 19055+0225 | 1.24 | 15.8 | 7.60e−12 | 3.86 | −171 | Arecibo |
| 19057+0141 | 0.89 | 8.2 | 4.52e−12 | 5.00 | −256 | Arecibo |
| 19060+1612 | 0.64 | | 3.03e−11 | 1.93 | 125 | Arecibo |
| 19061+1041 | 1.15 | 17.7 | 6.60e−12 | 4.13 | 83 | Arecibo |
| 19067+0811 | 2.62 | 16.4 | 9.92e−12 | 3.37 | −7 | Arecibo |
| 19068+0016 | 1.28 | 15.9 | 5.65e−12 | 4.47 | −298 | Arecibo |
| 19068+1127 | 0.94 | 15.9 | 1.92e−11 | 2.42 | 57 | Arecibo |
| 19069+0916 | 2.78 | 21.8 | 5.62e−12 | 4.48 | 25 | Arecibo |
| 19069+1335 | 2.19 | | 6.67e−12 | 4.11 | 167 | GLMP |
| 19071+0946 | 1.89 | 11.9 | 5.12e−12 | 4.70 | 41 | Arecibo |
| 19074+0336 | 1.10 | 15.9 | 5.16e−12 | 4.68 | −196 | Arecibo |
| 19075+1147 | 1.35 | 11.4 | 2.11e−12 | 7.31 | 173 | Arecibo |
| 19076+1247 | 1.66 | 7.2 | 2.49e−12 | 6.74 | 213 | Arecibo |
| 19079+1143 | 0.72 | 15.5 | 5.95e−12 | 4.36 | 94 | Arecibo |
| 19081+0322 | 2.55 | 15.7 | 1.18e−11 | 3.09 | −144 | Arecibo |
| 19083+0851 | 0.81 | 29.8 | 3.71e−11 | 1.74 | −5 | Arecibo |
| 19085+0755 | 3.04 | 19.6 | 4.27e−12 | 5.14 | −58 | Arecibo |
| 19087+0323 | 1.27 | 15.9 | 1.35e−11 | 2.89 | −142 | Arecibo |
| 19087+1006 | 2.84 | | 1.13e−12 | 9.98 | 55 | GLMP |
| 19088+1129 | 0.62 | 9.6 | 1.51e−11 | 2.74 | 44 | Arecibo |
| 19097+0411 | 0.86 | 1.3 | 9.79e−12 | 3.40 | −157 | Arecibo |
| 19112+0819 | 1.87 | 20.9 | 4.93e−12 | 4.79 | −88 | Arecibo |

*Continue in the next page.*

*Table C.1: Main observational parameters for the 'extended OH/IR sample' (continued)*

| IRAS | $\lambda$ | $V_{exp}$ [$km\,s^{-1}$] | $F_{bol}$ [$Wm^{-2}$] | D [kpc] | Z [pc] | sample |
|---|---|---|---|---|---|---|
| 19112+1220 | 2.28 | 16.6 | 1.47e−12 | 8.77 | 124 | GLMP |
| 19115+0752 | 3.58 | 17.2 | 4.75e−12 | 4.88 | −114 | Arecibo |
| 19116+1511 | 1.16 | 5.9 | 5.52e−12 | 4.52 | 162 | Arecibo |
| 19117+1558 | 1.25 | 18.0 | 2.89e−12 | 6.25 | 262 | Arecibo |
| 19122−0230 | 1.50 | 4.4 | 8.23e−12 | 3.70 | −408 | GLMP |
| 19128+0910 | 1.77 | 12.7 | 5.23e−12 | 4.65 | −82 | Arecibo |
| 19128+1310 | 1.62 | 15.4 | 8.00e−12 | 3.76 | 57 | Arecibo |
| 19129+2803 | 0.56 |  | 1.56e−11 | 2.69 | 361 | Arecibo |
| 19131+1157 | 1.49 | 18.4 | 2.09e−11 | 2.32 | 9 | Arecibo |
| 19140+0652 | 1.31 | 11.8 | 5.19e−12 | 4.67 | −192 | Arecibo |
| 19147+1349 | 0.81 | 17.7 | 1.58e−11 | 2.67 | 35 | Arecibo |
| 19149+1638 | 1.02 | 17.0 | 1.66e−11 | 2.61 | 93 | Arecibo |
| 19160+0755 | 1.34 | 12.7 | 4.40e−12 | 5.07 | −203 | Arecibo |
| 19161+2343 | 1.20 | 17.7 | 8.66e−11 | 1.14 | 101 | Arecibo |
| 19162+0607 | 1.18 | 10.7 | 2.22e−12 | 7.13 | −395 | Arecibo |
| 19167+1733 | 0.68 | 13.2 | 1.36e−11 | 2.88 | 105 | Arecibo |
| 19168+0814 | 0.50 |  | 3.61e−11 | 1.77 | −71 | Arecibo |
| 19172+1956 | 1.72 | 11.8 | 3.45e−12 | 5.72 | 309 | Arecibo |
| 19175+0958 | 0.87 | 14.1 | 4.66e−12 | 4.92 | −141 | Arecibo |
| 19175+1042 | 2.12 | 16.5 | 6.82e−12 | 4.07 | −93 | Arecibo |
| 19176+1939 | 1.07 | 13.2 | 9.48e−12 | 3.45 | 175 | Arecibo |
| 19177+1333 | 1.94 |  | 3.92e−12 | 5.36 | 0 | Arecibo |
| 19183+1148 | 2.43 | 16.1 | 2.58e−12 | 6.61 | −111 | Arecibo |
| 19184+1055 | 2.47 | 15.0 | 3.93e−12 | 5.36 | −131 | Arecibo |
| 19186+0315 | 0.97 | 15.9 | 1.37e−11 | 2.87 | −253 | Arecibo |
| 19186+1657 | 1.05 | 13.1 | 2.95e−11 | 1.96 | 48 | Arecibo |
| 19187+2221 | 0.77 | 17.5 | 4.68e−12 | 4.91 | 338 | Arecibo |
| 19188+1057 | 2.60 | 13.8 | 2.56e−12 | 6.64 | −170 | Arecibo |
| 19189+1758 | 0.90 | 14.1 | 2.21e−11 | 2.26 | 72 | Arecibo |
| 19190+1128 | 1.43 | 15.4 | 1.95e−11 | 2.41 | −53 | Arecibo |
| 19190+3035 | 1.18 | 12.7 | 4.26e−12 | 5.15 | 691 | Arecibo |
| 19192+0922 | 1.32 | 16.1 | 1.17e−10 | 0.98 | −39 | Arecibo |
| 19195+0522 | 0.91 | 5.9 | 2.45e−11 | 2.15 | −159 | Arecibo |
| 19195+1747 | 0.66 | 12.7 | 2.75e−11 | 2.03 | 57 | Arecibo |

*Continue in the next page.*

*Table C.1: Main observational parameters for the 'extended OH/IR sample' (continued)*

| IRAS | $\lambda$ | $V_{exp}$ [$km\,s^{-1}$] | $F_{bol}$ [$Wm^{-2}$] | D [kpc] | Z [pc] | sample |
|---|---|---|---|---|---|---|
| 19200+1536 | 2.18 | 12.7 | 3.67e−12 | 5.55 | 46 | Arecibo |
| 19201+1040 | 1.57 | 12.9 | 5.10e−12 | 4.71 | −154 | Arecibo |
| 19201+2101 | 2.03 | 13.4 | 1.41e−11 | 2.83 | 148 | Arecibo |
| 19206+2121 | 0.74 | 12.7 | 7.45e−12 | 3.89 | 209 | Arecibo |
| 19206+2216 | 0.89 | 11.6 | 5.49e−12 | 4.53 | 278 | Arecibo |
| 19206+2517 | 0.64 | 11.4 | 8.02e−12 | 3.75 | 322 | Arecibo |
| 19214+0513 | 1.12 | 16.4 | 9.27e−12 | 3.49 | −290 | Arecibo |
| 19218+0425 | 0.61 | 7.1 | 6.76e−12 | 4.09 | −371 | Arecibo |
| 19229+1708 | 0.82 | 2.1 | 5.20e−11 | 1.47 | 15 | Arecibo |
| 19231+3555 | 0.70 | 10.5 | 1.29e−10 | 0.94 | 152 | Arecibo |
| 19237+1430 | 1.06 | 12.7 | 1.75e−11 | 2.54 | −36 | Arecibo |
| 19241+3457 | 0.50 |  | 3.92e−11 | 1.70 | 258 | Arecibo |
| 19248+1122 | 0.66 |  | 6.02e−11 | 1.37 | −61 | Arecibo |
| 19248+1441 | 0.86 |  | 1.47e−11 | 2.77 | −47 | Arecibo |
| 19252+2420 | 0.51 | 11.3 | 6.05e−12 | 4.32 | 269 | Arecibo |
| 19253+1114 | 0.86 | 3.2 | 6.48e−12 | 4.17 | −199 | Arecibo |
| 19254+1631 | 3.08 | 18.8 | 9.89e−12 | 3.38 | −12 | Arecibo |
| 19254+1724 | 2.93 |  | 1.41e−12 | 8.93 | 31 | GLMP |
| 19256+0254 | 0.95 | 12.7 | 4.31e−12 | 5.12 | −602 | Arecibo |
| 19258+1111 | 0.45 | 16.4 | 8.62e−12 | 3.62 | −181 | Arecibo |
| 19259+0510 | 0.55 | 6.1 | 3.78e−11 | 1.73 | −173 | Arecibo |
| 19261+1003 | 0.67 | 10.2 | 3.35e−12 | 5.81 | −352 | Arecibo |
| 19261+1435 | 1.16 | 15.4 | 4.95e−12 | 4.77 | −109 | Arecibo |
| 19261+1849 | 1.96 | 10.2 | 7.12e−12 | 3.98 | 50 | Arecibo |
| 19265+3116 | 0.69 | 8.0 | 2.42e−11 | 2.16 | 248 | Arecibo |
| 19268+0254 | 1.19 | 10.4 | 1.29e−12 | 9.34 | −1142 | Arecibo |
| 19268+1539 | 2.12 | 10.2 | 2.50e−12 | 6.71 | −111 | Arecibo |
| 19269+0813 | 1.46 | 15.9 | 2.74e−12 | 6.42 | −507 | Arecibo |
| 19271+1354 | 0.61 | 1.1 | 3.80e−11 | 1.72 | −55 | Arecibo |
| 19274+0919 | 0.63 | 10.0 | 6.14e−12 | 4.29 | −308 | Arecibo |
| 19276+0739 | 0.76 |  | 6.75e−12 | 4.09 | −353 | Arecibo |
| 19276+1500 | 0.92 | 16.1 | 7.35e−12 | 3.92 | −96 | Arecibo |
| 19277+0947 | 0.73 | 14.0 | 7.47e−12 | 3.89 | −267 | Arecibo |
| 19283+1944 | 2.30 | 14.1 | 3.34e−11 | 1.84 | 23 | Arecibo |

*Continue in the next page.*

*Table C.1: Main observational parameters for the 'extended OH/IR sample' (continued)*

| IRAS | $\lambda$ | $V_{exp}$ [km s$^{-1}$] | $F_{bol}$ [Wm$^{-2}$] | D [kpc] | Z [pc] | sample |
|---|---|---|---|---|---|---|
| 19288+2923 | 1.35 | 15.4 | 3.25e−11 | 1.86 | 171 | Arecibo |
| 19290+1600 | 0.85 | 10.6 | 6.76e−12 | 4.09 | −87 | Arecibo |
| 19291+0502 | 0.61 | 10.0 | 2.47e−11 | 2.14 | −242 | Arecibo |
| 19295+2228 | 1.21 | 12.2 | 1.35e−11 | 2.89 | 91 | Arecibo |
| 19302+0110 | 0.80 | 5.0 | 4.87e−12 | 4.81 | −720 | Arecibo |
| 19303+1553 | 0.79 | 16.8 | 6.03e−12 | 4.33 | −117 | Arecibo |
| 19305+2410 | 0.60 | 15.6 | 1.47e−11 | 2.77 | 117 | Arecibo |
| 19310+2044 | 0.76 | 12.2 | 5.18e−12 | 4.67 | 54 | Arecibo |
| 19312+1130 | 0.72 | 12.7 | 1.14e−11 | 3.15 | −212 | Arecibo |
| 19314+2059 | 1.59 | 17.2 | 1.87e−12 | 7.77 | 96 | Arecibo |
| 19316+0919 | 0.57 |  | 7.13e−12 | 3.98 | −348 | Arecibo |
| 19319+2214 | 2.28 | 8.4 | 2.65e−12 | 6.53 | 139 | Arecibo |
| 19323+1952 | 2.42 | 16.4 | 2.69e−12 | 6.47 | −3 | Arecibo |
| 19327+0903 | 0.92 | 4.0 | 1.17e−11 | 3.10 | −292 | Arecibo |
| 19330+1245 | 0.90 | 13.2 | 1.12e−11 | 3.17 | −201 | Arecibo |
| 19333+1918 | 0.94 | 17.7 | 2.14e−11 | 2.30 | −20 | Arecibo |
| 19343+0912 | 0.74 | 4.8 | 1.89e−11 | 2.44 | −241 | Arecibo |
| 19344+0016 | 1.02 | 8.6 | 6.52e−12 | 4.16 | −718 | Arecibo |
| 19344+2457 | 1.36 | 11.7 | 3.54e−12 | 5.65 | 200 | Arecibo |
| 19346+0913 | 0.50 | 5.2 | 1.14e−11 | 3.14 | −312 | Arecibo |
| 19347+2755 | 1.03 | 13.7 | 8.01e−12 | 3.76 | 225 | Arecibo |
| 19352+1914 | 0.94 | 20.4 | 9.83e−12 | 3.39 | −55 | Arecibo |
| 19352+2030 | 2.25 | 1.8 | 3.17e−11 | 1.89 | −10 | Arecibo |
| 19359+1936 | 1.36 | 12.7 | 2.44e−12 | 6.80 | −108 | Arecibo |
| 19360+3442 | 1.34 | 12.2 | 6.26e−12 | 4.25 | 480 | Arecibo |
| 19366+1149 | 0.56 | 2.8 | 1.38e−11 | 2.86 | −243 | Arecibo |
| 19368+1935 | 1.62 | 15.0 | 3.66e−12 | 5.55 | −104 | Arecibo |
| 19371+2855 | 0.69 |  | 5.37e−11 | 1.45 | 87 | Arecibo |
| 19374+1626 | 2.14 | 13.6 | 1.81e−12 | 7.90 | −380 | Arecibo |
| 19378+1256 | 0.68 | 3.9 | 2.50e−11 | 2.12 | −170 | Arecibo |
| 19382+3400 | 0.70 | 9.1 | 1.23e−11 | 3.03 | 303 | Arecibo |
| 19386+1513 | 0.72 | 16.8 | 4.25e−11 | 1.63 | −103 | Arecibo |
| 19387+1527 | 1.05 | 13.2 | 9.14e−12 | 3.51 | −216 | Arecibo |
| 19395+1827 | 0.88 | 12.8 | 7.50e−12 | 3.88 | −148 | Arecibo |

*Continue in the next page.*

*Table C.1: Main observational parameters for the ‘extended OH/IR sample’ (continued)*

| IRAS | $\lambda$ | V$_{exp}$ [km s$^{-1}$] | F$_{bol}$ [Wm$^{-2}$] | D [kpc] | Z [pc] | sample |
|---|---|---|---|---|---|---|
| 19395+1949 | 0.89 | 1.6 | 1.67e−11 | 2.60 | −69 | Arecibo |
| 19396+2338 | 1.70 | 14.5 | 5.67e−12 | 4.46 | 28 | Arecibo |
| 19412+0337 | 0.56 | 14.5 | 1.24e−10 | 0.95 | −163 | Arecibo |
| 19412+1042 | 0.99 | 8.0 | 3.14e−12 | 5.99 | −669 | Arecibo |
| 19413+2829 | 1.07 | 15.2 | 4.89e−12 | 4.81 | 204 | Arecibo |
| 19414+2237 | 0.56 | 18.2 | 9.34e−11 | 1.10 | −9 | Arecibo |
| 19422+3506 | 0.77 | 17.0 | 1.49e−10 | 0.87 | 84 | Arecibo |
| 19425+3323 | 0.53 | 12.7 | 2.37e−11 | 2.18 | 177 | Arecibo |
| 19440+2251 | 2.03 | 17.2 | 6.17e−12 | 4.28 | −67 | Arecibo |
| 19448+2653 | 1.21 | 12.1 | 9.64e−12 | 3.42 | 58 | Arecibo |
| 19451+1628 | 1.41 | 15.4 | 6.19e−12 | 4.27 | −325 | Arecibo |
| 19453+1917 | 0.51 | 8.1 | 5.04e−12 | 4.73 | −246 | Arecibo |
| 19454+2536 | 0.83 | 13.7 | 2.07e−11 | 2.33 | 8 | Arecibo |
| 19456+1927 | 1.15 | 13.1 | 2.34e−12 | 6.95 | −356 | Arecibo |
| 19459+1716 | 1.10 | 11.8 | 3.51e−12 | 5.67 | −406 | Arecibo |
| 19462+2232 | 0.81 | 13.6 | 1.33e−11 | 2.91 | −76 | Arecibo |
| 19464+3514 | 1.28 | 12.5 | 9.30e−12 | 3.49 | 298 | Arecibo |
| 19467+2213 | 1.39 | 14.1 | 1.86e−12 | 7.78 | −239 | Arecibo |
| 19471+2944 | 0.85 | 13.8 | 8.35e−12 | 3.68 | 127 | Arecibo |
| 19479+2111 | 0.48 | 3.4 | 1.85e−11 | 2.47 | −109 | Arecibo |
| 19488+1346 | 0.56 | 5.6 | 1.27e−11 | 2.98 | −336 | Arecibo |
| 19488+1719 | 1.06 |  | 7.73e−12 | 3.82 | −313 | Arecibo |
| 19490+1049 | 1.41 | 14.5 | 2.26e−12 | 7.06 | −983 | Arecibo |
| 19493+2905 | 1.18 | 16.8 | 2.09e−11 | 2.32 | 50 | Arecibo |
| 19495+0835 | 0.78 | 13.1 | 6.79e−11 | 1.29 | −207 | Arecibo |
| 19499+2141 | 0.94 | 7.7 | 1.78e−11 | 2.52 | −117 | Arecibo |
| 19500+2239 | 0.91 | 13.9 | 9.35e−12 | 3.48 | −133 | Arecibo |
| 19508+2014 | 0.96 | 7.7 | 4.60e−12 | 4.95 | −311 | Arecibo |
| 19508+2659 | 1.00 | 15.4 | 1.91e−11 | 2.43 | −5 | Arecibo |
| 19516+2217 | 0.78 | 1.9 | 4.41e−12 | 5.06 | −239 | Arecibo |
| 19520+2729 | 1.37 | 14.9 | 1.28e−11 | 2.96 | −5 | Arecibo |
| 19522+1935 | 0.84 | 17.3 | 2.61e−11 | 2.08 | −152 | Arecibo |
| 19522+2653 | 1.02 | 16.3 | 5.19e−12 | 4.66 | −34 | Arecibo |
| 19527+2231 | 0.79 | 8.1 | 6.65e−12 | 4.12 | −201 | Arecibo |

*Continue in the next page.*

*Table C.1: Main observational parameters for the 'extended OH/IR sample' (continued)*

| IRAS | $\lambda$ | $V_{exp}$ [km s$^{-1}$] | $F_{bol}$ [Wm$^{-2}$] | D [kpc] | Z [pc] | sample |
|---|---|---|---|---|---|---|
| 19529+3634 | 0.80 | 4.3 | 7.38e−12 | 3.91 | 304 | Arecibo |
| 19534+2802 | 1.37 | 11.4 | 4.54e−12 | 4.98 | −5 | Arecibo |
| 19535+2157 | 0.66 | 7.9 | 5.46e−12 | 4.55 | −257 | Arecibo |
| 19547+1848 | 0.57 | 1.9 | 8.01e−11 | 1.19 | −106 | Arecibo |
| 19565+3140 | 1.95 | 10.7 | 7.16e−12 | 3.97 | 87 | Arecibo |
| 19566+3423 | 2.31 | 6.5 | 3.38e−11 | 1.83 | 85 | Arecibo |
| 19573+2204 | 1.17 | 11.4 | 2.11e−12 | 7.32 | −503 | Arecibo |
| 19575+1143 | 0.51 | 15.4 | 1.55e−11 | 2.70 | −438 | Arecibo |
| 19576+2814 | 2.14 | 10.9 | 1.38e−11 | 2.86 | −36 | Arecibo |
| 19579+2926 | 0.62 |  | 1.54e−11 | 2.71 | −7 | Arecibo |
| 19579+3223 | 0.58 | 6.8 | 4.71e−11 | 1.55 | 38 | Arecibo |
| 19588+2541 | 1.33 | 33.2 | 3.67e−12 | 5.55 | −224 | Arecibo |
| 20011+1752 | 1.13 | 10.0 | 2.14e−12 | 7.26 | −874 | Arecibo |
| 20015+3019 | 0.77 | 0.9 | 2.41e−10 | 0.68 | −4 | Arecibo |
| 20023+2855 | 2.97 | 12.2 | 6.39e−12 | 4.21 | −91 | Arecibo |
| 20024+1727 | 0.85 | 8.6 | 6.00e−11 | 1.37 | −176 | Arecibo |
| 20043+2653 | 2.37 | 13.7 | 1.48e−11 | 2.76 | −130 | Arecibo |
| 20047+1248 | 0.46 | 3.2 | 1.06e−10 | 1.03 | −184 | Arecibo |
| 20052+0554 | 0.63 | 15.7 | 1.65e−10 | 0.83 | −199 | Arecibo |
| 20095+2726 | 0.90 | 12.7 | 1.85e−11 | 2.47 | −145 | Arecibo |
| 20097+1107 | 1.08 | 18.1 | 6.69e−12 | 4.11 | −870 | Arecibo |
| 20110+3555 | 1.11 | 12.2 | 7.57e−12 | 3.86 | 69 | Arecibo |
| 20115+0844 | 0.79 | 7.8 | 1.46e−11 | 2.78 | −665 | Arecibo |
| 20123+0429 | 0.67 |  | 2.22e−11 | 2.25 | −628 | Arecibo |
| 20127+2430 | 0.73 | 12.7 | 3.22e−11 | 1.87 | −183 | Arecibo |
| 20137+2838 | 1.60 | 11.8 | 5.24e−12 | 4.64 | −283 | Arecibo |
| 20140+3620 | 2.15 | 12.0 | 3.44e−11 | 1.81 | 24 | Arecibo |
| 20149+3440 | 7.31 | 4.0 |  |  |  | Arecibo |
| 20153+2057 | 0.91 | 1.8 | 7.34e−12 | 3.92 | −551 | Arecibo |
| 20156+2130 | 0.79 | 7.1 | 2.13e−11 | 2.30 | −313 | Arecibo |
| 20171+2732 | 1.01 | 12.2 | 1.75e−11 | 2.54 | −209 | Arecibo |
| 20181+2234 | 1.16 | 11.3 | 2.00e−11 | 2.37 | −319 | Arecibo |
| 20194+1707 | 0.58 | 4.8 | 4.48e−11 | 1.59 | −302 | Arecibo |
| 20211+3100 | 0.82 | 13.1 | 1.15e−11 | 3.14 | −190 | Arecibo |

*Continue in the next page.*

*Table C.1: Main observational parameters for the ‘extended OH/IR sample’ (continued)*

| IRAS | $\lambda$ | $V_{exp}$ [$\mathrm{km\,s^{-1}}$] | $F_{bol}$ [$\mathrm{Wm^{-2}}$] | D [kpc] | Z [pc] | sample |
|---|---|---|---|---|---|---|
| 20215+3205 | 0.85 | 11.8 | 3.91e−11 | 1.70 | −87 | Arecibo |
| 20246+1456 | 0.50 | 5.5 | 3.30e−11 | 1.85 | −423 | Arecibo |
| 20246+2813 | 0.72 | 11.4 | 9.90e−12 | 3.38 | −336 | Arecibo |
| 20267+2105 | 1.23 | 16.3 | 5.22e−11 | 1.47 | −260 | Arecibo |
| 20272+3535 | 3.47 | 11.6 | 1.49e−11 | 2.75 | −88 | Arecibo |
| 20280+2631 | 0.95 | 6.8 | 1.44e−11 | 2.80 | −355 | Arecibo |
| 20296+3355 | 0.83 | 4.3 | 1.30e−11 | 2.95 | −166 | Arecibo |
| 20351+3450 | 0.57 | 5.7 | 4.41e−11 | 1.60 | −100 | Arecibo |
| 20363+3401 | 0.68 | 6.8 | 2.38e−11 | 2.18 | −162 | Arecibo |
| 20403+3143 | 1.00 | 17.2 | 9.05e−12 | 3.53 | −390 | Arecibo |
| 20403+3700 | 0.77 | 14.1 | 5.93e−11 | 1.38 | −74 | Arecibo |
| 20410+2949 | 0.89 | 10.7 | 6.50e−12 | 4.17 | −553 | Arecibo |
| 20423+2742 | 0.63 | 15.9 | 2.37e−11 | 2.18 | −347 | Arecibo |
| 20432+3151 | 0.62 | 12.7 | 4.84e−12 | 4.83 | −568 | Arecibo |
| 20440+0412 | 0.55 | 2.0 | 9.97e−11 | 1.06 | −417 | Arecibo |
| 20444+0540 | 0.91 | 8.9 | 3.42e−11 | 1.82 | −691 | Arecibo |
| 20460+3253 | 0.58 | 1.1 | 1.09e−11 | 3.22 | −368 | Arecibo |
| 20482+3325 | 1.07 | 10.9 | 7.54e−12 | 3.87 | −445 | Arecibo |
| 20529+3013 | 1.06 | 11.8 |  |  |  | Arecibo |
| 20531+2909 | 1.44 | 5.0 | 2.91e−12 | 6.23 | −1093 | Arecibo |
| 20547+0247 | 0.98 | 2.0 | 3.25e−11 | 1.86 | −820 | Arecibo |
| 21062+0058 | 0.66 | 5.2 | 1.60e−10 | 0.84 | −413 | Arecibo |
| 21074+1812 | 0.50 | 7.1 | 3.69e−11 | 1.75 | −586 | Arecibo |
| 21100+2205 | 1.46 | 8.6 | 1.68e−12 | 8.19 | −2469 | Arecibo |
| 21120+0736 | 0.62 | 13.2 | 4.83e−11 | 1.53 | −693 | Arecibo |
| 21174+1747 | 0.74 | 8.2 | 7.01e−12 | 4.01 | −1482 | Arecibo |
| 21305+2118 | 0.84 | 15.0 | 4.15e−11 | 1.65 | −608 | Arecibo |
| 21576+3259 | 0.76 | 5.0 | 4.62e−12 | 4.94 | −1460 | Arecibo |
| 22180+3225 | 0.57 | 4.3 | 5.94e−11 | 1.38 | −476 | Arecibo |
| 22402+1045 | 0.65 | 3.8 | 2.39e−11 | 2.17 | −1418 | Arecibo |
| 22510+3614 | 0.62 |  | 9.31e−11 | 1.10 | −386 | Arecibo |
| 22516+0838 | 0.55 | 10.2 | 1.45e−10 | 0.88 | −615 | Arecibo |
| 22517+2223 | 0.55 | 0.9 | 2.61e−11 | 2.08 | −1123 | Arecibo |

* OH/IR stars in the Galactic Bulge

# Appendix D

# NIR finding charts for the sources in the ‘monitoring sample’

**Figure D.1**: Near-IR finding charts of the sources in the 'monitoring sample'.

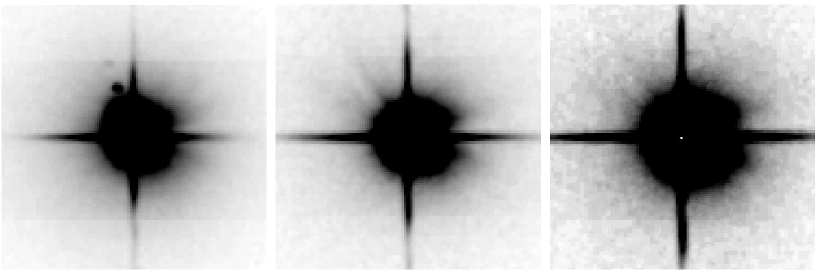

IRAS 02095-2355

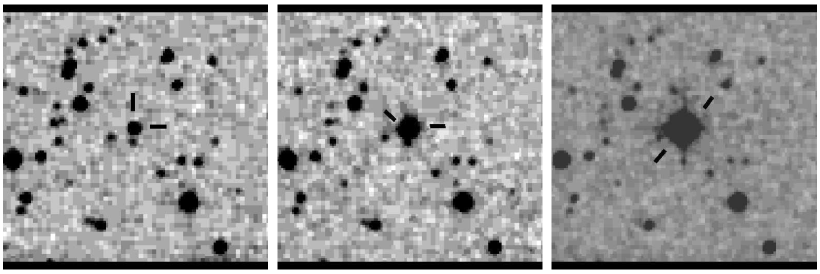

IRAS 03293+6010

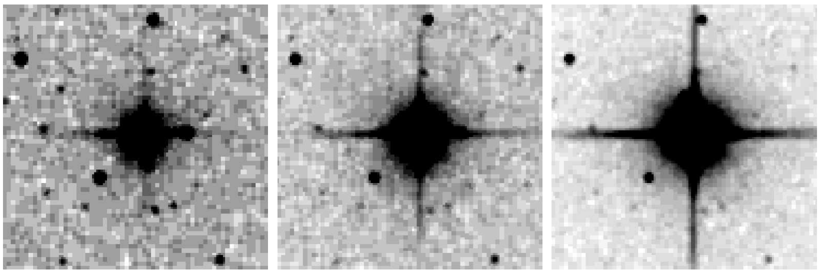

IRAS 04130+3918

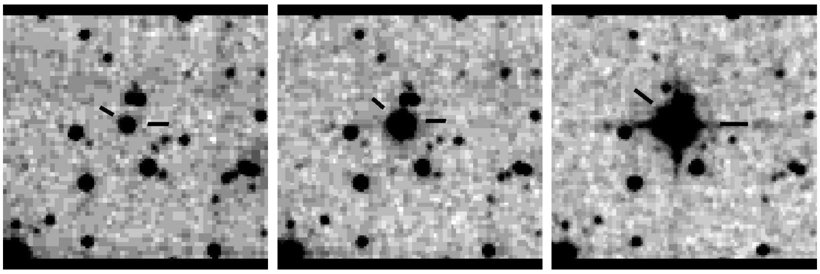

IRAS 05131+4530

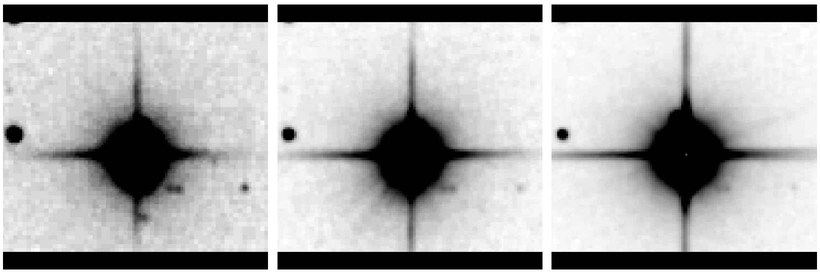

IRAS 06297+4045

*Continue in the next page.*

*Figure D.1: Near-IR finding charts of the sources in the 'monitoring sample' (continued)*

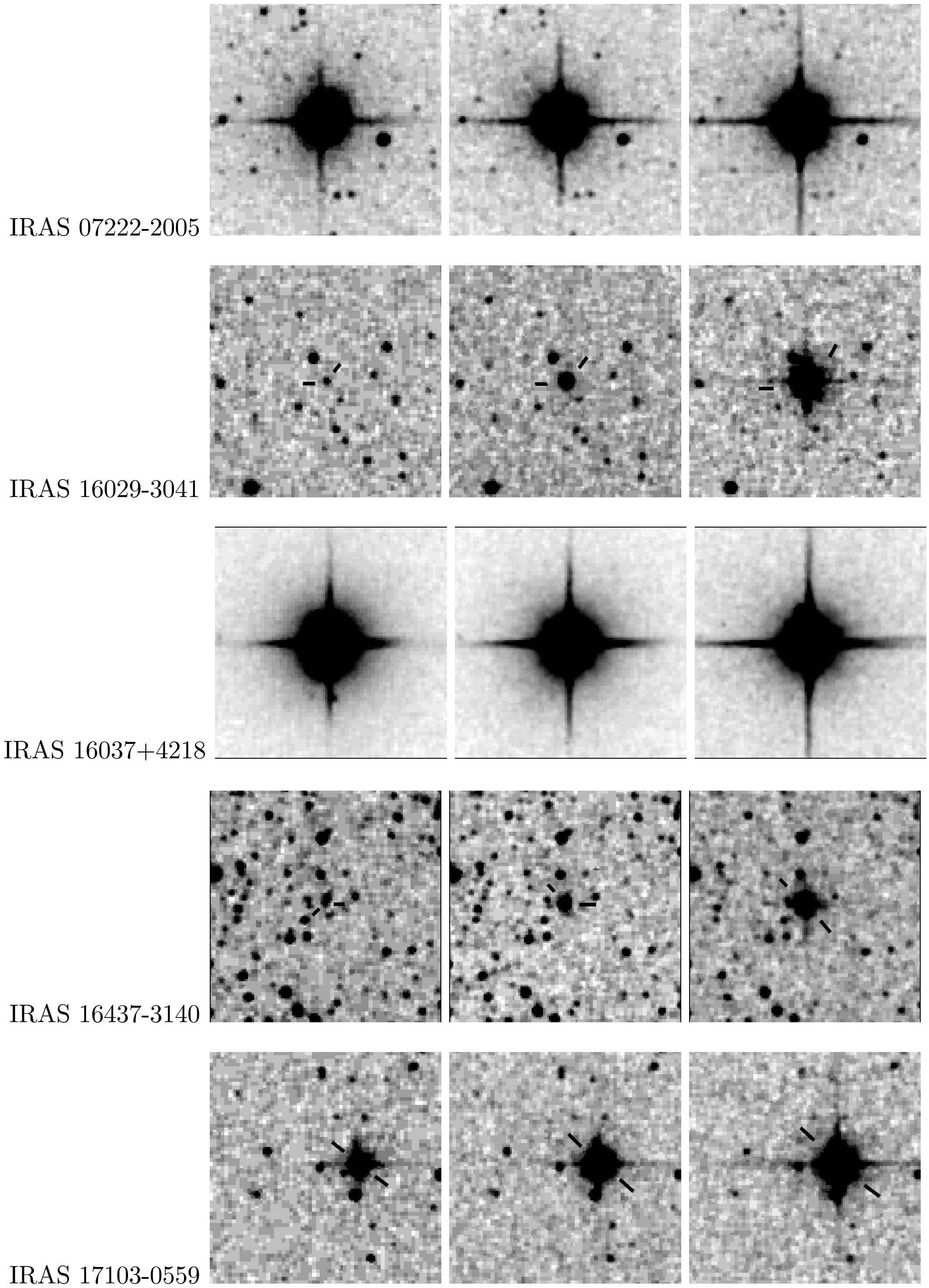

*Continue in the next page.*

*Figure D.1: Near-IR finding charts of the sources in the 'monitoring sample' (continued)*

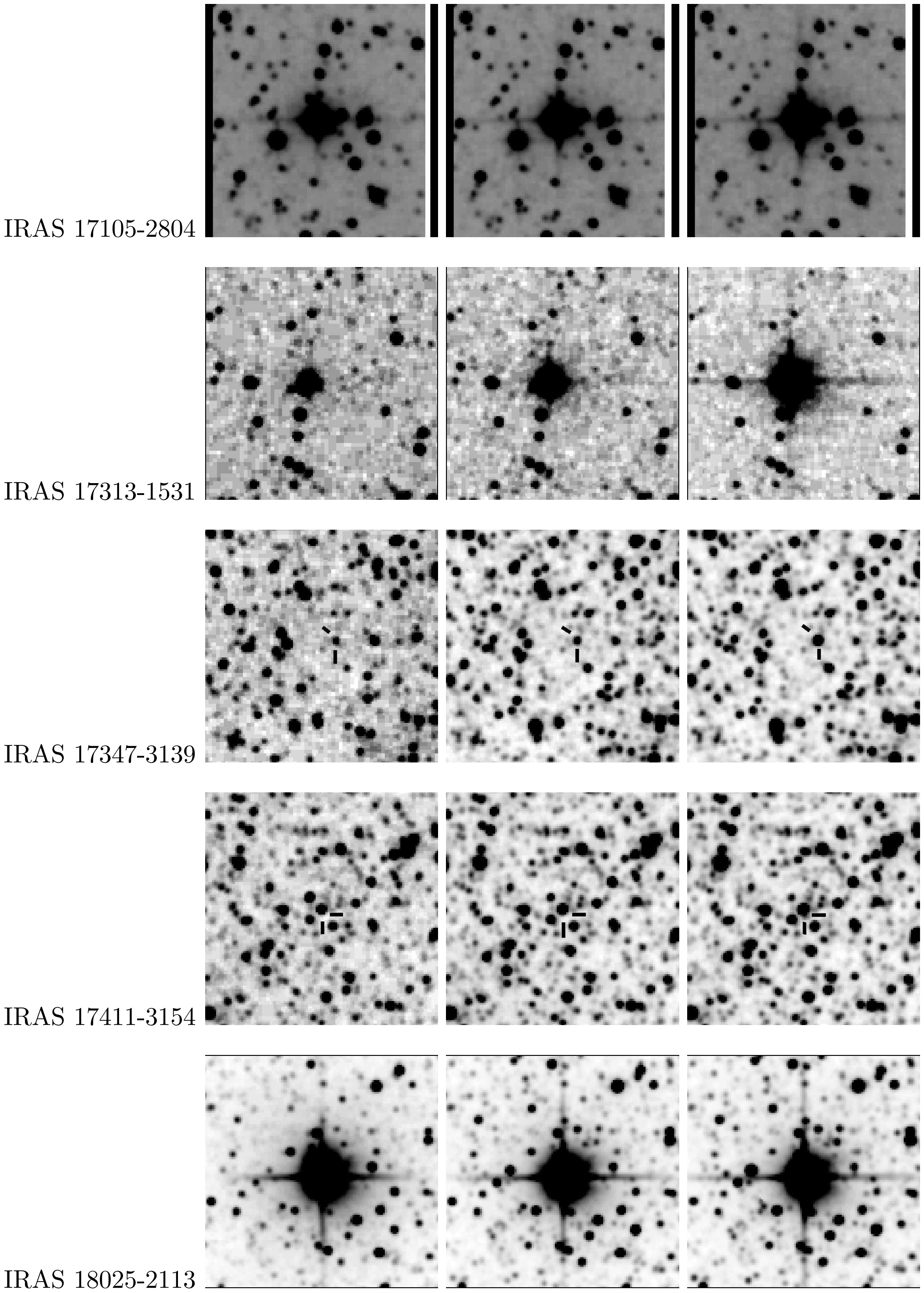

*Continue in the next page.*

*Figure D.1: Near-IR finding charts of the sources in the 'monitoring sample' (continued)*

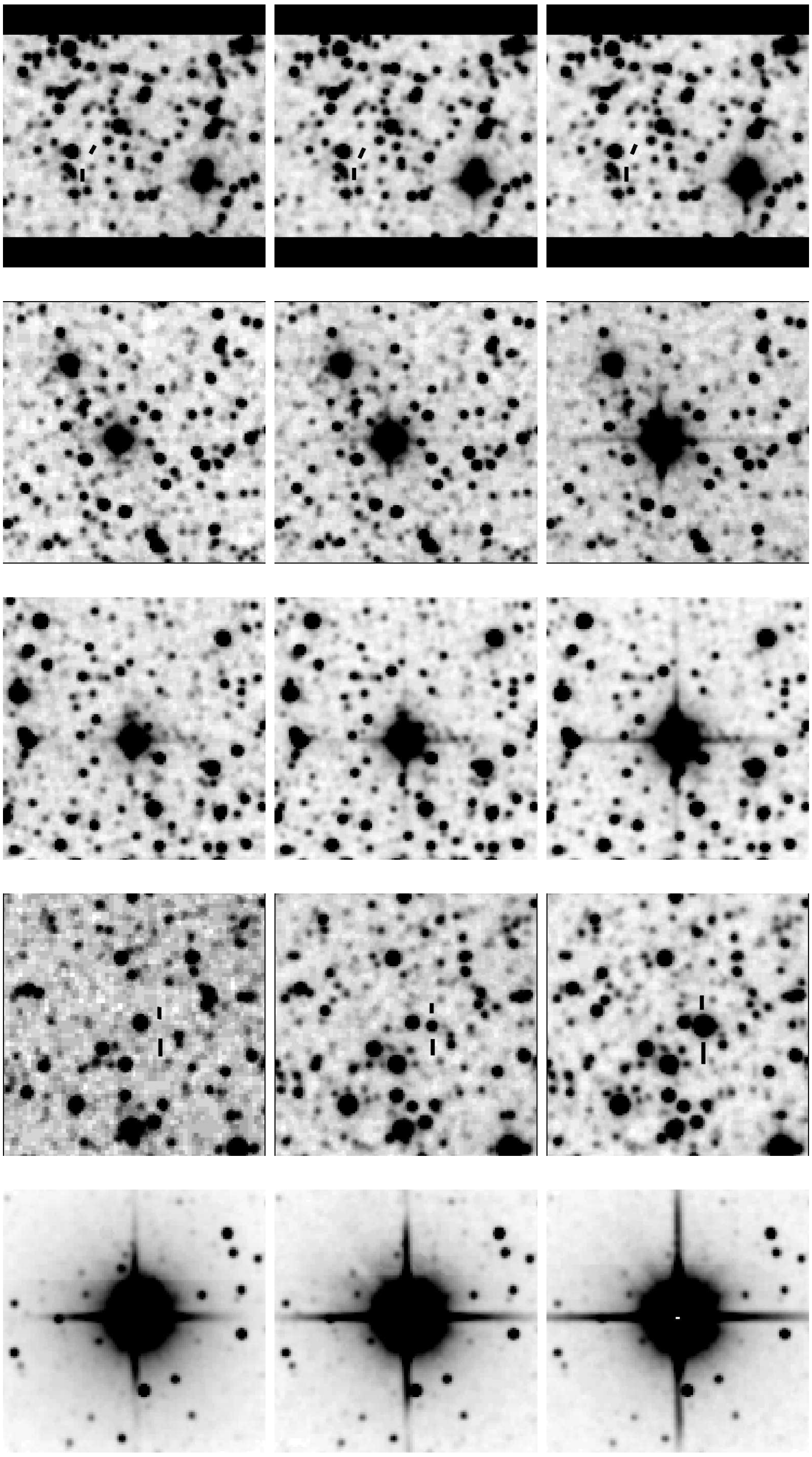

IRAS 18092-2347

IRAS 18299-1705

IRAS 18314-1131

IRAS 18327-0715

IRAS 18429-1721

*Continue in the next page.*

*Figure D.1: Near-IR finding charts of the sources in the 'monitoring sample' (continued)*

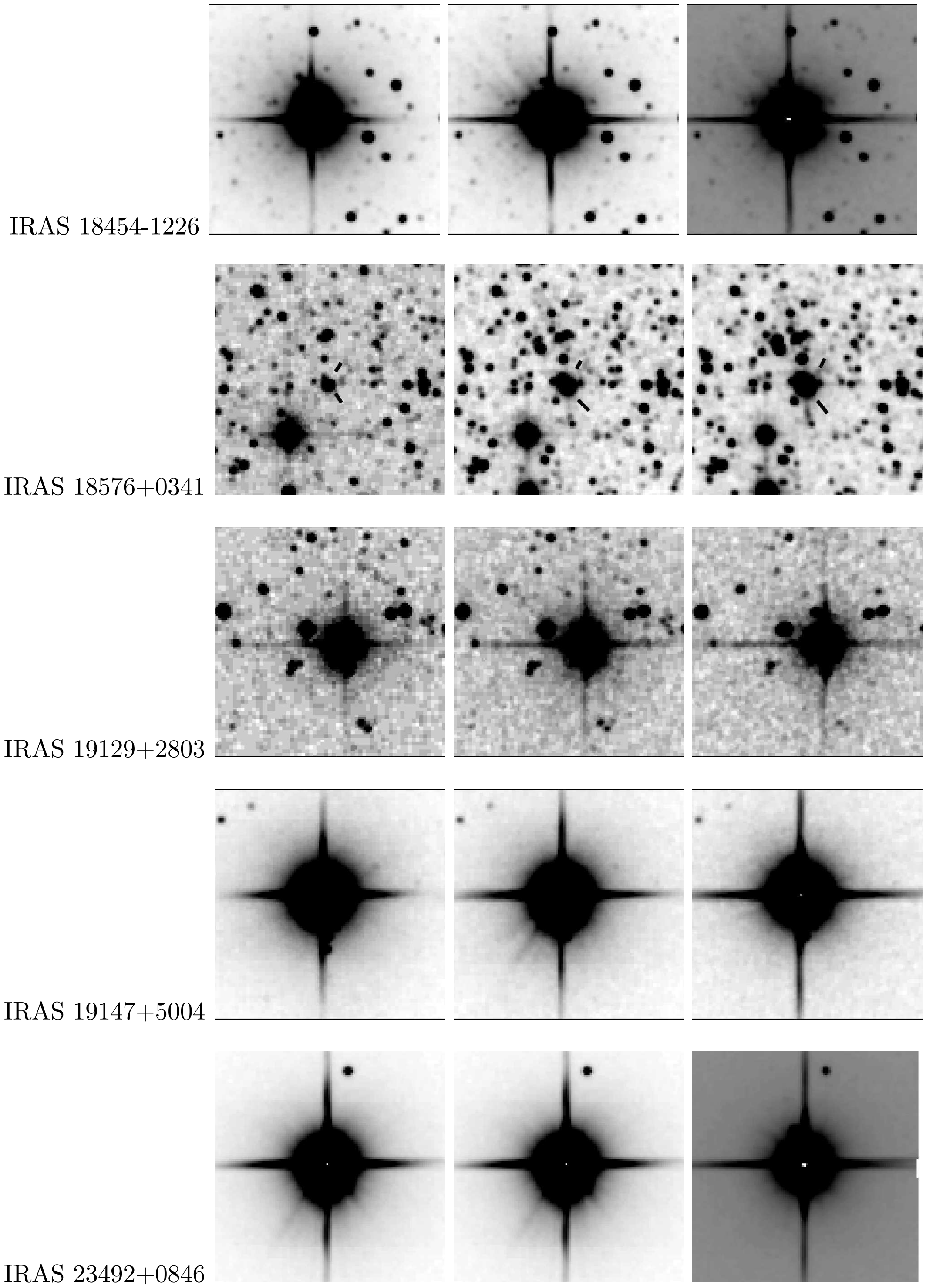

# Appendix E

# NIR photometry of the sources in the 'monitoring sample'

**Table E.1**: The near-infrared photometric data of the sources in our monitoring program. The Julian date is referred to 2 400 000.

| Julian Date | NIR magnitude [mag] | | | | Source |
|---|---|---|---|---|---|
| (2400000+) | J | H | K | L' | |
| | | | **IRAS 02095−2355** | | |
| 48488 | 3.32 ± 0.01 | 2.39 ± 0.01 | — | — | |
| 48509 | 3.26 ± 0.04 | 2.38 ± 0.02 | 2.04 ± 0.02 | — | |
| 48865 | 3.41 ± 0.05 | 2.43 ± 0.02 | 2.10 ± 0.01 | — | |
| 48880 | 3.34 ± 0.02 | 2.45 ± 0.02 | 2.12 ± 0.02 | — | |
| 48922 | 3.29 ± 0.06 | 2.38 ± 0.02 | 2.06 ± 0.02 | — | |
| 48944 | 3.24 ± 0.05 | 2.35 ± 0.02 | 2.02 ± 0.02 | 1.80 ± 0.03 | |
| 49229 | 3.35 ± 0.25 | 2.34 ± 0.06 | 2.03 ± 0.06 | 1.81 ± 0.06 | |
| 49320 | 3.24 ± 0.03 | 2.39 ± 0.09 | 2.08 ± 0.14 | — | |
| 49326 | 3.36 ± 0.02 | 2.45 ± 0.02 | 2.16 ± 0.02 | — | |
| 49385 | 3.42 ± 0.07 | 2.49 ± 0.05 | 2.14 ± 0.05 | — | |
| 49694 | 3.38 ± 0.03 | 2.50 ± 0.03 | 2.14 ± 0.02 | 2.01 ± 0.01 | |
| 49737 | 3.33 ± 0.03 | 2.46 ± 0.03 | 2.13 ± 0.03 | 1.85 ± 0.10 | |
| 49935 | 3.23 ± 0.03 | 2.36 ± 0.02 | 2.03 ± 0.02 | — | |
| 49936 | 3.44 ± 0.05 | 2.47 ± 0.03 | 2.12 ± 0.03 | — | |
| 49988 | 3.26 ± 0.03 | 2.38 ± 0.02 | 2.03 ± 0.01 | — | |
| 49997 | 3.21 ± 0.02 | 2.31 ± 0.02 | 2.00 ± 0.02 | 1.74 ± 0.08 | |

*Continue in the next page.*

*Table E.1: NIR photometry of the sources in our monitoring program (continued)*

| Julian Date<br>(2400000+) | NIR magnitude [mag]<br>J | <br>H | <br>K | <br>L’ | Source |
|---|---|---|---|---|---|
| 50056 | 3.20 ± 0.02 | 2.32 ± 0.02 | 2.03 ± 0.02 | 1.74 ± 0.06 | |
| 50305 | 3.34 ± 0.04 | 2.42 ± 0.03 | 2.08 ± 0.03 | — | |
| 50467 | 3.23 ± 0.02 | 2.36 ± 0.02 | 2.01 ± 0.02 | 1.72 ± 0.05 | |
| 51832 | 3.24 ± 0.01 | 2.35 ± 0.01 | 2.02 ± 0.01 | — | |
| | | | **IRAS 03293+6010** | | |
| 48362 | 13.41 ± 0.75 | 11.06 ± 0.06 | 8.09 ± 0.03 | — | |
| 48686 | 13.59 ± 0.16 | 10.10 ± 0.04 | 7.20 ± 0.04 | — | |
| 48944 | 13.17 ± 0.32 | 9.99 ± 0.02 | 7.12 ± 0.02 | — | |
| 49320 | 13.16 ± 0.26 | 9.85 ± 0.12 | 7.14 ± 0.16 | — | |
| 49325 | — | 9.62 ± 0.02 | 6.93 ± 0.02 | — | |
| 49328 | 12.83 ± 0.20 | 9.64 ± 0.03 | 6.93 ± 0.02 | 3.02 ± 0.06 | |
| 49385 | 12.96 ± 0.40 | 9.66 ± 0.06 | 7.02 ± 0.03 | — | |
| 49415 | 12.64 ± 0.21 | 9.70 ± 0.07 | 7.02 ± 0.04 | — | |
| 49737 | 13.95 ± 1.08 | 10.23 ± 0.04 | 7.56 ± 0.02 | 3.55 ± 0.10 | |
| 49936 | — | 10.71 ± 0.04 | 7.92 ± 0.03 | — | |
| 51366 | — | — | 7.34 ± 0.01 | — | MAGIC |
| 51832 | 14.49 ± 0.73 | 10.77 ± 0.07 | 7.95 ± 0.05 | — | |
| | | | **IRAS 04130+3918** | | |
| 48362 | 7.15 ± 0.01 | 5.16 ± 0.02 | 3.54 ± 0.02 | — | |
| 48509 | 6.47 ± 0.04 | 4.58 ± 0.02 | 3.04 ± 0.02 | — | |
| 48686 | 7.69 ± 0.03 | 5.63 ± 0.03 | 3.90 ± 0.03 | — | |
| 48865 | 7.58 ± 0.03 | 5.35 ± 0.02 | 3.72 ± 0.02 | — | |
| 48880 | 7.37 ± 0.01 | 5.31 ± 0.01 | 3.65 ± 0.01 | — | |
| 48922 | 6.82 ± 0.06 | 4.85 ± 0.02 | 3.29 ± 0.02 | — | |
| 48944 | 6.59 ± 0.04 | 4.70 ± 0.01 | 3.15 ± 0.01 | 1.25 ± 0.02 | |
| 49228 | 8.08 ± 0.07 | 5.68 ± 0.03 | 4.03 ± 0.05 | 2.00 ± 0.03 | |
| 49324 | 7.41 ± 0.02 | 5.27 ± 0.02 | 3.64 ± 0.02 | — | |
| 49386 | 6.91 ± 0.02 | 4.92 ± 0.02 | 3.37 ± 0.02 | 1.47 ± 0.11 | |
| 49415 | 6.54 ± 0.04 | 4.65 ± 0.03 | 3.13 ± 0.04 | 1.18 ± 0.05 | |
| 49426 | 6.57 ± 0.02 | 4.61 ± 0.02 | 3.10 ± 0.02 | 1.12 ± 0.05 | |
| 49737 | 7.76 ± 0.03 | 5.62 ± 0.02 | 3.88 ± 0.02 | 1.68 ± 0.07 | |
| 49936 | 6.75 ± 0.05 | 4.72 ± 0.03 | 3.12 ± 0.03 | — | |

*Continue in the next page.*

*Table E.1: NIR photometry of the sources in our monitoring program (continued)*

| Julian Date<br>(2400000+) | NIR magnitude [mag]<br>J | <br>H | <br>K | <br>L' | Source |
|---|---|---|---|---|---|
| 49988 | 6.87 ± 0.03 | 4.82 ± 0.02 | 3.21 ± 0.01 | — | |
| 50013 | 7.06 ± 0.02 | 4.97 ± 0.02 | 3.34 ± 0.02 | — | |
| 50043 | 7.30 ± 0.03 | 5.19 ± 0.02 | 3.51 ± 0.02 | — | |
| 50075 | 7.64 ± 0.02 | 5.50 ± 0.02 | 3.78 ± 0.03 | — | |
| 51832 | 6.34 ± 0.05 | 4.47 ± 0.03 | 3.00 ± 0.04 | — | |
| | | **IRAS 05131+4530** | | | |
| 48327 | 14.13 ± 0.38 | 10.69 ± 0.05 | 8.00 ± 0.05 | — | |
| 48341 | 14.59 ± 1.10 | 10.02 ± 0.30 | 7.26 ± 0.25 | — | |
| 48362 | 14.71 ± 1.32 | 9.80 ± 0.03 | 7.05 ± 0.03 | — | |
| 48686 | 15.01 ± 0.84 | 11.34 ± 0.07 | 8.28 ± 0.05 | — | |
| 48728 | 13.05 ± 0.21 | 10.09 ± 0.05 | 7.32 ± 0.04 | — | |
| 48922 | 11.46 ± 0.06 | 8.34 ± 0.02 | 5.82 ± 0.02 | — | |
| 48944 | 11.38 ± 0.07 | 8.28 ± 0.02 | 5.73 ± 0.02 | — | |
| 49004 | 11.20 ± 0.28 | 8.10 ± 0.25 | 5.65 ± 0.36 | — | |
| 49229 | 12.15 ± 0.62 | 8.72 ± 0.07 | 6.28 ± 0.06 | — | |
| 49324 | — | 9.07 ± 0.04 | 6.53 ± 0.02 | — | |
| 49328 | 12.50 ± 0.20 | 9.12 ± 0.03 | 6.58 ± 0.02 | 3.34 ± 0.06 | |
| 49386 | 13.07 ± 0.38 | 9.61 ± 0.03 | 6.94 ± 0.03 | — | |
| 49400 | 13.53 ± 0.56 | 9.64 ± 0.04 | 6.92 ± 0.03 | — | |
| 49415 | 13.12 ± 0.56 | 9.79 ± 0.05 | 7.02 ± 0.04 | — | |
| 49427 | 14.37 ± 2.07 | 9.88 ± 0.05 | 7.07 ± 0.02 | — | |
| 49456 | 14.44 ± 0.60 | 10.01 ± 0.03 | 7.22 ± 0.02 | — | |
| 49621 | — | 12.33 ± 0.10 | 8.95 ± 0.03 | — | |
| 49694 | 14.09 ± 0.61 | 12.65 ± 0.68 | 8.07 ± 0.02 | 4.09 ± 0.04 | |
| 49736 | — | 10.66 ± 0.03 | 7.51 ± 0.03 | — | |
| 49936 | 11.28 ± 0.05 | 8.23 ± 0.03 | 5.72 ± 0.03 | — | |
| 50043 | — | 8.07 ± 0.04 | 5.66 ± 0.03 | — | |
| 50057 | 11.09 ± 0.05 | 7.91 ± 0.03 | 5.50 ± 0.02 | — | |
| 50075 | — | 7.98 ± 0.03 | 5.63 ± 0.03 | — | |
| 50172 | — | 8.24 ± 0.02 | 5.74 ± 0.02 | — | |
| 50467 | 12.69 ± 0.20 | 9.31 ± 0.03 | 6.71 ± 0.02 | — | |
| 51832 | 13.86 ± 0.94 | 11.38 ± 0.12 | 8.26 ± 0.05 | — | |
| 52041 | 12.00 ± 0.03 | 8.55 ± 0.02 | 6.11 ± 0.03 | — | MAGIC |

*Continue in the next page.*

*Table E.1: NIR photometry of the sources in our monitoring program (continued)*

| Julian Date | NIR magnitude [mag] | | | | Source |
|---|---|---|---|---|---|
| (2400000+) | J | H | K | L' | |
| | | **IRAS 06297+4045** | | | |
| 48327 | 5.51 ± 0.02 | 4.00 ± 0.01 | 2.79 ± 0.01 | — | |
| 48341 | 5.44 ± 0.01 | 3.83 ± 0.01 | 2.62 ± 0.01 | — | |
| 48355 | 5.41 ± 0.01 | 3.80 ± 0.01 | 2.63 ± 0.02 | — | |
| 48362 | 5.38 ± 0.01 | 3.77 ± 0.01 | 2.58 ± 0.02 | — | |
| 48374 | 5.37 ± 0.01 | 3.78 ± 0.02 | 2.61 ± 0.02 | — | |
| 48664 | 7.13 ± 0.02 | 5.18 ± 0.02 | 3.71 ± 0.02 | — | |
| 48686 | 7.35 ± 0.02 | 5.33 ± 0.02 | 3.80 ± 0.03 | — | |
| 48728 | 7.59 ± 0.04 | 5.50 ± 0.03 | 3.90 ± 0.03 | — | |
| 48865 | 5.65 ± 0.04 | 3.82 ± 0.02 | 2.68 ± 0.03 | — | |
| 48922 | 5.22 ± 0.06 | 3.59 ± 0.02 | 2.48 ± 0.02 | — | |
| 48944 | 5.20 ± 0.04 | 3.64 ± 0.01 | 2.50 ± 0.01 | 1.01 ± 0.02 | |
| 49320 | 6.30 ± 0.03 | 4.48 ± 0.08 | 3.12 ± 0.13 | — | |
| 49324 | 6.18 ± 0.02 | 4.36 ± 0.02 | 3.03 ± 0.02 | — | |
| 49385 | 5.41 ± 0.03 | 3.75 ± 0.02 | 2.60 ± 0.02 | 1.06 ± 0.04 | |
| 49415 | 5.36 ± 0.03 | 3.75 ± 0.03 | 2.58 ± 0.03 | 1.00 ± 0.06 | |
| 49426 | 5.30 ± 0.03 | 3.64 ± 0.02 | 2.50 ± 0.02 | 0.94 ± 0.05 | |
| 49456 | 5.16 ± 0.02 | 3.54 ± 0.02 | 2.44 ± 0.01 | 0.95 ± 0.07 | |
| 49597 | 5.76 ± 0.02 | 4.10 ± 0.01 | 2.92 ± 0.02 | — | |
| 49621 | 5.89 ± 0.01 | 4.21 ± 0.01 | 3.05 ± 0.01 | — | |
| 49694 | 6.61 ± 0.02 | 4.76 ± 0.02 | 3.44 ± 0.02 | 1.83 ± 0.01 | |
| 49736 | 6.94 ± 0.02 | 5.00 ± 0.01 | 3.57 ± 0.02 | — | |
| 49840 | 6.56 ± 0.01 | 4.75 ± 0.01 | 3.31 ± 0.03 | — | |
| 51548 | 5.19 ± 0.02 | 3.51 ± 0.06 | 2.37 ± 0.04 | — | |
| 51860 | 6.26 ± 0.01 | 4.56 ± 0.01 | 3.30 ± 0.01 | — | |
| 52041 | 5.65 ± 0.01 | 4.42 ± 0.03 | 2.43 ± 0.05 | — | MAGIC |
| | | **IRAS 07222−2005** | | | |
| 48327 | 5.78 ± 0.02 | 4.86 ± 0.02 | 4.10 ± 0.02 | — | |
| 48341 | 5.98 ± 0.02 | 4.69 ± 0.01 | 3.98 ± 0.02 | — | |
| 48354 | 5.99 ± 0.01 | 4.67 ± 0.02 | 3.97 ± 0.02 | — | |
| 48664 | 6.56 ± 0.02 | 5.37 ± 0.03 | 4.54 ± 0.02 | — | |
| 48686 | 6.64 ± 0.03 | 5.42 ± 0.03 | 4.61 ± 0.03 | — | |

*Continue in the next page.*

*Table E.1: NIR photometry of the sources in our monitoring program (continued)*

| Julian Date<br>(2400000+) | NIR magnitude [mag]<br>J | <br>H | <br>K | <br>L' | Source |
|---|---|---|---|---|---|
| 48728 | 6.78 ± 0.05 | 5.59 ± 0.03 | 4.76 ± 0.04 | — | |
| 48740 | 6.87 ± 0.01 | 5.65 ± 0.01 | 4.78 ± 0.01 | — | |
| 48944 | 7.27 ± 0.05 | 6.07 ± 0.02 | 5.12 ± 0.02 | — | |
| 49004 | 7.19 ± 0.22 | 5.95 ± 0.25 | 5.23 ± 0.36 | — | |
| 49385 | 6.49 ± 0.05 | 5.40 ± 0.04 | 4.62 ± 0.03 | 3.25 ± 0.06 | |
| 49415 | 6.40 ± 0.04 | 5.24 ± 0.03 | 4.45 ± 0.04 | 3.41 ± 0.06 | |
| 49426 | 6.31 ± 0.03 | 5.13 ± 0.03 | 4.38 ± 0.02 | 3.14 ± 0.06 | |
| 49456 | 6.30 ± 0.02 | 5.11 ± 0.02 | 4.36 ± 0.02 | 3.37 ± 0.08 | |
| 49694 | 6.25 ± 0.03 | 4.92 ± 0.03 | 4.18 ± 0.02 | 3.26 ± 0.01 | |
| 49736 | 6.35 ± 0.02 | 5.04 ± 0.01 | 4.32 ± 0.02 | — | |
| 50044 | 7.30 ± 0.04 | 6.05 ± 0.04 | 5.15 ± 0.03 | — | |
| 51832 | 7.03 ± 0.06 | 5.94 ± 0.05 | 5.00 ± 0.06 | — | |
| | | | **IRAS 16029−3041** | | |
| 48341 | 13.32 ± 0.32 | 9.86 ± 0.02 | 6.54 ± 0.02 | — | |
| 48374 | 13.57 ± 0.41 | 10.15 ± 0.05 | 6.79 ± 0.02 | — | |
| 48740 | 12.10 ± 0.03 | 8.91 ± 0.02 | 5.71 ± 0.01 | — | |
| 48771 | 12.88 ± 0.08 | 9.60 ± 0.05 | 6.42 ± 0.05 | — | |
| 49840 | 12.55 ± 0.03 | 9.27 ± 0.01 | 5.66 ± 0.03 | — | |
| 49935 | 12.84 ± 0.11 | 9.59 ± 0.02 | 5.97 ± 0.02 | — | |
| 50174 | — | — | 8.41 ± 0.02 | — | |
| 50247 | — | — | 7.84 ± 0.02 | — | |
| 50248 | — | 12.06 ± 0.05 | 7.83 ± 0.02 | 2.33 ± 0.05 | |
| 50976 | 14.21 ± 0.40 | 10.44 ± 0.01 | 6.49 ± 0.01 | — | |
| 51369 | 13.99 ± 0.02 | 11.20 ± 0.10 | 7.10 ± 0.01 | — | |
| 51752 | — | — | 7.94 ± 0.04 | — | MAGIC |
| 52043 | — | — | 6.50 ± 0.06 | — | MAGIC* |
| 52087 | — | 11.38 ± 0.05 | 6.89 ± 0.04 | — | |
| | | | **IRAS 16037+4218** | | |
| 48327 | 4.62 ± 0.01 | 3.80 ± 0.01 | 3.36 ± 0.01 | — | |
| 48341 | 4.42 ± 0.02 | 3.64 ± 0.01 | 3.18 ± 0.01 | — | |
| 48355 | 4.44 ± 0.01 | 3.65 ± 0.02 | 3.19 ± 0.01 | — | |
| 48374 | 4.42 ± 0.01 | 3.63 ± 0.02 | 3.17 ± 0.01 | — | |

*Continue in the next page.*

*Table E.1: NIR photometry of the sources in our monitoring program (continued)*

| Julian Date (2400000+) | NIR magnitude [mag] J | H | K | L' | Source |
|---|---|---|---|---|---|
| 48484 | 5.15 ± 0.03 | 4.37 ± 0.10 | 4.17 ± 0.16 | — | |
| 48485 | 4.97 ± 0.02 | 4.22 ± 0.03 | 3.66 ± 0.04 | — | |
| 48499 | 5.10 ± 0.05 | 4.31 ± 0.07 | 3.74 ± 0.07 | — | |
| 48509 | 5.21 ± 0.04 | 4.45 ± 0.02 | 3.83 ± 0.04 | — | |
| 48664 | 4.76 ± 0.01 | 3.96 ± 0.01 | 3.45 ± 0.01 | — | |
| 48686 | 4.68 ± 0.02 | 3.87 ± 0.02 | 3.36 ± 0.02 | — | |
| 48728 | 4.58 ± 0.04 | 3.76 ± 0.02 | 3.25 ± 0.03 | — | |
| 48770 | 4.69 ± 0.02 | 3.89 ± 0.01 | 3.36 ± 0.01 | — | |
| 48824 | 4.99 ± 0.01 | 4.21 ± 0.01 | 3.63 ± 0.01 | — | |
| 48880 | 5.39 ± 0.02 | 4.56 ± 0.02 | 3.94 ± 0.02 | — | |
| 48921 | 5.44 ± 0.07 | 4.60 ± 0.03 | 3.96 ± 0.02 | — | |
| 49002 | 4.94 ± 0.03 | 4.17 ± 0.03 | 3.64 ± 0.01 | 2.78 ± 0.09 | |
| 49226 | 5.48 ± 0.02 | 4.58 ± 0.02 | 3.96 ± 0.01 | — | |
| 49386 | 4.89 ± 0.01 | 4.17 ± 0.01 | 3.64 ± 0.01 | 2.75 ± 0.09 | |
| 49400 | 4.75 ± 0.02 | 4.01 ± 0.02 | 3.53 ± 0.01 | 2.51 ± 0.03 | |
| 49427 | 4.69 ± 0.02 | 3.89 ± 0.02 | 3.38 ± 0.01 | 2.60 ± 0.03 | |
| 49439 | 4.63 ± 0.03 | 3.83 ± 0.04 | 3.32 ± 0.02 | — | |
| 49456 | 4.72 ± 0.01 | 3.82 ± 0.01 | 3.37 ± 0.01 | 2.64 ± 0.06 | |
| 49500 | 4.86 ± 0.02 | 4.03 ± 0.01 | 3.64 ± 0.02 | — | |
| 49597 | 5.51 ± 0.02 | 4.68 ± 0.01 | 4.03 ± 0.02 | — | |
| 49608 | 5.52 ± 0.02 | 4.70 ± 0.01 | 4.05 ± 0.01 | 3.04 ± 0.15 | |
| 49735 | 4.81 ± 0.02 | 4.03 ± 0.03 | 3.52 ± 0.06 | — | |
| 49839 | 4.56 ± 0.01 | 3.78 ± 0.01 | 3.33 ± 0.03 | — | |
| 50201 | 4.68 ± 0.02 | 3.90 ± 0.02 | 3.40 ± 0.02 | — | |
| 50226 | 4.95 ± 0.02 | 4.15 ± 0.02 | 3.59 ± 0.02 | — | |
| 50232 | 4.95 ± 0.02 | 4.23 ± 0.02 | 3.66 ± 0.02 | 2.84 ± 0.04 | |
| 50976 | 5.07 ± 0.01 | 4.33 ± 0.01 | 3.76 ± 0.01 | — | |
| 51360 | 5.25 ± 0.04 | 4.64 ± 0.05 | — | — | MAGIC |
| 51364 | 5.28 ± 0.02 | 4.50 ± 0.01 | 3.87 ± 0.01 | — | |
| 51367 | — | — | 3.83 ± 0.13 | — | MAGIC |
| 51745 | 5.35 ± 0.01 | 4.57 ± 0.01 | 3.89 ± 0.09 | — | MAGIC |
| 52041 | 5.39 ± 0.04 | 4.69 ± 0.03 | 3.59 ± 0.04 | — | MAGIC |
| 52117 | 5.60 ± 0.01 | 4.87 ± 0.01 | 4.21 ± 0.01 | — | |
| 52118 | 5.58 ± 0.07 | 4.84 ± 0.04 | 4.18 ± 0.05 | — | |

*Continue in the next page.*

*Table E.1: NIR photometry of the sources in our monitoring program (continued)*

| Julian Date | NIR magnitude [mag] | | | | Source |
|---|---|---|---|---|---|
| (2400000+) | J | H | K | L’ | |
| | | | **IRAS 16437−3140** | | |
| 48355 | — | 12.38 ± 0.13 | 8.91 ± 0.03 | — | |
| 48374 | — | 12.76 ± 0.49 | 9.06 ± 0.03 | — | |
| 49860 | — | 9.66 ± 0.03 | 6.52 ± 0.02 | 2.44 ± 0.75 | |
| 50226 | — | 12.52 ± 0.14 | 9.08 ± 0.02 | — | |
| 50976 | — | 12.79 ± 0.09 | 9.73 ± 0.01 | — | |
| 51369 | — | 11.40 ± 0.15 | 8.38 ± 0.01 | — | |
| 51745 | — | 10.84 ± 0.06 | 7.53 ± 0.03 | — | MAGIC |
| 52043 | — | 12.23 ± 0.07 | 8.70 ± 0.05 | — | MAGIC* |
| | | | **IRAS 17103−0559** | | |
| 48327 | 6.01 ± 0.01 | 4.74 ± 0.01 | 3.68 ± 0.01 | — | |
| 48341 | 5.69 ± 0.02 | 4.37 ± 0.01 | 3.42 ± 0.01 | — | |
| 48355 | 5.35 ± 0.01 | 4.11 ± 0.01 | 3.23 ± 0.02 | — | |
| 48374 | 5.11 ± 0.01 | 3.89 ± 0.02 | 3.07 ± 0.02 | — | |
| 48441 | 4.91 ± 0.04 | 3.62 ± 0.04 | 2.82 ± 0.04 | — | |
| 48486 | 4.97 ± 0.03 | 3.63 ± 0.04 | 2.83 ± 0.03 | — | |
| 48740 | 6.23 ± 0.01 | 4.70 ± 0.01 | 3.60 ± 0.01 | — | |
| 48771 | 5.85 ± 0.11 | 4.53 ± 0.12 | 3.51 ± 0.11 | — | |
| 48824 | 5.22 ± 0.02 | 3.96 ± 0.01 | 3.06 ± 0.02 | — | |
| 48865 | 5.02 ± 0.06 | 3.61 ± 0.03 | 2.82 ± 0.03 | — | |
| 48880 | 4.86 ± 0.01 | 3.59 ± 0.01 | 2.79 ± 0.01 | — | |
| 49228 | 5.96 ± 0.09 | 4.50 ± 0.03 | — | — | |
| 49405 | 5.81 ± 0.05 | 4.33 ± 0.04 | 3.39 ± 0.02 | 2.08 ± 0.08 | |
| 49840 | 5.82 ± 0.01 | 4.36 ± 0.01 | 3.34 ± 0.03 | — | |
| 49935 | 7.17 ± 0.02 | 5.59 ± 0.02 | 4.35 ± 0.02 | — | |
| 49952 | 7.54 ± 0.02 | 5.95 ± 0.02 | 4.68 ± 0.02 | — | |
| 50174 | 6.28 ± 0.03 | 4.97 ± 0.03 | 3.86 ± 0.03 | — | |
| 50201 | 6.23 ± 0.02 | 4.89 ± 0.02 | 3.81 ± 0.02 | — | |
| 50232 | 6.31 ± 0.02 | 4.99 ± 0.02 | 3.90 ± 0.02 | 2.22 ± 0.04 | |
| 50247 | 7.08 ± 0.10 | 5.39 ± 0.02 | 4.20 ± 0.03 | — | |
| 50976 | 7.26 ± 0.01 | 5.92 ± 0.01 | 4.55 ± 0.01 | — | |

*Continue in the next page.*

*Table E.1: NIR photometry of the sources in our monitoring program (continued)*

| Julian Date (2400000+) | J | H | K | L' | Source |
|---|---|---|---|---|---|
| | | | **IRAS 17105−2804** | | |
| 48327 | 6.35 ± 0.01 | 5.61 ± 0.01 | 4.89 ± 0.01 | — | |
| 48341 | 6.68 ± 0.02 | 5.56 ± 0.01 | 4.80 ± 0.01 | — | |
| 48355 | 6.79 ± 0.01 | 5.64 ± 0.02 | 4.87 ± 0.02 | — | |
| 48374 | 6.98 ± 0.01 | 5.81 ± 0.02 | 5.01 ± 0.02 | — | |
| 48441 | 7.57 ± 0.04 | 6.34 ± 0.04 | 5.36 ± 0.04 | — | |
| 48838 | 7.09 ± 0.03 | 5.97 ± 0.04 | 5.07 ± 0.05 | — | |
| 49860 | 5.79 ± 0.02 | 4.73 ± 0.03 | 3.99 ± 0.02 | — | |
| 50247 | 6.26 ± 0.02 | 5.27 ± 0.02 | 4.52 ± 0.02 | — | |
| 50301 | 5.67 ± 0.02 | 4.71 ± 0.04 | 4.07 ± 0.05 | — | |
| 50976 | 6.69 ± 0.01 | 5.71 ± 0.01 | 4.93 ± 0.01 | — | |
| 51310 | 7.07 ± 0.01 | 6.06 ± 0.01 | 5.24 ± 0.02 | — | |
| 51364 | 7.19 ± 0.02 | 6.14 ± 0.01 | 5.28 ± 0.01 | — | |
| | | | **IRAS 17313−1531** | | |
| 48327 | 7.60 ± 0.01 | 5.66 ± 0.01 | 4.27 ± 0.01 | — | |
| 48341 | 7.74 ± 0.02 | 5.70 ± 0.01 | 4.29 ± 0.01 | — | |
| 48374 | 8.01 ± 0.01 | 5.96 ± 0.02 | 4.54 ± 0.02 | — | |
| 48441 | 8.78 ± 0.04 | 6.60 ± 0.04 | 4.99 ± 0.04 | — | |
| 48838 | 7.91 ± 0.03 | 5.75 ± 0.04 | 4.20 ± 0.05 | — | |
| 49935 | 9.40 ± 0.02 | 7.16 ± 0.02 | 5.35 ± 0.02 | — | |
| 50269 | 8.02 ± 0.02 | 6.06 ± 0.02 | 4.58 ± 0.02 | — | |
| 50301 | 8.24 ± 0.02 | 6.31 ± 0.04 | 4.79 ± 0.05 | — | |
| 50976 | 8.85 ± 0.01 | 6.89 ± 0.01 | 5.21 ± 0.01 | — | |
| 51364 | 9.60 ± 0.03 | 7.41 ± 0.01 | 5.71 ± 0.01 | — | |
| 51365 | — | — | 5.70 ± 0.09 | — | MAGIC |
| | | | **IRAS 17347−3139** | | |
| 51753 | — | — | 10.12 ± 0.07 | — | MAGIC |
| | | | **IRAS 17411−3154** | | |
| 49860 | — | — | — | 3.82 ± 0.11 | |
| | | | **IRAS 18025−2113** | | |

*Continue in the next page.*

*Table E.1: NIR photometry of the sources in our monitoring program (continued)*

| Julian Date | NIR magnitude [mag] | | | | Source |
|---|---|---|---|---|---|
| (2400000+) | J | H | K | L’ | |
| 48824 | 4.28 ± 0.02 | 3.16 ± 0.01 | 2.51 ± 0.02 | — | |
| 48838 | 4.32 ± 0.03 | 3.17 ± 0.04 | 2.45 ± 0.04 | — | |
| 48865 | 4.43 ± 0.05 | 3.18 ± 0.03 | 2.53 ± 0.03 | — | |
| 50204 | 4.22 ± 0.05 | 3.14 ± 0.05 | 2.50 ± 0.05 | — | |
| 50300 | 3.99 ± 0.04 | 2.92 ± 0.05 | 2.27 ± 0.04 | — | |
| 50976 | 4.34 ± 0.01 | 3.22 ± 0.01 | 2.55 ± 0.01 | — | |
| 51364 | 4.37 ± 0.02 | 3.32 ± 0.01 | 2.67 ± 0.01 | — | |
| 51365 | — | — | 2.92 ± 0.21 | — | MAGIC |
| 51384 | 4.42 ± 0.01 | 3.36 ± 0.01 | 2.73 ± 0.01 | — | |
| | | **IRAS 18299−1705** | | | |
| 49229 | 8.13 ± 0.05 | 6.45 ± 0.03 | 5.00 ± 0.03 | — | |
| 49936 | 8.09 ± 0.05 | 6.55 ± 0.03 | 5.23 ± 0.03 | — | |
| 50232 | 8.22 ± 0.02 | 6.65 ± 0.02 | 5.31 ± 0.02 | — | |
| 50327 | 8.29 ± 0.02 | 6.69 ± 0.02 | 5.33 ± 0.02 | — | |
| 50976 | 8.00 ± 0.01 | 6.38 ± 0.01 | 5.02 ± 0.01 | — | |
| 51364 | 8.18 ± 0.02 | 6.62 ± 0.01 | 5.30 ± 0.01 | — | |
| 51365 | — | — | 5.26 ± 0.02 | — | MAGIC* |
| 51753 | 8.00 ± 0.03 | 6.39 ± 0.02 | 5.14 ± 0.01 | — | MAGIC |
| | | **IRAS 18314−1131** | | | |
| 49500 | 6.60 ± 0.03 | 4.61 ± 0.02 | 3.28 ± 0.03 | — | |
| 49597 | 5.69 ± 0.05 | 4.10 ± 0.01 | 3.36 ± 0.02 | — | |
| 49936 | 5.41 ± 0.05 | 3.82 ± 0.03 | 2.86 ± 0.03 | — | |
| 49953 | 5.67 ± 0.03 | 3.99 ± 0.03 | 3.02 ± 0.03 | — | |
| 50234 | 6.98 ± 0.02 | 5.28 ± 0.02 | 3.98 ± 0.02 | — | |
| 50306 | 5.48 ± 0.03 | 4.09 ± 0.02 | 3.12 ± 0.02 | 1.39 ± 0.06 | |
| 50976 | 6.21 ± 0.01 | 4.65 ± 0.01 | 3.48 ± 0.01 | — | |
| 51364 | 6.26 ± 0.02 | 4.70 ± 0.01 | 3.41 ± 0.01 | — | |
| 51365 | — | — | 3.44 ± 0.10 | — | MAGIC* |
| 51753 | 8.46 ± 0.10 | 6.07 ± 0.01 | 4.67 ± 0.07 | — | MAGIC |
| | | **IRAS 18327−0715** | | | |
| 51360 | — | — | 8.06 ± 0.04 | — | MAGIC* |

*Continue in the next page.*

*Table E.1: NIR photometry of the sources in our monitoring program (continued)*

| Julian Date | NIR magnitude [mag] | | | | Source |
|---|---|---|---|---|---|
| (2400000+) | J | H | K | L' | |
| 51753 | — | — | 8.85 ± 0.03 | — | MAGIC |
| | | | **IRAS 18429−1721** | | |
| 49597 | 3.29 ± 0.02 | 2.33 ± 0.01 | 1.75 ± 0.01 | — | |
| 49936 | 4.26 ± 0.05 | 3.41 ± 0.03 | 2.61 ± 0.03 | — | |
| 50234 | 4.56 ± 0.02 | 3.54 ± 0.02 | 2.77 ± 0.02 | 1.50 ± 0.06 | |
| 50305 | 4.53 ± 0.04 | 3.52 ± 0.03 | 2.72 ± 0.03 | — | |
| 50976 | 3.25 ± 0.01 | 2.30 ± 0.01 | 1.69 ± 0.01 | — | |
| 51364 | 4.38 ± 0.02 | 3.45 ± 0.01 | 2.61 ± 0.01 | — | |
| 51753 | 4.80 ± 0.06 | 3.62 ± 0.04 | 2.93 ± 0.04 | — | MAGIC |
| | | | **IRAS 18454−1226** | | |
| 48481 | 3.39 ± 0.04 | 2.37 ± 0.04 | 1.97 ± 0.03 | — | |
| 48499 | 3.38 ± 0.05 | 2.35 ± 0.07 | 1.93 ± 0.07 | — | |
| 49942 | 3.47 ± 0.04 | 2.43 ± 0.03 | 2.01 ± 0.03 | — | |
| 49952 | 3.40 ± 0.02 | 2.37 ± 0.01 | 1.95 ± 0.02 | — | |
| 50193 | 3.29 ± 0.10 | 2.31 ± 0.11 | 1.99 ± 0.10 | — | |
| 50234 | 3.45 ± 0.02 | 2.40 ± 0.02 | 2.01 ± 0.02 | 1.55 ± 0.06 | |
| 50269 | 3.46 ± 0.02 | 2.43 ± 0.02 | 2.00 ± 0.02 | 1.62 ± 0.05 | |
| 50301 | 3.46 ± 0.02 | 2.41 ± 0.04 | 2.00 ± 0.05 | — | |
| | | | **IRAS 18576+0341** | | |
| 48486 | 12.03 ± 0.11 | 8.83 ± 0.04 | 6.86 ± 0.04 | — | |
| 48830 | 12.78 ± 0.05 | 9.35 ± 0.03 | 7.37 ± 0.03 | — | |
| 48945 | 12.82 ± 0.03 | 9.26 ± 0.02 | 7.27 ± 0.02 | — | |
| 49228 | — | 9.39 ± 0.05 | 7.55 ± 0.08 | — | |
| 49936 | 11.92 ± 0.07 | 8.56 ± 0.03 | 6.62 ± 0.03 | — | |
| 49953 | 12.49 ± 0.15 | 8.67 ± 0.03 | 6.69 ± 0.03 | — | |
| 49989 | — | 8.41 ± 0.03 | 6.49 ± 0.02 | — | |
| 50201 | 11.36 ± 0.15 | 8.38 ± 0.02 | 6.50 ± 0.02 | — | |
| 50300 | — | 8.55 ± 0.05 | 6.63 ± 0.04 | — | |
| 50976 | 11.61 ± 0.05 | 8.53 ± 0.01 | 6.59 ± 0.01 | — | |
| 51365 | — | — | 6.99 ± 0.10 | — | MAGIC |
| 51369 | 12.55 ± 0.01 | 8.93 ± 0.02 | 6.96 ± 0.01 | — | |

*Continue in the next page.*

*Table E.1: NIR photometry of the sources in our monitoring program (continued)*

| Julian Date (2400000+) | NIR magnitude [mag] J | H | K | L’ | Source |
|---|---|---|---|---|---|
| 51384 | 12.00 ± 0.10 | 8.86 ± 0.01 | 6.93 ± 0.01 | — | |
| 51752 | — | — | 7.38 ± 0.01 | — | MAGIC |
| | | | **IRAS 19129+2803** | | |
| 48487 | 6.61 ± 0.02 | 5.50 ± 0.01 | 4.74 ± 0.01 | — | |
| 48509 | 6.65 ± 0.05 | 5.57 ± 0.02 | 4.80 ± 0.04 | — | |
| 48830 | 6.73 ± 0.03 | 5.70 ± 0.02 | 4.85 ± 0.03 | — | |
| 48865 | 6.62 ± 0.04 | 5.42 ± 0.02 | 4.69 ± 0.02 | — | |
| 48880 | 6.49 ± 0.01 | 5.41 ± 0.01 | 4.64 ± 0.01 | — | |
| 48922 | 6.52 ± 0.06 | 5.41 ± 0.02 | 4.65 ± 0.02 | — | |
| 48945 | 6.60 ± 0.01 | 5.45 ± 0.01 | 4.67 ± 0.02 | — | |
| 49227 | 7.37 ± 0.05 | 6.27 ± 0.06 | 5.34 ± 0.02 | — | |
| 49405 | 6.86 ± 0.05 | 5.73 ± 0.04 | 4.93 ± 0.02 | — | |
| 49597 | 8.37 ± 0.02 | 6.98 ± 0.01 | 5.81 ± 0.01 | — | |
| 49840 | 7.02 ± 0.01 | 5.90 ± 0.01 | 5.08 ± 0.03 | — | |
| 49936 | 8.00 ± 0.05 | 6.62 ± 0.03 | 5.60 ± 0.03 | — | |
| 49953 | 8.17 ± 0.03 | 6.76 ± 0.03 | 5.68 ± 0.03 | — | |
| 49997 | 8.42 ± 0.02 | 7.01 ± 0.02 | 5.80 ± 0.02 | — | |
| 50247 | 6.65 ± 0.02 | 5.49 ± 0.02 | 4.75 ± 0.02 | — | |
| 50248 | 6.70 ± 0.02 | 5.55 ± 0.02 | 4.78 ± 0.02 | 3.59 ± 0.05 | |
| 50249 | 6.71 ± 0.02 | 5.55 ± 0.02 | 4.78 ± 0.02 | 3.73 ± 0.05 | |
| 50300 | 6.96 ± 0.04 | 5.79 ± 0.05 | 4.98 ± 0.04 | — | |
| 51365 | 6.89 ± 0.03 | 5.73 ± 0.02 | 4.98 ± 0.03 | — | MAGIC* |
| 51748 | 8.00 ± 0.02 | 6.59 ± 0.01 | 5.51 ± 0.01 | — | MAGIC |
| 52041 | 7.75 ± 0.02 | 6.33 ± 0.02 | 5.49 ± 0.03 | — | MAGIC* |
| 52117 | 8.30 ± 0.02 | 6.87 ± 0.01 | 5.75 ± 0.01 | — | |
| 52118 | 8.38 ± 0.08 | 6.89 ± 0.05 | 5.75 ± 0.05 | — | |
| | | | **IRAS 19147+5004** | | |
| 48486 | 3.73 ± 0.03 | 2.88 ± 0.04 | 2.54 ± 0.03 | — | |
| 48509 | 3.75 ± 0.05 | 2.91 ± 0.03 | 2.58 ± 0.04 | — | |
| 48664 | 3.78 ± 0.02 | 2.92 ± 0.02 | 2.57 ± 0.02 | — | |
| 48838 | 3.74 ± 0.02 | 2.83 ± 0.03 | 2.44 ± 0.04 | — | |
| 48845 | 3.72 ± 0.03 | 2.84 ± 0.03 | 2.52 ± 0.02 | — | |

*Continue in the next page.*

*Table E.1: NIR photometry of the sources in our monitoring program (continued)*

| Julian Date | NIR magnitude [mag] | | | | Source |
|---|---|---|---|---|---|
| (2400000+) | J | H | K | L’ | |
| 48880 | 3.63 ± 0.01 | 2.77 ± 0.01 | 2.45 ± 0.01 | — | |
| 48922 | 3.74 ± 0.07 | 2.85 ± 0.03 | 2.52 ± 0.02 | — | |
| 48945 | 3.78 ± 0.02 | 2.93 ± 0.02 | 2.64 ± 0.04 | 2.27 ± 0.05 | |
| 49227 | 3.85 ± 0.02 | 2.88 ± 0.03 | 2.56 ± 0.02 | 2.26 ± 0.06 | |
| 49322 | 3.50 ± 0.07 | 2.58 ± 0.12 | 2.21 ± 0.11 | 2.07 ± 0.09 | |
| 49437 | 3.69 ± 0.02 | 2.85 ± 0.02 | 2.53 ± 0.02 | 2.30 ± 0.05 | |
| 49456 | 3.80 ± 0.02 | 2.84 ± 0.02 | 2.56 ± 0.01 | 2.26 ± 0.06 | |
| 49926 | 3.56 ± 0.07 | 2.73 ± 0.04 | 2.38 ± 0.05 | — | |
| 49935 | 3.62 ± 0.02 | 2.75 ± 0.02 | 2.43 ± 0.02 | — | |
| 49997 | 3.68 ± 0.02 | 2.88 ± 0.02 | 2.53 ± 0.02 | 2.36 ± 0.08 | |
| 50247 | 3.70 ± 0.02 | 2.84 ± 0.02 | 2.52 ± 0.02 | — | |
| 50248 | 3.71 ± 0.02 | 2.85 ± 0.02 | 2.52 ± 0.02 | 2.16 ± 0.05 | |
| 50269 | 3.71 ± 0.02 | 2.90 ± 0.02 | 2.47 ± 0.02 | 2.27 ± 0.05 | |
| 50298 | 3.78 ± 0.02 | 2.93 ± 0.02 | 2.57 ± 0.02 | 2.23 ± 0.04 | |
| **IRAS 23492+0846** | | | | | |
| 48487 | 2.60 ± 0.01 | 1.70 ± 0.01 | 1.34 ± 0.01 | — | |
| 49325 | 2.62 ± 0.02 | 1.70 ± 0.02 | 1.39 ± 0.02 | — | |
| 49952 | 2.67 ± 0.02 | 1.76 ± 0.01 | 1.39 ± 0.02 | 1.13 ± 0.10 | |
| 49988 | 2.64 ± 0.03 | 1.71 ± 0.02 | 1.35 ± 0.01 | — | |
| 50300 | 2.63 ± 0.04 | 1.74 ± 0.02 | 1.39 ± 0.04 | — | |
| 50306 | 2.64 ± 0.03 | 1.73 ± 0.02 | 1.37 ± 0.02 | 1.07 ± 0.06 | |

# Appendix F

# K-band light curves for the sources in the ‘monitoring sample’

**Figure F.1**: K magnitude data available for the variability analysis. The data obtained using the CST equipped with the CVF photometer are plotted with filled triangles; the data obtained using the 1.23 m telescope equipped with MAGIC are plotted with filled squares.

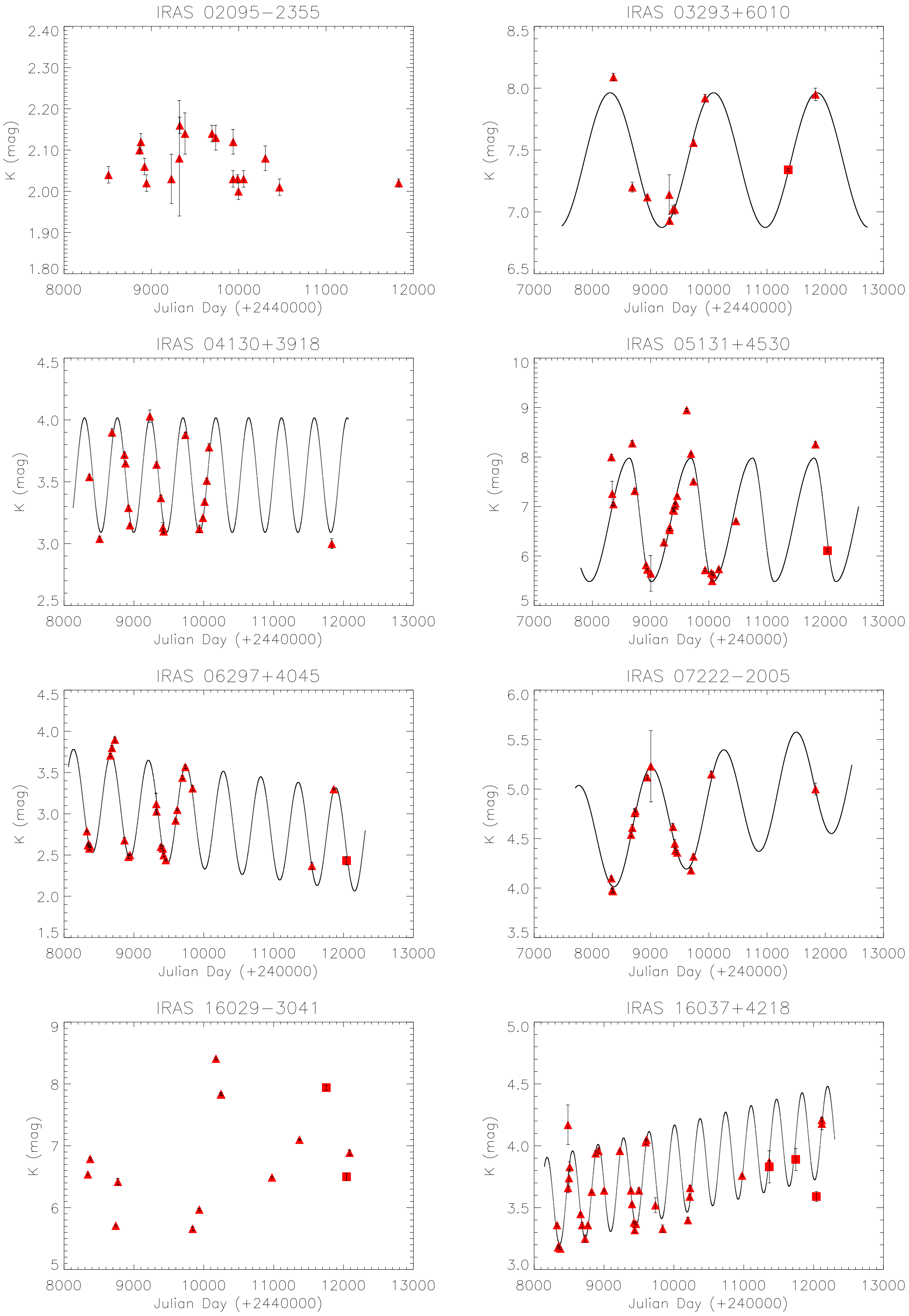

*Continue in the next page.*

*Figure F.1: Infrared K magnitude data available for the variability analysis (continued)*

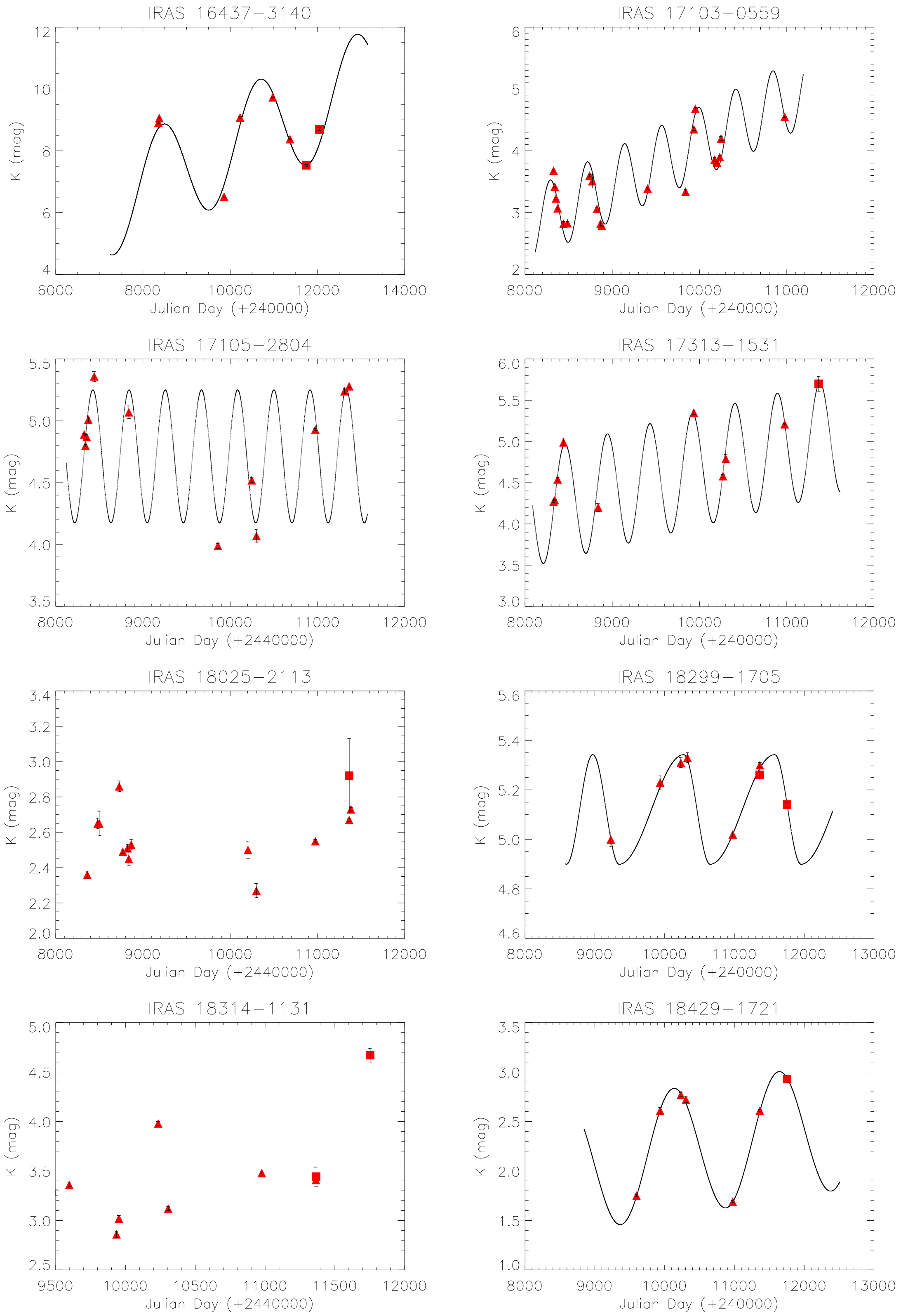

*Continue in the next page.*

*Fig.F.1: Infrared K magnitude data available for the variability analysis (continued)*

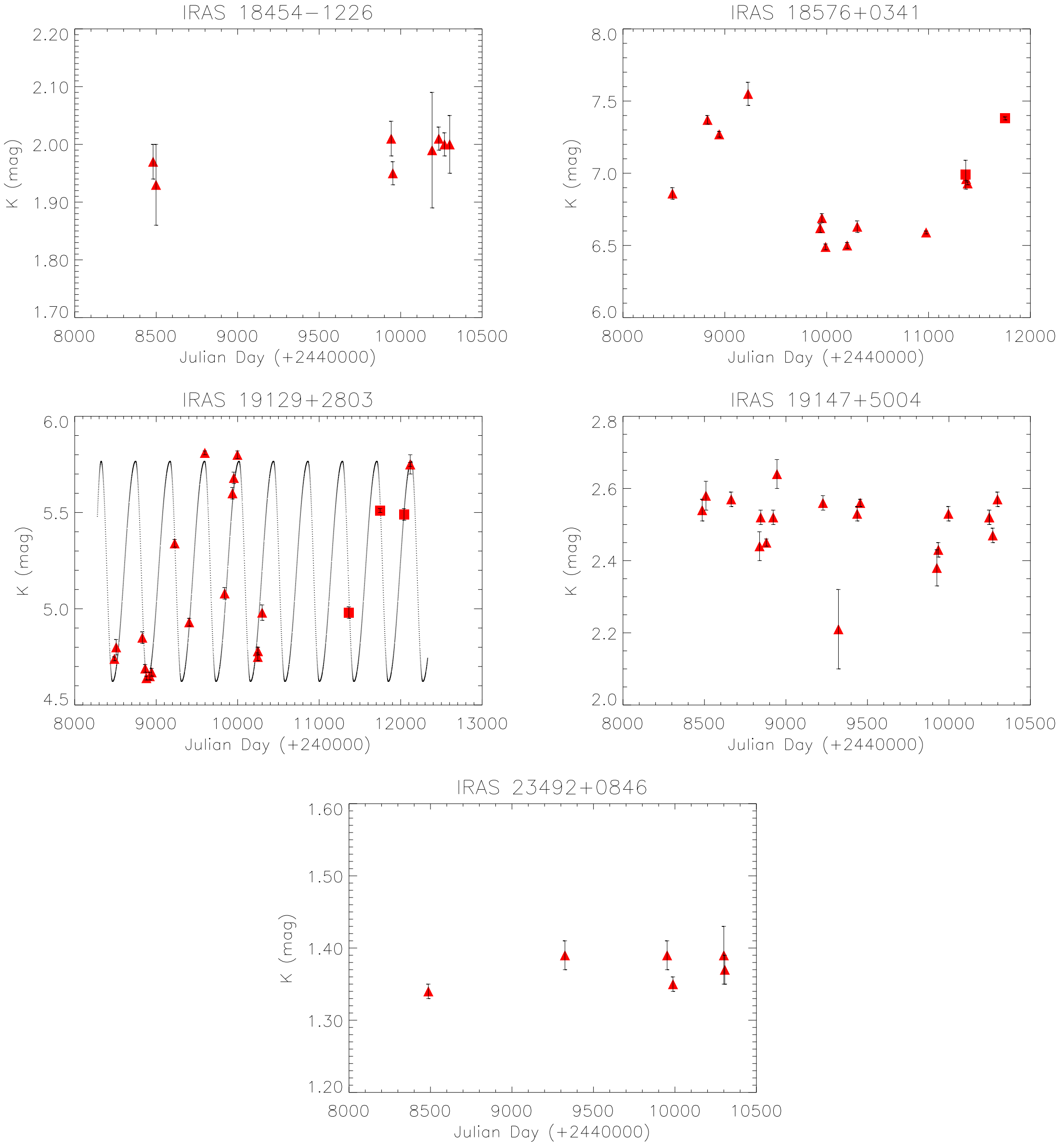

# Appendix G

# Phased K-band light curves for some sources in the ‘monitoring sample’

**Figure G.1**: Light curves derived from some sources in the monitoring program as a function of the variability phase.

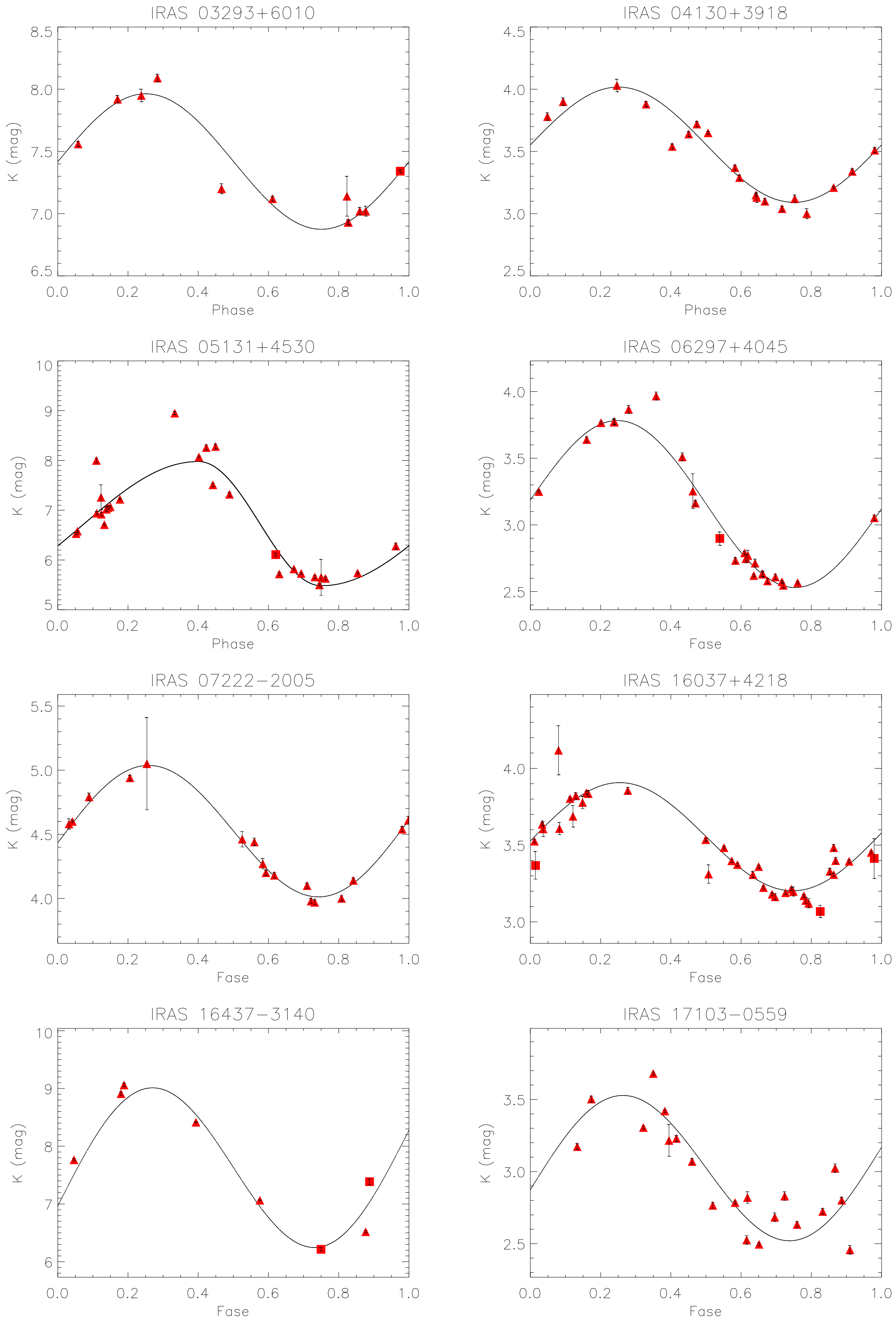

*Continue in the next page.*

*Figure G.1: Light curves obtained from the monitoring program (continued)*

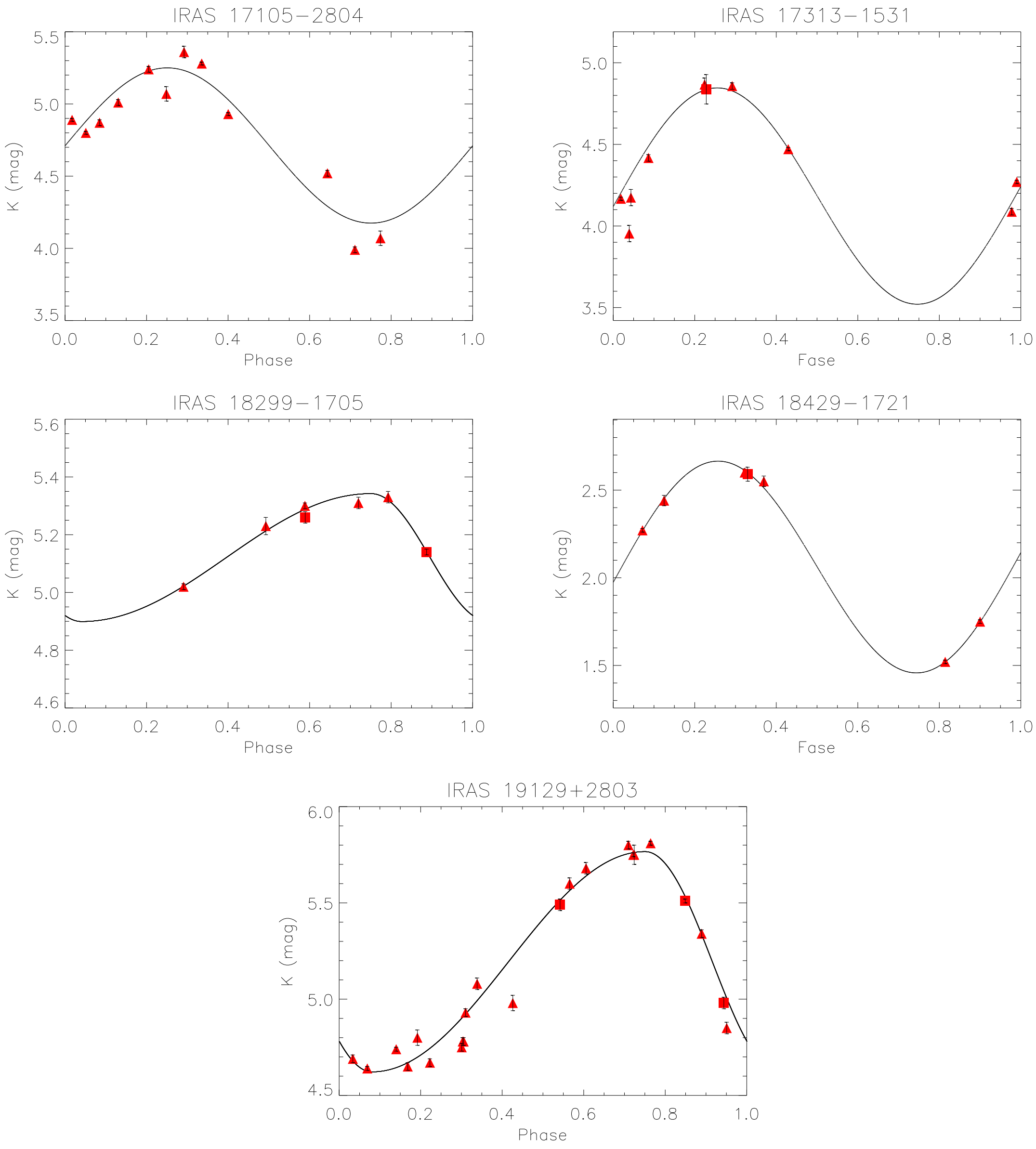

# Bibliography

Acker, A., Marcout, J., Ochsenbein, F., Stenholm, B., and Tylenda, R.: 1992, *Strasbourg - ESO catalogue of galactic planetary nebulae. Part 1; Part 2*, Garching: European Southern Observatory, 1992

Alcolea, J., Pardo, J. R., Bujarrabal, V., Bachiller, R., Barcia, A., Colomer, F., Gallego, J. D., Gómez-González, J., del Pino Cisneros, A., Planesas, P., del Río, S., Rodríguez-Franco, A., del Romero, A., Tafalla, M., and de Vicente, P.: 1999, A&AS **139**, 461

Allen, D. A., Hyland, A. R., Longmore, A. J., Caswell, J. L., Goss, W. M., and Haynes, R. F.: 1977, ApJ **217**, 108

Arribas, S. and Roger, C. M.: 1987, A&AS **70**, 303

Barnbaum, C., Omont, A., and Morris, M.: 1996, A&A **310**, 259

Barthès, D. and Luri, X.: 2001, A&A **365**, 519

Baud, B. and Habing, H. J.: 1983, A&A **127**, 73

Baud, B., Habing, H. J., Matthews, H. E., and Winnberg, A.: 1979, A&AS **36**, 193

Baud, B., Habing, H. J., Matthews, H. E., and Winnberg, A.: 1981a, A&A **95**, 171

Baud, B., Habing, H. J., Matthews, H. E., and Winnberg, A.: 1981b, A&A **95**, 156

Bedijn, P. J.: 1987, A&A **186**, 136

Beichman, C. A., Neugebauer, G., Habing, H. J., Clegg, P. E., and Chester, T. J.: 1988, in *Infrared astronomical satellite (IRAS) catalogs and atlases. Volume 1: Explanatory supplement*

Benson, P. J., Little-Marenin, I. R., Woods, T. C., Attridge, J. M., Blais, K. A., Rudolph, D. B., Rubiera, M. E., and Keefe, H. L.: 1990, ApJS **74**, 911

Bertin, E. and Arnouts, S.: 1996, A&AS **117**, 393

Bessell, M. S., Castelli, F., and Plez, B.: 1998, A&A **333**, 231

Blommaert, J.: 2003, in *ASSL Vol. 283: Mass-Losing Pulsating Stars and their Circumstellar Matter*, pp 355–+

Blommaert, J. A. D. L., van der Veen, W. E. C. J., van Langevelde, H. J., Habing, H. J., and Sjouwerman, L. O.: 1998, A&A **329**, 991

Blommaert, J. A. D. L., van Langevelde, H. J., and Michiels, W. F. P.: 1994, A&A **287**, 479

Boothroyd, A. I. and Sackmann, I.-J.: 1992, ApJ **393**, L21

Bowers, P. F. and Knapp, G. R.: 1989, ApJ **347**, 325

Bowers, P. F. and Sinha, R. P.: 1978, AJ **83**, 955

Bujarrabal, V., Alcolea, J., and Neri, R.: 1998, ApJ **504**, 915

Caswell, J. L. and Haynes, R. F.: 1975, MNRAS **173**, 649

Caswell, J. L., Haynes, R. F., Goss, W. M., and Mebold, U.: 1981, *Australian Journal of Physics* **34**, 333

Chan, S. J. and Kwok, S.: 1988, ApJ **334**, 362

Chen, P. S., Szczerba, R., Kwok, S., and Volk, K.: 2001, A&A **368**, 1006

Chengalur, J. N., Lewis, B. M., Eder, J., and Terzian, Y.: 1993, ApJS **89**, 189

Clark, J. S., Larionov, V. M., Crowther, P. A., Egan, M. P., and Arkharov, A.: 2003, A&A **403**, 653

Claussen, M. J., Kleinmann, S. G., Joyce, R. R., and Jura, M.: 1987, ApJS **65**, 385

Cohen, M., Wheaton, W. A., and Megeath, S. T.: 2003, AJ **126**, 1090

Cutri, R. M., Skrutskie, M. F., van Dyk, S., Beichman, C. A., Carpenter, J. M., Chester, T., Cambresy, L., Evans, T., Fowler, J., Gizis, J., Howard, E., Huchra, J., Jarrett, T., Kopan, E. L., Kirkpatrick, J. D., Light, R. M., Marsh, K. A., McCallon, H., Schneider, S., Stiening, R., Sykes, M., Weinberg, M., Wheaton, W. A., Wheelock, S., and Zacarias, N.: 2003, in *Two Micron All Sky Survey (2MASS) All-Sky Catalog of Point Sources*

D'Antona, F. and Mazzitelli, I.: 1996, ApJ **470**, 1093

David, P., Lesqueren, A. M., and Sivagnanam, P.: 1993, A&A **277**, 453

de Jong, T.: 1989, A&A **223**, L23+

Dickinson, D. F., Kollberg, E., and Yngvesson, S.: 1975, ApJ **199**, 131

Djorgovski, S. G., Gal, R. R., de Carvalho, R. R., Odewahn, S. C., Mahabal, A. A., Brunner, R., Lopes, P., and DPOSS Team: 2001, *Bulletin of the American Astronomical Society* **33**, 1461

Eder, J., Lewis, B. M., and Terzian, Y.: 1988, ApJS **66**, 183

Egan, M. P., Price, S. D., and Kraemer, K. E.: 2003, in *The Midcourse Space Experiment (MSX) Point Source Catalog Version 2.3*

Elias, J. H., Frogel, J. A., Matthews, K., and Neugebauer, G.: 1982, AJ **87**, 1029

Elitzur, M., Goldreich, P., and Scoville, N.: 1976, ApJ **205**, 384

Engels, D.: 2002, A&A **388**, 252

Engels, D., Kreysa, E., Schultz, G. V., and Sherwood, W. A.: 1983, A&A **124**, 123

Engels, D. and Lewis, B. M.: 1996, A&AS **116**, 117

Evans, N. J. and Beckwith, S.: 1977, ApJ **217**, 729

Feast, M. W., Glass, I. S., Whitelock, P. A., and Catchpole, R. M.: 1989, MNRAS **241**, 375

García-Lario, P.: 1992, *Ph.D. Thesis*

García-Lario, P., Manchado, A., Pych, W., and Pottasch, S. R.: 1997, A&AS **126**, 479

García-Lario, P. and Perea Calderón, J. V.: 2003, in *ESA SP-511: Exploiting the ISO Data Archive. Infrared Astronomy in the Internet Age*, pp 97–+

Gaylard, M. J., West, M. E., Whitelock, P. A., and Cohen, R. J.: 1989, MNRAS **236**, 247

Glass, I. S., Matsumoto, S., Carter, B. S., and Sekiguchi, K.: 2001, MNRAS **321**, 77

Glass, I. S. and Reid, N.: 1985, MNRAS **214**, 405

Glass, I. S., Whitelock, P. A., Catchpole, R. M., and Feast, M. W.: 1995, MNRAS **273**, 383

Goldreich, P. and Scoville, N.: 1976, ApJ **205**, 144

Groenewegen, M. A. T., de Jong, T., van der Bliek, N. S., Slijkhuis, S., and Willems, F. J.: 1992, A&A **253**, 150

Groenewegen, M. A. T. and Whitelock, P. A.: 1996, MNRAS **281**, 1347

Habing, H. J.: 1996, A&A Rev. **7**, 97

Habing, H. J., Olnon, F. M., Chester, T., Gillett, F., and Rowan-Robinson, M.: 1985, A&A **152**, L1

Harvey, P. M., Bechis, K. P., Wilson, W. J., and Ball, J. A.: 1974, ApJS **27**, 331

Herbst, T. M., Beckwith, S. V., Birk, C., Hippler, S., McCaughrean, M. J., Mannucci, F., and Wolf, J.: 1993, in *Proc. SPIE Vol. 1946, p. 605-609, Infrared Detectors and Instrumentation, Albert M. Fowler; Ed.*, pp 605–609

Herman, J., Burger, J. H., and Penninx, W. H.: 1986, A&A **167**, 247

Herman, J. and Habing, H. J.: 1985a, Phys. Rep. **124**, 257

Herman, J. and Habing, H. J.: 1985b, A&AS **59**, 523

Herman, J., Isaacman, R., Sargent, A., and Habing, H.: 1984, A&A **139**, 171

Hjalmarson, A. and Olofsson, H.: 1979, ApJ **234**, L199

Hrivnak, B. J., Kwok, S., and Volk, K. M.: 1988, ApJ **331**, 832

Hu, J. Y., Slijkhuis, S., de Jong, T., and Jiang, B. W.: 1993, A&AS **100**, 413

Hyland, A. R., Becklin, E. E., Frogel, J. A., and Neugebauer, G.: 1972, A&A **16**, 204

Jackson, T., Ivezić, Ž., and Knapp, G. R.: 2002, MNRAS **337**, 749

Jiménez-Esteban, F., Engels, D., and García-Lario, P.: 2001, in *Post-AGB Objects as a Phase of Stellar Evolution*, pp 49–+

Johansson, L. E. B., Andersson, C., Goss, W. M., and Winnberg, A.: 1977, A&AS **28**, 199

Jones, T. J., Bryja, C. O., Gehrz, R. D., Harrison, T. E., Johnson, J. J., Klebe, D. I., and Lawrence, G. F.: 1990, ApJS **74**, 785

Jones, T. J., McGregor, P. J., Gehrz, R. D., and Lawrence, G. F.: 1994, AJ **107**, 1111

Jura, M.: 1994, ApJ **422**, 102

Jura, M. and Kleinmann, S. G.: 1989, ApJ **341**, 359

Jura, M. and Kleinmann, S. G.: 1992, ApJS **79**, 105

Jura, M., Yamamoto, A., and Kleinmann, S. G.: 1993, ApJ **413**, 298

Kaifu, N., Buhl, D., and Snyder, L. E.: 1975, ApJ **195**, 359

Kistiakowsky, V. and Helfand, D. J.: 1995, AJ **110**, 2225

Klochkova, V. G.: 1995, MNRAS **272**, 710

Knauer, T. G., Ivezić, Ž., and Knapp, G. R.: 2001, ApJ **552**, 787

Knowles, S. H., Mayer, C. H., Cheung, A. C., Rank, D. M., and Townes, C. H.: 1969, *Science* **163**, 1055

Koornneef, J.: 1983a, A&AS **51**, 489

Koornneef, J.: 1983b, A&A **128**, 84

Kwok, S., Volk, K., and Bidelman, W. P.: 1997, ApJS **112**, 557

Lawrence, G., Jones, T. J., and Gehrz, R. D.: 1990, AJ **99**, 1232

Le Bertre, T.: 1988, *The Messenger* **51**, 24

Le Bertre, T.: 1992, A&AS **94**, 377

Le Bertre, T.: 1993, A&AS **97**, 729

Lepine, J. R. D., Ortiz, R., and Epchtein, N.: 1995, A&A **299**, 453

Lewis, B. M.: 1997, ApJS **109**, 489

Lewis, B. M.: 2002, ApJ **576**, 445

Lewis, B. M., Chengalur, J. N., Schmelz, J., and Terzian, Y.: 1990a, MNRAS **246**, 523

Lewis, B. M., Eder, J., and Terzian, Y.: 1987, AJ **94**, 1025

Lewis, B. M., Eder, J., and Terzian, Y.: 1990b, ApJ **362**, 634

Lewis, B. M. and Engels, D.: 1995, MNRAS **274**, 439

Lewis, B. M., Kopon, D. A., and Terzian, Y.: 2004, AJ **127**, 501

Likkel, L.: 1989, ApJ **344**, 350

Little-Marenin, I. R.: 1986, ApJ **307**, L15

Maciel, W. J. and Dutra, C. M.: 1992, A&A **262**, 271

Miller, G. E. and Scalo, J. M.: 1979, ApJS **41**, 513

Nakashima, J., Jiang, B. W., Deguchi, S., Sadakane, K., and Nakada, Y.: 2000, PASJ **52**, 275

Neugebauer, G. and Leighton, R. B.: 1969, *Two-micron sky survey. A preliminary catalogue*, NASA SP, Washington: NASA, 1969

Olivier, E. A., Whitelock, P., and Marang, F.: 2001, MNRAS **326**, 490

Olnon, F. M.: 1981, in *ASSL Vol. 88: Physical Processes in Red Giants*, pp 237–240

Olnon, F. M., Habing, H. J., Baud, B., Pottasch, S. R., de Jong, T., and Harris, S.: 1984, ApJ **278**, L41

Olnon, F. M., Raimond, E., Neugebauer, G., van Duinen, R. J., Habing, H. J., Aumann, H. H., Beintema, D. A., Boggess, N., Borgman, J., Clegg, P. E., Gillett, F. C., Hauser, M. G., Houck, J. R., Jennings, R. E., de Jong, T., Low, F. J., Marsden, P. L., Pottasch, S. R., Soifer, B. T., Walker, R. G., Emerson, J. P., Rowan-Robinson, M., Wesselius, P. R., Baud, B., Beichman, C. A., Gautier, T. N., Harris, S., Miley, G. K., and Young, E.: 1986, A&AS **65**, 607

Olofsson, H.: 1999, in *IAU Symp. 191: Asymptotic Giant Branch Stars*, pp 3–90

Ortiz, R. and Maciel, W. J.: 1994, A&A **287**, 552

Ortiz, R. and Maciel, W. J.: 1996, A&A **313**, 180

Price, S. D. and Walker, R. G.: 1976, *AFGL-TR-0208 Environemental Research papers*

Ratag, M. A. and Pottasch, S. R.: 1991, A&AS **91**, 481

Reid, I. N., Hughes, S. M. G., and Glass, I. S.: 1995, MNRAS **275**, 331

Reid, M. J.: 1993, ARA&A **31**, 345

Reid, M. J., Muhleman, D. O., Moran, J. M., Johnston, K. J., and Schwartz, P. R.: 1977, ApJ **214**, 60

Reid, N., Glass, I. S., and Catchpole, R. M.: 1988, MNRAS **232**, 53

Renzini, A.: 1981, in *ASSL Vol. 88: Physical Processes in Red Giants*, pp 431–446

Rowan-Robinson, M. and Chester, T.: 1987, ApJ **313**, 413

Schultz, G. V., Kreysa, E., and Sherwood, W. A.: 1976, A&A **50**, 171

Schwarzschild, M. and Härm, R.: 1965, ApJ **142**, 855

Sevenster, M. N., Chapman, J. M., Habing, H. J., Killeen, N. E. B., and Lindqvist, M.: 1997, A&AS **122**, 79

Sevenster, M. N., van Langevelde, H. J., Moody, R. A., Chapman, J. M., Habing, H. J., and Killeen, N. E. B.: 2001, A&A **366**, 481

Shklovskii, I. S.: 1956, *Astron. J. U.S.S.R.* **33**, 315

Sivagnanam, P. and Le Squeren, A.: 1990, in *From Miras to Planetary Nebulae: Which Path for Stellar Evolution?*, pp 225–238

Sivagnanam, P., Le Squeren, A. M., Minh, F. T., and Braz, M. A.: 1990, A&A **233**, 112

Skinner, C. J., Griffin, I., and Whitmore, B.: 1990, MNRAS **243**, 78

Smith, B. J.: 2003, AJ **126**, 935

Stellingwerf, R. F.: 1978, ApJ **224**, 953

Straniero, O., Chieffi, A., Limongi, M., Busso, M., Gallino, R., and Arlandini, C.: 1997, ApJ **478**, 332

te Lintel-Hekkert, P.: 1990, *Ph.D. Thesis*

te Lintel-Hekkert, P.: 1991, A&A **248**, 209

te Lintel-Hekkert, P., Caswell, J. L., Habing, H. J., Haynes, R. F., Haynes, R. F., and Norris, R. P.: 1991, A&AS **90**, 327

te Lintel-Hekkert, P., Versteege-Hensel, H. A., Habing, H. J., and Wiertz, M.: 1989, A&AS **78**, 399

van der Veen, W. E. C. J.: 1988, *Ph.D. Thesis*

van der Veen, W. E. C. J. and Breukers, R. J. L. H.: 1989, A&A **213**, 133

van der Veen, W. E. C. J. and Habing, H. J.: 1988, A&A **194**, 125 van der Veen, W. E. C. J. and Habing, H. J.: 1990, A&A **231**, 404

van Langevelde, H. J., Janssens, A. M., Goss, W. M., Habing, H. J., and Winnberg, A.: 1993, A&AS **101**, 109

van Langevelde, H. J., van der Heiden, R., and van Schooneveld, C.: 1990, A&A **239**, 193

Vassiliadis, E. and Wood, P. R.: 1993, ApJ **413**, 641

Volk, K. and Cohen, M.: 1989, AJ **98**, 931

Volk, K. and Kwok, S.: 1988, ApJ **331**, 435

Wagenhuber, J. and Groenewegen, M. A. T.: 1998, A&A **340**, 183

Wallerstein, G. and Knapp, G. R.: 1998, ARA&A **36**, 369

Weidemann, V.: 1990, ARA&A **28**, 103

Whitelock, P.: 1997, *Stellar Evolution in Real Time, 23rd meeting of the IAU, Joint Discussion 8, 22-23 August 1997, Kyoto, Japan.* 8

Whitelock, P., Feast, M., and Catchpole, R.: 1991, MNRAS **248**, 276

Whitelock, P., Marang, F., and Feast, M.: 2000, MNRAS **319**, 728

Whitelock, P., Menzies, J., Feast, M., Catchpole, R., Marang, F., and Carter, B.: 1995, MNRAS **276**, 219

Whitelock, P., Menzies, J., Feast, M., Marang, F., Carter, B., Roberts, G., Catchpole, R., and Chapman, J.: 1994, MNRAS **267**, 711

Whitelock, P. A., Feast, M. W., van Loon, J. T., and Zijlstra, A. A.: 2003, MNRAS **342**, 86

Willems, F. J. and de Jong, T.: 1986, ApJ **309**, L39

Wilson, W. J. and Barrett, A. H.: 1968, *Science* **161**, 778

Wilson, W. J. and Barrett, A. H.: 1972, A&A **17**, 385

Winters, J. M., Fleischer, A. J., Gauger, A., and Sedlmayr, E.: 1994, A&A **290**, 623

Wood, P. R.: 1998, A&A **338**, 592

Wood, P. R., Bessell, M. S., and Paltoglou, G.: 1985, ApJ **290**, 477

Wood, P. R. and Cahn, J. H.: 1977, ApJ **211**, 499

Wood, P. R., Habing, H. J., and McGregor, P. J.: 1998, A&A **336**, 925

Wood, P. R., Whiteoak, J. B., Hughes, S. M. G., Bessell, M. S., Gardner, F. F., and Hyland, A. R.: 1992, ApJ **397**, 552

Woolf, N. J. and Ney, E. P.: 1969, ApJ **155**, L181+

Zijlstra, A. A., Te Lintel Hekkert, P., Pottasch, S. R., Caswell, J. L., Ratag, M., and Habing, H. J.: 1989, A&A **217**, 157